LUT UNIVERSITY
LUT School of Energy Systems
LUT Mechanical Engineering

Joona Kauppila

INTRODUCTION OF A PROBABILISTIC FATIGUE ANALYSIS METHOD FOR COMPONENTS MADE OF SPHEROIDAL GRAPHITE CAST IRON, QUENCHED AND TEMPERED STEEL AND STRUCTURAL STEEL

25.10.2020

Examiner(s): Professor Timo Björk
M.Sc. (Tech.) Toni Kilpeläinen

TIIVISTELMÄ

LUT-Yliopisto
LUT School of Energy Systems
LUT Kone

Joona Kauppila

Todennäköisyysteoriaan perustuvan väsymisanalyysimenetelmän käyttöönotto pallografiittivaluraudasta, nuorrutusteräksestä ja rakenneteräksestä valmistetuille koneenosille

Diplomityö

2020

160 sivua, 80 kuvaa, 13 taulukkoa ja 8 liitettä

Tarkastajat: Professori Timo Björk
DI Toni Kilpeläinen

Hakusanat: Haigh diagrammi, Moniaksiaalinen väsyminen, Nuorrutusteräs, Pallografiittivalurauta, Rakenneteräs, S-N käyrä, Todennäköisyysteoria, Väsymisanalyysi

Tämän työn tarkoituksena on esitellä käyttöönotettavaksi todennäköisyysteoriaan perustuva väsymisanalyysimenetelmä pallografiittivaluraudasta, nuorrutusteräksestä ja rakenneteräksestä valmistetuille koneenosille. Menetelmän tulee perustua elementtimenetelmällä laskettujen paikallisten jännitysten käyttöön, ilman tarvetta määrittää nimellisiä jännityksiä. Lisäksi menetelmän tulee kyetä ottaa huomioon moniaksiaalinen väsyminen suhteisissa ja epäsuhteisissa kuormitustapauksissa. Työn tuloksena tulisi olla määritetty yksiselitteiset ohjeet siten että menetelmä voidaan ohjelmoida automaattiseksi työkaluksi.

Menetelminä tässä työssä käytetään kirjallisuusselvitystä, olemassa olevan väsytyskoedatan hyödyntämistä ja elementtimenetelmää. Lisäksi analyysimenetelmän vaiheet esitellään melko yksinkertaisen komponentin ja kuormitustapauksen esimerkkianalyysillä.

Työn tuloksena esitellään vaatimukset käyttäjän syöttämistä arvoista ja menetelmän tulosteista, sekä menetelmän eri laskentavaiheet. Lisäksi esitellään esimerkkianalyysin tuloksia. Tuloksiin perustuen johtopäätöksinä voidaan todeta, että esitelty menetelmä ei vaadi nimellisjännitysten käyttöä ja että moniaksiaalinen väsyminen voidaan käsitellä kattavasti. Tämän lisäksi esitellyt vuokaaviot antavat hyvän pohjan ohjelmointityölle.

ABSTRACT

LUT University
LUT School of Energy Systems
LUT Mechanical Engineering

Joona Kauppila

Introduction of a probabilistic fatigue analysis method for components made of spheroidal graphite cast iron, quenched and tempered steel and structural steel

Master's thesis

2020

160 pages, 80 figures, 13 tables and 8 appendices

Examiners: Professor Timo Björk
M. Sc. (Tech.) Toni Kilpeläinen

Keywords: Fatigue analysis, Haigh diagram, Multiaxial fatigue, Probabilistic, Quenched and tempered steel, S-N curve, Spheroidal graphite cast iron, Structural steel

The aim of this thesis is to introduce a probabilistic fatigue analysis method for components made of spheroidal graphite cast iron, quenched and tempered steel and structural steel. The method should be based on using local stresses calculated with finite element analysis, without the need to consider nominal stresses. Also, it should be able to consider multiaxial fatigue in proportional and non-proportional loading cases. As a result of this work, clear guidelines and steps for the method should be established in such a way that it is possible to program an automated analysis tool for fatigue analysis according to this method.

The methods used in this work include literature study, use of existing fatigue test data and finite element analysis. Also, the finished workflow is demonstrated with an example analysis of a relatively simple component and load case to clarify the different steps of the analysis.

As a result, required inputs from the user, outputs and different stages of the analysis method are presented. In addition, the results of the example analysis are shown. Based on the results, it is concluded that the introduced method does not require the use of nominal stresses and that multiaxial fatigue can be handled in a comprehensive manner. Furthermore, the flowcharts depicting the workflow give a good basis for the programming work.

ACKNOWLEDGEMENTS

I would like to thank Professor Timo Björk at LUT for guidance and help during the thesis project. Also, thank you for contacting me about this thesis topic when it was offered by The Switch.

Thank you to Toni Kilpeläinen and Tomi Knuutila from The Switch for providing me with this interesting and challenging topic. I would also like to thank Toni for guidance and monitoring of the work.

Also, thank you to Roger Rabb for giving a lot of important suggestions and recommendations regarding the topics covered in his book “Väsyminen ja Todennäköisyysteoria” which was an essential part of this work.

Joona Kauppila
Lappeenranta 9.9.2020

TABLE OF CONTENTS

LIST OF SYMBOLS AND ABBREVIATIONS

A	Area [mm^2]
A	Constant [-]
A_{eff}	Effective area [mm^2]
A_{ref}	Reference area [mm^2]
a	Crack length [mm]
a	Constant in Dang Van criterion [-]
a	Major semi-axis of an elliptical hole [mm]
a_0	Initial crack size [mm]
a_0	Intrinsic crack length [µm]
a_{ext}	Extrapolated defect size [µm]
a_f	Final crack size [mm]
a_{med}	Median value of defect distribution [µm]
a_σ	Material constant [-]
$\sqrt{area_R}$	The equivalent defect size for surface roughness [µm]
B	Constant [-]
$2b$	Pitch of the surface roughness [µm]
b	Auxiliary variable [-]
b	Minor semi-axis of an elliptical hole [mm]
C	Constant [-]
C	Constant which considers the mean stress effect [-]
C	Material constant [(mm/cycle)/(MPa·m$^{1/2}$)^m]
C_μ	Confidence level [-]
c	Half-width of a crack [mm]
D	Damage sum [-]
D	Findley damage [MPa]
D_{HC}	High cycle damage sum [-]
D_{LC}	Low cycle damage sum [-]
D_{tot}	Total damage sum, $D_{HC} + D_{LC}$ [-]
d	Slip band length [µm]
dA	Surface element [-]

da/dN	Cyclic crack growth rate [mm/cycle]
$\mathrm{dev}\rho_{ij}$	Deviatoric part of stabilized residual stress tensor [MPa]
$E(x)$	Expected value [-]
$E(\sigma_{af})$	Expected value [MPa]
F	Axial force [N]
F	Geometry factor [-]
$F(\sigma)$	Cumulative distribution function (CDF) [-]
F_e	Embedding energy [J]
F_i	Force acting on atom i [N]
F_o	Surface roughness factor [MPa]
f	Fatigue limit in shear [MPa]
$f(\sigma_{af})$	Probability density function (PDF) [-]
$f_Z(Z)$	Multivariate probability density function of Z
G	Shear modulus [MPa]
H_V	Vickers hardness [MPa]
K	Stress intensity factor [MPa·m$^{1/2}$]
K_A	Anisotropy factor [-]
K_{AT}	Anisotropy and technological factor [-]
K_c	Fracture toughness [MPa·m$^{1/2}$]
K_I	Stress intensity factor for Mode I crack [MPa·m$^{1/2}$]
K_{Ic}	Plane strain fracture toughness [MPa·m$^{1/2}$]
K_N	Life factor [-]
K_R	Surface roughness factor [-]
K_{size}	Statistical size factor [-]
K_T	Technological factor [-]
K_t	Stress concentration factor [-]
ΔK	Stress intensity range [MPa·m$^{1/2}$]
ΔK_{th}	Threshold stress intensity range [MPa·m$^{1/2}$]
k	Normal stress sensitivity [-]
k	Slope exponent of S-N curve [-]
k	Slope of Haigh diagram [-]
k_0	Slope exponent of an unnotched test specimen [-]
k_∞	Slope exponent of a very sharp notch [-]

L	Load effect [-]
L	Material length scale [µm]
M	Additive inverse of the slope of Haigh diagram k [-]
m_i	Mass of the atom i [u]
m	Number of links [-]
m	Slope of the crack growth log-log plot [-]
N	Fatigue life [cycles]
N	Total number of discrete values [-]
N_{af}	Number of cycles at knee-point of S-N curve [cycles]
N_{eq}	Equivalent number of cycles [cycles]
N_g	Number of cycles required for crack nucleation [cycles]
N_i	Shape function for node i [-]
n	Frequency [-]
n	Notch sensitivity [-]
n	Number of links [-]
n	Number of test specimens [-]
$\vec{n}_{cr}$	Normalized direction vector of critical plane [-]
n_{ref}	Reference number of cycles [cycles]
P	Failure probability [-]
p	Exponent which considers the effect of relative stress gradient χ^* [-]
p_i	Probability of x_i [-]
$\boldsymbol{Q}$	Rotation matrix [-]
R	Resistance effect [-]
R	Stress ratio [-]
R	Survival probability [-]
R_i	Reliability of i [-]
R_m	Ultimate strength [MPa]
R_m^*	Fictive ultimate strength [MPa]
R_{mc}	Ultimate compressive strength [MPa]
R_{mSmin}	Material constant [MPa]
$R_{p0.2}$	Yield strength [MPa]
R_z	Height of the surface roughness profile [µm]
r	Exponent which considers how C changes as a function of χ^* [-]

r	Radius, polar coordinate [mm]
r_c	Critical distance [µm]
r_{ij}	Separation between atoms [Å]
S	Remote stress [MPa]
S_F	Safety factor on stress [-]
$S_{F,H}$	Safety factor on stress of Haibach S-N curve extension [-]
S_N	Safety factor on fatigue life [-]
$S_{F,rad}$	Radial safety factor [-]
$S_{F,ver}$	Vertical safety factor[-]
s	Standard deviation [-]
s^2	Variance [-]
s_{ln}	Logarithmic standard deviation [-]
$s_{ln,H}$	Logarithmic standard deviation of fatigue strength for Haibach S-N curve extension [-]
s_N	Logarithmic standard deviation of fatigue life [-]
s_N^2	Variance of fatigue life [-]
s_r	Relative standard deviation [-]
s_{rC10}	Standard deviation with a confidence level of 10 % [-]
s_{rC90}	Standard deviation with a confidence level of 90 % [-]
s_σ	Standard deviation [MPa]
s_σ^2	Variance [-]
T	Return period [-]
T	Torque [Nmm]
t	Normalized variable [-]
t	Time [s]
t_2	Variable for Student's distribution [-]
U	Potential energy [J]
$V(\sigma_{af})$	Variance [-]
V_{ij}	Pair potential contribution to the potential energy of atom i [J]
W_c	Specific fracture energy per unit area [kJ/m^2]
W_i	Weight coefficient [-]
X	Discrete random variable [-]
$\boldsymbol{X}$	Global nodal coordinates [-]

$\boldsymbol{x_i}$	Position vector of atom *i* [-]
x_i	Values of discrete random variable [-]
$\overline{x}$	Sample mean value [-]
$\boldsymbol{Y}$	Global nodal coordinates [-]
$\boldsymbol{Z}$	Global nodal coordinates [-]
α	Parameter [-]
α_k	Stress concentration factor [-]
β	Weibull distribution shape parameter [-]
β_k	Notch factor [-]
β_R	Reliability index [-]
$\Gamma(t)$	Gamma function [-]
$\Delta\sigma$	Normal stress range [MPa]
$\Delta\sigma_{af}$	Fatigue limit range [MPa]
$\Delta\tau$	Shear stress range [MPa]
$\Delta\overline{\tau}$	Average shear stress range of a slip band [MPa]
ζ	Natural coordinate [-]
η	Natural coordinate [-]
θ	Angle, polar coordinate [°]
λ	Parameter of standard normal distribution [-]
μ_{ln}	Logarithmic mean value [-]
μ_{ln+SD}	Logarithmic mean value + one standard deviation [-]
ν	Poisson's ratio [-]
ξ	Natural coordinate [-]
ρ	Notch root radius [mm]
ρ_{ij}	Contribution of atom *j* to the total electron density at atom *i* [-]
ρ_{ij}	Stabilized residual stress tensor [MPa]
$\rho_{ij,h}$	Hydrostatic part of stabilized residual stress tensor [MPa]
$\Sigma_{ij}(t_i)$	Macroscopic stress tensor [MPa]
σ	Normal stress [MPa]
$[\sigma]$	Stress matrix [MPa]
$\sigma_{0.2}$	Yield strength [MPa]
σ_a	Normal stress amplitude [MPa]

σ_{ac}	Critical stress amplitude [MPa]
$\sigma_{a,eq}$	Equivalent stress amplitude [-]
σ_{af}	Fatigue limit [MPa]
$\overline{\sigma}_{af}$	Expected value of fatigue limit [MPa]
$\sigma_{af,P}$	Fatigue limit reduced to failure probability P [MPa]
$\sigma_{a,ref}$	Reference stress amplitude [MPa]
$\sigma_{aR=0}$	Fatigue limit for pulsating load [MPa]
$\sigma_{aR=-1}$	Fatigue limit for completely reversed loading [MPa]
$\overline{\sigma}_{af,c_\mu}$	Population value for the mean of fatigue limit [MPa]
σ_b	Ultimate strength [MPa]
$\sigma_{b,comp}$	Ultimate compressive strength [MPa]
σ_{ch}	Characteristic stress [MPa]
$\sigma_h(t_i)$	Hydrostatic stress when time is t_i [MPa]
$\sigma_{ij}(t_i)$	Microscopic stress tensor [MPa]
σ_m	Mean stress [MPa]
$\sigma_{mR=0}$	Means stress when $R = 0$ [MPa]
σ_{med}	Median value of stress [MPa]
σ_n	Normal stress [MPa]
σ_{nom}	Nominal stress [MPa]
σ_{peak}	Peak stress [MPa]
σ_{tr}	Threshold value for fatigue limit [MPa]
σ_{VM}	Von Mises stress [MPa]
σ_x	X normal stress component [MPa]
σ_y	Y normal stress component [MPa]
σ_z	Z normal stress component [MPa]
τ_a	Shear stress amplitude [MPa]
$\tau_a(t_i)$	Microscopic shear stress amplitude when time is t_i [MPa]
$\tau_{af,\sigma h=0}$	Fatigue limit in shear when hydrostatic stress is zero [MPa]
τ_{CRSS}	Critical resolved shear stress [MPa]
τ_{xy}	XY shear stress component [MPa]
τ_{yz}	YZ shear stress component [MPa]
τ_{zx}	ZX shear stress component [MPa]
Φ	Cumulative distribution function of standard normal distribution [-]

χ^*	Relative stress gradient [mm^{-1}]

CDF	Cumulative distribution function
CGF	Continuous grain flow
CRSS	Critical resolved shear stress
EAM	Embedded atom method
FEA	Finite Element analysis
FEM	Finite Element method
FFM	Finite fracture mechanics
HCF	High cycle fatigue
ICM	Imaginary crack method
K-T	Kitagawa-Takahashi
LCF	Low cycle fatigue
LEFM	Linear elastic fracture mechanics
LM	Line method
MD	Molecular dynamics
PDF	Probability density function
PM	Point method
SD	Standard deviation
SEM	Scanning electron microscope
SIF	Stress intensity factor
TCD	The Theory of critical distances
VHCF	Very high cycle fatigue

1 INTRODUCTION

The Switch specializes in electrical drive train technology, focusing on permanent magnet, solid rotor and variable speed drive technologies in areas of wind, marine and turbo/industry solutions (The Switch 2020). Design of components for these kinds of applications need to consider material fatigue and now, The Switch is looking to develop a new in-house fatigue analysis method.

1.1 Background

Currently The Switch performs fatigue analyses of castings and machined parts according to the method described in DNVGL-ST-0361. This has been found problematic because the method is based on nominal stresses which can be difficult or impossible to obtain from finite element analysis results, especially in the cases of more complex geometries.

Another problem is that although DNVGL-ST-0361 gives some guidance about multiaxial stresses, they are not treated properly in the current analysis process. This may yield unconservative results in some cases.

Evaluation of defects observed during manufacturing is difficult. It would be desirable to have allowable defect size for critical areas of the component, but the present analysis method is not capable of providing this information. In other words, the direct link between defect size and local fatigue strength is missing.

1.1.1 DNVGL-ST-0361

DNVGL-ST-0361 Machinery for wind turbines gives guidelines for the design of wind turbine machinery components and structures. It is based on safe life design method and for the fatigue limit state the typical design life time for wind turbines is 20 years. (DNVGL-ST-0361 2016, p. 9, 36.)

Current fatigue analysis method from DNVGL-ST-0361 is based on calculation of synthetic S-N curves. This calculation is applicable for non-welded forged and rolled parts and for cast steel and spheroidal graphite cast iron. (DNVGL-ST-0361 2016, p. 50-52.) The process

flow charts for *Non-welded forged and rolled parts* and *Cast steel and spheroidal graphite cast iron* are presented in figures 1 and 2.

4.6.2 Non-welded forged and rolled parts

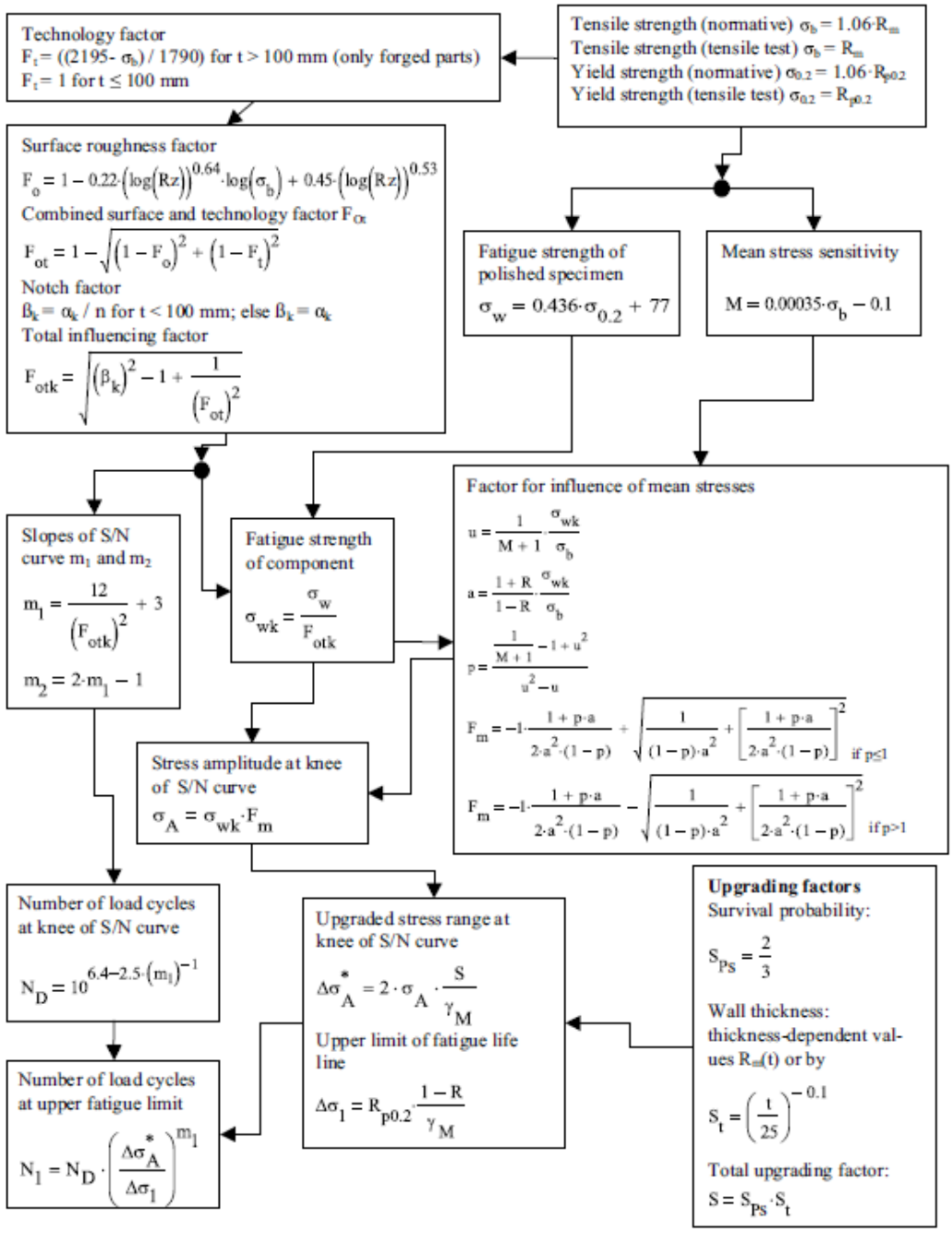

Figure 1. Calculation of synthetic S-N curve for non-welded forged and rolled parts (DNVGL-ST-0361 2016, p. 51).

4.6.3 Cast steel and spheroidal graphite cast iron

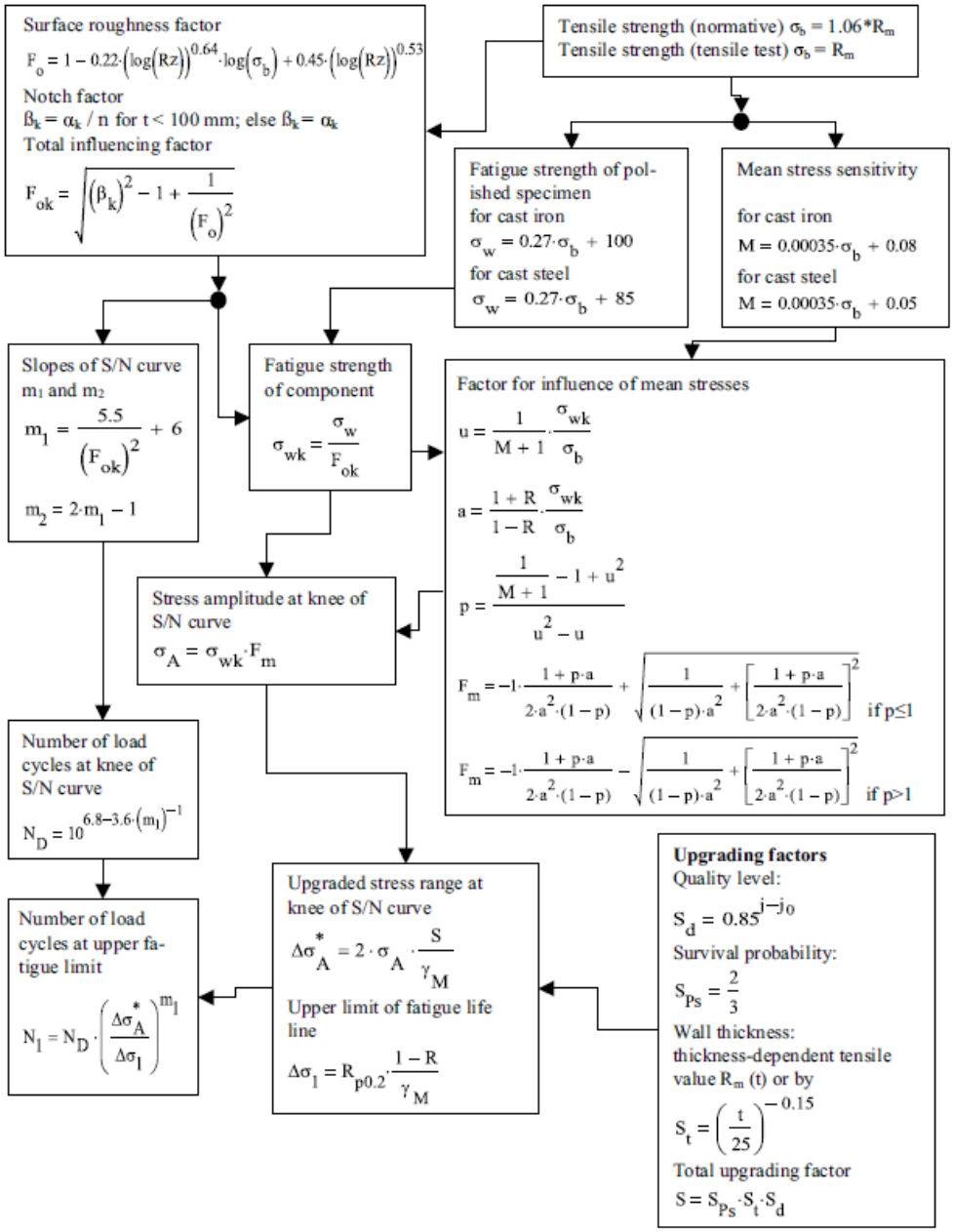

Figure 2. Calculation of synthetic S-N curve for cast steel and spheroidal graphite cast iron (DNVGL-ST-0361 2016, p. 52).

One of the problems of this method is the use of notch factor β_k:

$$\beta_k = \frac{\alpha_k}{n} \tag{1.1}$$

In equation (1.1) α_k is stress concentration factor and n is notch sensitivity (DNVGL-ST-0361 2016, p. 51-52). It may be difficult to define nominal stress and the corresponding stress concentration factor from the modern Finite Element analysis (FEA) results, especially if the geometry is complex. Nowadays FEA models can accurately and relatively quickly calculate the local stresses and thus the use of nominal stress based methods is not effective.

Haigh diagrams for different grades of spheroidal graphite cast iron, structural steel (S355) and quenched and tempered steel (42CrMO4) constructed on the basis of the flowcharts above are presented in figures 3 and 4. These are valid when nominal stresses are considered but again, this may not be useful if there are problems with defining the actual nominal stress in the component. Furthermore, these diagrams do not indicate how the material behaves when there is local plasticity.

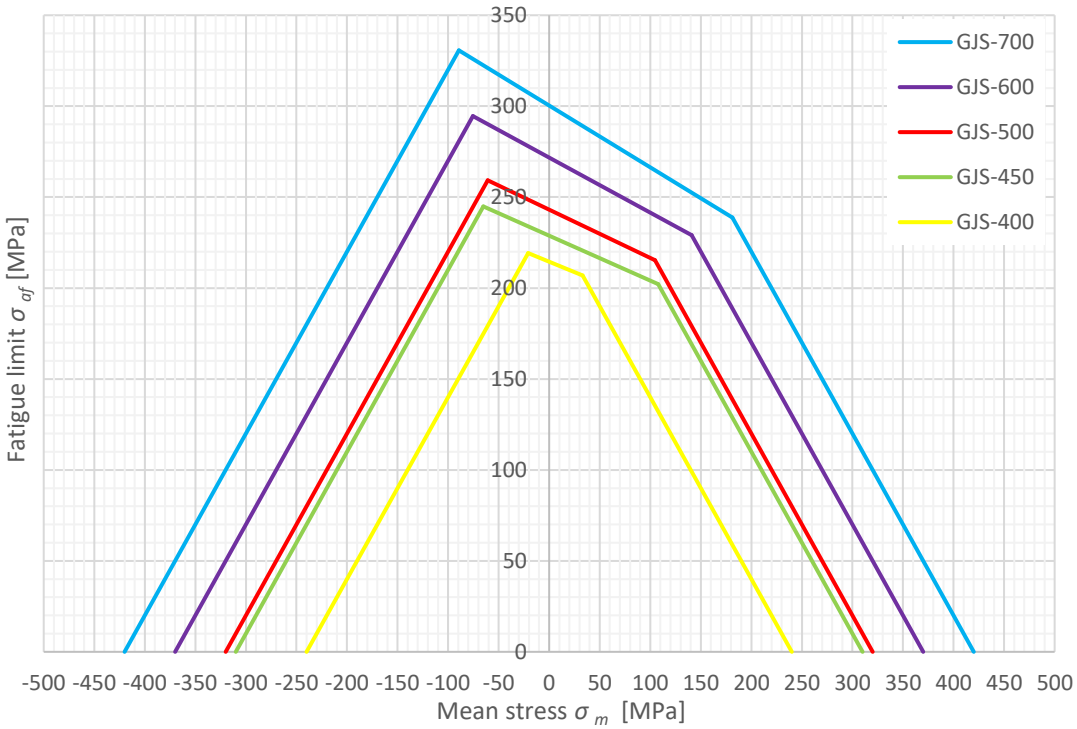

Figure 3. Haigh diagram for spheroidal graphite cast iron according to DNVGL-ST-0361 (2016, p. 46, 52).

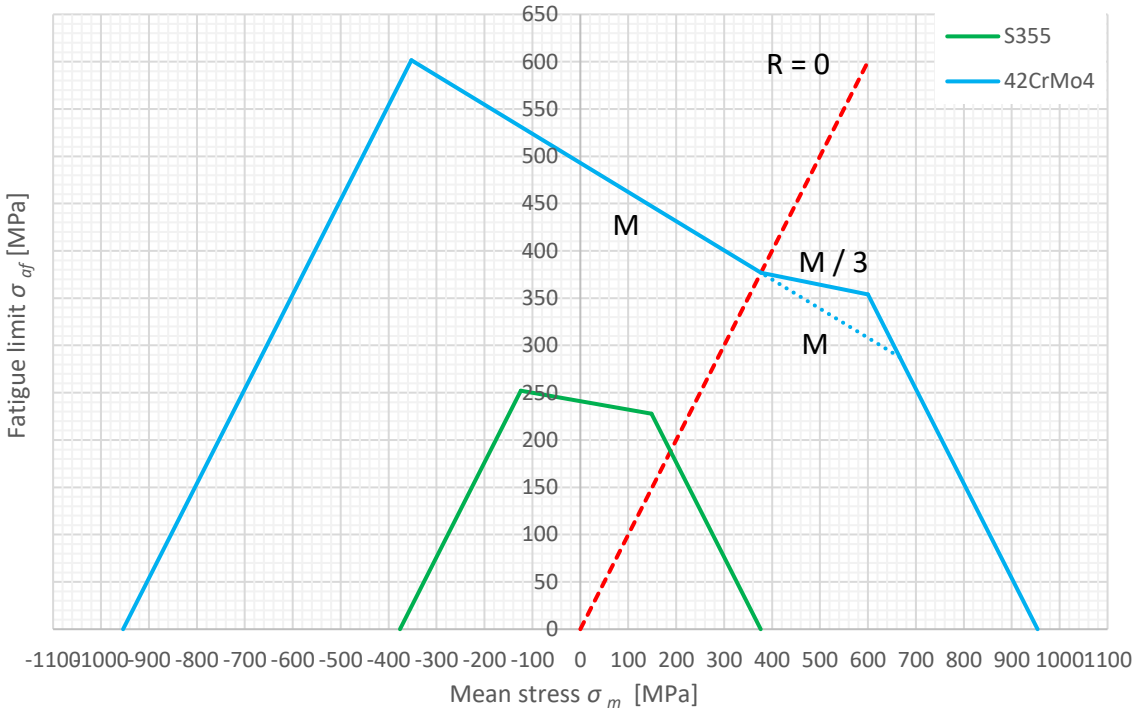

Figure 4. Haigh diagram for S355 and 42CrMo4 according to DNVGL-ST-0361 (2016, p. 46, 51).

1.2 Objectives

The objective of this thesis is to introduce a new method for fatigue analysis. The method should be based on using local stresses calculated with Finite Element Method (FEM) and it should consider multiaxial fatigue in proportional and non-proportional load cases. Also, the method should be based on probabilistic approach on fatigue and the determination of component's actual failure probability should be straightforward. Furthermore, a connection between defect size and local fatigue strength should be demonstrated so that it would be possible to give quality requirements for critical areas of components.

As a result of this work, clear guidelines and algorithms should be established so that it is possible to program a tool for the utilization of the new method. Also, an example analysis is performed with the new method.

1.3 Scope

Scope of this thesis is defined on the basis of materials used by The Switch in their components. There is no limitation on the type of component, so the new analysis method covers all components made of specified materials.

Materials within the scope of this thesis include spheroidal graphite cast iron, structural steel and quenched and tempered steel. The main focus is on various strength grades of spheroidal graphite cast iron, S355 structural steel and 42CrMo4 quenched and tempered steel.

This work covers non-welded forged and rolled components, castings and machined parts. In essence, the new analysis method should be applicable to at least the same extent as the method described in DNVGL-ST-0361.

1.4 Methods

The objective will be reached by introducing options for different aspects of fatigue analysis and utilizing the best suited one regarding the objective and scope of this thesis. The basis of the new method will be probabilistic approach on fatigue as per Roger Rabb's research and suggestions.

The methods used in development of the new analysis procedure include literature study, utilization of existing fatigue testing data and finite element analysis. No fatigue testing will be conducted as a part of this work.

1.5 Fatigue

Material, structures and components that are being subjected to repeated loads and the cyclic stresses caused by these loads are prone to suffer from microscopic damage. Even at stress levels where yielding does not dominate the behavior, this microscopic damage can accumulate and develop into a macroscopic crack. As the cycling continues, the crack grows and eventually failure of the component or structure will occur. This whole chain of events is called fatigue. (Dowling 2013, p. 416–417, 424.)

Cyclic loading can be described with a few factors and equations. The important definitions include stress range $\Delta\sigma$, maximum stress σ_{max}, minimum stress σ_{min}, stress amplitude σ_a, mean stress σ_m and stress ratio R. These are explained in the following equations and in figure 5.

For amplitude and mean stress (Dowling 2013, p. 419):

$$\sigma_a = \frac{\Delta\sigma}{2} = \frac{\sigma_{max} - \sigma_{min}}{2} \tag{1.2}$$

$$\sigma_m = \frac{\sigma_{max} + \sigma_{min}}{2} \tag{1.3}$$

For maximum and minimum stresses (Dowling 2013, p. 419):

$$\sigma_{max} = \sigma_m + \sigma_a \tag{1.4}$$

$$\sigma_{min} = \sigma_m - \sigma_a \tag{1.5}$$

And for *R* (Dowling 2013, p. 419):

$$R = \frac{\sigma_{min}}{\sigma_{max}} \tag{1.6}$$

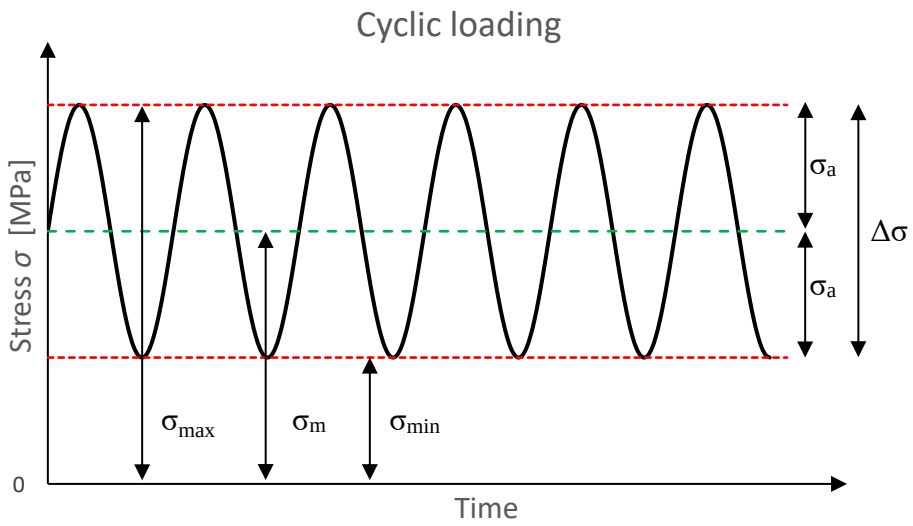

Figure 5. Constant amplitude cyclic loading.

The fatigue life consists of two periods: a *crack initiation* and a *crack growth period*, after which the final failure occurs. During the initiation period microcracks nucleate in slip bands in the material and start growing erratically due to effects caused by the microstructure of the material. After the microcrack growth has progressed away from the nucleation site, the growth becomes more regular and the crack growth period begins. These two periods are

separated since they are affected by different factors. (Schijve 2009, p. 14–15.) The phases of the fatigue life and the factors affecting them are presented in figure 6.

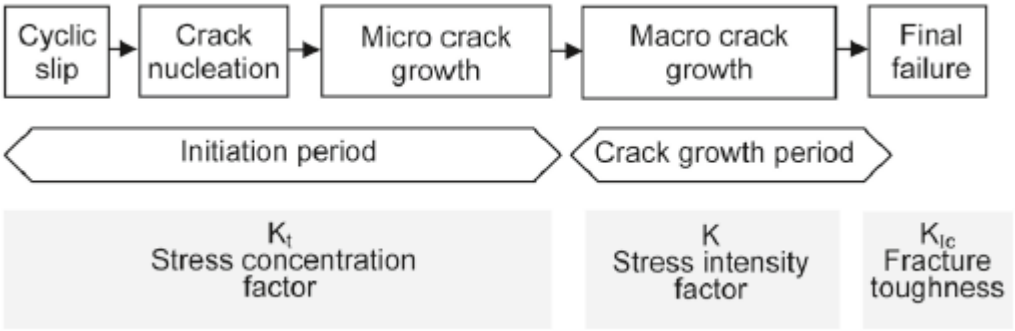

Figure 6. Phases of the fatigue life (Schijve 2009, p. 15).

1.5.1 Crack initiation

The fatigue crack nucleation is caused by cyclic slip which means that cyclic plastic deformation happens in a small number of grains. This microplasticity often happens in the grains which are located on the free surface of the material because there the plastic deformation is less constrained by the neighboring grains. As the constraint on the slip is lower on the surface, it can occur at lower stress levels than in more constrained subsurface grains. (Schijve 2009, p. 16.)

Cyclic shear stresses are required to cause cyclic slip. Depending on the size, shape and orientation of the grains as well as elastic anisotropy of the material, the shear stress on slip planes is varying between grains. On the surface of the material aforementioned conditions may be more favorable in some grains than in others and slip can occur. When slip occurs in a grain, a slip step is created on the material surface and a portion of new material (i.e. material that has not been in contact with the surrounding environment) is exposed and covered by a tightly adhering oxide layer. Additionally, some strain hardening occurs in the slip band during loading. Because of the oxide layer and the strain hardening, a higher, reversed shear stress will form on the same slip band. Reversed slip will therefore occur in the same slip band but on an adjacent parallel slip plane. (Schijve 2009, p. 15–17.) The principle of cyclic slip is shown in figure 7.

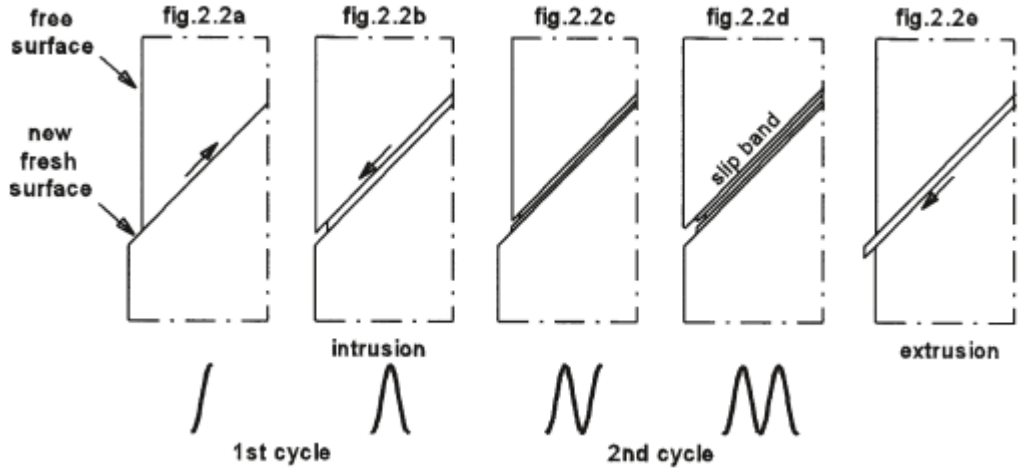

Figure 7. Formation of slip bands (Schijve 2009, p. 16).

As is shown in figure 7, single cycle is enough for a microscopical intrusion to form. This intrusion is a start of a microcrack and as the mechanism that occurred during the first cycle is repeated in the consequent cycles, the crack starts to extend. An extrusion could be formed if the reversed slip occurred on the lower side of the slip band. However, an intrusion is more probable according to minimum potential strain energy principle. (Schijve 2009, p. 17–18.)

Inclusions, such as impurities, can be found in most materials. They affect the stress distribution of the material on microlevel and they can interact with cyclic slip thus providing a nucleation site for a microcrack. The nucleation of a microcrack at an inclusion often happens near the surface of the material because of the aforementioned lower restraint on slip. Sometimes nucleation can happen deeper in the material, for example due to a large inclusion and the presence of tensile residual stress. (Schijve 2009, p. 25–26.)

As was mentioned, crack initiation starts on the surface of the material because of the lower restraint on cyclic slip. In addition to this, geometric discontinuities like holes and notches promote the initiation from the surface by causing stress concentrations. The magnitude of the stress concentration is dependent on the shape of the notch. The stress concentration can be described with stress concentration factor K_t which is the ratio between the peak stress σ_{peak} at the root of the notch and the nominal stress σ_{nom} affecting in an area of the part where there are no stress concentrations (see figure 8). (Schijve 2009, p.59–61.)

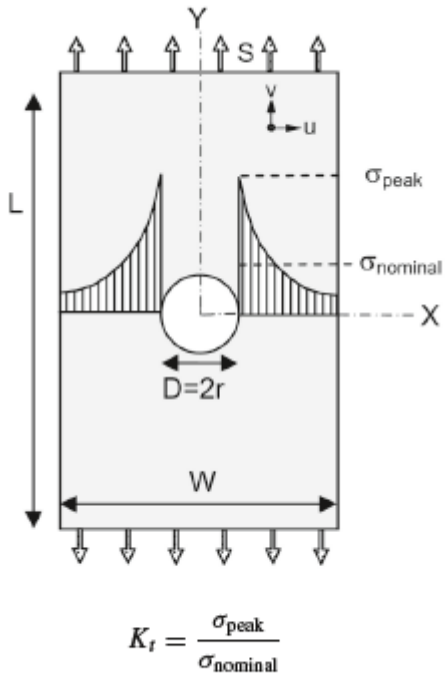

Figure 8. Definition of stress concentration factor K_t (Mod. Schijve 2009, p. 60).

It should be noted that peak stress σ_{peak} obtained by using the K_t factor is an elastic concept i.e. all deformations should be elastic (Schijve 2009, p. 61). When K_t is known, the peak stress at the notch can be calculated (Schijve 2009, p. 60):

$$\sigma_{peak} = K_t \sigma_{nom} \tag{1.7}$$

As was mentioned above, the shape of the notch affects the magnitude of K_t. Notch root radius ρ is an important factor and its effect on K_t for an elliptical hole in an infinite sheet loaded in tension can be seen below (Schijve 2009 p. 64):

$$K_t = 1 + 2\frac{a}{b} = 1 + 2\sqrt{\frac{a}{\rho}} \tag{1.8}$$

, where a and b are the semi-axes of an elliptical hole. Figure 9 shows the effect of different dimensions on K_t for tension loaded circular bar with a notch.

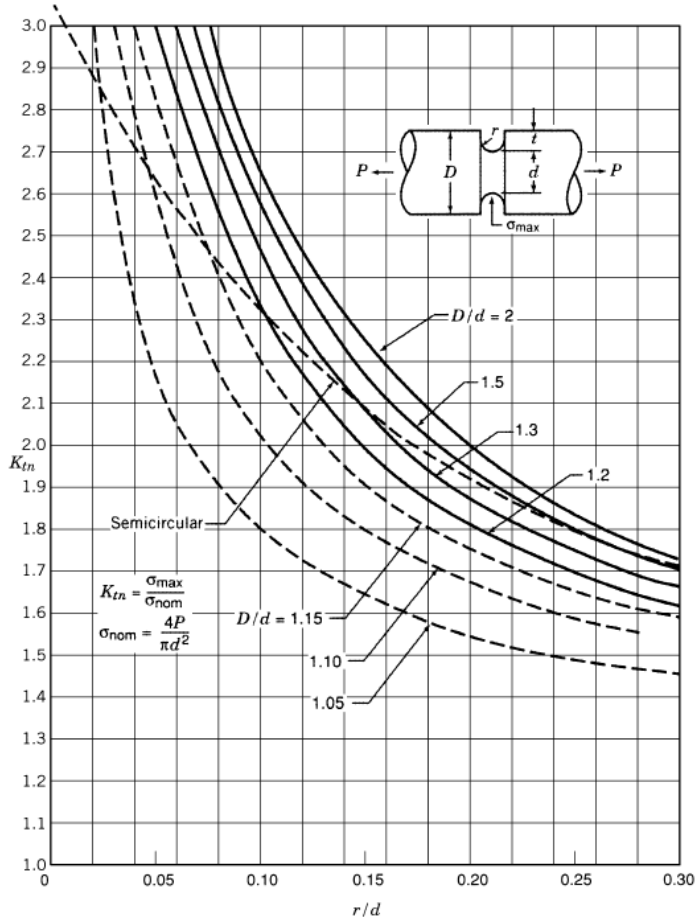

Figure 9. Effect of different dimensions on K_t for tension loaded circular bar (Pilkey 1997, p. 99). Similar charts can be found for different geometries and loading cases.

Stress gradient of σ_y along the X-axis (figure 10) can be used to consider the size effect on the fatigue limit. The stress gradient at the root of a notch provides information about the size of the volume of highly stressed material. (Schijve 2009, p. 65–66.)

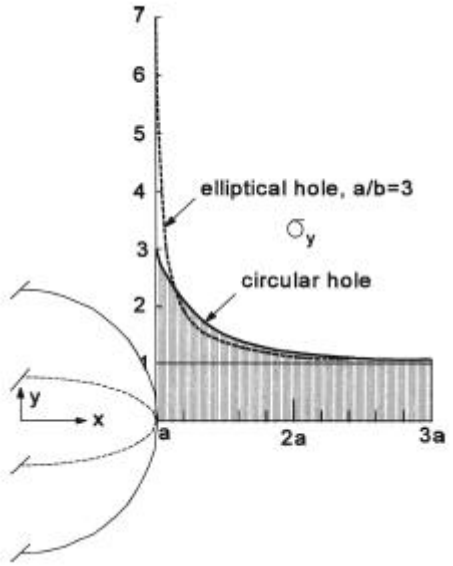

Figure 10. Stress gradients at the root of a notch (Schijve 2009, p. 66).

However, the gradient of tangential stress decreases relatively slowly compared to the stress along the X-axis (in figure 10). As was mentioned earlier, the crack nucleation starts at the material surface and because of this, the stress gradient along the edge of the notch may have a greater importance on crack nucleation than the gradient in X-direction (in figure 10). (Schijve 2009, p. 67–68.) Relatively slow decrease of stress in tangential direction compared to the perpendicular direction is illustrated in figure 11.

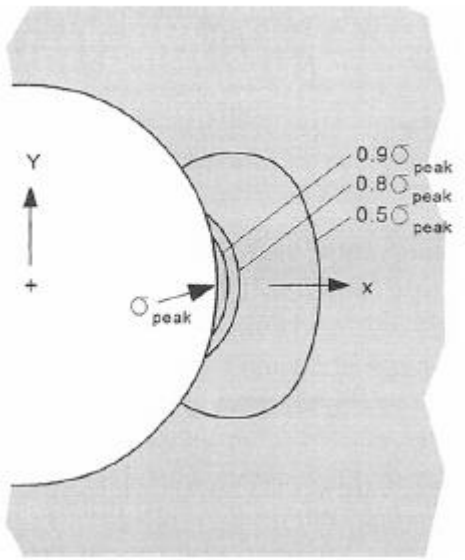

Figure 11. Stress along the edge of the notch. Lines represent constant principal stress under tension loading (Y-direction). (Schijve 2009, p. 68.)

1.5.2 Crack growth

During the crack growth period, growth is no longer affected by surface conditions. Instead, the crack growth becomes a bulk material phenomenon. After the crack grows away from the free surface and its effect, slip deformations happen on more than one slip plane and the microcrack deviates from the initial direction of the slip band as shown in figure 12. Usually, at this stage the crack starts to grow perpendicular to the main principal stress. (Schijve 2009, p. 19, p. 39–40.)

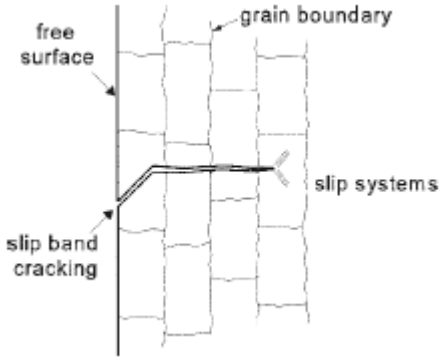

Figure 12. A crack growing further into the material from the surface (Schijve 2009, p. 19).

During loading the plastic deformation at the crack tip opens the crack and slip deformation causes some crack extension. There are two symmetric slip systems which are the zones of the maximum shear stress. (Shijve 2009, p. 40.) Principle of crack extension during a single load cycle is presented in figure 13.

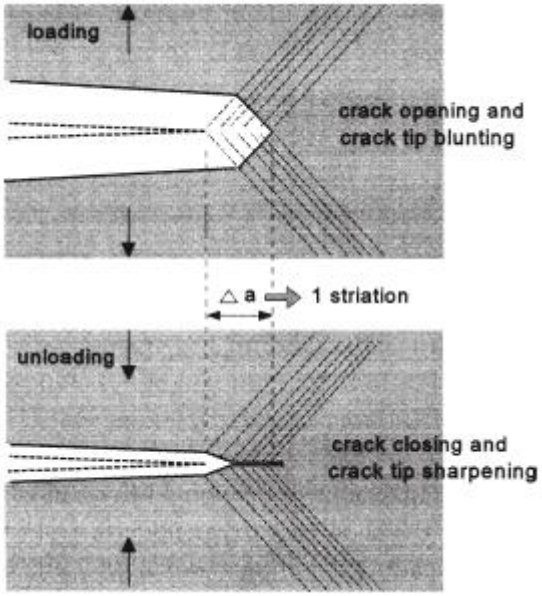

Figure 13. Crack extension as a result of one loading and unloading cycle (Schijve 2009, p. 40).

A crack can have three different modes of displacement or a combination of them (Figure 14). Mode I is called *opening mode* and it is caused by perpendicular tensile loading. Mode II is called *sliding mode* and mode III is called *tearing mode*, and they are caused by shear loading in different directions. The most important one to consider with fatigue cracks is Mode I since the other modes, although possible, often transition to Mode I. (Dowling 2013, p. 344; Schijve 2009, p. 108.)

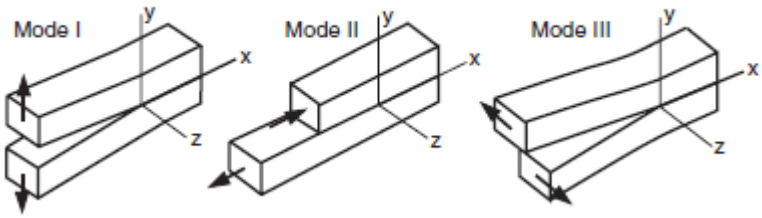

Figure 14. The crack opening modes (Dowling 2013, p. 344).

Because crack has a zero tip radius, K_t would be infinite (see for example equation (1.8)). Therefore, the severity and intensity of the crack tip stress distribution is described with another factor called stress intensity factor (SIF) *K*. (Schijve 2009, p. 105–107.)

$$K = FS\sqrt{\pi a} \tag{1.9}$$

In equation (1.9), S is remote stress from loading, a is the crack length, and F is a dimensionless factor related to the geometry of the cracked component (Schijve 2009, p. 105–107). The stress intensity factor K is defined with an assumption that material behaves in linear-elastic manner and hence the name of the approach is Linear Elastic Fracture Mechanics (LEFM) (Dowling 2013, p. 339).

The stress components around the crack tip for Mode I crack can be derived from the theory of linear elasticity (Dowling 2013, p. 347). If the region of the crack tip is presented in the coordinate system shown in figure 15, the stresses near the crack tip can be expressed as follows (Dowling 2013, p. 346):

$$\sigma_x = \frac{K_I}{\sqrt{2\pi r}} cos\frac{\theta}{2}\left(1 - sin\frac{\theta}{2}sin\frac{3\theta}{2}\right) + \cdots \tag{1.10}$$

$$\sigma_y = \frac{K_I}{\sqrt{2\pi r}} cos\frac{\theta}{2}\left(1 + sin\frac{\theta}{2}sin\frac{3\theta}{2}\right) + \cdots \tag{1.11}$$

$$\tau_{xy} = \frac{K_I}{\sqrt{2\pi r}} cos\frac{\theta}{2}sin\frac{\theta}{2}\cos\frac{3\theta}{2} + \cdots \tag{1.12}$$

$$\sigma_z = 0 \qquad \text{(plane stress)} \tag{1.13}$$

$$\sigma_z = \nu(\sigma_x + \sigma_y) \qquad \text{(plane strain; } \epsilon_z = 0) \tag{1.14}$$

$$\tau_{yz} = \tau_{zx} = 0 \tag{1.15}$$

, where K_I is the stress intensity factor for Mode I crack, ν is Poisson's ratio, θ and r are polar coordinates and σ and τ with different subscripts are normal and shear stress components.

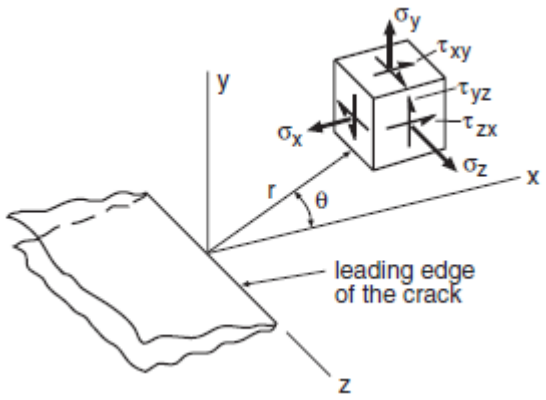

Figure 15. Coordinate system for crack tip area (Dowling 2013, p. 346).

The equations above give a good approximation for the crack tip region and they are correct for small values of *r* (i.e. $r \ll a$). However, it can be seen that if *r* approaches zero, the stress distribution approaches infinity. This is not possible, and it suggest that some crack tip plasticity occurs. As long as the plastic zone is small enough, *K* gives reliable indication of the stress intensity. (Dowling 2013, p. 347; Schijve 2009, p. 109–110, p. 138.)

The fatigue crack growth behaviour of a given material can be described with Paris' equation which describes the cyclic crack growth rate *da/dN* with the help of stress intensity range ΔK.

$$\frac{da}{dN} = C(\Delta K)^m \tag{1.16}$$

In equation (1.16), *C* is a material dependent constant and *m* is the slope of the log-log plot of a fitted curve for crack growth test data. Equation (1.16) is applicable in the region II of the log-log plot of *da/dN* – ΔK shown in figure 16. The threshold stress intensity range or fatigue crack growth threshold ΔK_{th} is a limiting value for crack growth i.e. when $\Delta K < \Delta K_{th}$ large cracks will not grow. (Dowling 2013, p. 564–565.)

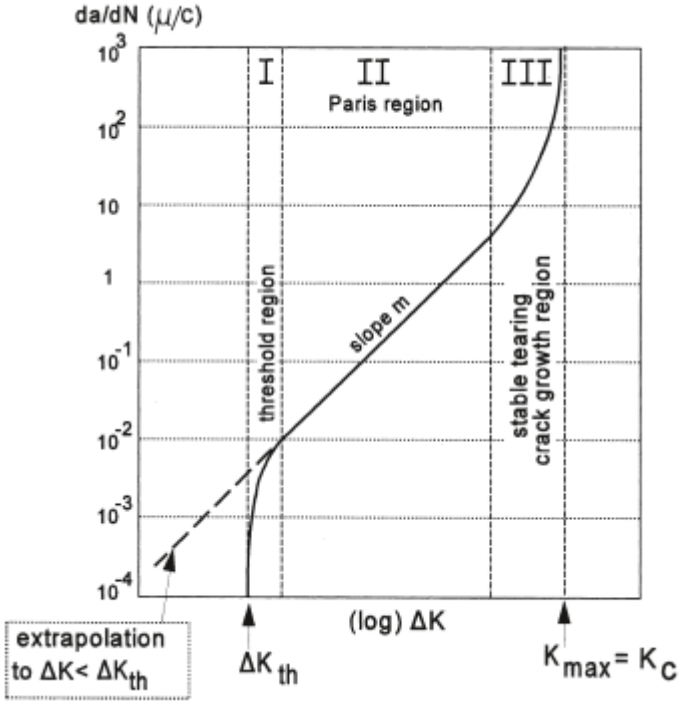

Figure 16. The three crack growth regions (Schijve 2009, p. 218).

The other asymptote of the curve is fracture toughness K_c which defines the material's ability to resist fracture in the presence of a crack. Value of K_c for a given material depends on temperature, loading rate and up to a point, thickness of the component. Thicker the component, the lower the K_c until the worst-case value is reached which is called plane strain fracture toughness K_{Ic}. (Dowling 2013, p. 339.)

1.5.3 Defect size

As was mentioned in chapter 1.5.1 fatigue cracks often nucleate at inclusions. Inclusions or other material defects such as pores can be linked to the fatigue limit of the material with the help of fracture mechanics (Rabb 2017, p. 529). However, these kinds of defects are often so small that the crack growth behaviour is affected by the microstructure and LEFM is not applicable anymore. For example, decrease in the threshold value ΔK_{th} have been shown for very small cracks. (Murakami 2002, p. 35–36; Dowling 2013, p. 614.) Therefore, the analysis must be based on something that considers effects associated with very small cracks.

One such method has been proposed by El Haddad, Smith and Topper (1979). In this method the LEFM solution is modified by introducing an intrinsic crack length value a_0 into equation (1.9) to account for the difference in ΔK_{th} values for small and large cracks.

$$\Delta K = \Delta\sigma\sqrt{\pi(a + a_0)} \tag{1.17}$$

$$a_0 = \frac{1}{\pi}\left(\frac{\Delta K_{th}}{\Delta\sigma_{af}}\right)^2 \tag{1.18}$$

a_0 is a constant for a given material and material condition and it can be calculated from equation (1.18), where ΔK_{th} is threshold stress intensity range for large cracks and $\Delta\sigma_{af}$ is stress range corresponding the fatigue limit of the material (small, smooth specimen). (El Haddad et al. 1979, p. 42.)

The fatigue limit can be plotted as a function of the defect size by modifying Kitagawa-Takahashi (K-T) diagram with the method proposed by El Haddad et al. (Rabb 2017, p. 529). The relation between fatigue limit range $\Delta\sigma_{af}$ and ΔK_{th} can be obtained by modifying equation (1.17) (Rabb 2017, p. 534):

$$\Delta\sigma_{af} = \frac{\Delta K_{th}}{F\sqrt{\pi(a + a_0)}} \tag{1.19}$$

, where F is geometry factor. For internal crack F = 0.637 and for semi elliptic surface crack F = 0.713 when a/c = 1. a is crack length and c is half-width of the crack. (Rabb 2017, p. 534.) An example of a modified K-T diagram showing fatigue limit as a function of defect size for GJS-500-7 is shown in figure 17.

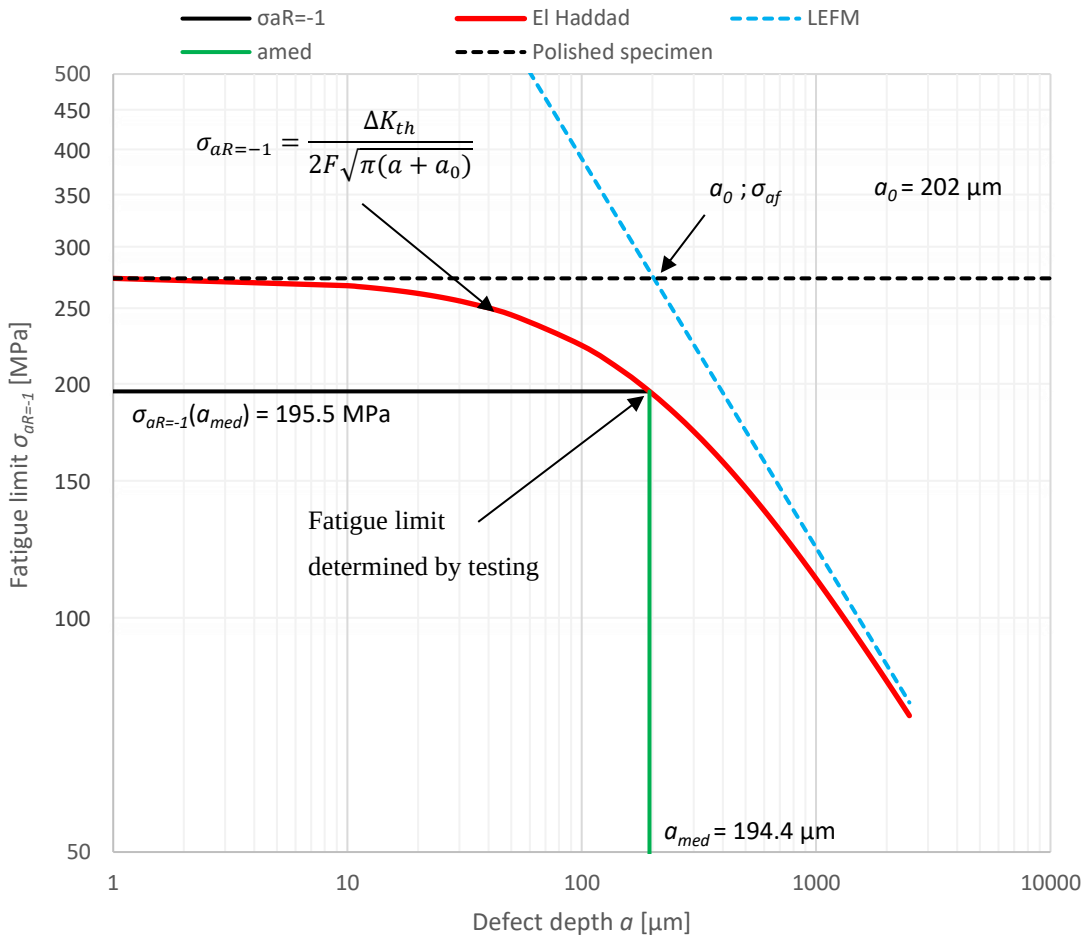

Figure 17. An example of a modified K-T diagram (R = -1) based on testing for GJS-500-7 showing the fatigue limit and corresponding defect size (Mod. Rabb 2017, p. 169).

1.6 Probability and Statistics

Fatigue limit of material is a random variable which can be represented with a certain distribution (Rabb 2013, p. 49). Therefore, basic principles and terms of probability and statistics are presented in this chapter.

1.6.1 Discrete random variable

Fatigue limit is obtained by testing a number of test pieces. Each test piece gives one discrete value and because of this, it is useful to know the fundamentals of discrete random variable. (Rabb 2013, p. 49–50.)

Discrete random variable X is a variable which has a finite or countably infinite set of possible values x_i with probabilities p_i (Bronshtein et al. 2015, p. 811–812). There are some base quantities associated with discrete random variable which are presented below.

The arithmetic mean value (sample mean) $\overline{x}$ or expected value $E(x)$ (Henttonen, Peltomäki & Uusitalo 2006, p. 292):

$$\overline{x} = E(x) = \frac{n_1}{N}x_1 + \frac{n_2}{N}x_2 + \cdots + \frac{n_n}{N}x_n = \sum_{i=1}^{n}\frac{n_i x_i}{N} \tag{1.20}$$

, where n_i is the frequency of x_i and N is the total number of values ($N = n_1 + n_2 + \ldots + n_i$). $E(x)$ can also be calculated with the help of probabilities (Henttonen, Peltomäki & Uusitalo 2006, p. 292):

$$E(x) = p_1x_1 + p_2x_2 + \cdots + p_nx_n = \sum_{i=1}^{n} p_i x_i \tag{1.21}$$

, where p_i is the probability of x_i.

Another important parameter is variance s^2 which is the average of the squared differences from the mean value. In other words, it measures how varied the values of X are in relation to its mean value $\overline{x}$. The unbiased estimate of variance is often used, which means that instead of just N in the denominator, $N-1$ is used in the calculation. This is called Bessel's correction and it usually gives more accurate results because the calculation of sample variance contains a little bias which is corrected by the subtraction. (Henttonen et al. 2006, p. 314; Statics How To 2020a; Statics How to 2020b.)

$$s^2 = \frac{\sum_{i=1}^{n}(x_i - \overline{x})^2}{N-1} \tag{1.22}$$

Standard deviation (SD) s defines how far in average the values of X are from $\overline{x}$, and it can be calculated from the square root of variance (Henttonen et al. 2006, p. 314–315):

$$s = \sqrt{s^2} \tag{1.23}$$

1.6.2 Fatigue strength distributions

The commonly used distributions for the scatter of fatigue limit include Normal distribution, Log-normal distribution and Weibull distribution (Rabb 2013, p. 49). Mainly log-normal distribution is utilized in this work since the use of normal distribution may sometimes be too conservative and Weibull distribution is more difficult to use due to it having more parameters (which are difficult to define) (Rabb 2017, p. 68). Nevertheless, short description of each distribution is presented in this chapter.

Continuous variables such as fatigue limit can have an infinite number of different values. Probability density function (PDF) represents the probabilities, and the area between PDF and abscissa equals 1. Probability for a given range of values [*a, b*] for the continuous variable corresponds the area between PDF and abscissa between *a* and b (probability mass). The area is obtained by integrating PDF from *a* to *b*, and this integral is called cumulative distribution function (CDF). (Kontkanen, Lehtonen, Luosto 2012, p. 126–127.)

Normal distribution

If fatigue limit scatter is described with normal distribution the probability density function $f(\sigma_{af})$ and the cumulative distribution function $F(\sigma)$ are as follows (Rabb 2013, p. 51):

$$f(\sigma_{af}) = \frac{1}{s_\sigma \sqrt{2\pi}} \cdot e^{-\frac{(\sigma_{af} - \overline{\sigma}_{af})^2}{2s_\sigma^2}} \tag{1.24}$$

$$F(\sigma) = P(\sigma_{af} \leq \sigma) = \int_{-\infty}^{\sigma} f(\sigma) d\sigma = \frac{1}{s_\sigma \sqrt{2\pi}} \int_{-\infty}^{\sigma} e^{-\frac{(\sigma - \overline{\sigma}_{af})^2}{2s_\sigma^2}} d\sigma \tag{1.25}$$

, where σ_{af} is fatigue limit, $\overline{\sigma}_{af}$ is expected value, s_σ^2 is variance and s_σ is standard deviation. *P* is probability and when CDF is calculated at point σ, the probability for $\sigma_{af} < \sigma$ is obtained. This is also called failure probability, and if the survival probability (reliability) *R* is required, it can be calculated by taking the complement of *P* (Rabb 2013, p. 51).

$$R = 1 - P \tag{1.26}$$

In other words, R gives the probability for $\sigma_{af} > \sigma$. The expected value (mean value) $E(\sigma_{af})$ can be obtained by calculating the center of mass for the area under the PDF curve along the abscissa (Rabb 2013, p. 52):

$$\overline{\sigma}_{af} = E(\sigma_{af}) = \int_{-\infty}^{\infty} \sigma_{af} f(\sigma_{af}) d\sigma_{af} \tag{1.27}$$

Variance corresponds to moment of inertia of the mass distribution about the center of mass $\overline{\sigma}_{af}$ (Rabb 2013, p. 52):

$$s_{\sigma}^2 = V(\sigma_{af}) = E\left[(\sigma_{af} - \overline{\sigma}_{af})^2\right] = \int_{-\infty}^{\infty} (\sigma_{af} - \overline{\sigma}_{af})^2 f(\sigma_{af}) d\sigma_{af} \tag{1.28}$$

Usually, instead of equations (1.24) and (1.25), standard normal distribution is utilized. In that case, the mean value is 0 and standard deviation is 1, which yields (Rabb 2013, p. 53):

$$f(x) = \frac{1}{\sqrt{2\pi}} e^{-\frac{x^2}{2}} \tag{1.29}$$

$$P(x \leq \lambda) = \frac{1}{\sqrt{2\pi}} \int_{-\infty}^{\lambda} e^{-\frac{x^2}{2}} dx \tag{1.30}$$

Now, λ acts as a multiplier which tells how many times the standard deviation has to be subtracted from the mean value to have failure probability that is smaller or equal to the required P. (Rabb 2013, p. 53.)

When calculating the probability of failure for a certain stress amplitude σ_a, equation (1.30) needs to be integrated (Rabb 2013, p 54). In this case λ can be calculated when the mean value, the standard deviation and stress amplitude σ_a are known (Rabb 2013, p 54):

$$\lambda = \frac{\sigma_a - \overline{\sigma}_{af}}{s_{\sigma}} \tag{1.31}$$

An example of normal distribution is presented in figure 18. The distribution is drawn according to an example provided by Rabb (2013, p. 58) in his book.

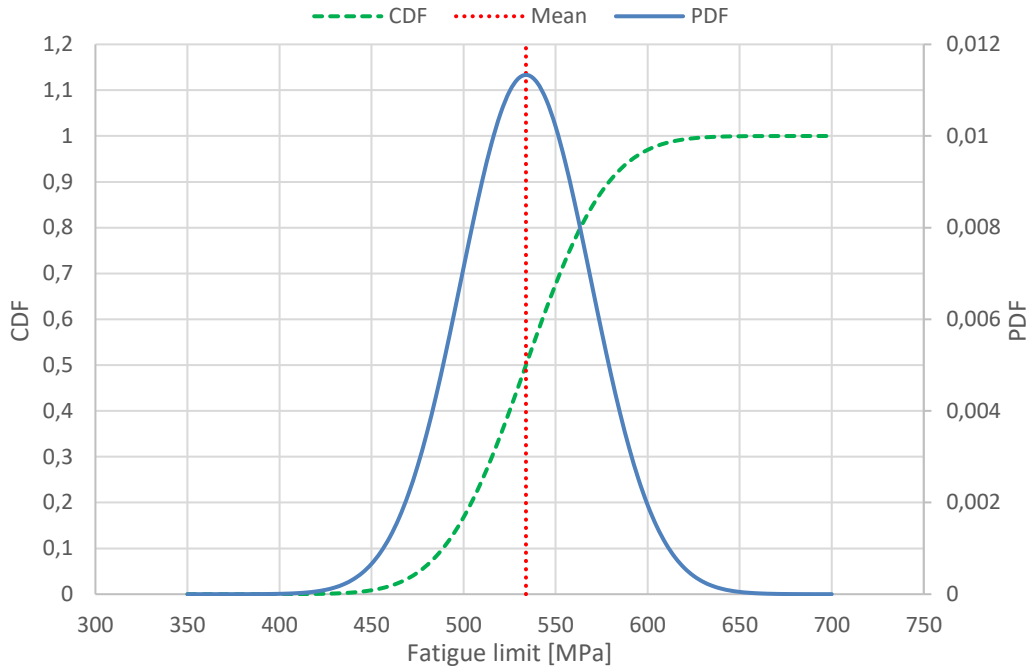

Figure 18. Normal distribution for fatigue limit with $\overline{\sigma}_{af}$ = 533.9 MPa and s_σ = 35.2 MPa (Mod. Rabb 2013, p. 58).

Log-normal distribution

The use of log-normal distribution is advisable when normal distribution gives too conservative results and use of Weibull distribution is not possible (requires three parameters which may be difficult to define accurately). With log-normal distribution the logarithm of fatigue limit follows normal distribution and values of the random variable start from zero. PDF of log-normal distribution is symmetric on a logarithmic scale (abscissa = lnσ) but when it is presented on a normal scale (abscissa = σ) it becomes asymmetric. This means that the mean value $\overline{\sigma}_{af}$ and median value σ_{med} are not equal anymore, mean value being a little higher than median value. Median value is the value where CDF yields 0.5; $F(\sigma_{med})$ = 0.5. (Rabb 2013, p. 55-56.)

PDF and CDF for log-normal distribution are expressed as follows (Rabb 2013, p. 56):

$$f(\sigma_{af}) = \frac{1}{s_{ln}\sigma_{af}\sqrt{2\pi}} e^{-\frac{(ln\sigma_{af}-\mu_{ln})^2}{2s_{ln}^2}} \quad , 0 \leq \sigma_{af} \leq \infty \tag{1.32}$$

$$F(\sigma) = P(\sigma_{af} \leq \sigma) = \frac{1}{s_{ln}\sqrt{2\pi}} \int_0^{\sigma} \frac{1}{\sigma} e^{-\frac{(\ln\sigma - \mu_{ln})^2}{2s_{ln}^2}} d\sigma \quad (1.33)$$

, where s_{ln} is logarithmic standard deviation and μ_{ln} is logarithmic mean value.

Calculation of CDF is done by integrating standard normal distribution from -∞ to λ (Rabb 2013, p. 56). λ is obtained by reducing logarithmic mean value to correspond the calculated stress amplitude σ_a (Rabb 2013, p. 56):

$$\lambda = \frac{\ln\sigma_a - \mu_{ln}}{s_{ln}} \quad (1.34)$$

The expected value (mean value) $\overline{\sigma}_{af}$, median value σ_{med}, variance s_σ^2 and standard deviation s_σ for log-normal distributed fatigue limit are obtained as follows (Rabb 2013, p. 56; Rabb 2017, p. 69):

$$\overline{\sigma}_{af} = E(\sigma_{af}) = e^{(\mu_{ln} + \frac{s_{ln}^2}{2})} \quad (1.35)$$

$$\sigma_{med} = e^{\mu_{ln}} \quad (1.36)$$

$$s_\sigma^2 = V(\sigma_{af}) = (e^{s_{ln}^2} - 1)e^{(2\mu_{ln} + s_{ln}^2)} \quad (1.37)$$

$$s_\sigma = \sqrt{s_\sigma^2} \quad (1.38)$$

Often in practice, mean value for fatigue limit obtained using normal distribution is almost equal to that obtained with log-normal distribution. Also, logarithmic standard deviation s_{ln} is so close to the relative standard deviation s_r ($s_r = s_\sigma / \overline{\sigma}_{af}$) that when $s_r < 0.25$, in calculations it can be assumed that $s_{ln} = s_r$. (Rabb 2017, p. 72.)

For log-normal distribution the link between safety factor S_F and failure probability P is (Rabb 2017, p. 70):

$$\ln\sigma_{af,P} = \mu_{ln} + \lambda s_{ln} = \ln(\sigma_{med}) + \lambda s_{ln} \quad (1.39)$$

$$S_F = \frac{\sigma_{med}}{\sigma_{af,P}} = e^{-\lambda s_{ln}} \quad (1.40)$$

$$\lambda = -\frac{\ln S_F}{s_{ln}} \tag{1.41}$$

, where $\sigma_{af,P}$ is fatigue limit reduced to failure probability P.

If the mean value $\overline{\sigma}_{af}$ and the standard deviation s_σ are obtained with normal distribution, the corresponding logarithmic values for log-normal distribution can be calculated with reasonable accuracy using equations (1.35) and (1.37) (Rabb 2013, p. 57). For this purpose, they have to be modified (Rabb 2013, p. 57):

$$s_{ln} = \sqrt{\ln\left(1 + \frac{s_\sigma^2}{e^{2ln\overline{\sigma}_{af}}}\right)} \tag{1.42}$$

$$\mu_{ln} = \ln \overline{\sigma}_{af} - \frac{s_{ln}^2}{2} \tag{1.43}$$

An example of log-normal distribution is presented in figure 19. The distribution is drawn according to an example provided by Rabb (2013, p. 58) in his book. The abscissa has values of ln(σ) on it, so the distribution is symmetric. The same distribution drawn with σ on the abscissa can be seen in figure 21.

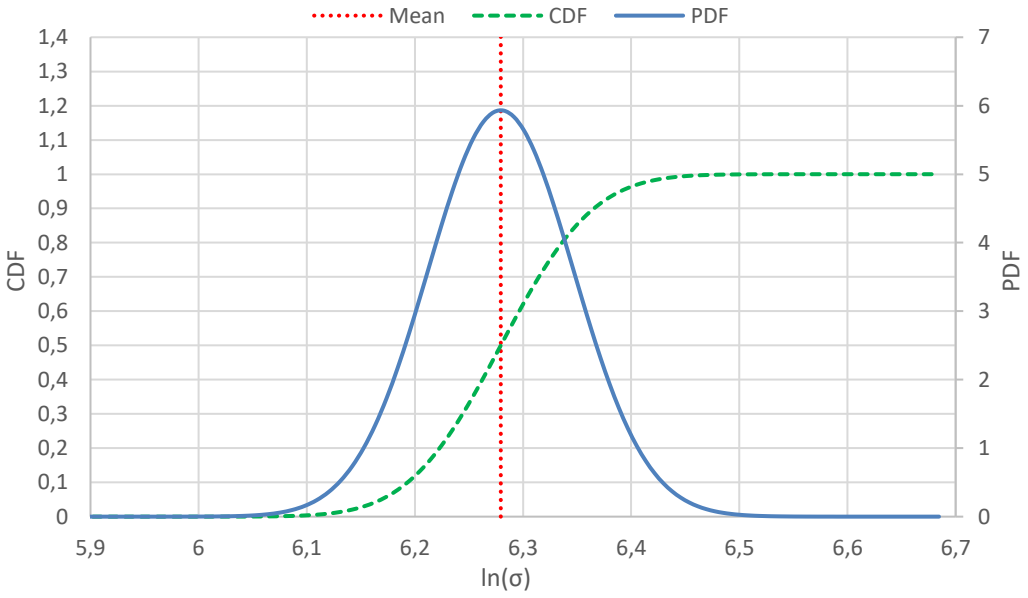

Figure 19. Log-normal distribution for fatigue limit with μ_{ln} = 6.2794 and s_{ln} = 0.06724 (Mod. Rabb 2013, p. 58).

Weibull distribution

PDF for Weibull distribution is expressed as (Rabb 2013, p. 61):

$$f(\sigma_{af}) = \frac{\beta(\sigma_{af} - \sigma_{tr})^{\beta-1}}{(\sigma_{ch} - \sigma_{tr})^{\beta}} e^{-\left(\frac{\sigma_{af}-\sigma_{tr}}{\sigma_{ch}-\sigma_{tr}}\right)^{\beta}} \tag{1.44}$$

, where σ_{af} is fatigue limit, σ_{tr} is threshold value for fatigue limit, σ_{ch} is characteristic stress and β is shape parameter which defines the magnitude of scatter.

There are three parameters in Weibull distribution that are obtained from fatigue test results: σ_{tr}, σ_{ch} and β. It is not easy to determine these parameters from the test results and that is why the use of this distribution is somewhat difficult. However, this problem can be solved by assuming that the threshold value σ_{tr} is very small or zero. Then, the distribution resembles log-normal distribution. (Rabb 2013, p. 61.)

CDF for Weibull distribution is obtained in a closed form because it is possible to directly integrate PDF (Rabb 2013, p. 61):

$$F(\sigma) = P(\sigma_{af} \leq \sigma) = 1 - e^{-\left(\frac{\sigma-\sigma_{tr}}{\sigma_{ch}-\sigma_{tr}}\right)^{\beta}} \tag{1.45}$$

The fatigue limit for a certain failure probability can be obtained from equation (1.45) by modifying it into the following form (Rabb 2013, p. 61):

$$\sigma_{af,P} = \sigma_{tr} + (\sigma_{ch} - \sigma_{tr}) \cdot \sqrt[\beta]{-\ln(1-P)} \tag{1.46}$$

As Weibull distribution is asymmetric, its median value is not equal to its mean value (expected value). The median value σ_{med} which is used in reduction to the required failure probability is obtained by setting P = 0.5 in equation (1.46) (Rabb 2013, p. 62):

$$\sigma_{med} = \sigma_{tr} + (\sigma_{ch} - \sigma_{tr}) \cdot \sqrt[\beta]{-\ln 0.5} \tag{1.47}$$

The mean value $\overline{\sigma}_{af}$ and variance s_σ^2 can be calculated from (Rabb 2013, p. 62):

$$\overline{\sigma}_{af} = \sigma_{tr} + (\sigma_{ch} - \sigma_{tr}) \cdot \Gamma\left(1 + \frac{1}{\beta}\right) \tag{1.48}$$

$$s_\sigma^2 = (\sigma_{ch} - \sigma_{tr})^2 \left[\Gamma\left(1 + \frac{2}{\beta}\right) - \Gamma^2\left(1 + \frac{1}{\beta}\right)\right] \tag{1.49}$$

, where Γ is gamma function. If the argument $1 + 2 / \beta$ is denoted as t, the following integral can be obtained (Rabb 2013, p. 62):

$$\Gamma(t) = \int_0^\infty x^{t-1} e^{-x} dx \tag{1.50}$$

This does not have a closed form solution and it has to be solved numerically. Fitting test data to Weibull distribution is challenging if only information available is the values for normal or log-normal distribution. (Rabb 2013, p. 62.)

An example of Weibull distribution is presented in figure 20. The distribution is drawn according to an example provided by Rabb (2013, p. 62) in his book.

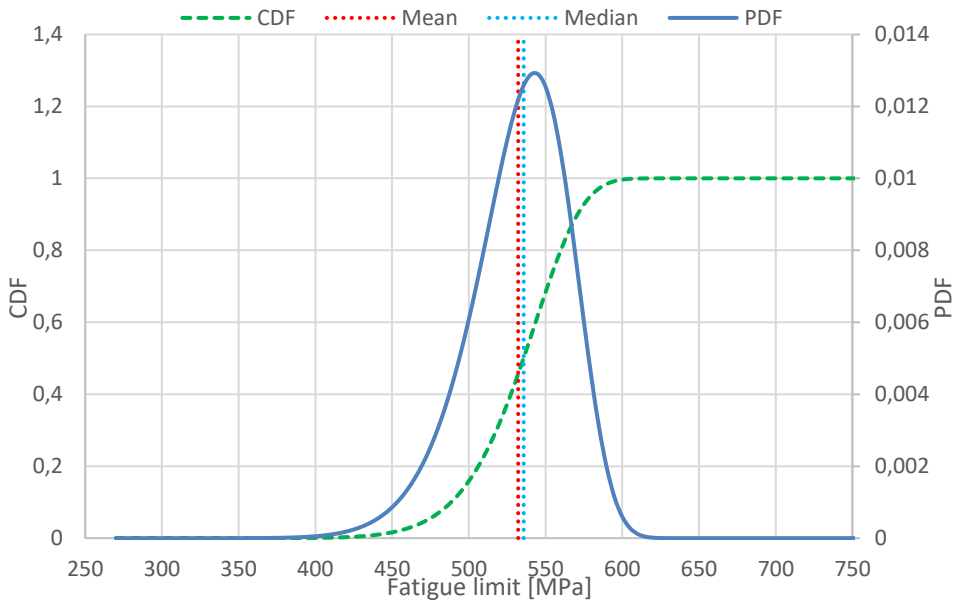

Figure 20. Weibull distribution for fatigue limit with σ_{tr} = 267 MPa, σ_{ch} = 546 MPa, β = 9.752, $\overline{\sigma}_{af}$ = 532.2 MPa, σ_{med} = 535.8 MPa and s_σ = 32.7 MPa (Mod. Rabb 2013, p. 62).

A comparison of different distributions is presented in figure 21. All the distributions from figures 18-20 are representing the same set of fatigue test results and they are plotted in same graph to show the difference between different distributions. The fatigue test results are by Rabb (2013, p. 58–59, 62).

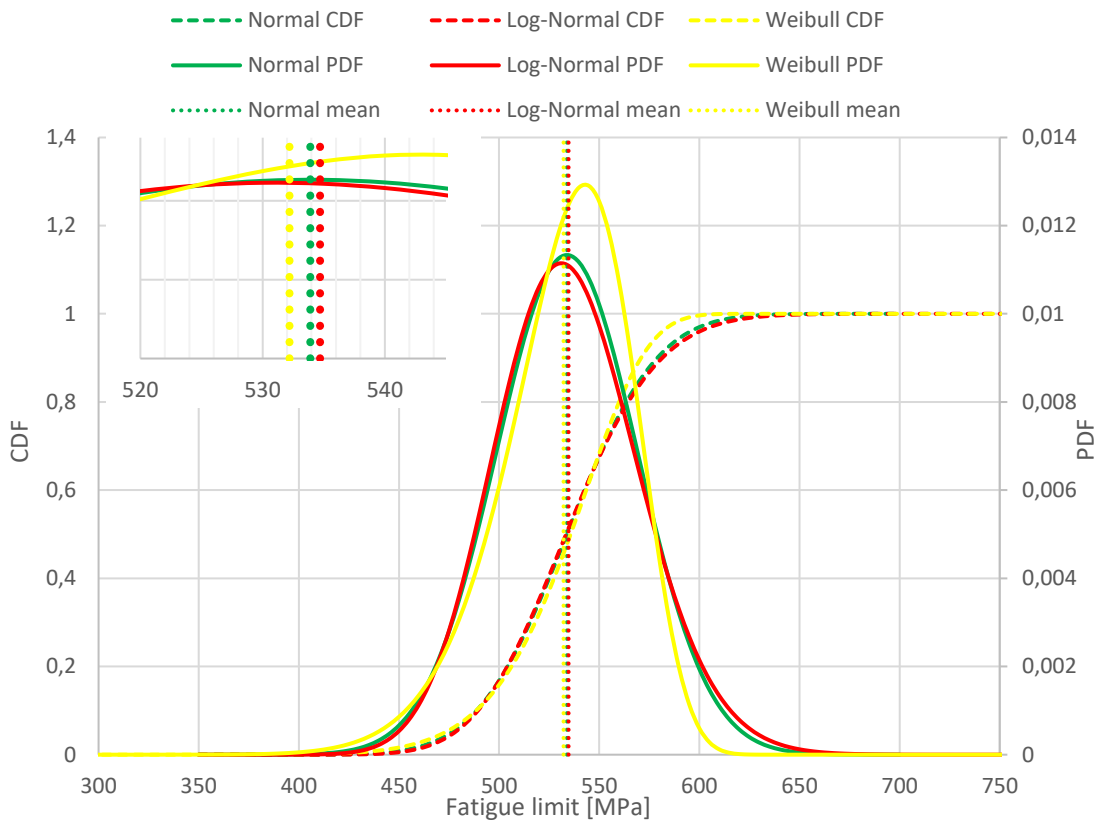

Figure 21. Comparison of different fatigue limit distributions (Mod. Rabb 2013, p. 58, 62).

1.6.3 Confidence intervals of sample values

The fatigue tests give only sample values for mean and standard deviation. These need to be modified so that with a certain probability they are within given bounds i.e. the obtained sample values are conservative in respect to the actual population values. (Rabb 2017, p. 115.)

Basically, aforementioned means that the sample values themselves are random variables. The sample mean value follows Student's distribution and the sample standard deviation follows χ^2 -distribution (chi-squared distribution). With these distributions, the population

values for mean and standard deviation can be obtained. (Rabb 2017, p. 115–116.) The theory of the distributions can be found for example in Rabb's book (2017) and it is not explained thoroughly here but instead, only the main equations are given.

The population value for the mean of fatigue limit according to Student's distribution is obtained as follows (Rabb 2017, p. 116–117):

$$\sigma_{af} = \overline{\sigma}_{af,C_\mu} = \overline{\sigma}_{af} - \frac{t_2 s}{\sqrt{n}} \tag{1.51}$$

, where C_μ denotes the confidence level, t_2 is the variable of the Student's distribution corresponding a specific confidence, s is sample standard deviation (from the fatigue test) and n is the number of test specimens.

For example, C_μ = 90 % would mean that if the fatigue test was repeated, 90 % of the obtained sample means from the new tests would be equal to or higher than $\overline{\sigma}_{af,C90}$ (Rabb 2017, p. 116). t_2 is determined according to number of degrees of freedom: D.O.F = n - 1. Some t_2 values can be found tabulated in Rabb's book (2017, p. 119) or in mathematics handbooks by Råde & Westergren (2014, p. 472) or Bronshtein et al. (2015, p. 1138).

The population value for standard deviation can be obtained according to χ^2 -distribution as follows (Rabb 2017, p. 120–121):

$$s_\sigma = s_{\sigma C} = \sqrt{\frac{n-1}{h_1}} \cdot s \tag{1.52}$$

, where s is sample standard deviation, n is number of test specimens and h_1 is the variable of χ^2 -distribution corresponding a specific confidence. h_1 values can be found tabulated by Rabb (2017, p. 123) or Råde & Westergren (2014, p. 469–470) and like in the case of t_2, they are determined according to number of degrees of freedom: D.O.F = n - 1.

Often, staircase test used for fatigue limit testing underestimates the size of standard deviation. Consequently, the real distribution of sample standard deviation may differ considerably from χ^2 -distribution and this should be considered when defining the population value. (Rabb 2017, p. 125.) Rabb (2017) has given detailed explanation of this in his book. The explanation is not presented here since no tests are conducted within this thesis. The relative standard deviation of sample values and population values for spheroidal graphite cast iron and steels are presented in tables 1 and 2 respectively.

Table 1. Relative standard deviation, sample (n = 25) and population values for spheroidal graphite cast irons ($s_r = s_{ln}$) (Mod. Rabb 2017, p. 259).

Machined surface			**Shot peened**			**Casting surface**		
s_r (sample)	s_{rC90}	s_{rC10}	s_r (sample)	s_{rC90}	s_{rC10}	s_r (sample)	s_{rC90}	s_{rC10}
0.1	0.12… (0.13)	0.085	0.145	0.18	0.12	0.15	0.21	0.13

Table 2. Relative standard deviation, sample (n = 25) and population values for steels ($s_r = s_{ln}$) (Mod. Rabb 2017, p. 258).

Machined surface								**Shot peened**	
On surface				Below surface					
Parallel grain flow		Perpendicular grain flow		Parallel grain flow		Perpendicular grain flow			
s_r	s_{rC90}	s_r	s_{rC90}	s_r	s_{rC90}	s_r	s_{rC90}	s_r	s_{rC90}
0.065	0.08	0.065	0.08	0.10	0.12	0.08	0.10	0.10	0.12

2 FATIGUE ANALYSIS METHODS

This chapter presents the methods for analysing fatigue of materials and components. Most of the methods below are incorporated in the final analysis procedure and they are explained more thoroughly. However, a few additional methods are explained more briefly just to show that there are variety of possibilities to analyse fatigue damage.

2.1 Haigh diagram

There are multiple equations which can be drawn in $\sigma_{af} - \sigma_m$ diagram to describe the effect of mean stress on fatigue limit. These include for example Goodman line, Gerber parabola and Soderberg line but often these consider only tensile mean stresses. In order to demonstrate the effect of compressive mean stresses, a more sophisticated diagram is needed. (Milella 2013, p. 282–285.)

Two common diagrams which show the effect of both tensile and compressive mean stresses are called Haigh diagram and Smith diagram. (Milella 2013, p. 294–296.) In this work Haigh diagram will be utilized since this is preferred by Rabb (2017, p. 40) and also, it seems to be more demonstrative and easier to read.

Haigh diagrams present the fatigue limit σ_{af} as a function of mean stress σ_m. Often they are constructed in such a way that only the elastic behaviour is plotted, as is the case with the diagrams drawn according to DNVGL-ST-0361 in chapter 1.1.1. However, this does not provide enough information if the maximum stress exceeds the yield strength of the material. Yield strength may be exceeded locally near (sharp) notches and this local plasticity can be modelled with FEM. In that case, it is useful to know the shape of the plastic portions of the Haigh diagram as well. (Rabb 2017, p. 40.)

For the purposes of this work, new diagrams are made according to recommendations made by Rabb (2017, p. 40–45, 128–138) because it has been found that the diagrams provided in DNVGL-ST-0361 may be unconservative when spheroidal graphite cast irons are consid-

ered. According to The Switch, this is especially so when relatively large castings are considered. When quenched and tempered steels and structural steels are considered, the diagrams by DNVGL are closer to those suggested by Rabb (2017, p. 40–45).

2.1.1 Quenched and tempered steel 42CrMo4

Haigh diagram for 42CrMo4 is based on the static strength values provided in SFS-EN ISO 683-2. Haigh diagram based on Rabb's suggestions and DNVGL-ST-0361 for comparison are shown in figure 22.

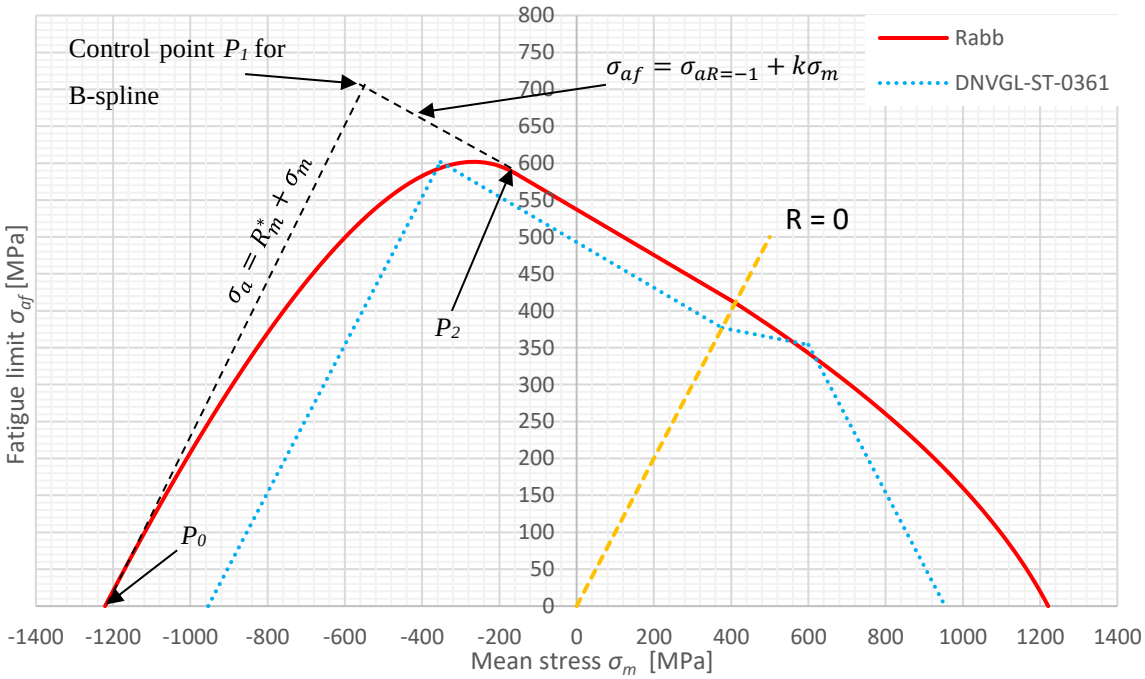

Figure 22. Haigh diagrams for 42CrMo4.

Ultimate strength and yield strength can be used to obtain the fatigue limit for completely reversed loading as follows (Mourier 2002, p. 83):

$$\sigma_{aR=-1} = 1.04\left(0.144R_m + 0.309R_{p0.2}\right) + 56\ \text{MPa} \tag{2.1}$$

This is conservative and includes the required confidence level in respect to sample value. The equation (2.1) is valid for most steel types (R_m up to 1400 MPa) when the effective area of the reference specimen is 225 mm^2. (Rabb 2017, p. 42, 258.)

When normative static strength values are used, they can be increased by 6 %. This comes from the fact that the tensile strength of material must not be less than the minimum value stated in standards. Naturally, this leads to the median value of tensile strength being higher (c. 7.4 % higher) than the normative value given in standards as material manufacturers must ensure that the minimum requirement is met. (Rabb 2017, p. 79.)

The slope *k* of the linear part (Rabb 2017, p. 43):

$$k = 0.1 - 0.00035R_m \tag{2.2}$$

It can be noted that this is the same equation provided in DNVGL-ST-0361. The linear part is then as follows (Rabb 2017, p. 43):

$$\sigma_{af} = \sigma_{aR=-1} + k\sigma_m \qquad (\sigma_{m,P2} \leq \sigma_m \leq \sigma_{mR=0}) \tag{2.3}$$

The end point P_2 for the linear part on the compression side can be calculated with the following equations (Rabb 2017, p. 44):

$$\sigma_{m,P2} = \frac{\sigma_{aR=-1} - R_{p0.2}}{2(1-k)} \qquad (P_2, \text{fig. } 22) \tag{2.4}$$

$$\sigma_{a,P2} = \sigma_{aR=-1} + k\sigma_{m,P2} \qquad (P_2, \text{fig. } 22) \tag{2.5}$$

The curve between P_0 and P_2 is constructed as a quadratic B-spline with the following equations for points P_0 and P_1 (Rabb 2017, p. 40, 44.):

The starting point P_0:

$$\sigma_{m,P0} = -R_m^* \tag{2.6}$$

$$\sigma_{a,P0} = 0 \tag{2.7}$$

$$R_m^* = \frac{(1+2M)\sigma_{aR=-1}}{M(2+M)} \tag{2.8}$$

, where M is $-k$ and R_m^* is fictive ultimate strength which takes into account that the true ultimate strength is about 30-60 % higher than the nominal value due to necking.

The intermediate point P_1 (Rabb 2017, p. 44):

$$\sigma_{m,P1} = \frac{R_m^* - \sigma_{aR=-1}}{k-1} \tag{2.9}$$

$$\sigma_{a,P1} = R_m^* + \sigma_{m,P1} = \sigma_{aR=-1} + k\sigma_{m,P1} \tag{2.10}$$

The end point P_2 is calculated with equations (2.4) and (2.5) and the spline is then constructed with the following equations (Rabb 2017, p. 44):

$$\sigma_{af} = (1-t)^2\sigma_{a,P0} + 2t(1-t)\sigma_{a,P1} + t^2\sigma_{a,P2} \tag{2.11}$$

$$\sigma_m = (1-t)^2\sigma_{m,P0} + 2t(1-t)\sigma_{m,P1} + t^2\sigma_{m,P2} \tag{2.12}$$

, where t is a normalized variable. Corresponding t for mean stress σ_m can be calculated between $\sigma_{m,P0} \leq \sigma_m \leq \sigma_{m,P2}$ as follows (Rabb 2017, p. 44-45):

$$t = \frac{\sigma_{m,P0} - \sigma_{m,P1}}{\sigma_{m,P0} - 2\sigma_{m,P1} + \sigma_{m,P2}} \pm \sqrt{\left(\frac{\sigma_{m,P0} - \sigma_{m,P1}}{\sigma_{m,P0} - 2\sigma_{m,P1} + \sigma_{m,P2}}\right)^2 - \frac{\sigma_{m,P0} - \sigma_m}{\sigma_{m,P0} - 2\sigma_{m,P1} + \sigma_{m,P2}}} \tag{2.13}$$

If the first term is positive minus is used in front of the square root and if it is negative, then plus. In other words, the normalized variable has values from 0 to 1. (Rabb 2017, p. 45.)

The tensile side of the diagram is constructed as a sideways parabola between $\sigma_{mR=0} \leq \sigma_m \leq R_m^*$ as follows (Rabb 2017, p. 43–44):

$$\sigma_{af} = \sigma_{aR=-1}\left(\frac{1-b}{2-b} + \sqrt{\frac{1}{(2-b)^2} - \frac{b\sigma_m}{(2-b)R_m^*}}\right) \tag{2.14}$$

$$b = \frac{2(1+2M)}{2+2M-M^2} \tag{2.15}$$

$$\sigma_{aR=0} = \frac{\sigma_{aR=-1}}{1-k} \tag{2.16}$$

$$\sigma_{mR=0} = \sigma_{aR=0} \tag{2.17}$$

, where M is -k and R_m^* is the same as earlier.

2.1.2 Structural steel S355

Haigh diagram for S355 is based on the static strength values which are provided in SFS-EN ISO 10025-2. Haigh diagram based on Rabb's suggestions and DNVGL-ST-0361 for comparison are shown in figure 23.

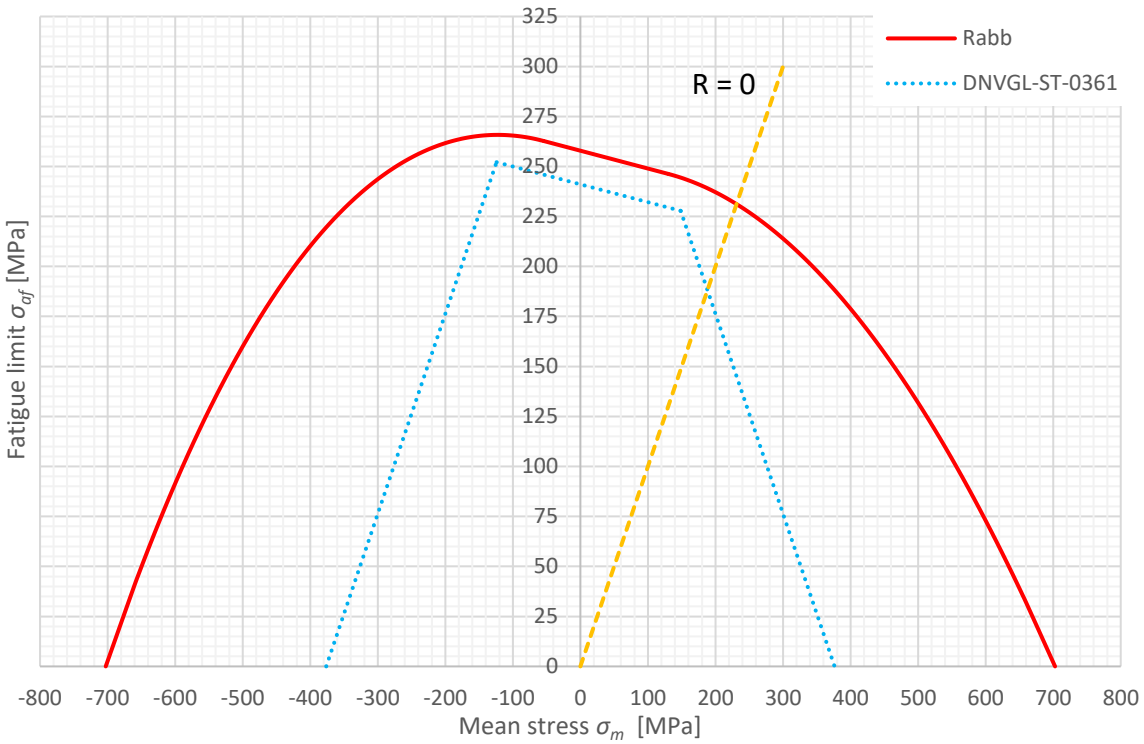

Figure 23. Haigh diagrams for S355.

The Haigh diagrams for structural steels are constructed much the same way as for the quenched and tempered steels (eqs. (2.1)–(2.13)). However, the fictive ultimate strength R_m^* is now calculated as follows (Rabb 2013, p. 41):

$$R_m^* \approx 1.3R_m \tag{2.18}$$

This is because the slope of the diagram for structural steels is relatively small and calculating R_m^* as it is calculated in case of quenched and tempered steels would result in way too high a value for R_m^*. (Rabb 2013, p. 41.)

Another difference is that the parabola on the tensile side is now constructed as a second order parabola as follows (Rabb 2013, p. 41):

$$\sigma_{m1} = \frac{R_{p0.2} - \sigma_{aR=-1}}{1 + k} \tag{2.19}$$

$$\sigma_{a1} = \sigma_{aR=-1} + k\sigma_{m1} \tag{2.20}$$

, where $\sigma_{aR=-1}$ is calculated from equation (2.1).

The parabola between $\sigma_{m1} \leq \sigma_m \leq R_m^*$ follows the equation (Rabb 2013, p. 41):

$$\sigma_{af} = A\sigma_m^2 + B\sigma_m + C \tag{2.21}$$

The constants *A*, *B* and *C* are calculated from (Rabb 2013, p. 42):

$$A = \frac{k\sigma_{m1} - \sigma_{a1} - kR_m^*}{(R_m^* - \sigma_{m1})^2} \tag{2.22}$$

$$B = k - 2A\sigma_{m1} \tag{2.23}$$

$$C = A\sigma_{m1}^2 + \sigma_{a1} - k\sigma_{m1} \tag{2.24}$$

2.1.3 Spheroidal graphite cast iron

Haigh diagram for spheroidal graphite cast irons is constructed based on static strength values provided in SFS-EN 1563. Haigh diagrams based on Rabb's suggestions and DNVGL-ST-0361 for comparison are shown in figure 24.

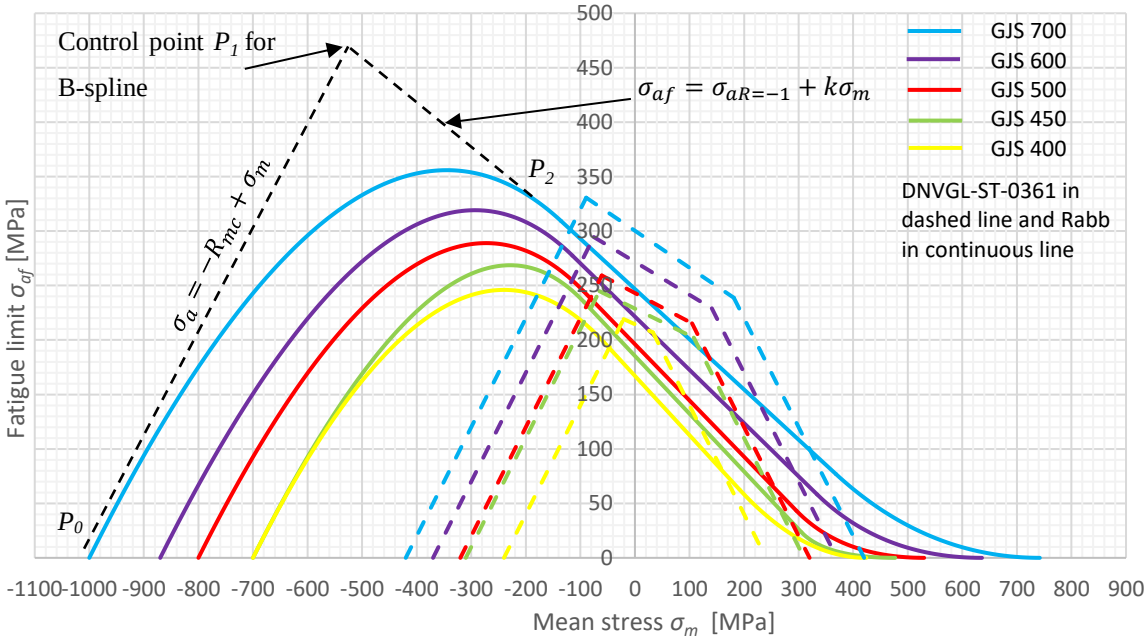

Figure 24. Haigh diagrams for GJS400, GJS450, GJS500, GJS600 and GJS700.

Fatigue limit for completely reversed loading $\sigma_{aR=-1}$ and the slope k of the linear part are obtained by fitting a function to data points provided by Rabb (2017, p. 259). The effective area of the test specimens is A_{ref} = 1039 mm^2 (Rabb 2017, p. 259).

For $\sigma_{aR=-1}$ based on the static and fatigue tests conducted by Rabb the following is obtained:

$$\sigma_{aR=-1} = 0.1798 \cdot R_m + 0.11845 \cdot R_{p0.2} + 60.6699 \quad \text{MPa} \tag{2.25}$$

And for k:

$$k = 0.000261 \cdot R_m - 0.65493 \tag{2.26}$$

The linear part between σ_{m2} and σ_{m1} is (Rabb 2017, p. 259):

$$\sigma_{af} = \sigma_{aR=-1} + k\sigma_m \tag{2.27}$$

$$\sigma_{m2} = \frac{\sigma_{aR=-1} - R_{p0.2}}{1-k} \tag{2.28}$$

$$\sigma_{m1} = \frac{R_{p0.2} - \sigma_{aR=-1}}{1+k} \tag{2.29}$$

The compression side of the diagram is constructed as a B-spline like in the cases of different steels but the points along the spline are calculated a bit differently (Rabb 2017, p. 259).

For P_0 (Rabb 2017, p. 259):

$$\sigma_{m,P0} = R_{mc} \tag{2.30}$$

$$\sigma_{a,P0} = 0 \tag{2.31}$$

, where R_{mc} is ultimate compressive strength. It should be noted that for cast irons the compressive strength is considerably higher than the tensile strength. Also, as the slope of the linear part of the diagram is so steep, the fictive ultimate strength R_m^* is not used for cast iron but rather, the diagram is constructed between R_{mc} and R_m. (Rabb 2017, p. 129, 259.)

For P_1 (Rabb 2017, p. 259):

$$\sigma_{m,P1} = \frac{\sigma_{aR=-1} + R_{mc}}{1-k} \tag{2.32}$$

$$\sigma_{a,P1} = \sigma_{aR=-1} + k\sigma_{m,P1} \tag{2.33}$$

And for P_2 (Rabb 2017, p. 259):

$$\sigma_{m,P2} = \sigma_{m2} = \frac{\sigma_{aR=-1} - R_{p0.2}}{1-k} \tag{2.34}$$

$$\sigma_{a,P2} = \sigma_{aR=-1} + k\sigma_{m,P2} \tag{2.35}$$

Using points P_0, P_1 and P_2 the compression B-spline can be drawn with the following equations (Rabb 2017, p. 259):

$$\sigma_{af} = 2t \cdot (1-t) \cdot \sigma_{a,P1} + t^2 \cdot \sigma_{a,P2} \tag{2.36}$$

$$\sigma_m = (1-t)^2 \cdot \sigma_{m,P0} + 2t \cdot (1-t) \cdot \sigma_{m,P1} + t^2 \cdot \sigma_{m,P2} \tag{2.37}$$

, where t is calculated from equation (2.13).

The right side of the diagram is also drawn as a B-spline. The starting point P_0 is (Rabb 2017, p. 259):

$$\sigma_{m,P0} = \sigma_{m1} = \frac{R_{p0.2} - \sigma_{aR=-1}}{1+k} \tag{2.38}$$

$$\sigma_{a,P0} = \sigma_{aR=-1} + k\sigma_{m,P0} \tag{2.39}$$

For P_1 on the tensile side (Rabb 2017, p. 259):

$$\sigma_{m,P1} = \frac{-\sigma_{aR-1}}{k} \tag{2.40}$$

$$\sigma_{a,P1} = 0 \tag{2.41}$$

For P_2 on the tensile side (Rabb 2017, p. 259):

$$\sigma_{m,P2} = R_m \tag{2.42}$$

$$\sigma_{a,P2} = 0 \tag{2.43}$$

The B-spline is then as follows (Rabb 2017, p. 259):

$$\sigma_{af} = (1-t)^2 \cdot \sigma_{a,P0} \tag{2.44}$$

$$\sigma_m = (1-t)^2 \cdot \sigma_{m,P0} + 2t \cdot (1-t) \cdot \sigma_{m,P1} + t^2\sigma_{m,P2} \tag{2.45}$$

, where t is according to equation (2.13).

2.1.4 Verification of the Haigh diagrams using literature sources

As the Haigh diagrams suggested by Rabb provide more capacity in some cases than what is given in diagrams by DNVGL-ST-0361, an attempt to verify their accuracy using fatigue test data from literature is made. The size factor K_{size} (see chapter 2.2.3) is taken into account using the effective areas of the test specimens when comparing the test data and the Haigh diagrams.

Test data for spheroidal graphite cast iron by Meyer (2014) and Tanaka et al. (1995) seem to agree with the curves drawn according to previous chapters. The plotted data can be seen in Appendix I,1.

Pallarés-Santasmartas et al. (2018) have tested the fatigue properties of 34CrNiMo6 and also this seems to follow the suggested curve quite well (see Appendix I,2). Some other material data points from previous studies were provided in the same source. The original sources for them were unavailable so no size factor could be defined but trendlines drawn in Excel give somewhat similar shape for the Haigh diagrams as the suggestion in chapter 2.1.1.

Very little data was found for structural steels. Data points provided by Ukrainetz (1960) shows similar trend to the curve as suggested by Rabb but the data seems to fall slightly below the suggested curve (see Appendix I,3).

2.2 Reduction factors

The fatigue limit for smooth test specimen from Haigh diagram must be reduced with different reduction factors in order to obtain the fatigue limit of the actual machine element. Different reduction factors take into account the size effect, surface roughness, anisotropy and effects associated with Very High Cycle Fatigue (VHCF).

2.2.1 Surface roughness factor K_R

Surface roughness can have a large effect on fatigue limit. Therefore, the fatigue limit from Haigh diagram is reduced with a surface roughness factor K_R which describes the effect of different surface conditions, such as casting surface or ground surface, to the fatigue limit. Fatigue limit is usually tested with polished specimens and in that case, K_R is 1. (Rabb 2017, p. 195–196.)

DNVGL-ST-0361 gives the following equation for surface roughness factor:

$$F_o = 1 - 0.22 \cdot (\log(R_z))^{0.64} \cdot \log(\sigma_b) + 0.45 \cdot (\log(R_z))^{0.53} \quad (2.46)$$

, where R_z is the height of the surface roughness profile [µm] and σ_b is ultimate strength [MPa]. The same equation is given for both *non-welded forged and rolled parts* and *cast steel and spheroidal graphite cast iron*. (DNVGL-ST-0361 2016, p. 51–52.)

However, it can be seen in figure 25, that some sources give different values for K_R depending whether steel or cast iron is concerned. For example, TGL 19341/01 (1988, p. 5) gives noticeably larger value for K_R in case of spheroidal graphite cast iron than what is obtained with equation (2.46). Based on bending staircase test by Rabb (2017, p. 197–198) with polished and casting surface specimens it seems that TGL 19341/01 gives better estimation for K_R (TGL 19341/01 1988, p. 5):

$$K_R = 1 - a_\sigma \cdot \lg(R_z) \cdot \lg\left(2 \cdot \frac{R_m}{R_{mSmin}}\right) \quad (2.47)$$

In equation (2.47) a_σ is 0.16 and R_{mSmin} is 400 MPa for spheroidal graphite cast iron (TGL 19341/01 1988, p. 5).

There are also approaches which are based on fracture mechanics to define the surface roughness factor. According to Sperle (2013, p. 86) K_R can be expressed by the following equation (see figure 26):

$$K_R = \sqrt{1 + a\left(\frac{2S_{r0}}{\Delta K_{th}}\right)^2} \quad (2.48)$$

$$S_r = \frac{S_{r0}}{K_R} \quad (2.49)$$

, where S_{r0} is the fatigue limit of smooth specimen, a is crack depth (conservatively $a = R_z$) and R is stress ratio. Using this, it is possible to present the fatigue limit and the surface roughness in K-T diagram as is shown in figure 26 for 42CrMo4.

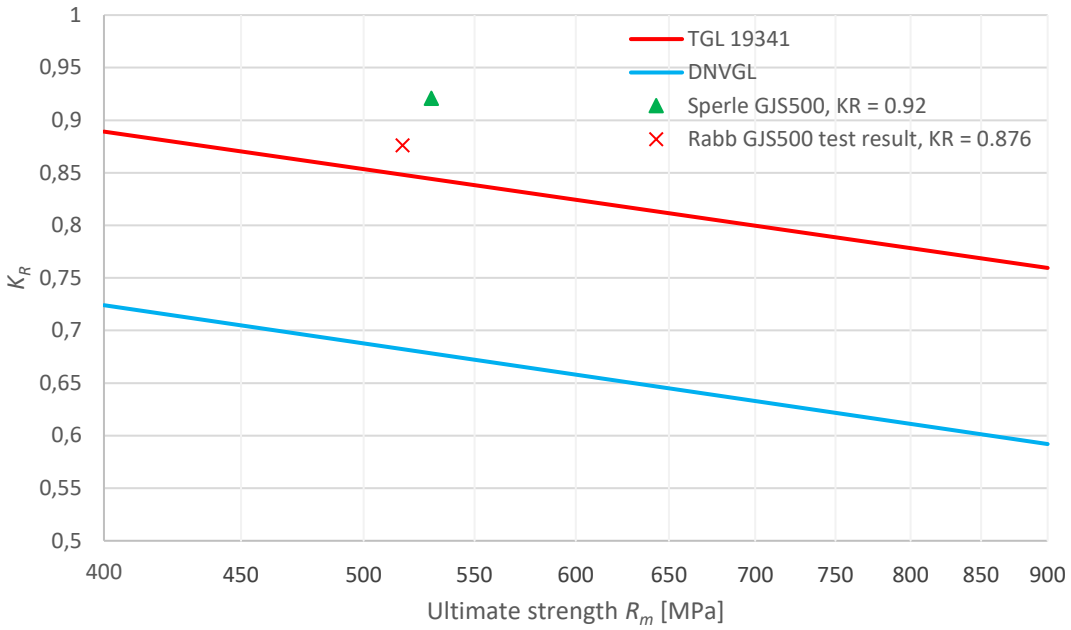

Figure 25. Comparison of K_R for spheroidal graphite cast iron casting surface (R_z = 200 µm) between TGL 19341/01, DNVGL-ST-0361 and Sperle (2013).

The plot in figure 26 can be divided into two regimes: crack initiation and crack growth. The transition point depends on degree of crack opening and the state of residual stress which affects the local *R*. The crack growth regime is described with the following equation. (Sperle 2013, p. 87.)

$$S_{rp} = \frac{1}{2} \cdot \frac{\Delta K_{th}}{\sqrt{a}} \tag{2.50}$$

In equation (2.50), S_{rp} is the stress level required to propagate a crack of size *a* (Sperle 2013, p. 87).

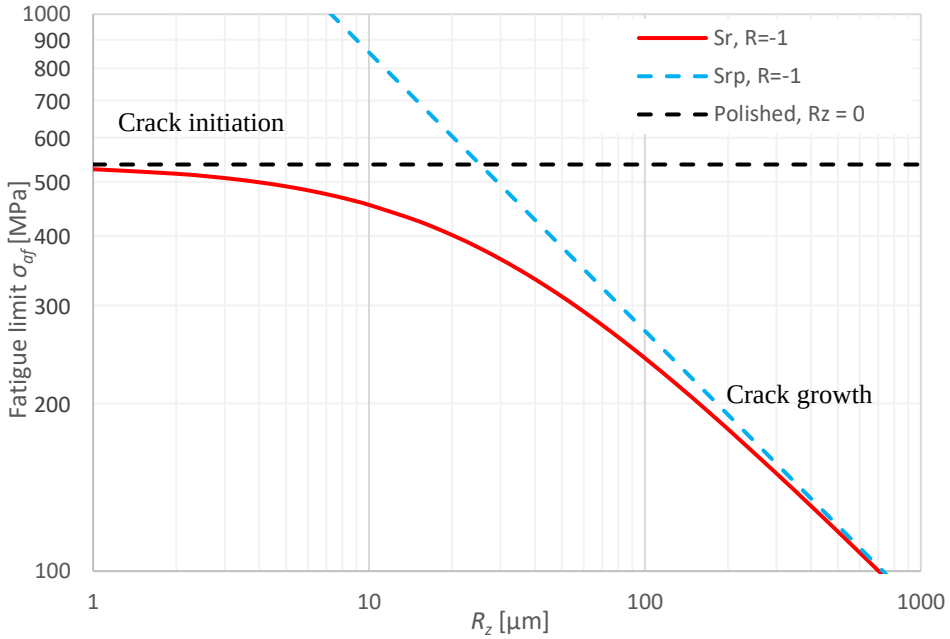

Figure 26. Fatigue limit as a function of R_z according to equation (2.49) for 42CrMo4.

Murakami (2002) has also suggested method based on fracture mechanics and $\sqrt{area}$ parameter model. The quantitative evaluation of surface roughness effect is based on two surface roughness parameters: depth a and pitch $2b$ (pitch considers the interference between the surface roughness notches). To simplify the analysis, these two parameters have been combined in one representative parameter, the equivalent defect size for roughness $\sqrt{area_R}$. (Murakami 2002, p. 313.)

The equivalent defect size for roughness can be obtained from the following (Murakami 2002, p. 316):

$$\sqrt{area_R} = \left(\frac{F}{0.65}\right)^2 \cdot a \tag{2.51}$$

, where a is depth of the surface roughness and F is geometric correction factor. When $K_I = K_{Imax}$ for arbitrarily shaped surface crack, $F = 0.65$ and consequently, the fatigue limit can be calculated as follows (Murakami 2002, p. 102–104):

$$\sigma_{af} = \frac{1.43(H_V + 120)}{(\sqrt{area_R})^{1/6}} \cdot \left(\frac{1-R}{2}\right)^{\alpha} \quad (2.52)$$

$$\alpha = 0.226 + H_V \cdot 10^{-4} \quad (2.53)$$

, where H_V is Vickers hardness. A comparison of $\sqrt{area_R}$ model, Sperle (2013) and DNVGL-ST-0361 is presented in figure 27.

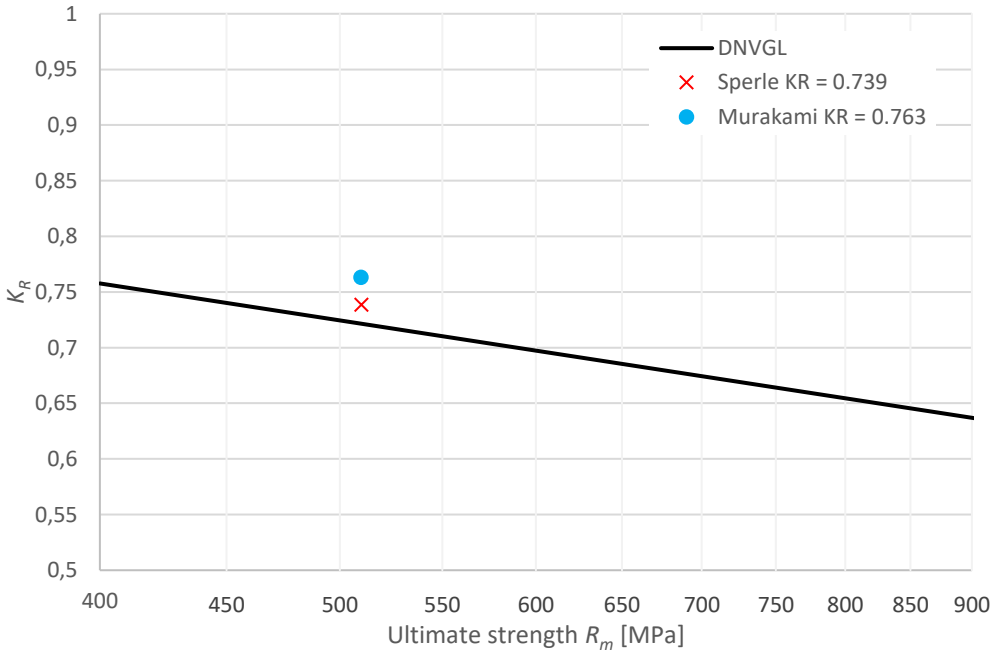

Figure 27. Comparison of K_R for S355 (R_z = 100 µm) between DNVGL-ST-0361 (2016), Sperle (2013) and Murakami (2002).

2.2.2 Anisotropy factor K_A and technological factor K_T

Anisotropy means that fatigue limit is lower in perpendicular direction to the grain flow (orientation) of the material than in parallel direction with grain flow. This results from the effect of forming processes which flatten and elongate grains and defects. In rolling processes, the grain flow direction is parallel to the rolling direction but in forging it can vary in different parts of the machine element. (Rabb 2017, p. 201.)

The effects of anisotropy and technological effect of forming degree can be taken into account with the combined anisotropy and technological factor K_{AT}. If conservative estimates are required, the following can be used (Rabb 2017, p. 205, 219):

$$K_{AT} = \frac{2069 - R_m}{1790} \quad \text{(Open die forging)} \tag{2.54}$$

$$K_{AT} = \frac{2313 - R_m}{1790} \quad \text{(Continuous Grain Flow, CGF)} \tag{2.55}$$

$$K_{AT} = \frac{2195 - R_m}{1790} \quad \text{(Average)} \tag{2.56}$$

Equations (2.54)–(2.56) are applicable for forged steel components and rolled steel rods and sheets when stress flow is perpendicular to grain flow (Rabb 2017, p. 204). However, based on testing, Rabb (2017, p. 219) recommends the values in table 3 for rolled and forged steel components.

Table 3. Technological factor and anisotropy factor for steel for CGF forgings (Mod. Rabb 2017, p. 219).

	On surface		**Below surface**	
	Parallel	Perpendicular	Parallel	Perpendicular
Technological factor K_T	1.0	1.0	1.0	1.0
Anisotropy factor K_A	1.0	0.8	1.0	0.8
Relative sample SD s_r	0.065	0.065	0.10	0.08
Population value s_{rC90}	0.080	0.080	0.12	0.10
s_{ln} = -ln(1- s_{rC90})	0.0834	0.0834	0.1278	0.1054

2.2.3 Statistical size factor K_{size}

Statistical size factor takes into account the effect of size of the component to the fatigue limit. It has been found that larger machine elements have lower fatigue limits than what smooth test specimens give and that sharp notches have actually higher fatigue limits than what would be expected based on the fatigue tests of smooth specimens. This happens because it is more probable to find a critical material defect in a larger surface than finding the same size defect in a smaller surface. (Rabb 2017, p. 139.)

Statistical size factor can be calculated using the weakest link theory. The machine element is considered to be divided into “links” and according to the theory it will break if fatigue

crack nucleates and grows in any one of these links. Therefore, reliability for the whole machine element is as follows. (Rabb 2017, p. 139.)

$$R_s = \prod_{i=1}^{n} R_i \tag{2.57}$$

, where n is number of links and R_i is reliability of a single link.

If mean value is used (P = 0.5), the reliability of a single link must be defined so that the reliability of the whole system is the required 0.5 (Rabb 2017, p. 140). If reliability for each link is taken as equal the following is obtained for the reliability of a single link (Rabb 2017, p. 140):

$$R_1 = R_2 = \cdots = R_n = R \tag{2.58}$$

$$R_s = R_1 \cdot R_2 \cdot \ldots \cdot R_n = R^n = 0.5 \tag{2.59}$$

$$\rightarrow \quad R = \sqrt[n]{0.5} \tag{2.60}$$

Let us assume that one link represents one test specimen and that the stressed area in the machine element is n times larger than that of the test specimen's. Now, the fatigue limit obtained with the test specimens must be reduced to the reliability obtained from equation (2.60) in order to have the same reliability R = 0.5 for the machine element when the equal loading is affecting its stressed surface. (Rabb 2017, p. 140.) The failure probability for this reduced fatigue limit and the corresponding λ value are obtained iteratively from the following (Rabb 2017, p. 140):

$$P = 1 - R \tag{2.61}$$

$$P = \frac{1}{\sqrt{2\pi}} \int_{-\infty}^{\lambda} e^{-\frac{x^2}{2}} dx \tag{2.62}$$

The statistical size factor K_{size} which corrects the fatigue limit from Haigh diagram can now be calculated from (Rabb 2017, p. 140–141):

$$K_{size} = \frac{1}{1 + \lambda s_r} \qquad (\text{normal dist.}) \tag{2.63}$$

$$K_{size} = e^{-\lambda s_{ln}} \qquad (\log - \text{normal dist.}) \tag{2.64}$$

, where s_r is relative standard deviation of fatigue limit and s_{ln} is logarithmic standard deviation of fatigue limit ($s_r \approx s_{ln}$).

When the weakest link theory is used to calculate K_{size} for real machine elements their stress distribution must be taken into account when calculating the number of links. The number of links can be obtained by calculating the ratio between the effective stress areas of the studied machine element and the test specimen. (Rabb 2017, p. 141.)

Let us say that stress amplitude σ_{a1} is acting on area A_1 and that $\sigma_{a1} = \sigma_{af}$. Thus, it can be stated that the reliability corresponding σ_{a1} is $R_1 = 0.5$. Then, there is another stress amplitude σ_{a2} affecting area A_2 and $\sigma_{a2} < \sigma_{a1}$. Now, the failure probability of A_2 in relation to A_1 is required and the question is to what size $A_{2,eff}$ the area A_2 needs to be reduced so that the combination $A_{2,eff}$ and σ_{a1} have the same failure probability as the combination A_2 and σ_{a2} (see figure 28). The reliability for combination A_1 and σ_{a2} can be obtained from the following. (Rabb 2017, p. 142.)

$$\sigma_{a2} = \sigma_{a1}(1 + \lambda s_r) \tag{2.65}$$

$$\rightarrow \quad \lambda_2 = \frac{1}{s_r}\left(\frac{\sigma_{a2}}{\sigma_{a1}} - 1\right) \qquad (\text{normal dist.}) \tag{2.66}$$

$$\ln \sigma_{a2} = \ln \sigma_{a1} + \lambda \cdot s_{ln} \tag{2.67}$$

$$\rightarrow \quad \lambda_2 = -\frac{1}{s_{ln}} \ln\left(\frac{\sigma_{a1}}{\sigma_{a2}}\right) \qquad (\log - \text{normal dist.}) \tag{2.68}$$

$$R_2 = \frac{1}{\sqrt{2\pi}} \int_{\lambda_2}^{\infty} e^{-\frac{x^2}{2}} dx = 1 - P_2 \tag{2.69}$$

m number of links with reliability of R_2 are needed to obtain the reliability of R_1. Therefore, the number of links corresponds the ratio between A_2 and $A_{2,eff}$ (Rabb 2017, p. 142–143):

$$m = \frac{A_2}{A_{2,eff}} \tag{2.70}$$

$$\rightarrow \quad R_2^m = R_2^{\frac{A_2}{A_{2,eff}}} = R_1 \tag{2.71}$$

$$A_{2,eff} = A_2 \frac{\ln R_2}{\ln R_1} = A_2 \frac{\ln R_2}{\ln 0.5} \tag{2.72}$$

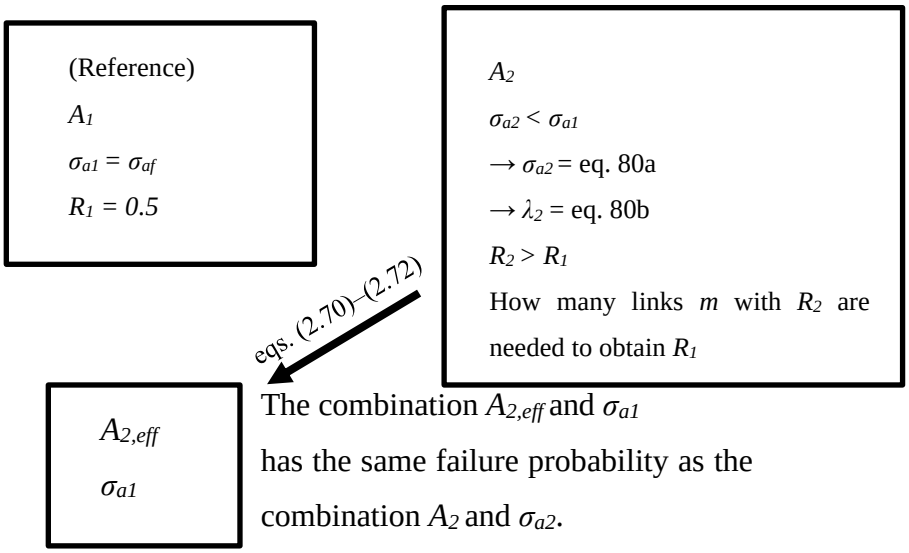

Figure 28. Effective stress area (Mod. Rabb 2017, p. 142).

This means that the statistical size factor K_{size} between A_1 (reference) and A_2 is obtained using the number of links between $A_{2,eff}$ and A_1 as follows (Rabb 2017, p. 143):

$$n = \frac{A_{2,eff}}{A_1} \qquad (\text{when } A_{2,eff} > A_1) \tag{2.73}$$

$$n = \frac{A_1}{A_{2,eff}} \qquad (\text{when } A_{2,eff} < A_1) \tag{2.74}$$

K_{size} is then calculated with equations (2.58)–(2.64). Statistical size factor is used either as a multiplier or a divisor for the fatigue limit of the reference specimen when calculating the fatigue limit of the actual machine element (Rabb 2017, p. 143, 145–146):

$$\sigma_{af,machine\ element} = \frac{\sigma_{af,Haigh\ diagram}}{K_{size}} \qquad (A_{eff} > A_{ref}) \qquad (2.75)$$

$$\sigma_{af,machine\ element} = \sigma_{af,Haigh\ diagram} \cdot K_{size} \qquad (A_{eff} < A_{ref}) \qquad (2.76)$$

Determination of statistical size factor K_{size} from FE-analysis results is presented in chapter 2.9.1.

It should be noted that when calculating K_{size} for an actual machine element, confidence intervals of sample values need to be considered (see chapter 1.6.3). For example, according to lognormal distribution, K_{size} is as follows when confidence is taken into account:

$$K_{size} = e^{-\lambda s_{ln,C90}} \qquad (A_{eff} > A_{ref}) \qquad (2.77)$$

$$K_{size} = e^{-\lambda s_{ln,C10}} \qquad (A_{eff} < A_{ref}) \qquad (2.78)$$

, where *C90* and *C10* denote the confidence levels for 90 % and 10 % respectively. (Rabb 2017, p. 261.)

Another way of determining K_{size} is to use the defect distribution of material. A modified K-T diagram mentioned in chapter 1.5.3 can be fitted to the defect distribution of material by defining the intrinsic crack length a_0 in such a way that $\sigma_{af} = \sigma_{aR=-1}$ when a is the median value a_{med} of the defect distribution. (Rabb 2017, p. 152, 534–535.)

Also, the standard deviations of defect size and fatigue limit need to match so that their intersections are on the El Haddad curve (see figure 29). This means that standard deviation of fatigue limit is calculated on the basis of standard deviation of the defect distribution. It can be done as follows if the defect distribution is known. (Rabb 2017, p. 153.)

$$\sigma_{af}(a_{med}) = \frac{\Delta K_{th}}{2F\sqrt{\pi(a_{med} + a_0)}} = \sigma_{aR=-1} \qquad (2.79)$$

$$\mu_{ln} + s_{ln}(a) = \mu_{ln+SD} \tag{2.80}$$

$$\rightarrow \quad a_2 = e^{\mu_{ln+SD}} \tag{2.81}$$

$$\rightarrow \quad \sigma_{af}(a_2) = \sigma_{af2} \tag{2.82}$$

$$K_{size} = e^{-\lambda s_{ln}} = \frac{\sigma_{aR=-1}}{\sigma_{af2}} \qquad (-\lambda = 1) \tag{2.83}$$

$$\rightarrow \quad s_{ln} = \ln\left(\frac{\sigma_{aR=-1}}{\sigma_{af2}}\right) \tag{2.84}$$

In equations (2.79)–(2.84) μ_{ln} is logarithmic mean value of defect size, $s_{ln}(a)$ is logarithmic standard deviation of defect size and s_{ln} is logarithmic standard deviation of fatigue limit. (Rabb 2017, p. 153.)

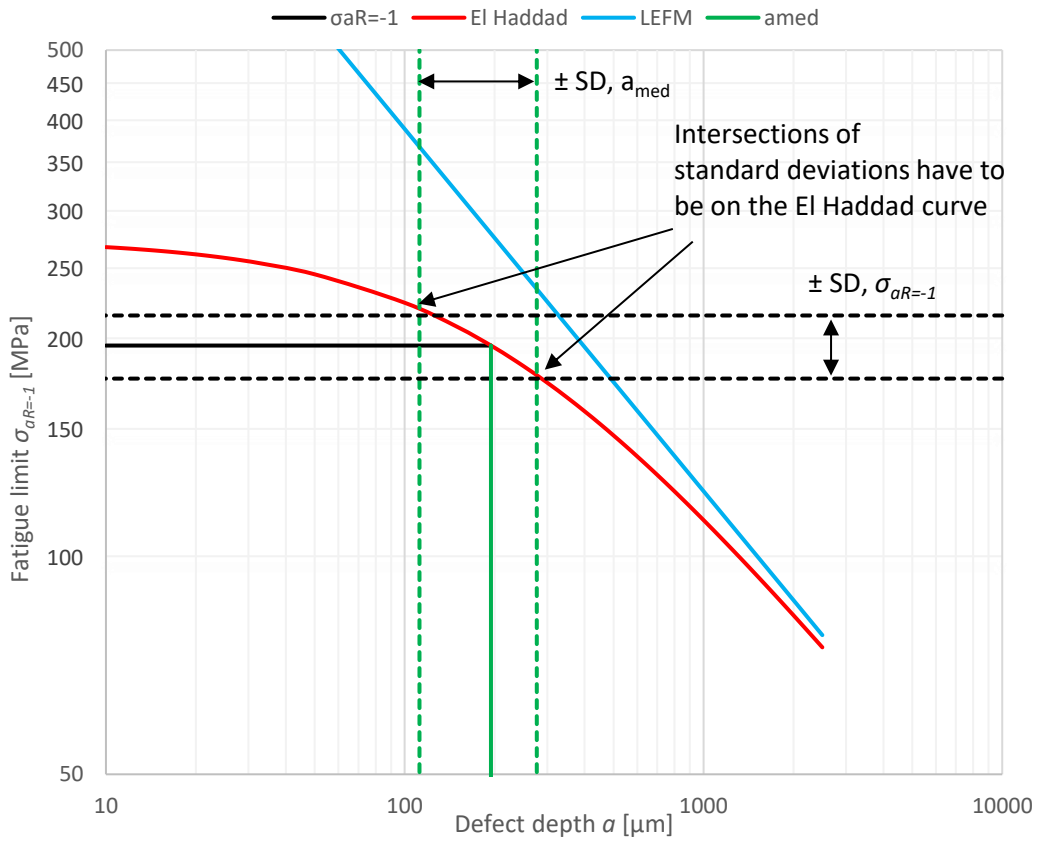

Figure 29. A modified K-T diagram (R = -1) for GJS-500-7 (Mod. Rabb 2017, p. 169).

K_{size} as a function of defect size is shown in figure 30. In this case, size factor is calculated as follows (Rabb 2017, p. 161):

$$K_{size} = \frac{\sigma_{aR=-1}}{\sigma_{aR=-1}(a_{med})} \tag{2.85}$$

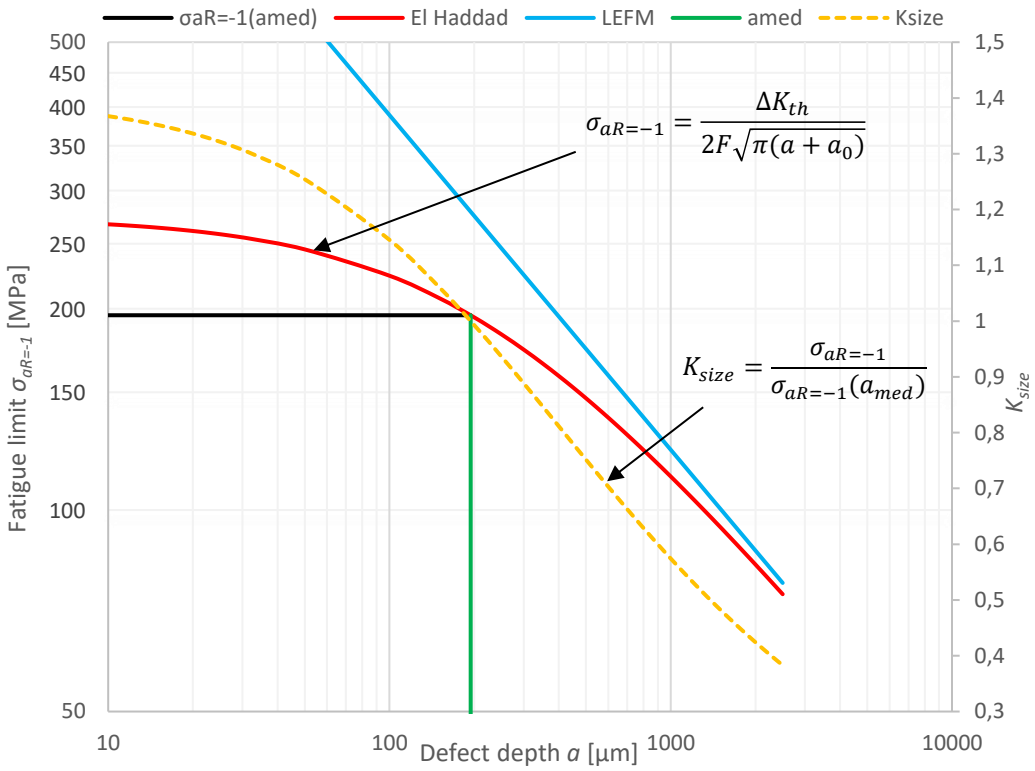

Figure 30. A modified K-T diagram for GJS-500-7 (R = -1) showing size factor K_{size}. In this figure, K_{size} is presented in such a way that it is always a multiplier for reference fatigue limit. (Mod. Rabb 2017, p. 169.)

Defect distribution of material can be used to calculate the size of expected material defect on a certain size material surface in a machine element. The expected material defect in some surface can be extrapolated from the defect distribution of material by using return period T. Since fatigue failure starts from the largest material defect, the defect distribution is an extreme value distribution. Extreme values of defects from the test specimens are fitted to distribution $F(a)$ and a is not exceeded with the probability of $P_{ref}(a)$. (Rabb 2017, p. 491, 496.)

$$P_{ref}(a) = F(a) \tag{2.86}$$

The return period *T* for defect distribution is expressed as follows (Rabb 2017, p. 496):

$$T = \frac{A_{eff} + A_{ref}}{A_{ref}} \tag{2.87}$$

The median value for defect size corresponding return period is obtained from the CDF of the defect distribution at point *P* (Rabb 2017, p. 496–497):

$$P = 1 - \frac{1}{T} \tag{2.88}$$

or

$$n = \frac{A_{eff}}{A_{ref}} \tag{2.89}$$

$$P = \frac{n}{n+1} \tag{2.90}$$

Note that number of links *n* can now be < 1 whereas in the case of the weakest link theory *n* is always > 1. The defect size (median) is obtained from the inverse function of CDF (Rabb 2017, p. 497):

$$F\left(a_{ref,50\%}\right) = 0.5 \qquad \text{(reference)} \tag{2.91}$$

$$F\left(a_{machine\ element,50\%}\right) = P \qquad \text{(machine element)} \tag{2.92}$$

$$\rightarrow$$

$$a_{ref,50\%} = F^{-1}(0.5) \tag{2.93}$$

$$a_{machine\ element,50\%} = F^{-1}(P) \qquad \text{(extrapolated defect size)} \tag{2.94}$$

, where function *F*(*a*) is CDF of defect distribution. From this, the following is obtained for K_{size} (Rabb 2017, p. 497):

$$K_{size} = \frac{\sigma_{aR=-1}(a_{machine\ element,50\%})}{\sigma_{aR=-1}(a_{ref,50\%})} \qquad (A_{eff} < A_{ref}) \tag{2.95}$$

$$K_{size} = \frac{\sigma_{aR=-1}(a_{ref,50\%})}{\sigma_{aR=-1}(a_{machine\ element,50\%})} \qquad (A_{eff} > A_{ref}) \tag{2.96}$$

It is advisable to use log-normal distribution for defect size. Even though it is not actually an extreme value distribution it seems to fit test data quite well. (Rabb 2017, p. 495.)

Using the defect distribution and K-T diagram to calculate K_{size} is more accurate than using the weakest link theory (shown earlier). However, there are some difficulties in utilization of the modified K-T diagram. First, reliable values for threshold ΔK_{th} are difficult to find from literature and therefore they might have to be obtained by testing (Rabb 2017, p.164, 171, 529.) Secondly, the defect distribution is needed, which also requires testing and recording the defects found in test pieces. These tests may be time consuming so determination of K_{size} using the first method may have to be used. However, in many cases the defect distributions for GJS-500 and 34CrNiMo6 provided by Rabb (2017, p. 163, 168) can be utilized because they are based on extensive testing. Also, as K_{size} is a relative value, error in ΔK_{th} does not cause significant problems.

2.2.4 Life factor K_N

It has been found that fatigue failure may happen at high cycle numbers even with stress levels lower than the fatigue limit (often defined at 10^7 cycles). This "gigacycle fatigue" or Very High Cycle Fatigue (VHCF) is happening when cycle numbers reach beyond 10^7 cycles all the way up to 10^8 and 10^9 cycles. These kinds of cycle numbers may be experienced for example by turbine blades which are subjected to vibration. (Murakami 2002, p. 273.)

In the case of VHCF, the nucleation of fatigue cracks always happens below the material surface. Consequently, if there is a relatively sharp notch on the machine element, the phenomenon caused by VHCF can be ignored because the notch forces the nucleation to occur on the surface. (Rabb 2017, p. 221.)

The reason why nucleation happens below the surface in VHCF is hydrogen trapped by nonmetallic inclusions. The mechanism is not entirely clear but apparently hydrogen enhances the mobility of screw and edge dislocations and reduces internal friction. This kind of fatigue failure can be recognized by the distinctive "fish-eye" pattern on the fracture surface. (Murakami 2002, p. 274–284.)

The life factor K_N which considers the effect of VHCF for steels and cast irons is expressed as follows (Rabb 2017, p. 222):

$$K_N = 1 - (\log_{10}(N) - 6) \cdot 0.05 \qquad 10^6 < N < 10^{10} \tag{2.97}$$

, where N is fatigue life in cycles. In case of steels and cast irons, the nucleation will happen on surface if stress at the critical point on surface is 20 % higher than at the critical point underneath the surface (provided the defect size is the same). When surface nucleation is considered K_N = 1 and by contrast, in the case of internal nucleation, the surface roughness factor K_R = 1. (Rabb 2017, p. 222.)

2.3 Reduction of the Haigh diagram to the allowed probability of failure

Haigh diagrams are initially constructed using mean values (P = 0.5) which is not safe enough to be used in actual design or analysis. Therefore, they are reduced to a safer failure probability like for example P = 0,1 % or P = 0,01 % depending on the consequences of failure.

Before reduction to a certain failure probability, the reduction factors presented in previous chapters should be considered. Fatigue limit for completely reversed loading is as follows (Rabb 2017, p.261):

$$\sigma_{aR=-1,red} = \frac{K_R \cdot K_{AT} \cdot K_N}{K_{size}} \cdot \sigma_{aR=-1} \qquad (A_{eff} > A_{ref}) \tag{2.98}$$

$$\sigma_{aR=-1,red} = K_{size} \cdot K_R \cdot K_{AT} \cdot K_N \cdot \sigma_{aR=-1} \quad (A_{eff} < A_{ref}) \tag{2.99}$$

It should be noted that if the nucleation happens below the surface then K_R = 1, and if it happens on the surface K_N = 1. Also, confidence level should be taken into account in calculation of K_{size}. (Rabb 2017, p. 261.)

The same reduction factors are applied to the slope of the linear part of the diagram (Rabb 2017, p. 261):

$$k_{red} = \frac{K_R \cdot K_{AT} \cdot K_N}{K_{size}} \cdot k \qquad (A_{eff} > A_{ref}) \tag{2.100}$$

$$k_{red} = K_{size} \cdot K_R \cdot K_{AT} \cdot K_N \cdot k \qquad (A_{eff} < A_{ref}) \tag{2.101}$$

$K_R = 1$ or $K_N = 1$ chosen based on the nucleation location as with the fatigue limit.

$\sigma_{aR=-1,red}$ and k_{red} can then be reduced to the required failure probability P by subtracting λ number of standard deviations from the median value of fatigue limit (λ corresponds a specific failure probability) (Rabb 2017, p. 48). Using lognormal distribution (eq. (1.40)), the following is obtained for safety factor S_F (Rabb 2017, p. 261):

$$S_F = -\frac{\sigma_{aR=-1,red}}{\sigma_{af,P}} = e^{-\lambda s_{ln,C90}} \tag{2.102}$$

, where $s_{ln,C90}$ is population value of logarithmic standard deviation. Then, $\sigma_{aR=-1,red,P}$ and $k_{red,P}$ for the required P are as follows (Rabb 2017, p. 50):

$$\sigma_{aR=-1,red,P} = \frac{\sigma_{aR=-1,red}}{S_F} \tag{2.103}$$

$$k_{red,P} = \frac{k_{red}}{S_F} \tag{2.104}$$

And thus, the linear part of the Haigh diagram reduced to the failure probability P is as follows (Rabb 2017, p. 50):

$$\sigma_{af,P} = \sigma_{aR=-1,red,P} + k_{red,P} \cdot \sigma_m \tag{2.105}$$

The plastic parts of the diagram are reduced as well. If failure probability is calculated for a stress point (σ_m ; σ_a) that is on either of the plastic parts, it has to be searched for iteratively so that the reduced curve intersects the stress point. (Rabb 2017, p. 50.) As an example,

Haigh diagram for 42CrMo4 reduced to failure probability of P = 0.1 % is shown in figure 31.

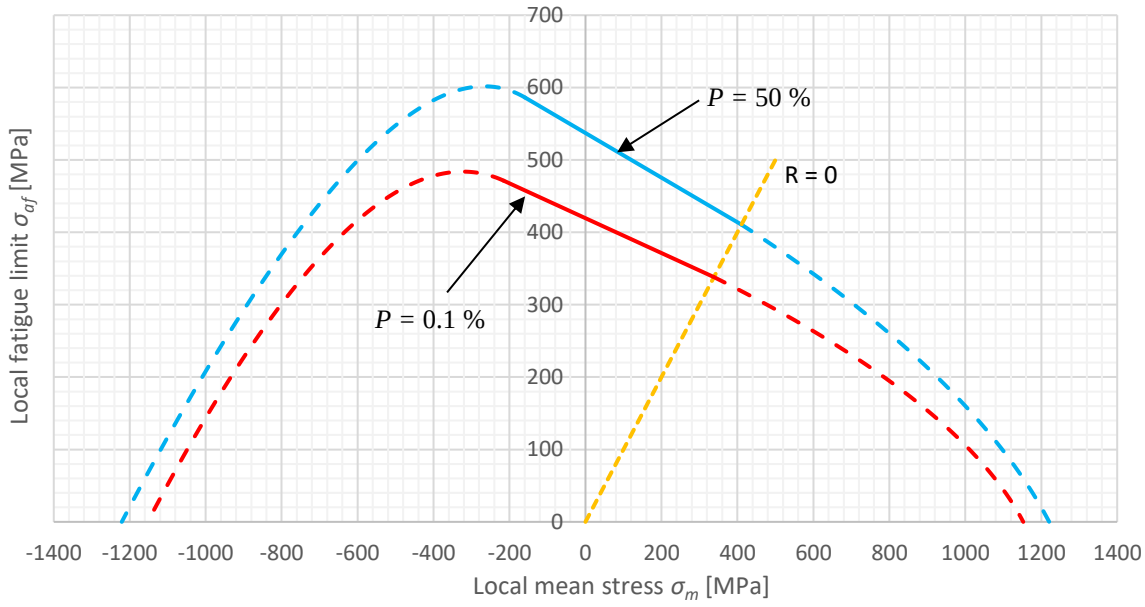

Figure 31. Mean curve P = 50 % and P = 0.1 % curve for 42CrMo4 (without any reduction factors).

2.4 S-N curves

A stress-life curve (S-N curve) or Wöhler curve is a plot of stress amplitude σ_a versus number of cycles to failure N. In essence, as the stress amplitude increases the number of cycles to failure decreases. An S-N curve is tested by conducting fatigue tests at different stress amplitudes to obtain the fatigue lives at these amplitudes. The testing can be done with constant R or with constant σ_m at every stress amplitude level. (Dowling 2013, p. 422–423; Schijve 2009, p. 144–145.)

In some materials, there is a distinct stress level below which the failure does not ordinarily occur. This horizontal asymptote in the S-N plot is the fatigue limit σ_{af} (see figure 33). The term fatigue strength on the other hand refers to a particular stress amplitude σ_{ai} at the corresponding fatigue life N_i. (Dowling 2013, p. 423.)

2.4.1 Formulation of S-N curves

Usually, S-N curves are plotted in log-log plot because this way they form straight lines (Rabb 2017, p. 107):

$$N = N_{af}\left(\frac{\sigma_{af}}{\sigma_a}\right)^k \tag{2.106}$$

, where N is the number of cycles to failure at σ_a, N_{af} is the fatigue life at σ_{af} and k is the slope exponent of the S-N curve (often $1/k$ is referred to as the slope exponent but here this notation is used).

The S-N curve is obtained by fitting equation (2.106) into the test data using the method of linear least squares regression (Rabb 2017, p. 107):

$$\ln N = A - k \cdot \ln \sigma_a \tag{2.107}$$

$$A = \ln(N_{af}\sigma_{af}^k) \tag{2.108}$$

As the test results are composed of pairs of N_i and σ_{ai} the following is obtained (Rabb 2017, p. 108):

$$F(N) = \sum_{i=1}^{n}[\ln N_i - (A - k \cdot \ln \sigma_{ai})]^2 \tag{2.109}$$

, where n is number of tests.

A and k are then defined so that equation (2.109) is minimized. This is done by differentiating equation (2.109) in respect to A and k respectively and marking the derivatives equal to zero. The following equations are then obtained for A and k. (Rabb 2017, p. 108.)

$$k = \frac{\sum_{i=1}^{n}(\ln N_i \ln \sigma_{ai}) - \frac{\sum_{i=1}^{n}(\ln \sigma_{ai}) \cdot \sum_{i=1}^{n}(\ln N_i)}{n}}{\frac{(\sum_{i=1}^{n}\sigma_{ai})^2}{n} - \sum_{i=1}^{n}(\ln \sigma_{ai})^2} \tag{2.110}$$

$$A = \frac{k\sum_{i=1}^{n} \ln \sigma_{ai} + \sum_{i=1}^{n} N_i}{n} \tag{2.111}$$

When A and k are known, the knee-point N_{af} is obtained as follows (Rabb 2017, p. 108):

$$N_{af} = \frac{e^A}{\sigma_{af}^k} \tag{2.112}$$

There is scatter in the fatigue test results and when finite fatigue life is considered, it is often presumed that fatigue life N follows log-normal distribution. It should be noted that at lower fatigue lives the scatter is smaller and when the fatigue limit is approached, the scatter increases. Usually, this is not taken into account and the defined standard deviation is an average value. Variance and standard deviation for mean value of fatigue life are obtained from the following equations. (Rabb 2017, p. 108.)

$$s_N^2 = \frac{1}{n-1}\sum_{i=1}^{n} [\ln N_i - (A - k \ln \sigma_{ai})]^2 \tag{2.113}$$

$$s_N = \sqrt{s_N^2} \tag{2.114}$$

An example of a set of test data and a fitted curve are shown in figure 32 for 42CrMo4. Test data is by Rabb (2017, p. 111).

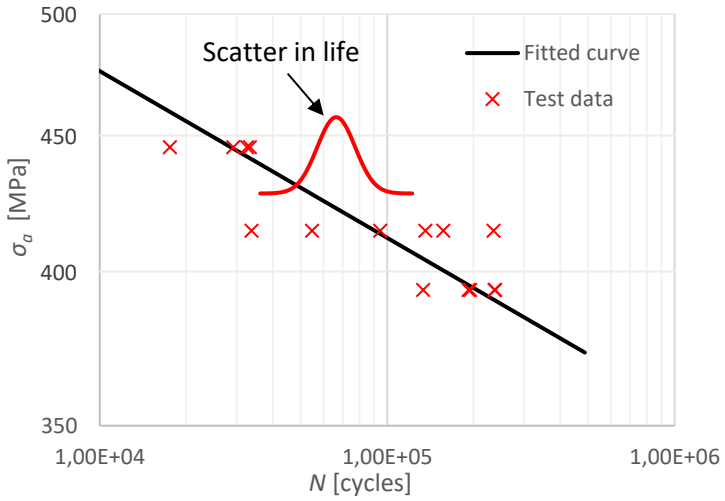

Figure 32. An example of a fitted curve. Data by Rabb (2017, p. 111).

2.4.2 Reduction of S-N curves to the allowed probability of failure

Safety factor S_N in respect to the median value of fatigue life N can be calculated when the logarithmic standard deviation of life s_N and λ corresponding the required failure probability P are known (cf. reduction of Haigh diagram) (Rabb 2017, p. 109):

$$S_N = \frac{N_{af}}{N_P} = e^{-\lambda s_N} \tag{2.115}$$

However, the reduction is usually performed with fatigue strength rather than fatigue life. The logarithmic standard deviation for fatigue strength s_{ln} can be obtained from s_N as follows (Rabb 2017, p. 109):

$$s_{ln} = \frac{s_N}{k} \tag{2.116}$$

$$\rightarrow \quad S_N = e^{-\lambda s_N} = e^{-\lambda s_{ln} k} = S_F^k \tag{2.117}$$

Thus, the required safety factor in respect to fatigue strength is (Rabb 2017, p. 109):

$$S_F = \frac{\sigma_{af}}{\sigma_{aP}} = e^{-\frac{\lambda s_N}{k}} \tag{2.118}$$

Generally, it is presumed that the knee-point does not change. The S-N curve reduced to a specified failure probability is then calculated with the equations below. (Rabb 2017, p. 109–110.)

$$\sigma_{af,P} = \frac{\sigma_{af}}{S_F} \tag{2.119}$$

$$N_P = N_{af} \left(\frac{\sigma_{af,P}}{\sigma_a} \right)^k \tag{2.120}$$

An example of an S-N curve for 42CrMo4 is presented in figure 33. The figure shows the mean curve (P = 50 %) and a reduced curve (P = 0.1 %).

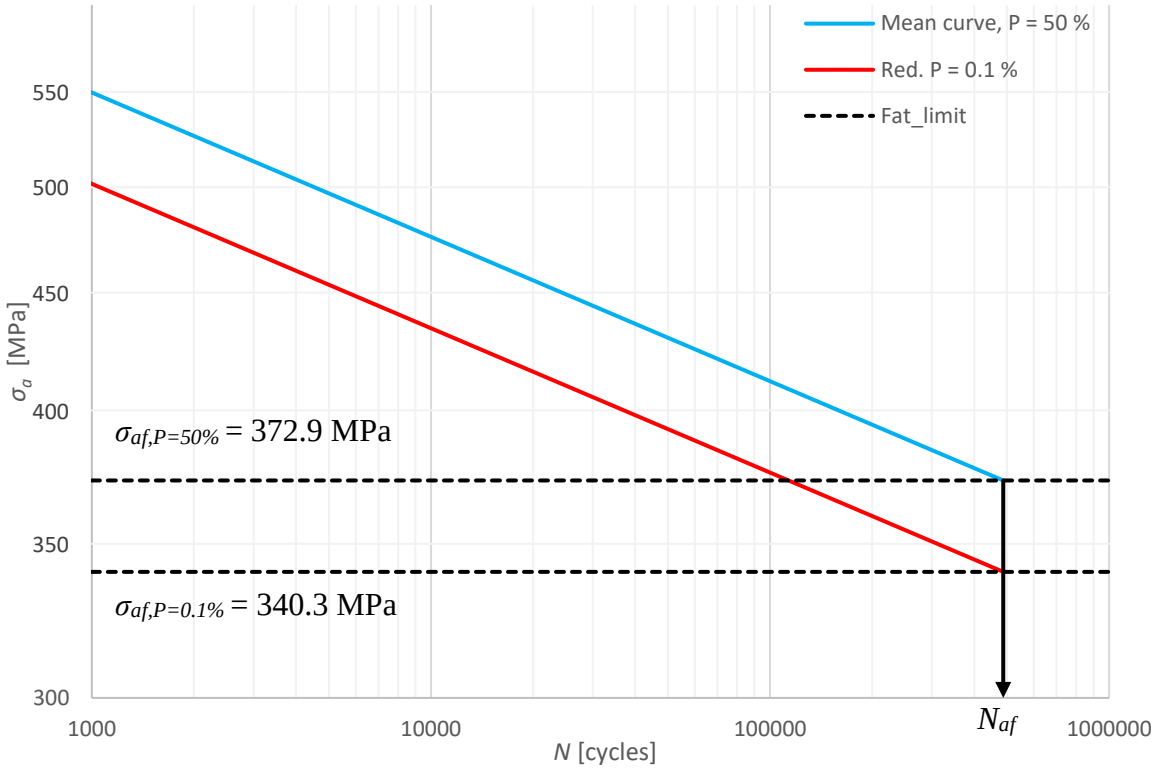

Figure 33. S-N curves for P = 50 % and P = 0.1 % for 42CrMo4 at R = 0.1 (Mod. Rabb 2017, p. 111–112).

2.5 Variable amplitude loading

Stress amplitude σ_a and mean stress σ_m may not be constant in actual machine elements but the loading may be variable with smaller and larger cycles in succession. Also, the loading can be highly irregular, or it can have some pattern to it. Examples of different kinds of loading histories are shown in figure 34.

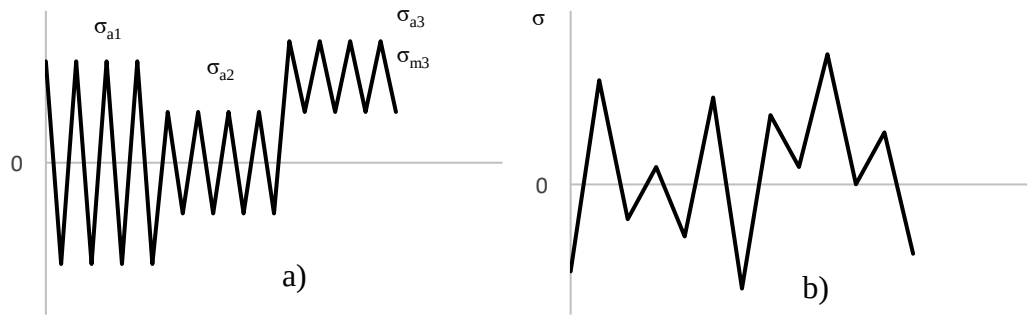

Figure 34. Variable amplitude loading. a) shows more regular stress history with mean stress shift and b) shows highly irregular history.

Larger stress amplitudes that exceed the fatigue limit reduced with safety factor and usually appear more rarely during the loading history are often referred to as low-cycle stresses. High-cycle stresses on the other hand are appearing more frequently and they are below the fatigue limit. Often, when amplitudes exceed the fatigue limit reduced with safety factor, Low cycle fatigue (LCF) is said to be affecting, and when amplitudes are below the reduced fatigue limit High cycle fatigue (HCF) is acting. Also, when number of cycles is in hundreds of millions or in billions, Very High Cycle Fatigue (VHCF) effects should be considered (see chapter 2.2.4). (Rabb 2017, p. 315.)

As was explained in chapter 2.2.4, in the case of VHCF the fatigue limit is not constant but decreases as the number of cycles increases. Similar effect is observed in the case of variable amplitude loading when the loading history includes low-cycle stresses. S-N curve does not end at N_{af} but continues to descend with a larger slope exponent i.e. the curve becomes more gradual. (Rabb 2017, p. 317.) This is explained in chapter 2.5.2.

2.5.1 Rain-flow cycle counting

For Rain-flow cycle counting loading history is illustrated so that stress is on abscissa and time is on ordinate. This makes the loading history plot resemble an Asian pagoda and now the load cycles are formed by rain flows along the “roofs” (hence the name Rain-flow cycle counting). By following the rules below, individual cycles can be formed from the loading history. (Rabb 2017, p. 409.)

1. The loading history has to be modified so that it begins and ends at its maximum value.
2. Each point where the loading history changes direction is a starting point for a new rain-flow. These flows continue to the end of the loading history unless some of the following occurs:
    a. Flow starts from a maximum point (peak) and stops opposite another maximum point which is higher than the starting point of the flow
    b. Flow starts from a minimum point (valley) and stops opposite another minimum point which is deeper than the starting point of the flow
    c. Flow stops when it encounters another flow (Rabb 2017, p. 410.)

An example of Rain-flow cycle counting is presented in Appendix II. The rules mentioned above are applied to find individual half cycles from the loading history.

Downing and Socie (1982) have suggested easily programmable algorithm for Rainflow cycle counting. First, the loading history is arranged so that it starts from the maximum or minimum value. X is used for range that is being evaluated, and Y is used for the previous range next to X. (Downing & Socie 1982, p. 32; Rabb 2017, p. 413.) Then, the algorithm follows the steps below (Downing & Socie 1982, p. 32):

1. Read the next peak or valley (if out of data, stop)
2. If there are less than three points left, go to step one. Otherwise, X and Y ranges are formed using the last three maximum and minimum values.
3. Comparison of X and Y ranges:
    a. If X < Y, go to step 1
    b. If Y ≥ Y, go to step 4
4. Form a cycle from Y, discard the minimum and maximum forming this range from the loading history and go to step 2.

2.5.2 The Palmgren-Miner rule

The Palmgren-Miner rule states that fatigue failure will happen when the fatigue life has been consumed by small fractions formed by number of different stress amplitudes. That is to say, stress amplitude σ_{a1} is applied for n_1 times, σ_{a2} is applied for n_2 times and so forth resulting in the fact that the fraction of the life consumed by a certain stress amplitude σ_{ai} is n_i / N_i. Thus, the following equation for damage sum D can be obtained. (Dowling 2013, p. 468.)

$$D = \sum_1^n \frac{n_i}{N_i} \leq 1 \tag{2.121}$$

In equation (2.121) n_i is the number of cycles of σ_{ai} and N_i is the number of cycles to failure at σ_{ai} from the S-N curve (Dowling 2013, p. 468).

As was mentioned earlier, in case of variable amplitude loading fatigue damage will progress even with stress amplitudes below the fatigue limit (HCF) if there are some cycles that are higher than the fatigue limit (LCF). The basis for analysing cumulative damage from LCF and HCF is an S-N curve that has been extended beyond the knee-point N_{af}. (Rabb 2017, p. 319–320.) Commonly used extension for cycles beyond the knee-point of an S-N curve has been proposed by Haibach (2006, p. 285–290):

$$N_i = N_{af}\left(\frac{\sigma_{af,P}}{\sigma_{ai}}\right)^{2k-l} \qquad \sigma_{ai} \leq \sigma_{af,P} \tag{2.122}$$

In equation (2.122) k is the slope exponent of the S-N curve, $l = 1$ for rolled and forged steel components and $l = 2$ for cast and welded components (Rabb 2017, p. 321). When using the Haibach extension the allowed damage sum D should be chosen according to table 4.

Table 4. The allowed damage sum D for steel and aluminium when using the Haibach extension (Mod. Rabb 2017, p. 322).

	Allowed damage sum *D*	
	Constant σ_m	Variable σ_m
Non welded components (rolled, forged)	0.3	0.1
Welded and cast components	0.5	0.2
Machined components	1.0	1.0

When reducing the extended S-N curve to the allowed failure probability, the logarithmic standard deviation of life s_N is considered to be approximately equal in low cycle and high cycle areas. Also, the standard deviation of life is defined using the standard deviation of fatigue strength and the slope exponent of the base S-N curve. (Rabb 2017, p. 325.) The reduction is demonstrated in figure 35.

The following equations and relations describe the reduced S-N curve with the Haibach extension (Rabb 2017, p. 325–326):

$$N = N_{af}\left(\frac{\sigma_{af}}{\sigma_a}\right)^k \quad \text{Base S– N curve (median)} \quad (2.123)$$

$$N_H = N_{af}\left(\frac{\sigma_{af}}{\sigma_a}\right)^{2k-l} \quad \text{Haibach extension in high cycle area} \quad (2.124)$$

$$s_{ln} = s_r \quad \text{Logarithmic SD of fatigue limit} \quad (2.125)$$

$$S_F = e^{-\lambda s_{ln}} \quad \text{Safety factor, fatigue strength} \quad (2.126)$$

$$\sigma_{af,P} = \frac{\sigma_{af}}{S_F} \quad \text{Fatigue limit for failure probability } P \quad (2.127)$$

$$s_N = k s_{ln} \quad \text{Logarithmic SD of life (both curves)} \quad (2.128)$$

$$S_N = e^{-\lambda s_N} \quad \text{Safety factor, fatigue life} \quad (2.129)$$

$$s_{ln,H} = \frac{s_N}{2k-l} \quad \text{SD of fatigue strength of the extension} \quad (2.130)$$

$$S_{F,H} = e^{-\lambda s_{ln,H}} \quad \text{Safety factor for the extension} \quad (2.131)$$

$$\sigma_{af,PH} = \frac{\sigma_{af}}{S_{F,H}} \quad \text{Fatigue strength of the extension at } N_{af} \text{ when failure probability is } P \quad (2.132)$$

From the equations above, the following is obtained for reduced S-N curve and Haibach extension (Rabb 2017, p. 326):

$$N_P = N_{af}\left(\frac{\sigma_{af,P}}{\sigma_a}\right)^k \quad \text{in low cycle area} \quad (2.133)$$

$$N_{PH} = N_{af}\left(\frac{\sigma_{af,PH}}{\sigma_a}\right)^{2k-l} = N_{af,P}\left(\frac{\sigma_{af}}{\sigma_a}\right)^{2k-l} \quad \text{in high cycle area} \quad (2.134)$$

Because none of the high cycle amplitudes may exceed the allowed amplitude $\sigma_{af,P}$, there is a horizontal part between N_{af} and $N_{af,2}$ in the reduced curve (Rabb 2017, p. 326):

$$N_{af,2} = N_{af}\left(\frac{\sigma_{af,PH}}{\sigma_{af,P}}\right)^{2k-l} \quad (2.135)$$

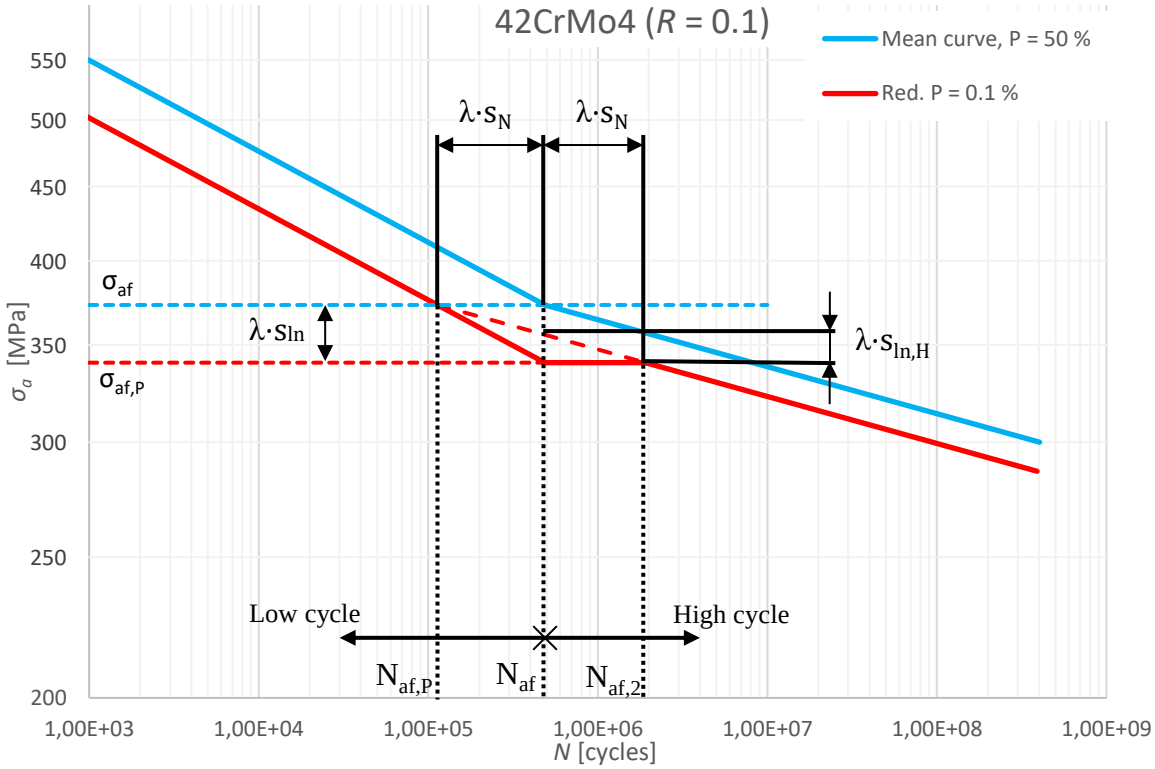

Figure 35. The reduction of Haibach extension (Mod. Rabb 2017, p. 325–326).

When the damage sum is calculated, low cycle and high cycle stresses should be considered with appropriate equation, meaning low cycle stresses are considered with base S-N curve and high cycle stresses with the Haibach extension. Consequently, the damage sum D is composed of high cycle damage sum D_{HC} and low cycle damage sum D_{LC} (Rabb 2017, p. 330):

$$D = D_{LC} + D_{HC} = \frac{1}{N_{af}} \sum n_i \left(\frac{\sigma_{ai}}{\sigma_{af,P}} \right)^k + \frac{1}{N_{af}} \sum n_j \left(\frac{\sigma_{ai}}{\sigma_{af,PH}} \right)^{2k-l} \qquad (2.136)$$

The damage sum can be transformed into an equivalent stress amplitude corresponding a specified number of cycles n_{ref}, or an equivalent number of allowed cycles can be calculated according to some constant amplitude $\sigma_{a,ref}$. When the equivalent stress amplitude $\sigma_{a,eq}$ corresponding a certain reference number of cycles n_{ref} is calculated, the equivalent fatigue life N_{eq} corresponding the damage sum calculated from equation (2.136) is needed. (Rabb 2017, p. 330.)

$$N_{eq} = N_{af}\left(\frac{\sigma_{af,P}}{\sigma_{a,eq}}\right)^{k} \tag{2.137}$$

N_{eq} is then substituted into the following (Rabb 2017 p. 330):

$$D = \frac{n_{ref}}{N_{eq}} \tag{2.138}$$

Consequently, the equivalent stress amplitude can be calculated from (Rabb 2017, p. 330):

$$\sigma_{a,eq} = \frac{\sigma_{af,P}}{\sqrt[k]{\frac{n_{ref}}{N_{af} \cdot D}}} \tag{2.139}$$

The slope exponent *k* can be calculated with the help of relative stress gradient χ^* which can be obtained from FEA (see chapter 2.9.2). For steel, the slope exponent is calculated with the following equation which is based on S-N curve tests conducted with smooth and notched specimens. (Rabb 2017, p. 338.)

$$k = \frac{k_0 - k_\infty}{(1+\chi^*)^{p_1} + \frac{1}{K_R^{p_2}} - 1} + k_\infty \tag{2.140}$$

$$\chi^* = \frac{1}{\sigma_{max}} \cdot \frac{d\sigma}{dr} \tag{2.141}$$

, where (Rabb 2017, p. 338; Rabb 2020b; Rabb 2020d):

χ^*	relative stress gradient (at the distance of $L = 2r_c$ from the surface, see chapter 2.7.1)
k_0	slope exponent for unnotched test specimen ($R = -1$) $k_0 = 11.6$ (surface nucleation) $k_0 = 16.8$ (internal nucleation)
k_∞	exponent for very sharp notch ≈ 3

K_R	Surface roughness factor
p_1	0.87
$p_2 = p_1$	0.87

Reference curve for slope exponent k as a function of relative stress gradient χ^* for steel is shown in figure 36.

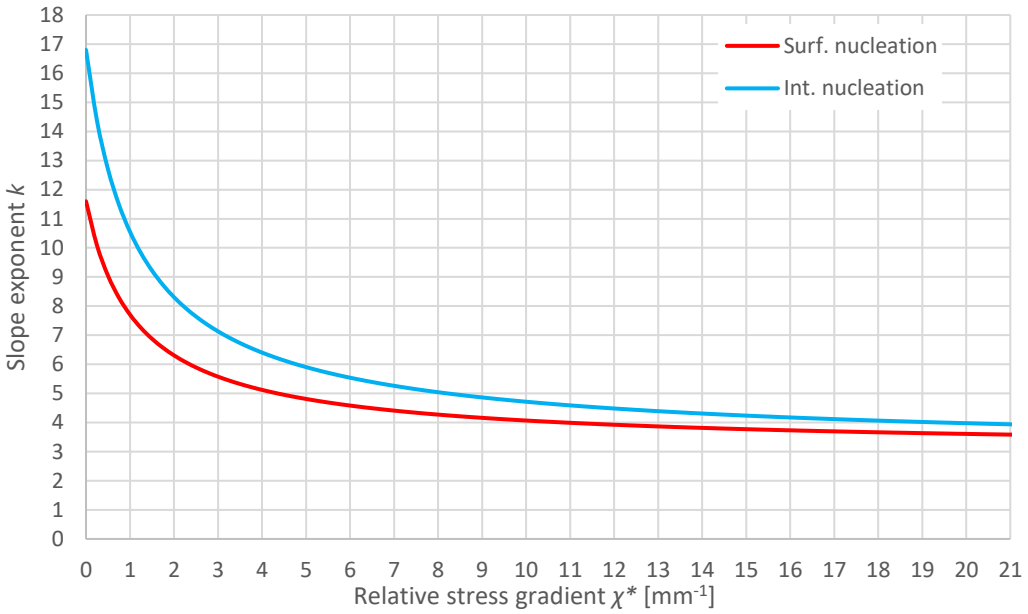

Figure 36. Reference curve (steel) for slope exponent k as a function of relative stress gradient χ^* (Mod. Rabb 2017, p. 338). χ^* value is obtained at the critical distance $2r_c = L$ from the surface.

Similar equation can also be obtained for cast iron. The difference is that for cast irons, k is dependent on mean stress. (Rabb 2017, p. 345.)

$$k = \frac{k_0 - k_\infty}{(1+\chi^*)^{p_1} + \frac{1}{K_R^{p_2}} - 1} \cdot \left[1 - \frac{C \cdot \frac{\sigma_m}{R_m}}{(1+\chi^*)^r}\right] + k_\infty \qquad (2.142)$$

, where (Rabb 2017, p. 345; Rabb 2020b; Rabb 2020d):

k_0	12, (R = -1)
k_∞	3

p_1	1.031
p_2	0.80
C	constant which considers the mean stress effect = 1.65
r	0.01, exponent which considers how C changes as a function of relative stress gradient χ^*

Reference curves for slope exponent k as a function of relative stress gradient χ^* for GJS for different σ_m / R_m ratios are shown in figure 37.

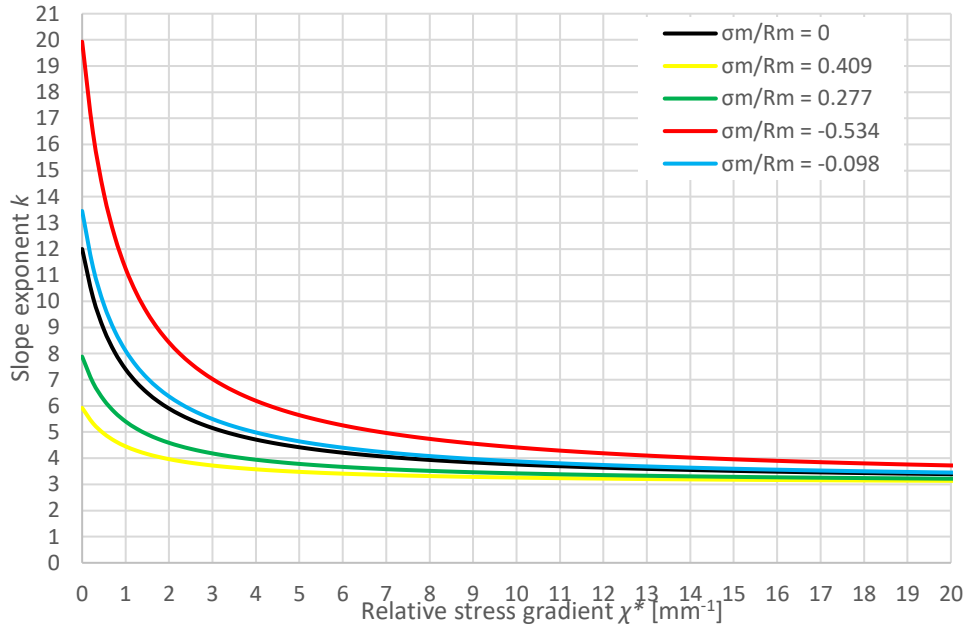

Figure 37. Reference curves (GJS) for slope exponent k as a function of relative stress gradient χ^* (Mod. Rabb 2017, p. 347). χ^* value is obtained at the critical distance $2r_c = L$ from the surface.

Values of p_1 and p_2 for both materials are modified from the values provided in Rabb's book (2017, p. 345). This is done to describe the situation when χ^* is obtained at the distance dictated by the theory of critical distances from the surface of the material (see chapter 2.7.1). Values in the book are determined on the basis that χ^* obtained on the surface.

The number of cycles at the knee-point of an S-N curve for steels when surface nucleation is considered is based on tests conducted by Rabb (Rabb 2020c):

$$N_{af} = 6.2 \cdot 10^5 \tag{2.143}$$

The equation for N_{af} from DNVGL-ST-0361 can be used if nucleation is happening below surface (when effective volume $V_{eff} \geq 400$ mm^3). In this case k should be determined at the nucleation location. (Rabb 2020c; DNVGL-ST-0361 2016, p. 51.)

$$N_{af} = 10^{6.4-\frac{2.5}{k}} \tag{2.144}$$

N_{af} for spheroidal graphite cast iron can be calculated using the equation from DNVGL-ST-0361 (Rabb 2020c; DNVGL-ST-0361 2016, p. 52):

$$N_{af} = 10^{6.8-\frac{3.6}{k}} \tag{2.145}$$

2.6 Multiaxial fatigue

Multiaxial loading cases are the most general loading cases in real components. There are often more than one loading acting on the component and the stresses may be acting in different directions. Stress components in different directions may be *proportional* or *non-proportional* meaning that they may be changing simultaneously and in the same quantity so that the principal axes remain fixed, or the stress components are not in phase and the principal axes rotate with time (see figure 38). A quite common loading case is combined bending and torsion, which can be found for example in many shafts or helical springs. (Milella 2013, p. 477.)

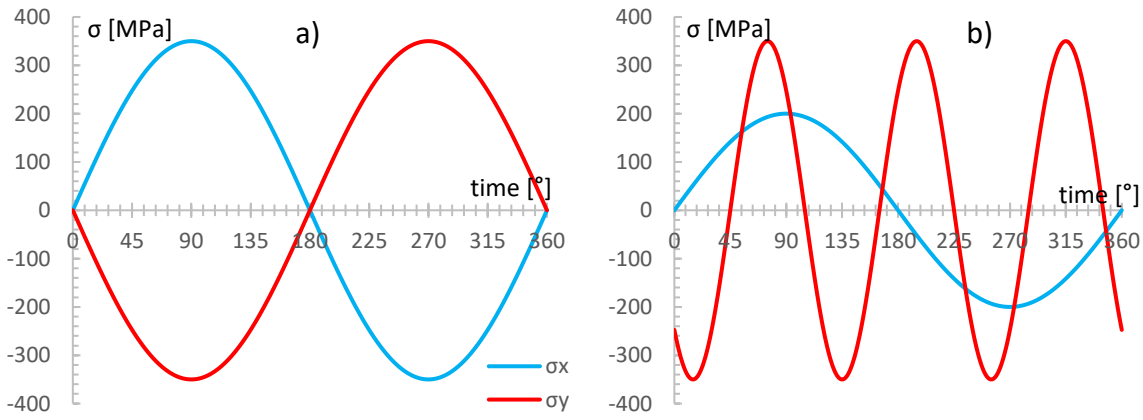

Figure 38. Examples of a) proportional loading and b) non-proportional loading.

General multiaxial stress state includes the three normal stresses σ_x, σ_y and σ_z as well as the six shear stress components τ_{ij}. However, it is common to have biaxial stress state with only three stress components, σ_x, σ_y and τ_{xy}, affecting the machine element because often, free surface where fatigue failure usually starts is not affected by any external forces (except in pressure vessels). (Milella 2013, p. 477.)

Critical plane theories are based on finding the most severely loaded plane within the material. As the fatigue damage is initiated by cyclic shear stresses causing slip in grains, the critical plane is the plane where the combination of shear stress and some stress that has an opening effect on the crack (see figure 39) induces the maximum damage. It has been found that normal stress acting on planes has an opening effect on the crack which reduces friction between the crack surfaces and thus promotes the microcrack growth. (Milella 2013, p. 496–499.)

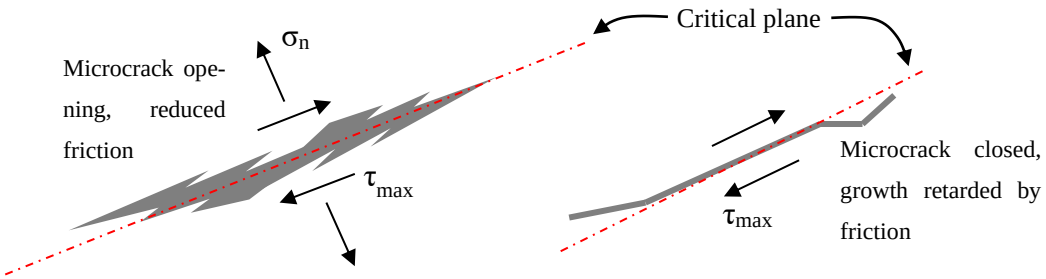

Figure 39. Normal stress on the critical plane opens the crack and reduces friction interlocking effect (Mod. Milella 2013, p. 497).

There are other options besides the critical plane theories for analysis of multiaxial fatigue. For example, methods such as signed von Mises, maximum shear stress theory or Sines criterion are stress based multiaxial fatigue criteria. The problem with these however is that they can only really be used in proportional loading cases and sometimes even in proportional cases, the results may be too inaccurate. (Altair Engineering 2020; Rabb 2017, p. 429–431; Milella 2013, p. 482–483.) Because of this, these criteria are not presented here in detail, but more accurate critical plane theories are explained instead.

Presented below are two critical plane theories: Dang Van and Findley. In practice, both of these require use of computer programs in the analysis even in relatively simple cases, but

the advantage is that they are markedly more accurate than many of the simpler criteria. Findley criteria is chosen over Dang Van criteria as the one to be used in the proposed fatigue analysis method because it works for both steels and spheroidal graphite cast iron (Rabb 2017, p. 450).

2.6.1 Dang Van

As was explained in chapter 1.5.1, fatigue crack nucleation and growth start with microscopic cyclic shear stresses causing cyclic slip in grains, which forms slip bands. Dang Van criterion is based on using these microscopic shear stresses and microscopic hydrostatic stress, which has an opening effect on the cracks formed by the slip bands, to analyse whether fatigue failure will occur. (Altair Engineering 2020.)

The critical plane in Dang Van criterion is the plane where the sum of the microscopic shear stress amplitude (according to Tresca) and the hydrostatic stress multiplied by a constant has its maximum value. The Dang Van criterion is expressed with the equation below. (Rabb 2017, p. 457.)

$$D(t_i) = \tau_a(t_i) + a \cdot \sigma_h(t_i) \leq \tau_{af,\sigma_h=0} \quad , i = 1,2, \ldots \tag{2.146}$$

$$\tau_{af,\sigma_h=0} = \frac{\sigma_{aR=-1} \cdot \sigma_{aR=0}}{2(2\sigma_{aR=0} - \sigma_{aR=-1})} \tag{2.147}$$

$$a = \frac{3(\sigma_{aR=-1} - \sigma_{aR=0})}{2(2\sigma_{aR=0} - \sigma_{aR=-1})} \tag{2.148}$$

, where (Rabb 2017, p.458):

$D(t_i)$	Fatigue damage when time is t_i
$\tau_a(t_i)$	Microscopic shear stress amplitude when time is t_i
a	Constant of Dang Van criterion
$\sigma_h(t_i)$	Hydrostatic stress when time is t_i
$\tau_{af,\sigma_h=0}$	Fatigue limit in shear (when σ_h = 0) according to Dang Van criterion

Hydrostatic stress can be calculated from the macroscopic stress tensor (for example stress matrix from FEA) corresponding a specific time. The macroscopic stress tensors are expressed as follows. (Rabb 2017, p. 458–459.)

$$\sum_{ij}(t_1) = \begin{bmatrix} \sigma_{x1} & \tau_{xy1} & \tau_{xz1} \\ \tau_{xy1} & \sigma_{y1} & \tau_{yz1} \\ \tau_{xz1} & \tau_{yz1} & \sigma_{z1} \end{bmatrix} \tag{2.149}$$

$$\sum_{ij}(t_2) = \begin{bmatrix} \sigma_{x2} & \tau_{xy2} & \tau_{xz2} \\ \tau_{xy2} & \sigma_{y2} & \tau_{yz2} \\ \tau_{xz2} & \tau_{yz2} & \sigma_{z2} \end{bmatrix} \tag{2.150}$$

$$\sum_{ij}(t_i) = \begin{bmatrix} \sigma_{xi} & \tau_{xyi} & \tau_{xzi} \\ \tau_{xyi} & \sigma_{yi} & \tau_{yzi} \\ \tau_{xzi} & \tau_{yzi} & \sigma_{zi} \end{bmatrix} \quad , i = 1,2, \ldots \tag{2.151}$$

The hydrostatic stress at a specific time is obtained from the trace of the matrix (Rabb 2017, p. 459):

$$\sigma_h(t_i) = \frac{\mathrm{tr}[\sum_{ij}(t_i)]}{3} = \frac{\sigma_{xi} + \sigma_{yi} + \sigma_{zi}}{3} \tag{2.152}$$

The shear stress amplitudes oscillate around *stabilized residual stress tensor*. When loading is proportional, the stabilized residual stress tensor is calculated as follows from the two extreme macroscopic stress tensors. (Rabb 2017, p. 459; Tampere University of Technology 2015, p. 77.)

$$\begin{aligned} \rho_{ij} &= -\frac{1}{2}\left[\sum_{ij}(t_1) + \sum_{ij}(t_2)\right] \\ &= \begin{bmatrix} -\frac{\sigma_{x1} + \sigma_{x2}}{2} & -\frac{\tau_{xy1} + \tau_{xy2}}{2} & -\frac{\tau_{xz1} + \tau_{xz2}}{2} \\ -\frac{\tau_{xy1} + \tau_{xy2}}{2} & -\frac{\sigma_{y1} + \sigma_{y2}}{2} & -\frac{\tau_{yz1} + \tau_{yz2}}{2} \\ -\frac{\tau_{xz1} + \tau_{xz2}}{2} & -\frac{\tau_{yz1} + \tau_{yz2}}{2} & -\frac{\sigma_{z1} + \sigma_{z2}}{2} \end{bmatrix} \end{aligned} \tag{2.153}$$

, where t_1 and t_2 are the times of the extreme values of the macroscopic stress (Tampere University of Technology 2015, p. 77).

The stabilized residual stress tensor is then split into hydrostatic and deviatoric (pure shear) parts (Rabb 2017, p. 459):

$$\rho_h = \frac{\mathrm{tr}\rho_{ij}}{3} = \frac{\rho_{11} + \rho_{22} + \rho_{33}}{3} \quad \text{(hydrostatic part)} \tag{2.154}$$

$$\rho_{ij} = \rho_{ij,h} + \mathrm{dev}\rho_{ij} = \begin{bmatrix} \rho_h & 0 & 0 \\ 0 & \rho_h & 0 \\ 0 & 0 & \rho_h \end{bmatrix} + \begin{bmatrix} \rho_{11} - \rho_h & \rho_{12} & \rho_{13} \\ \rho_{21} & \rho_{22} - \rho_h & \rho_{23} \\ \rho_{31} & \rho_{32} & \rho_{33} - \rho_h \end{bmatrix} \tag{2.155}$$

, where ρ_{ij} is the stabilized residual stress tensor. In other words, deviatoric part is obtained by subtracting the hydrostatic part from the stabilized residual stress tensor.

The deviatoric part is symmetric ($\rho_{ij} = \rho_{ji}$) and it can be used in calculation of microscopic stress tensors as follows (Rabb 2017, p. 459):

$$\sigma_{ij}(t_1) = \sum\nolimits_{ij}(t_1) + \mathrm{dev}\,\rho_{ij} \tag{2.156}$$

$$\sigma_{ij}(t_2) = \sum\nolimits_{ij}(t_2) + \mathrm{dev}\,\rho_{ij} \tag{2.157}$$

$$\sigma_{ij}(t_i) = \sum\nolimits_{ij}(t_i) + \mathrm{dev}\,\rho_{ij} \tag{2.158}$$

The hydrostatic stress at a specific time can also be calculated from the microscopic stress tensor (Rabb 2017, p. 460):

$$\sigma_h(t_i) = \frac{\mathrm{tr}[\sigma_{ij}(t_i)]}{3} \tag{2.159}$$

Each microscopic stress tensor is associated with a shear stress amplitude which is obtained with the help of the principal stresses of the microscopic stress tensors. The principal stresses and their directions are the eigenvalues and eigenvectors of the equation shown below. (Rabb 2017, p. 460.)

$$\begin{bmatrix} \sigma_{11}-\sigma & \sigma_{12} & \sigma_{13} \\ \sigma_{12} & \sigma_{22}-\sigma & \sigma_{23} \\ \sigma_{13} & \sigma_{23} & \sigma_{33}-\sigma \end{bmatrix} \cdot \begin{bmatrix} l \\ m \\ n \end{bmatrix} = \begin{bmatrix} 0 \\ 0 \\ 0 \end{bmatrix} \quad (2.160)$$

, where *l*, *m* and *n* are the direction cosines of the principal stresses in relation to *x*-, *y*- and *z*-axes (Rabb 2017, p. 460). An example showing the determination of the principal stresses is presented in Appendix III.

The microscopic shear stress amplitude at a specific time is calculated according to the Tresca maximum shear stress theory as follows (Rabb 2017, p. 460):

$$\tau_a(t_i) = \frac{\sigma_I(t_i) - \sigma_{III}(t_i)}{2} \quad (2.161)$$

In equation (2.161) σ_I is the maximum principal stress of the microscopic stress tensor and σ_{III} is the minimum principal stress of the microscopic stress tensor (Rabb 2017, p. 460).

The critical amplitude is the one that maximizes equation (2.146), and the corresponding critical plane is obtained from the following (Rabb 2017, p. 460):

$$\begin{cases} \overrightarrow{n_I} = l_I\vec{\imath} + m_I\vec{\jmath} + n_I\vec{k} \\ \overrightarrow{n_{II}} = l_{II}\vec{\imath} + m_{II}\vec{\jmath} + n_{II}\vec{k} \\ \overrightarrow{n_{III}} = l_{III}\vec{\imath} + m_{III}\vec{\jmath} + n_{III}\vec{k} \end{cases} \quad (2.162)$$

, where $\vec{\imath}$, $\vec{\jmath}$ and $\vec{k}$ are unit vectors of coordinate axes. Normalized direction vector of the critical plane is then as follows. (Rabb 2017, p. 460.) Critical plane is shown in figure 40.

$$\vec{n}_{cr} = \frac{\overrightarrow{n_I} + \overrightarrow{n_{III}}}{\sqrt{|\overrightarrow{n_I}|^2 + |\overrightarrow{n_{III}}|^2}} \quad (2.163)$$

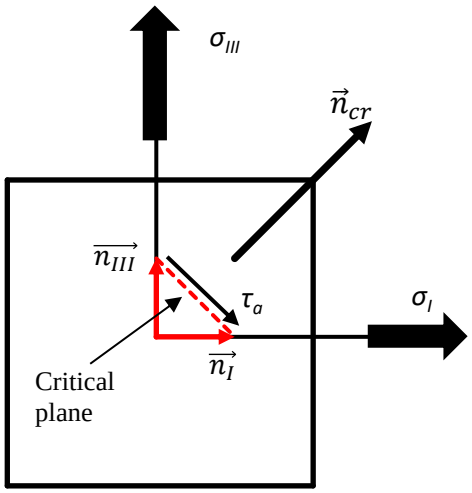

Figure 40. Critical plane according to Dang Van criterion (Mod. Rabb 2017, p. 460).

If the loading is non-proportional the stabilized residual stress tensor is calculated in a nine- or six-dimensional hypersphere. In that case, the center of the hypersphere defines the stabilized residual stress tensor and the sphere is composed of all six stress components (or nine if symmetry components $\tau_{ij} = \tau_{ji}$ are considered). (Rabb 2017, p. 459.) Calculation of the smallest hypersphere is somewhat demanding but computer programs such as *Miniball* by Gärtner (2013) can be found. If also yielding is occurring, the elastic shakedown effect needs to be considered (see figure 41) (Rabb 2017, p. 459; Altair Engineering 2020).

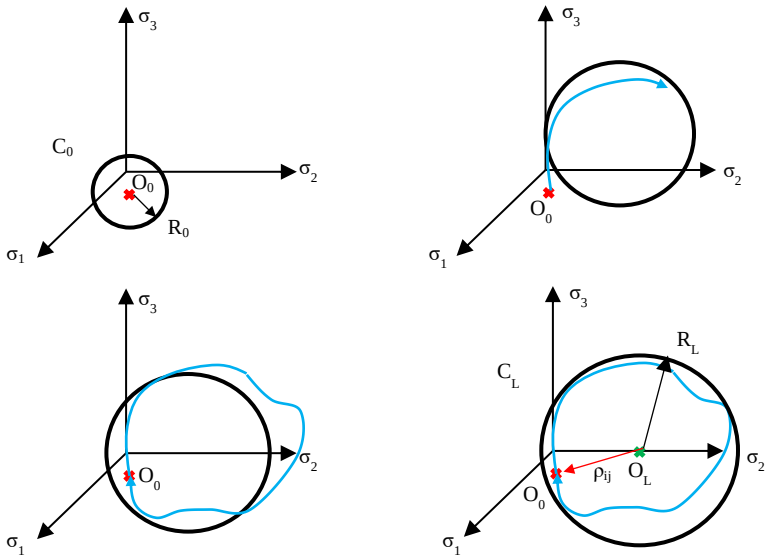

Figure 41. If yielding occurs, the initial elastic domain of the material (C_0) expands and shifts due to kinematic and isotropic hardening. After some repetitions of the load path (blue), the domain stabilizes (C_L) and the stabilized residual stress tensor corresponds to O_L – O_0. (Mod. Altair engineering 2020.)

In order to obtain safety factor, equation (2.146) can be modified into the following form and it can be plotted in Dang Van diagram (see figure 42) (Rabb 2017, p. 461).

$$\tau_{af} = \tau_{af,\sigma_h=0} - a\sigma_h \tag{2.164}$$

It is possible to define two safety factors for Dang Van criterion; radial safety factor $S_{F,rad}$ and vertical safety factor $S_{F,ver}$. Safety factors are obtained from the following. (Rabb 2017, p. 462.)

$$S_{F,rad} = \frac{\tau_{af,\sigma_h=0}}{D} \tag{2.165}$$

$$S_{F,ver} = \frac{\tau_{af,\sigma_h=0} - a\sigma_h}{\tau_a} \tag{2.166}$$

Determination of safety factors is shown in figure 42. More accurate way of determining the safety factor would be to reduce the Dang Van criterion line to intersect the studied stress point (σ_h ; τ_a) because then radial and vertical safety factors converge towards the same value. (Rabb 2017, p. 462.)

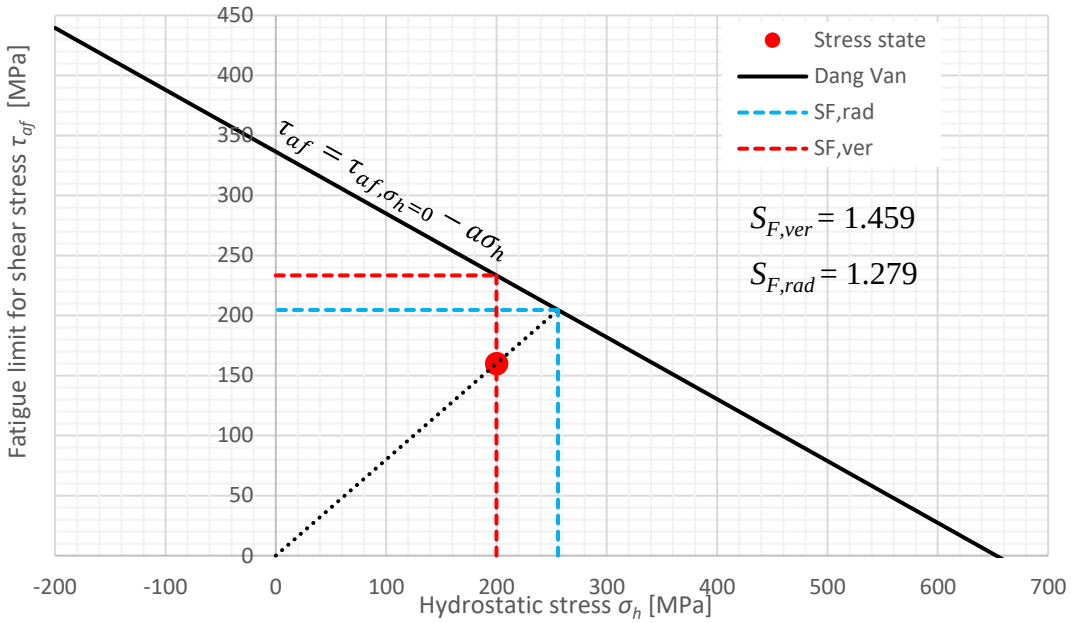

Figure 42. Vertical and radial safety factors in Dang Van diagram (Mod. Rabb 2017, p. 462).

It is possible to determine equivalent uniaxial stress state which inflicts equal damage as the original multiaxial loading. In that case according to Tresca criterion, the critical plane is in 45° angle in respect to the principal stress. For uniaxial stress state (now in x direction) the following is obtained. (Rabb 2017, p. 461.)

$$\Delta\sigma_x = \sigma_{x,max} - \sigma_{x,min} \tag{2.167}$$

$$\Delta\tau = 2\tau_a = \Delta\sigma_x \frac{\sin 2\alpha}{2} = \frac{\Delta\sigma_x}{2} \tag{2.168}$$

$$\sigma_h = \frac{\sigma_{x,max}}{3} \tag{2.169}$$

When shear stress amplitude and hydrostatic stress are known, the following gives the maximum and minimum stress for the equivalent stress state (Rabb 2017, p. 462):

$$\sigma_{x,max} = 3\sigma_h \tag{2.170}$$

$$\sigma_{x,min} = \sigma_{x,max} - 4\tau_a \tag{2.171}$$

2.6.2 Findley

According to Findley criterion, the critical plane is the plane on which the linear combination of shear stress amplitude and the normal stress of the plane has its maximum value. Consequently, Findley criterion is expressed with the following equations. (Rabb 2017, p. 433; Altair Engineering 2020.)

$$D = \left(\frac{\Delta\tau}{2} + k\sigma_n\right)_{max} \leq f \tag{2.172}$$

$$\frac{k + \sqrt{1 + k^2}}{2k + \sqrt{1 + 4k^2}} = \frac{\sigma_{aR=0,red}}{\sigma_{aR=-1,red}} \quad \text{(solve } k \text{ iteratively)} \tag{2.173}$$

$$\rightarrow \quad k = 0.2 \ldots 0.3 \text{ (typically for ductile materials)}$$

$$f = \frac{k + \sqrt{1 + k^2}}{2} \cdot \sigma_{aR=-1,red} \tag{2.174}$$

, where $\Delta\tau$ is shear stress range, σ_n is normal stress of the critical plane, k is normal stress sensitivity which describes normal stress portion of the fatigue damage, f is fatigue limit in shear, and $\sigma_{aR=0,red}$ and $\sigma_{aR=-1,red}$ are reduced fatigue limits for $R = 0$ and $R = -1$ with reduction factors taken into account. In non-proportional loading case, the maximum normal stress may be occurring on an independent time point from the time points defining the maximum shear stress amplitude. In that case, it is recommended to use the independent maximum of normal stress and the maximum shear stress amplitude (that is to say maximize the linear combination regardless whether the maximum normal stress occurs simultaneously with any of the shear stress states defining $\Delta\tau$). (Rabb 2017, p. 433–434.)

The critical plane can be found by rotating the coordinate system and determining shear stress and normal stress of the first face of stress element in every load case and direction. The rotation matrix is expressed as follows. (Rabb 2017, p. 435–436.)

$$Q = \begin{bmatrix} \sin\varphi\cos\theta & -\sin\theta & -\cos\varphi\cos\theta \\ \sin\varphi\sin\theta & \cos\theta & -\cos\varphi\sin\theta \\ \cos\varphi & 0 & \sin\varphi \end{bmatrix} = \begin{bmatrix} a_{11} & a_{12} & a_{13} \\ a_{21} & a_{22} & a_{23} \\ a_{31} & a_{32} & a_{33} \end{bmatrix} \tag{2.175}$$

Using the rotation matrix $\boldsymbol{Q}$ and stress tensor $[\sigma]$ in the base coordinate system (for example from FEA), the stress element and stress matrix in a rotated coordinate system can be obtained (see figure 43a) (Rabb 2017, p. 436):

$$[\sigma'] = Q^T[\sigma]Q = \begin{bmatrix} \sigma_{x\prime} & \tau_{x\prime y\prime} & \tau_{x\prime z\prime} \\ \tau_{x\prime y\prime} & \sigma_{y\prime} & \tau_{y\prime z\prime} \\ \tau_{x\prime z\prime} & \tau_{y\prime z\prime} & \sigma_{z\prime} \end{bmatrix} \tag{2.176}$$

In order to analyse all possible planes, the angles φ and θ of the rotation matrix have to be checked incrementally from 0 to 180 degrees (see figure 43b) (Rabb 2017, p. 436). The chosen increment should be small enough, for example $d\varphi = d\theta = 0.1 \ldots 0.5$, so that the maximum values are found with sufficient accuracy. Using an increment of $d\varphi = d\theta = 0.1$ would mean that 3 240 000 possible planes are examined and therefore the analysis requires a computer program for the calculation.

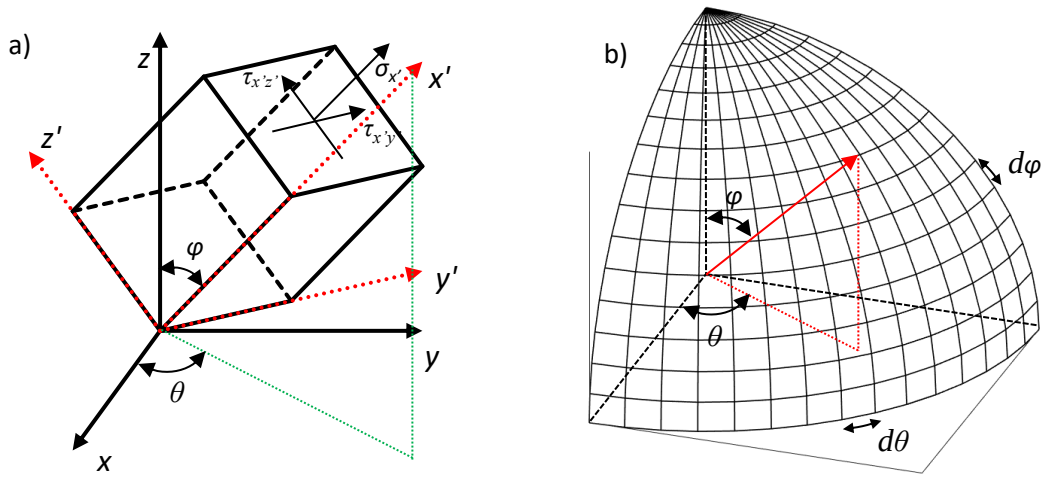

Figure 43. a) rotation of the stress element when searching for the critical plane and b) angle increments (Mod. Rabb 2017, p. 435; Mod. Lönnqvist 2008, p. 133).

Only $\sigma_{x'}$, $\tau_{x',y'}$ and $\tau_{x'z'}$ need to be considered. Consequently, the stress components of the first face of the rotated stress element are obtained from the following. (Rabb 2017, p. 436.)

$$\sigma_{x'} = \sigma_x a_{11}^2 + \sigma_y a_{21}^2 + \sigma_z a_{31}^2 + 2\left(\tau_{xy} a_{11} a_{21} + \tau_{xz} a_{11} a_{31} + \tau_{yz} a_{21} a_{31}\right) \quad (2.177)$$

$$\tau_{x'y'} = \sigma_x a_{11} a_{12} + \sigma_y a_{21} a_{22} + \sigma_z a_{31} a_{32} + \tau_{xy}(a_{11} a_{22} + a_{12} a_{21}) + \tau_{xz}(a_{11} a_{32} + a_{12} a_{31}) + \tau_{yz}(a_{21} a_{32} + a_{22} a_{31}) \quad (2.178)$$

$$\tau_{x'z'} = \sigma_x a_{11} a_{13} + \sigma_y a_{21} a_{23} + \sigma_z a_{31} a_{33} + \tau_{xy}(a_{11} a_{23} + a_{13} a_{21}) + \tau_{xz}(a_{11} a_{33} + a_{13} a_{31}) + \tau_{yz}(a_{21} a_{33} + a_{23} a_{31}) \quad (2.179)$$

Each analysed plane will have the same number of shear stress states as there are load increments. The shear stress ranges between different load increments can be calculated by using the longest chord or a radius of the smallest circle enclosing the shear stress states (see figure 44). In non-proportional loading case both methods could be used but it is advisable to utilise the radius method since in some cases it is more conservative. (Rabb 2017, p. 437.)

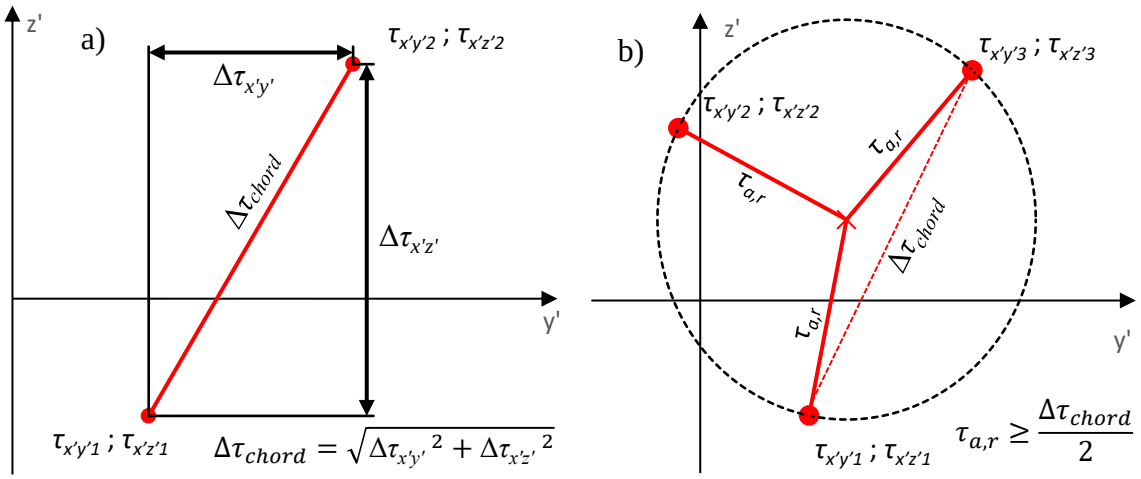

Figure 44. a) proportional loading and b) non-proportional loading (Mod. Rabb 2017, p. 437).

The chord from figure 44 a) can be calculated as follows (Rabb 2017, p. 437):

$$\Delta\tau = \Delta\tau_{chord} = \sqrt{\Delta\tau_{x'y'}^2 + \Delta\tau_{x'z'}^2} \quad (2.180)$$

The radius of the smallest circle which is defined by three points and which encloses the shear stress states (figure 44 b)) is obtained from the following determinant (Rabb 2017, p. 437):

$$\begin{vmatrix} \tau_{x\prime y\prime}^2 + \tau_{x\prime z\prime}^2 & \tau_{x\prime y\prime} & \tau_{x\prime z\prime} & 1 \\ \tau_{x\prime y\prime 1}^2 + \tau_{x\prime z\prime 1}^2 & \tau_{x\prime y\prime 1} & \tau_{x\prime z\prime 1} & 1 \\ \tau_{x\prime y\prime 2}^2 + \tau_{x\prime z\prime 2}^2 & \tau_{x\prime y\prime 2} & \tau_{x\prime z\prime 2} & 1 \\ \tau_{x\prime y\prime 3}^2 + \tau_{x\prime z\prime 3}^2 & \tau_{x\prime y\prime 3} & \tau_{x\prime z\prime 3} & 1 \end{vmatrix} = 0 \quad (2.181)$$

This yields the following form for circle equation $(x - x_0)^2 + (y - y_0)^2 = r^2$ (Rabb 2017, p. 438):

$$\alpha\left(\tau_{x'y'} + \frac{b_{\tau_{x'y'}}}{2\alpha}\right)^2 + \alpha\left(\tau_{x'z'} + \frac{b_{\tau_{x'z'}}}{2\alpha}\right)^2 - \frac{b_{\tau_{x'y'}}^2}{4\alpha} - \frac{b_{\tau_{x'z'}}^2}{4\alpha} + c = 0 \quad (2.182)$$

, where (Rabb 2017, p. 438):

$$\alpha = \begin{vmatrix} \tau_{x\prime y\prime 1} & \tau_{x\prime z\prime 1} & 1 \\ \tau_{x\prime y\prime 2} & \tau_{x\prime z\prime 2} & 1 \\ \tau_{x\prime y\prime 3} & \tau_{x\prime z\prime 3} & 1 \end{vmatrix} \quad (2.183)$$

$$b_{\tau_{x'y'}} = -\begin{vmatrix} \tau_{x\prime y\prime 1}^2 + \tau_{x\prime z\prime 1}^2 & \tau_{x\prime z\prime 1} & 1 \\ \tau_{x\prime y\prime 2}^2 + \tau_{x\prime z\prime 2}^2 & \tau_{x\prime z\prime 2} & 1 \\ \tau_{x\prime y\prime 3}^2 + \tau_{x\prime z\prime 3}^2 & \tau_{x\prime z\prime 3} & 1 \end{vmatrix} \quad (2.184)$$

$$b_{\tau_{x'z'}} = \begin{vmatrix} \tau_{x\prime y\prime 1}^2 + \tau_{x\prime z\prime 1}^2 & \tau_{x\prime y\prime 1} & 1 \\ \tau_{x\prime y\prime 2}^2 + \tau_{x\prime z\prime 2}^2 & \tau_{x\prime y\prime 2} & 1 \\ \tau_{x\prime y\prime 3}^2 + \tau_{x\prime z\prime 3}^2 & \tau_{x\prime y\prime 3} & 1 \end{vmatrix} \quad (2.185)$$

$$c = -\begin{vmatrix} \tau_{x\prime y\prime 1}^2 + \tau_{x\prime z\prime 1}^2 & \tau_{x\prime y\prime 1} & \tau_{x\prime z\prime 1} \\ \tau_{x\prime y\prime 2}^2 + \tau_{x\prime z\prime 2}^2 & \tau_{x\prime y\prime 2} & \tau_{x\prime z\prime 2} \\ \tau_{x\prime y\prime 3}^2 + \tau_{x\prime z\prime 3}^2 & \tau_{x\prime y\prime 3} & \tau_{x\prime z\prime 3} \end{vmatrix} \quad (2.186)$$

The centre of the circle is thus (Rabb 2017, p. 438):

$$\tau_{x'y'0} = -\frac{b_{\tau_{x'y'}}}{2\alpha} \tag{2.187}$$

$$\tau_{x'z'0} = -\frac{b_{\tau_{x'z'}}}{2\alpha} \tag{2.188}$$

and the diameter of the circle which describes the shear stress range is obtained from (Rabb 2017, p. 438):

$$\Delta\tau = \frac{\sqrt{b^2_{\tau_{x'y'}} + b^2_{\tau_{x'z'}} - 4\alpha c}}{|\alpha|} \tag{2.189}$$

If there are more than three shear stress points on the plane (see figure 45), some kind of algorithm for calculation is needed. For example, Weber et al. (1999) introduce an algorithm for finding the smallest enclosing circle of the shear stress points. Flowchart of the algorithm is presented in Appendix VII.

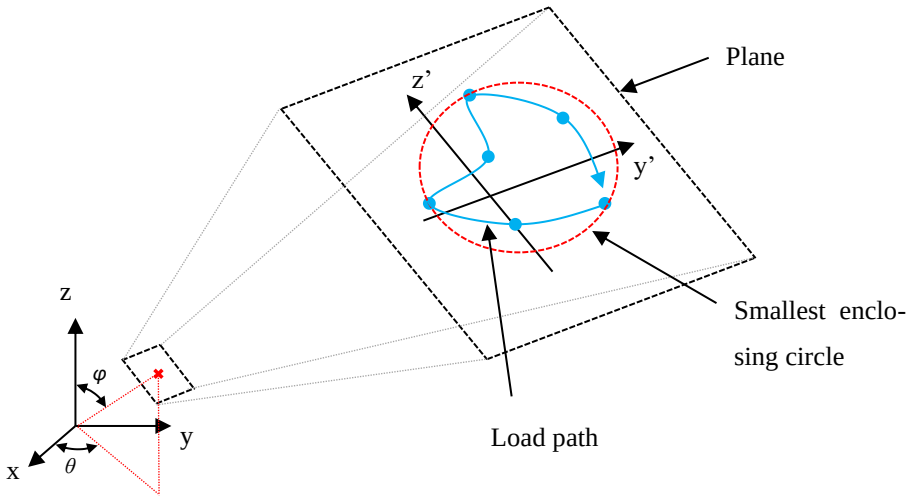

Figure 45. Shear stress range of the plane is defined by the smallest circle that encloses the load path on the plane.

As with Dang Van criterion, there are two safety factors for Findley criterion, vertical and radial (see figure 46). By modifying equation (2.172) into the following form, the safety factors can be obtained. (Rabb 2017, p. 440.)

$$\tau_a = \frac{\Delta\tau}{2} = f - k\sigma_n \tag{2.190}$$

$$S_{ver} = \frac{f - k\sigma_n}{\tau_a} \tag{2.191}$$

$$S_{rad} = \frac{f}{D} = \frac{f}{\frac{\Delta\tau}{2} + k\sigma_n} \tag{2.192}$$

Again, more accurate way of defining the safety factor would be to reduce the Findley line to intersect the studied stress state (Rabb 2017, p. 440).

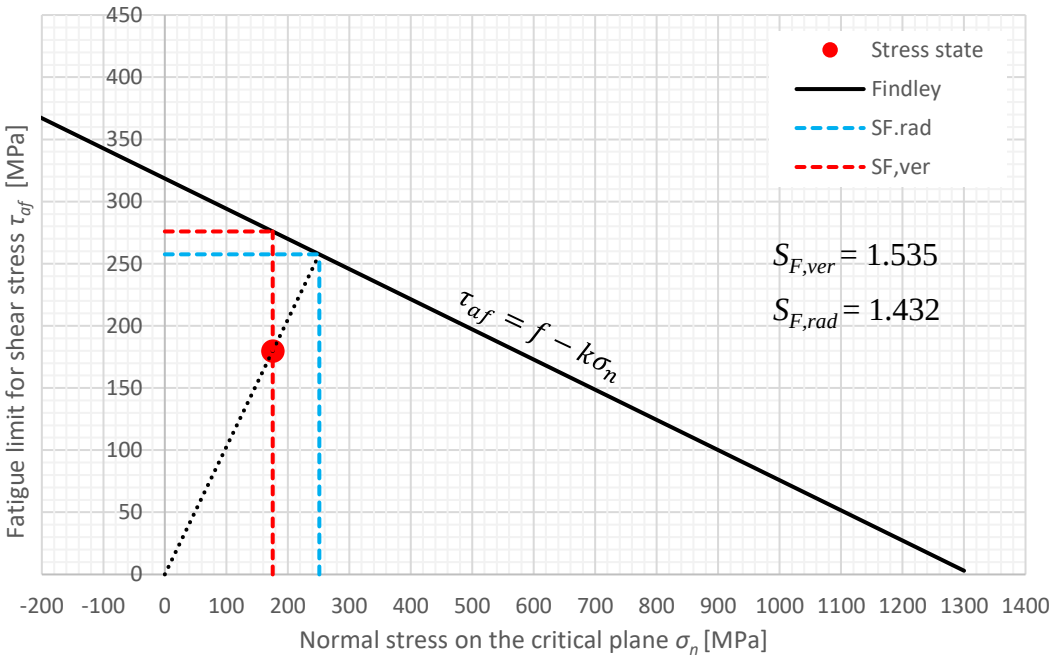

Figure 46. Vertical and radial safety factors in Findley diagram (Mod. Rabb 2017, p. 440).

The equivalent uniaxial stress state of Findley criterion is obtained from the following (Rabb 2017, p. 440):

$$\Delta\tau = \left(\sigma_{x,max} - \sigma_{x,min}\right) \cdot \frac{|\sin 2\theta|}{2} \tag{2.193}$$

$$\sigma_n = \sigma_{x,max} \cdot \cos^2\theta \tag{2.194}$$

$$\rightarrow$$

$$\sigma_{x,max} = \frac{\sigma_n}{\cos^2\theta} \tag{2.195}$$

$$\sigma_{x,min} = \sigma_{x,max} - \frac{2\Delta\tau}{\sin 2\theta} \tag{2.196}$$

The direction of the critical plane for the equivalent loading is obtained by maximizing Findley fatigue damage *D* in respect to θ (Rabb 2017, p. 441).

$$D = \frac{\Delta\tau}{2} + k\sigma_n = \frac{\sigma_{x,max} - \sigma_{x,min}}{4} \cdot \sin 2\theta + k \cdot \sigma_{x,max} \cdot \cos^2\theta \tag{2.197}$$

By differentiating in respect to θ and multiplying by sin(2θ)cos(θ) the following is obtained (Rabb 2017, p. 441):

$$\begin{aligned} &\frac{\sigma_{x,max} - \sigma_{x,min}}{4} \cdot \sin 2\theta \cdot 2\cos\theta\cos 2\theta \\ &-k\sigma_{x,max}\cos^2\theta \cdot 2\sin\theta\sin 2\theta = 0 \end{aligned} \tag{2.198}$$

With equations (2.193) and (2.194), this yields (Rabb 2017, p. 441):

$$\frac{\Delta\tau}{2} - k\sigma_n \tan\theta \tan 2\theta = 0 \tag{2.199}$$

Using the following equation from trigonometry the angle of the critical plane θ_{eq} for equivalent loading can be calculated (Rabb 2017, p. 442):

$$\tan 2\theta = \frac{2\tan\theta}{1 - \tan^2\theta} \tag{2.200}$$

$$\rightarrow$$

$$\theta_{eq} = \tan^{-1}\left(\pm\sqrt{\frac{\Delta\tau}{\Delta\tau + 4k\sigma_n}}\right) + i \cdot 180° \quad i = 0{,}1, \ldots \tag{2.201}$$

Figure 47 illustrates the transformation of multiaxial loading into equivalent uniaxial loading.

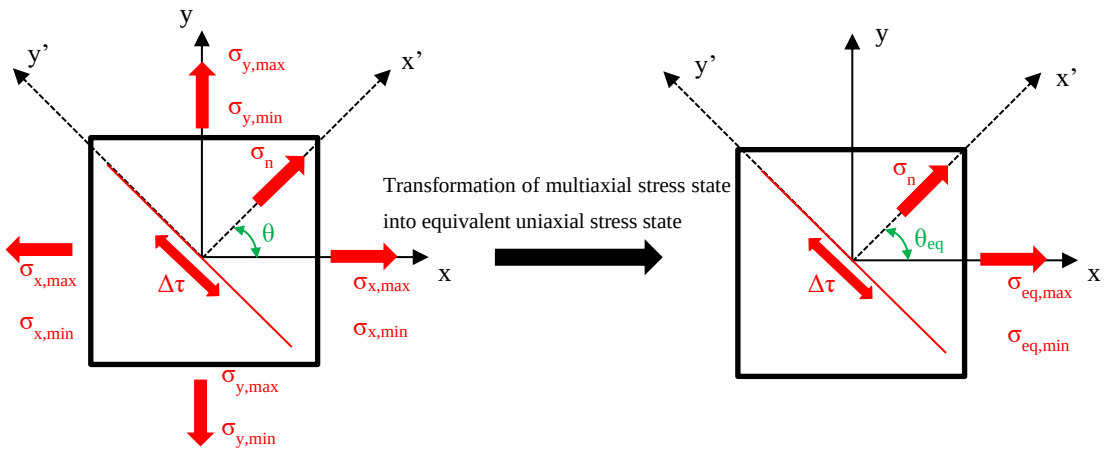

Figure 47. Transformation of multiaxial stress state into equivalent uniaxial stress state. Both load cases inflict the equal Findley damage.

Mean stress and amplitude for the equivalent uniaxial loading are obtained from the following (Rabb 2017, p. 442):

$$\sigma_{m,eq} = \frac{\sigma_{x,max} + \sigma_{x,min}}{2} \tag{2.202}$$

$$\sigma_{a,eq} = \frac{\sigma_{x,max} - \sigma_{x,min}}{2} \tag{2.203}$$

2.7 Linear elastic fracture mechanics (LEFM)

The basis of LEFM was already explained in chapter 1.5.2. Equation (1.16) which defines the Paris crack growth law can be utilized in estimation of fatigue life by integrating it from an initial crack length a_0 to a final, critical crack length a_f (Anderson 2005, p. 452).

$$N = \int_{a_0}^{a_f} \frac{da}{C(\Delta K)^m} \tag{2.204}$$

There are some limitations for the use LEFM. One, that was already mentioned earlier, is the limitation for small cracks. This means that when crack is small enough it will interact

with microstructural features and consequently its behaviour differs from what would be expected based on the assumptions of isotropic and homogenous solid. In metals this usually means that small cracks grow faster than what Paris law estimates. (Dowling 2013, p. 613–614.)

Small cracks, whose all dimensions are smaller than the largest microstructural dimension, grow faster within a grain than what is expected based on Paris law, and when they encounter a grain boundary the growth is temporarily retarded. *Short cracks* on the other hand have one dimension that is larger than the microstructural dimensions, and because of this the effect is not so drastic. (Dowling 2013, p. 613–614.) Figure 48 illustrates the behaviour of small cracks and short cracks.

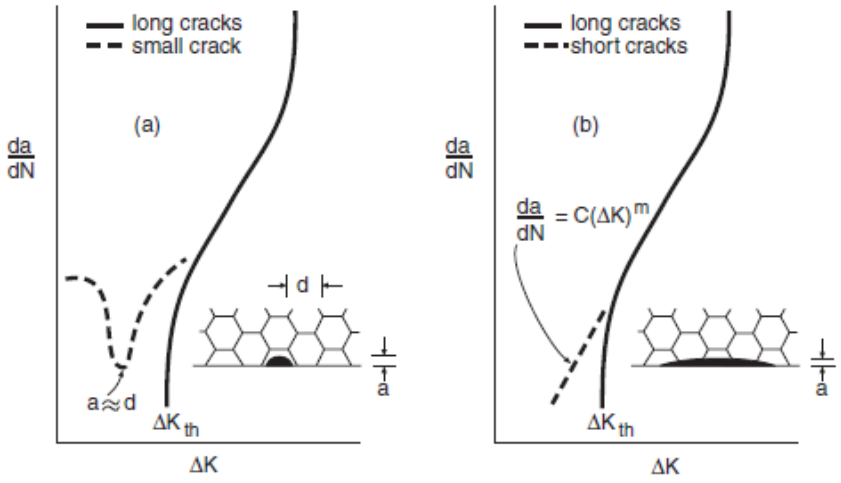

Figure 48. Behaviour of a) small cracks and b) short cracks. Unlike *small cracks*, the behaviour of *short cracks* at low ΔK can be approximated by extrapolating the Paris law curve. (Dowling 2013, p. 614.)

Another limitation for LEFM is the size of the plastic zone around the crack tip. If it is too large, crack growth rate increases too much and cannot be predicted by Paris law anymore. The limitation below can be applied to peak stress to account for the plasticity (Dowling 2013, p. 612–613.)

$$a, (b-a), h \geq \frac{4}{\pi}\left(\frac{K_{max}}{\sigma_{peak}}\right)^2 \tag{2.205}$$

, where dimensions *a*, *b* and *h* are shown in figure 49.

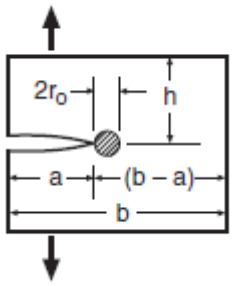

Figure 49. Dimensions for equation (2.205) (Mod. Dowling 2013, p. 387).

For example, BS 7910 (2013) gives guidelines for assessing flaws of metallic structures with LEFM approach. Two possible crack growth laws are provided in BS 7910 (2013, p. 75); Paris law with constant slope *m* and more precise two-stage relationship with two slopes (see figure 50).

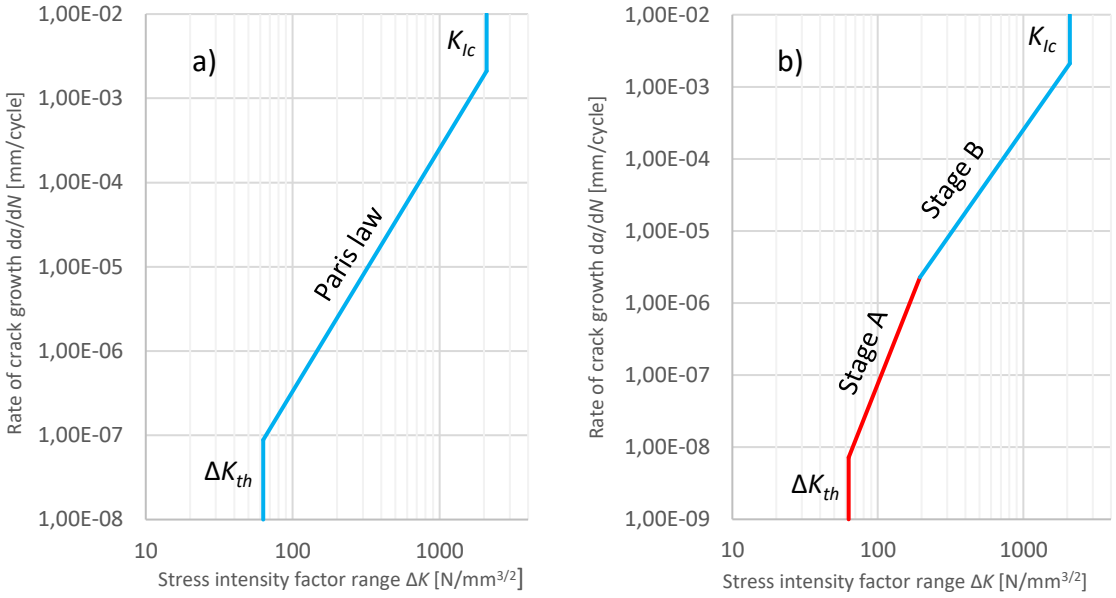

Figure 50. a) Paris law with constant *m* and b) two-stage crack growth relationship. Data from BS 7910 (2013, p. 77, 81) and Dowling (2013, p. 340).

There is relatively large variation in crack growth rate and for example according to Dowling (2013, p. 905) typical Coefficient of Variation (=relative standard deviation) for crack growth rate in fatigue is 50 %. Some recommended values for parameters *C* and *m* and uncertainty of *C* (standard deviation) are shown in table 5 for the two-stage model (BS 7910 2013, p. 220).

Table 5. Uncertainties in Paris parameter C for the two-stage model in air and freely corroding marine environment (Mod. BS 7910 2013, p. 220).

Environment	***R***	***m***	**Mean curve**	
			***C* [N, mm]**	**SD of log(*C*)**
In air				
Stage A	<0.5	8.16	1.2×10^{-26}	0.279
	>0.5	5.10	4.8×10^{-18}	0.320
Stage B	<0.5	2.88	3.9×10^{-13}	0.115
	>0.5	2.88	5.8×10^{-13}	0.171
Freely corroding marine environment				
Stage A	<0.5	3.42	3.0×10^{-14}	0.227
	>0.5	3.42	5.3×10^{-14}	0.253
Stage B	<0.5	1.30	1.2×10^{-7}	0.091
	>0.5	1.11	5.6×10^{-7}	0.060

The standard also gives guidance about probabilistic methods for LEFM analysis which may be of interest because deterministic procedures can sometimes give over-conservative results. Two levels of reliability analyses are given; Level I method which is semi-probabilistic approach based on partial safety factors and Level II method based on first order second moment methods assuming the load (L) and resistance (R) effects are following normal distribution. For fatigue crack growth assessment, Level II method is utilized. The limit state function for any number of random variables according to Level II method is defined with the following equation. (BS 7910 2013, p. 215–218.)

$$R - L = g(Z) \quad \text{(failure when } g(Z) < 0) \tag{2.206}$$

The failure probability P_F is defined as follows and it is related to the reliability index β_R (BS 7910 2013, p. 217):

$$P_F = P[g(Z) < 0] \int_{g(Z) \leq 0} f_z(Z) dz \tag{2.207}$$

$$P_F = 1 - \Phi(\beta_R) = \Phi(-\beta_R) \tag{2.208}$$

, where Φ is the cumulative distribution function of standard normal distribution and $f_Z(Z)$ is multivariate probability density function of Z. If reliability index corresponding a specified failure probability is required it can be calculated as follows (BS 7910 2013, p. 217):

$$\beta_T = \Phi^{-1}(1 - P_F) \tag{2.209}$$

2.7.1 The Theory of critical distances (TCD)

The theory of critical distances (TCD) is an LEFM based method developed by Taylor (2007), which can be used in predicting the effect of notches and for example material defects on the fatigue behaviour of material. TCD uses a material length scale L to assess the possibility of fatigue failure (Taylor 2007, p. 1696; Rabb 2017, p. 294). The length scale L is defined as follows (Taylor 2007, p. 1696):

$$L = \frac{1}{\pi}\left(\frac{\Delta K_{th}}{\Delta \sigma_{af}}\right)^2 \tag{2.210}$$

, where $\Delta\sigma_{af}$ is fatigue limit range. There are four different TCD methods to predict the fatigue failure. Two of these methods are stress-based and they are called point method (PM) and line method (LM). In PM, the critical amplitude σ_{ac} is at a distance of r_c from the surface, where $r_c = L / 2$, and in LM σ_{ac} is defined as an average stress within $2L$ from the surface. (Taylor 2007, p. 1699.) Principle of PM and LM are shown in figure 51.

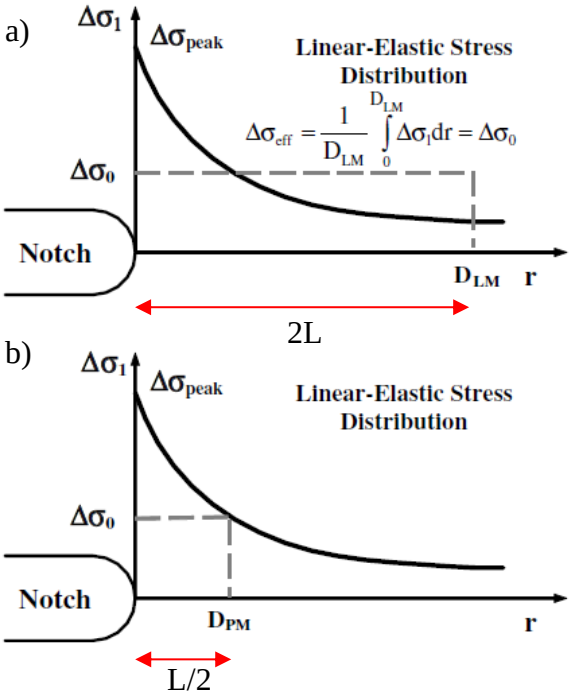

Figure 51. Principles of a) Line Method and b) Point Method (Mod. Susmel 2006, p. 1708).

The other two methods are based on stress intensity. The imaginary crack method (ICM) which is similar to El Haddad's (1979) method, assumes that there is an imaginary crack at the root of the notch and that the length of this crack is *L*. In case of fatigue, the failure will occur when the stress intensity of this crack reaches ΔK_{th}. The other stress intensity-based method is finite fracture mechanics (FFM) in which the condition for failure is derived from energy balance assuming a finite amount of crack extension (which would be 2*L*). (Taylor 2007, p. 1699.) The failure criterion for FFM is expressed as follows (Taylor 2007, p 1699):

$$\int_0^{2L} K^2 da = K_c^2 \cdot 2L \tag{2.211}$$

Rabb (2017, p. 294–295) recommends using point method in which, as mentioned earlier, the critical stress amplitude σ_{ac} is obtained at the distance $r_c = L / 2$ from the surface. With PM, the theory of critical distances is expressed with the following equations when also size factor is considered (Rabb 2017, p. 295; Rabb 2020a):

$$L = \frac{1}{\pi}\left(\frac{\Delta K_{th}}{K_{size} \cdot \Delta\sigma_{af}}\right)^2 \quad (2.212)$$

$$r_c = \frac{L}{2} \quad (2.213)$$

$$\sigma_{ac} \leq \frac{K_{size} \cdot \sigma_{aR,smooth}}{S_F} = \frac{K_{size} \cdot \Delta\sigma_{af}}{2S_F} \quad (2.214)$$

$$\chi^* = \frac{1}{\sigma_{max}} \cdot \frac{d\sigma}{dr} \quad (2.215)$$

, where $\sigma_{aR,smooth}$ is fatigue limit for smooth reference specimen and χ^* is relative stress gradient (see chapter 2.9.2).

TCD can be utilized in a case of a sharp notch where relative stress gradient is very steep and consequently, there is a large difference in stress between the lowest and the deepest points of a (large) material defect. Therefore, stress intensity may drop considerably between these points and the critical point is not located on the surface but slightly below it. In cases like this, statistical theory may give too conservative estimates because it assumes that the stress amplitude is approximately equal over the material defect. (Rabb 2017, p. 293.)

Rabb (2017, p. 297) states that statistical theory works well when $k_t \leq 2$ for spheroidal graphite cast iron and with notches sharper than this, phenomenon explained above may have to be considered. With steel, TCD needs to be considered when stress state is singular like sometimes in the case of fretting fatigue (Rabb 2017, p. 297).

TCD is also utilised in calculation of slope exponent *k* for S-N curves. In that case, the critical distance is *L* rather than *L* / 2. Using *L* as critical distance increases the value of slope exponent in the same amount as it is increased in nominal stress method when notch sensitivity factor is considered. (Rabb 2020d.)

2.8 Multiscale modelling of fatigue

As was explained in chapter 1.5, fatigue process consists of crack initiation and crack growth phases. It can be seen that fatigue process involves different length scales and thus the analysis of fatigue life from the start of the cyclic slip to “large” crack growth requires consideration of multiple length scales (Božic et al. 2014, p. 1044).

Crack nucleation happens as a result of dislocation movement which develops slip bands within grains. Dislocation development is within nanoscale and can be analysed with atomistic scale simulation methods. The consequent crack nucleation and microcrack growth are still affected by the microstructure and they are happening within mesoscale. As such, they need analysis methods which can consider the relevant effects. After the microcrack has grown sufficiently large, its propagation in macroscale can be analysed for example with fracture mechanics. (Božic et al. 2014, p. 1044–1045.) Different length scales are shown in figure 52.

The modelling methods fall into two categories based on how they describe materials. Discrete methods or atomistic methods combined with stochastic methods can be used in modelling time-controlled phenomena such as diffusion, aging or deformation mechanisms in nanoscale. Continuous methods on the other hand are based on solid or fracture mechanics and they are used in modelling macroscale continuous behaviour. (Laukkanen, Holmberg & Wallin 2013, p. 11–12.) Examples of modelling methods for different spatial and temporal scales are presented in figure 52.

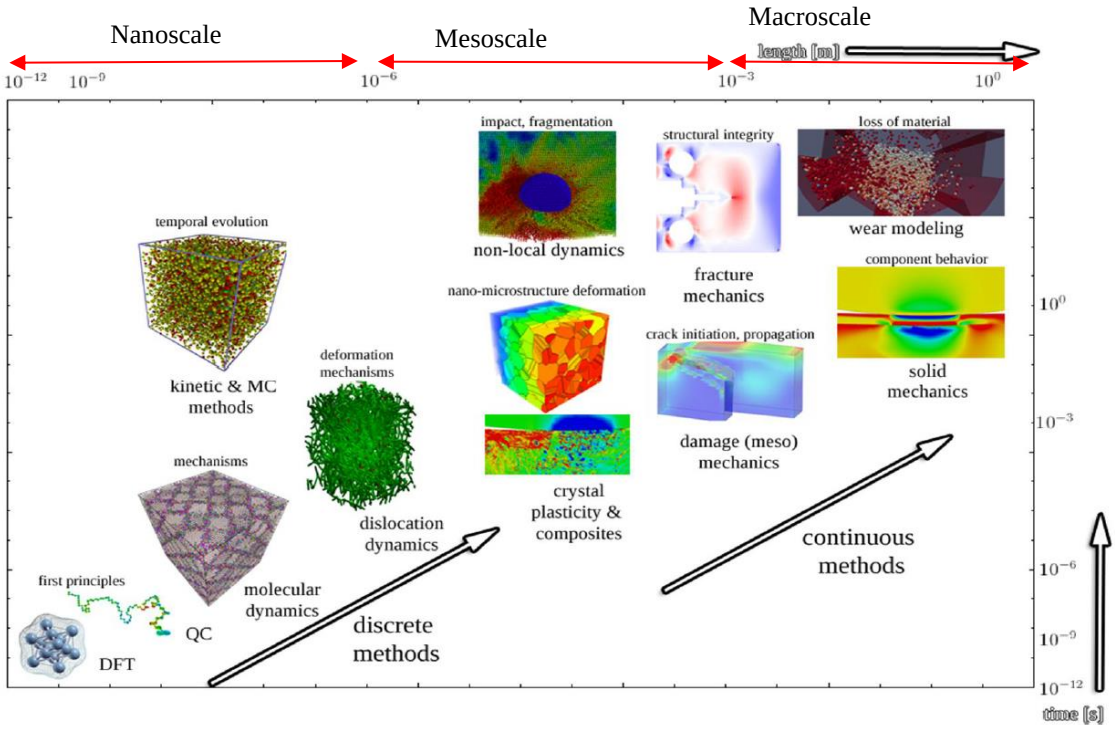

Figure 52. Modelling methods for different spatial and temporal scales (Mod. Laukkanen, Holmberg & Wallin 2013, p. 13).

2.8.1 Nanoscale

Dislocation nucleation and movement can be modelled using molecular dynamics (MD). Often the models in MD are based on assumptions (the Born-Oppenheimer approximation) that allow the use of Newton's second law in expressing the equations of motion for atomic nuclei. Use of this classical approach instead of quantum mechanics is needed because solution based on quantum mechanics would quickly become too complicated to compute. (Božic et al. 2014, p. 1045; Leimkuhler & Matthews 2015, p. 5–7.)

The Newtonian equation of motion for atoms is expressed as follows and it is solved in every time step of the MD analysis (Eidel, Hartmaier & Gumbsch 2010, p. 11; Božic et al. 2014, p. 1045):

$$F_i = m_i \frac{d^2 \boldsymbol{x_i}}{dt^2} \tag{2.216}$$

, where $\boldsymbol{x_i}$ is the position vector of atom i, t is time and m_i is the mass of the atom. The force F_i acting on atom i is obtained by taking the derivative of the potential energy U which depends on the position of all atoms (Eidel, Hartmaier & Gumbsch 2010, p. 11):

$$F_i = -\frac{dU(x)}{d\boldsymbol{x_i}} \tag{2.217}$$

The potential energy U is often obtained by using Embedded atom method (EAM) (Eidel, Hartmaier & Gumbsch 2010, p. 8):

$$U_{tot} = \frac{1}{2}\sum_{i,j\neq i} V_{ij}(r_{ij}) + \sum_i F_e(\rho_i) \tag{2.218}$$

$$\rho_i = \sum_{j\neq i} \rho_{ij}(r_{ij}) \tag{2.219}$$

, where ρ_{ij} is the contribution of atom j to the total electron density at atom i, F_e is the embedding energy associated with placing atom i in this environment, r_{ij} is the separation between atoms i and j, and V_{ij} is the pair potential contribution to the potential energy of atom i.

Molecular dynamics modelling yields material parameters that can be utilised in micromechanics modelling (in mesoscale). An important parameter that can be defined with MD is critical resolved shear stress (CRSS) which is the stress required to initiate slip in a crystal. (Božic et al. 2014, p. 1047; Milella 2013, p. 36.) Figure 53 shows an MD model of iron with a notch.

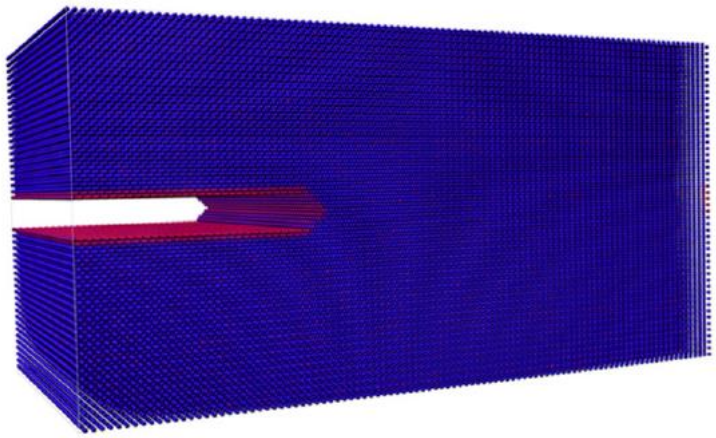

Figure 53. Body centred crystal iron cuboid with a notch (486 000 atoms). Von Mises stress is indicated with red (high) and blue (low). (Božic et al. 2014, p. 1046.)

2.8.2 Mesoscale

Crack nucleation can be predicted for example with Tanaka-Mura model. According to the model, fatigue crack nucleation is induced by accumulation of dislocation dipoles in a single grain during strain cycling. The number of stress cycles needed for crack nucleation is obtained when a critical value of the self-strain energy of the accumulated dislocation dipoles is reached. Number of cycles required for the crack nucleation in a single grain is expressed as follows. (Božic et al. 2014, p. 1047.)

$$N_g = \frac{8GW_c}{\pi(1-\nu)\cdot d\cdot(\Delta\overline{\tau}-2\cdot\tau_{CRSS})^2} \tag{2.220}$$

According to equation (2.220), crack nucleation on a slip band depends on slip band length d which is the distance along the slip band between grain boundaries of a single grain, and the average shear stress range of the slip band $\Delta\overline{\tau}$. In addition, G is shear modulus, W_c is specific fracture energy per unit area, ν is Poisson's ratio and τ_{CRSS} is critical resolved shear stress. (Božic et al. 2014, p. 1047.)

The grain structure of the material can be modelled in 2D or 3D in FEM. One approach is to use the Voronoi tessellation (figure 54) which creates a random grain structure by dividing the space into regions using randomly distributed seed points. (Nygårds 2003, p. 14–15.)

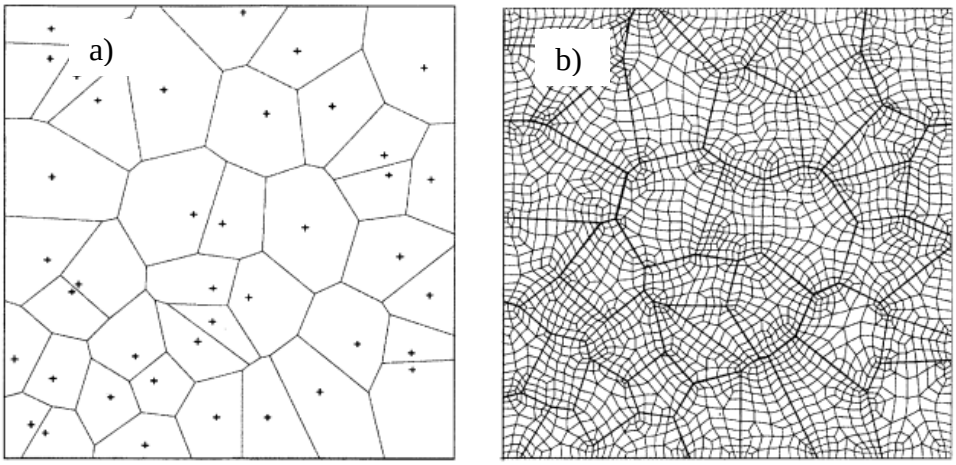

Figure 54. a) 2D Voronoi tessellation with seed points and b) FE mesh of the tessellation (Weyer et al. 2002, p. 949).

Another option to model the grain structure is to use a scanning electron microscope (SEM) image of the actual microstructure of material. The microstructural phases can be segmented from the SEM image and FE mesh can be generated on the resulting material distribution. (Laukkanen, Holmberg & Wallin 2013, p. 15–16.) Modelling of microstructure based on SEM image is shown in figure 55.

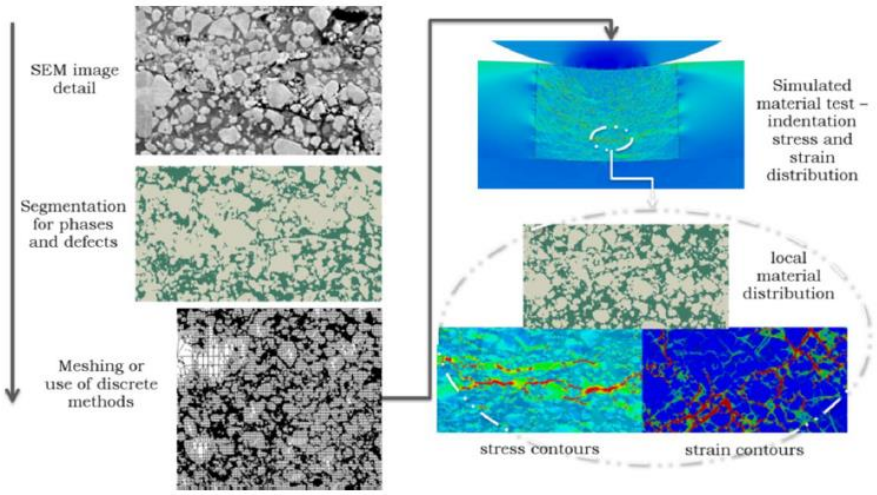

Figure 55. Modelling of the microstructure of a metal matrix composite coating. (Laukkanen, Holmberg & Wallin 2013, p. 16).

After the FE-mesh is generated, the Tanaka-Mura model can be incorporated in it, and grains where the crack nucleation condition $|\Delta\overline{\tau}| > 2 \cdot \tau_{CRSS}$ is met, can be found (Mlikota, Schmauder & Božic 2018, p. 292). An example of two-scale FE-model is shown in figure 56.

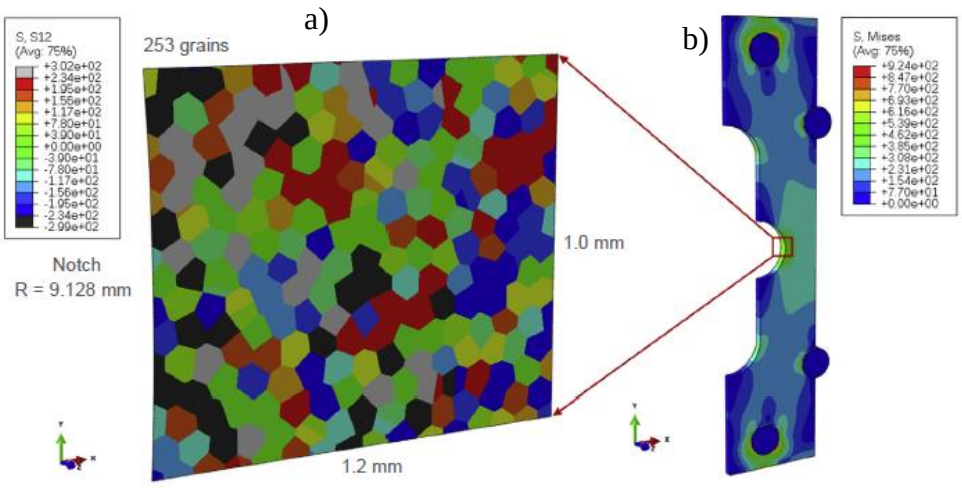

Figure 56. a) shear stresses in 3D deformable shell sub-model. The Tanaka-Mura nucleation condition is satisfied in black and grey grains. b) 3D global model. (Mlikota, Schmauder & Božic 2018, p. 292.)

2.8.3 Macroscale

Crack growth of "large" cracks in macroscale can be analysed with LEFM. By combining the LEFM results with the results from the initiation analysis done with Tanaka-Mura model the total fatigue life (initiation + propagation) can be obtained. In essence, two macroscale models are needed. One is used with the grain structure sub-model to analyse the initiation, and the other is used for LEFM analysis and determination of stress intensity factor range ΔK. (Mlikota, Schmauder & Božic 2018; Mlikota, Staib, Schmauder & Božic 2017.)

Multiscale models could be used, instead of testing, to obtain different material parameters. For example, Mlikota, Schmauder & Božic (2018) used a two-scale model to define S-N curve and fatigue limit for AISI 1141 steel, and in another study a two-scale model was used by Mlikota, Staib, Schmauder & Božic (2017) to determine Paris law constants for carbon steel.

2.9 Finite element analysis

In addition to calculation of stresses, finite element analysis (FEA) is utilized in calculation of effective stress area which is needed for size factor K_{size}. Also, as the use of notch factor from DNVGL-ST-0361 has been found to be problematic with complex geometries, FEA can be utilized in calculation of relative stress gradient χ^*. When stress gradient is used for calculation of the slope of synthetic S-N curves, there is no need for the notch factor.

2.9.1 Determination of effective area

Statistical size factor is determined based on the effective area of the studied machine element and this means that the elemental face areas are needed (see figure 57). The area of the element face located on the surface of the component can be obtained with the help of the element shape functions and global nodal coordinates (Lönnqvist 2008, p. 221).

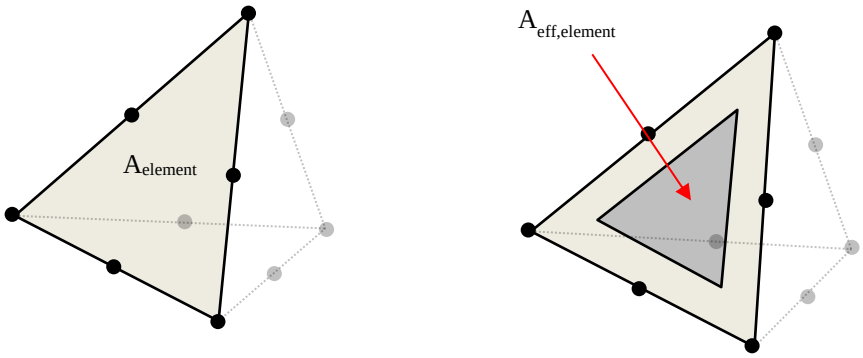

Figure 57. Effective area is calculated for each elemental face that is on the surface of the component, and the effective area of the whole component is the total of elemental effective areas.

The elements used in an example analysis in chapter 3.2 are ten-node tetrahedron solid elements and thus, the calculation procedure for triangular face area is presented below. Since the tetrahedrons are quadratic, the shape of the elemental face is that of a quadratic triangular 2D element. The shape functions N_i for quadratic triangular element (T6) which is shown in figure 58, are expressed as follows (Cook, Malkus & Plesha 1989, p. 154, 182):

$$N_1 = \xi(2\xi - 1) \tag{2.221}$$

$$N_2 = \eta(2\eta - 1) \tag{2.222}$$

$$N_3 = \zeta(2\zeta - 1) \tag{2.223}$$

$$N_4 = 4\xi\eta \tag{2.224}$$

$$N_5 = 4\eta\zeta \tag{2.225}$$

$$N_6 = 4\zeta\xi \tag{2.226}$$

, where ξ and η are natural coordinates of the element's coordinate system and $\zeta = 1 - \xi - \eta$.

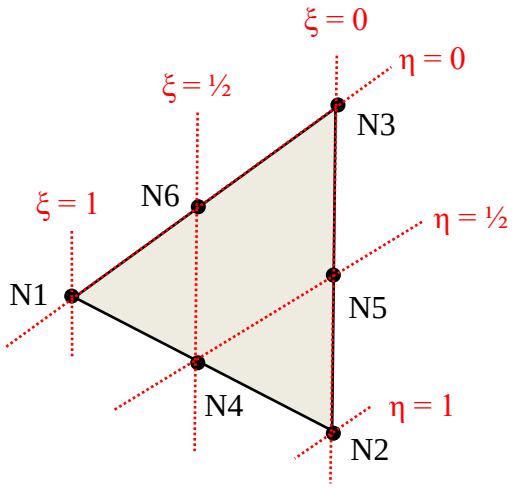

Figure 58. Quadratic triangular element (T6) with node numbering (black) and natural coordinates (red).

The area element *dA* of the elemental face in elemental coordinate system is expressed as the norm of cross product $d\xi \times d\eta$ (see figure 59). When area element is mapped onto the element surface in global coordinate system, it becomes a parallelogram. (Khan Academy 2020.)

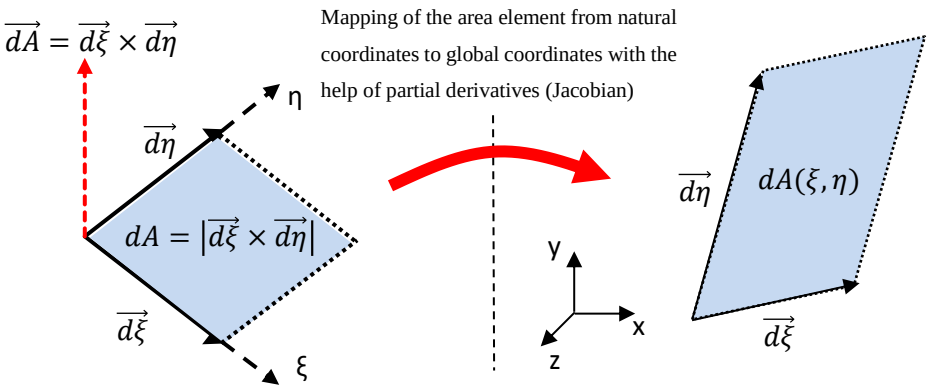

Figure 59. Area element defined in elemental coordinate system mapped into global coordinate system.

The vectors $\overrightarrow{d\eta}$ and $\overrightarrow{d\xi}$ and their cross product is obtained as follows (Khan Academy 2020; Henttonen, Oinonen & Uusitalo 2007, p. 236; Lönnqvist 2008, p. 225):

$$\overrightarrow{d\xi} = \frac{\partial X}{\partial \xi} d\xi \bar{\imath} + \frac{\partial Y}{\partial \xi} d\xi \bar{\jmath} + \frac{\partial Z}{\partial \xi} d\xi \bar{k} \tag{2.227}$$

$$\overrightarrow{d\eta} = \frac{\partial X}{\partial \eta} d\eta \bar{\imath} + \frac{\partial Y}{\partial \eta} d\eta \bar{\jmath} + \frac{\partial Z}{\partial \eta} d\eta \bar{k} \tag{2.228}$$

$$\begin{aligned} \overrightarrow{dA} = \overrightarrow{d\xi} \times \overrightarrow{d\eta} = \begin{vmatrix} \bar{\imath} & \bar{\jmath} & \bar{k} \\ \frac{\partial X}{\partial \xi} & \frac{\partial Y}{\partial \xi} & \frac{\partial Z}{\partial \xi} \\ \frac{\partial X}{\partial \eta} & \frac{\partial Y}{\partial \eta} & \frac{\partial Z}{\partial \eta} \end{vmatrix} d\xi d\eta = \left(\frac{\partial Y}{\partial \xi} \cdot \frac{\partial Z}{\partial \eta} - \frac{\partial Z}{\partial \xi} \cdot \frac{\partial Y}{\partial \eta}\right) \bar{\imath} \ldots \\ \ldots - \left(\frac{\partial X}{\partial \xi} \cdot \frac{\partial Z}{\partial \eta} - \frac{\partial Z}{\partial \xi} \cdot \frac{\partial X}{\partial \eta}\right) \bar{\jmath} + \left(\frac{\partial X}{\partial \xi} \cdot \frac{\partial Y}{\partial \eta} - \frac{\partial Y}{\partial \xi} \cdot \frac{\partial X}{\partial \eta}\right) \bar{k} \quad d\xi d\eta \\ = dA_x \bar{\imath} + dA_y \bar{\jmath} + dA_z \bar{k} \end{aligned} \tag{2.229}$$

, where X, Y and Z are the global coordinates within the element face. Global coordinates within the element face are obtained using the shape functions and global nodal coordinates of the element (Cook, Malkus & Plesha 1989, p. 182):

$$X(\xi, \eta) = \sum_{i=1}^{6} N_i \boldsymbol{x}_i \tag{2.230}$$

$$Y(\xi, \eta) = \sum_{i=1}^{6} N_i \boldsymbol{y}_i \tag{2.231}$$

$$Z(\xi, \eta) = \sum_{i=1}^{6} N_i \boldsymbol{z}_i \tag{2.232}$$

$i = 1 \ldots 6$ for T6 element

, where $\boldsymbol{x}$, $\boldsymbol{y}$ and $\boldsymbol{z}$ are the element's nodal coordinates in global coordinate system.

The parallelogram area element of the elemental face in global coordinate system is the norm of dA_x, dA_y and dA_z (Khan Academy 2020):

$$dA(\xi,\eta) = \sqrt{dA_x^2 + dA_y^2 + dA_z^2}\, d\xi d\eta \tag{2.233}$$

The area of the element face can then be calculated with a surface integral of the differential equation (2.233) (Khan Academy 2020). It needs to be integrated numerically and this can be done with Gaussian quadrature. Since Gaussian quadrature in its commonly known form gives integral for square element in range [-1≤ ξ, $\eta \leq 1$], it needs to be modified so that the integration can be done for triangular element which is defined in the range of [$0 \leq \xi$, $\eta \leq 1$] (see figure 58). Thus, the following is obtained for Gaussian quadrature for triangular element. (Cook, Malkus & Plesha 1989, p. 183.)

$$\begin{aligned} A &= \int_0^1 \int_0^{1-\eta} dA(\xi,\eta)\, d\xi d\eta \\ &= \frac{1}{2} \cdot \sum_{i=1}^{n} W_i \cdot dA(\xi_i,\eta_i) \end{aligned} \tag{2.234}$$

, where ξ_i and η_i are Gaussian integration points and W_i is weight coefficient. Values of integration points and weight coefficients can be found in Appendix IV. When there are multiple sampling points with the same weight factor (see Appendix IV, multiplicity column), integration point values are given for one of them and the rest are obtained by cyclic permutation (Cook, Malkus & Plesha 1989, p. 183). For example, for three sampling points with the same weight factor, the area element function is calculated at three locations (Cook, Malkus & Plesha 1989, p. 183):

1: $$\begin{cases} \xi_1 = \frac{2}{3} \\ \xi_2 = \xi_3 = \frac{1}{6} \end{cases} \tag{2.235}$$

2: $$\begin{cases} \xi_2 = \frac{2}{3} \\ \xi_3 = \xi_1 = \frac{1}{6} \end{cases} \tag{2.236}$$

3: $$\begin{cases} \xi_3 = \frac{2}{3} \\ \xi_1 = \xi_2 = \frac{1}{6} \end{cases} \tag{2.237}$$

, where area coordinates correspond natural coordinates: $\xi_1 = \xi$, $\xi_2 = \eta$ and $\xi_3 = 1 - \xi - \eta$.

Method explained above can be used with other types of elements as well (also with axisymmetric elements) if correct shape functions and Gauss integration function are chosen. For example, face area of 20-node hexahedral element could be calculated with the shape functions of quadratic quadrilateral element (Q8). In that case, the Gauss integration would have to be modified so that the domain of the surface area integral is square $[-1 \leq \xi, \eta \leq 1]$.

After the surface face area is calculated for each element, the effective area can be calculated with equations (2.67)–(2.72). As the examined area is divided into small portions, that is to say FE-elements, the element with maximum stress amplitude or multiaxial failure criteria value is presumed to have failure probability of 50 %. Consequently, rest of the elements will have lower failure probabilities according to their stress amplitude or multiaxial failure criteria value. Variable λ of standard normal distribution that corresponds a certain reliability can be calculated from the following for each element (according to log-normal distribution). (Rabb 2017, p. 144.)

$$\lambda_i = \frac{1}{s_{ln}} \ln\left(\frac{\sigma_{ai}}{\sigma_{a,max}}\right) \tag{2.238}$$

or

$$\lambda_i = \frac{1}{s_{ln}} \ln\left(\frac{D_i}{D_{max}}\right) \tag{2.239}$$

NOTE! use sample value for s_{ln}

, where σ_{ai} is the average stress amplitude of element i, $\sigma_{a,max}$ is the maximum average stress amplitude, D_i is the multiaxial failure criteria value for element i and D_{max} is the maximum multiaxial failure criteria value. The effective areas for reference test pieces have been calculated with $s_{ln} = 0.065$ (steel) and $s_{ln} = 0.1$ (GJS) and consequently, these should be used when calculating effective area for the studied component.

Reliability for each element can then be calculated as follows (Rabb 2017, p. 145):

$$R_i = 1 - P_i = \frac{1}{\sqrt{2\pi}} \int_{\lambda_i}^{\infty} e^{-\frac{x^2}{2}} dx \tag{2.240}$$

Finally, the effective area of the component is calculated as the sum of individual effective areas (Rabb 2017, p. 145):

$$A_{eff} = \sum_{i=1}^{n} \frac{\ln R_i}{\ln 0.5} \cdot A_i \tag{2.241}$$

, where A_i is the face area of element *i*. Rabb (2017, p. 149) provides a rule of thumb which states that the effective area for cast irons (sample $s_r = 0.1$) is the area where the stress amplitude is 94 % of the maximum amplitude. Corresponding value for steels is 96 % (sample $s_r = 0.065$).

2.9.2 Determination of relative stress gradient

Relative stress gradient which is needed for calculation of S-N curve slope exponent is calculated with equation (2.141) which is also shown below:

$$\chi^* = \frac{1}{\sigma_{max}} \cdot \frac{d\sigma}{dr} \tag{2.141}$$

, where σ_{max} is the maximum normal stress on the surface and $d\sigma$ is change in stress at the depth of dr from the surface (along the surface normal). When multiaxial stress state needs to be considered, χ^* can be calculated using Von Mises criterion. Von Mises stress is defined as follows. (Rabb 2020a.)

$$\sigma_{VM} = \sqrt{\begin{matrix} \sigma_x^2 + \sigma_y^2 + \sigma_z^2 - \sigma_x\sigma_y \ldots \\ \ldots - \sigma_x\sigma_z - \sigma_y\sigma_z + 3(\tau_{xy}^2 + \tau_{xz}^2 + \tau_{yz}^2) \end{matrix}} \tag{2.242}$$

Relative stress gradient could be defined using Findley damage criterion as well and presumably, this would be a little more accurate. However, using Von Mises is simpler and faster and thus advisable. (Rabb 2020a.)

The depth at which χ^* should be calculated is defined by the theory of critical distances. The material length scale L and the critical distance r_c are as follows. (Rabb 2020a; Rabb 2020d.)

$$L = \frac{1}{\pi}\left(\frac{\Delta K_{th,R}}{2 \cdot K_{size} \cdot \sigma_{aR}}\right)^2 \tag{2.243}$$

$$2r_c = L \tag{2.244}$$

, where $\Delta K_{th,R}$ is threshold stress intensity when stress ratio is R, K_{size} is statistical size factor of the critical area and σ_{aR} is reference specimen fatigue limit from Haigh diagram for stress ratio R. Note that distance L is used in S-N curve slope exponent calculation. However, if TCD is used in estimation of fatigue limit, the distance is L / 2.

The FE-model for determination of relative stress gradient needs to have a reasonably fine mesh so that the stress values can be accurately obtained at the required distance. Especially if the critical distance is very small like for example for some steels ($L \approx 0.024$ mm), the mesh should be refined enough near the surface. In figure 60, in the case of the coarsest mesh, it can be seen that the value of χ^* at dr = 0.024 mm cannot be obtained reliably. However, deeper in the material, at the distance of dr = 0.215 mm (= L for GJS-500), relative stress gradient obtained with the coarsest mesh differs only about 0.6 % from the finer meshes.

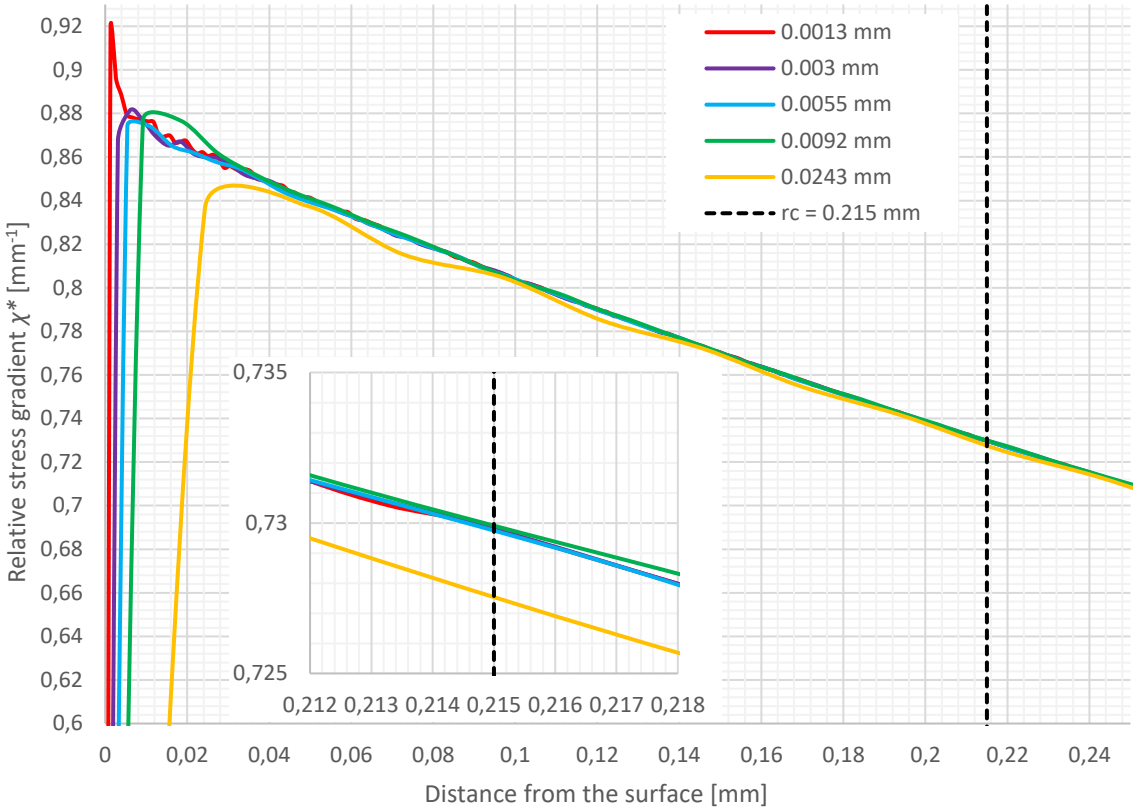

Figure 60. Relative stress gradient with different node spacings.

Based on the results in figure 60 it can be concluded that there should be at least 20 nodes along the distance L if χ^* is required near the surface. With node spacing of 0.0243 mm there is not remarkable difference in χ^* value at the depth of L = 0.215 mm when compared to finer meshes and thus even ~10 nodes along L should give adequately accurate results for slope exponent calculation.

In practice, making such fine meshes for actual machine elements requires submodeling. In Ansys, a global model of the studied component can be solved first and then, the area of interest (submodel) can be cut out from the global model. The solution of the global model can be imported into the submodel and used as a boundary condition. The required data, in this case displacements, is then interpolated from the global solution onto the cut boundaries. (Ansys Help 2020.) As an example, an FE-model of a fatigue test specimen for GJS-500 is shown in figures 61 and 62. The calculated relative stress gradient from the model is shown in figure 63.

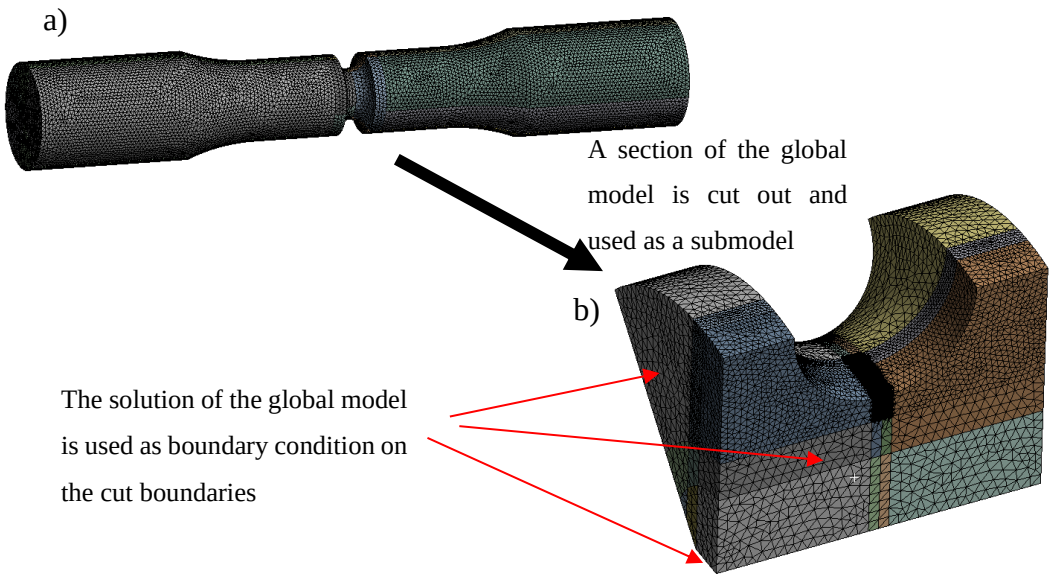

Figure 61. Global (a) and local (b) FE-models for determination of relative stress gradient.

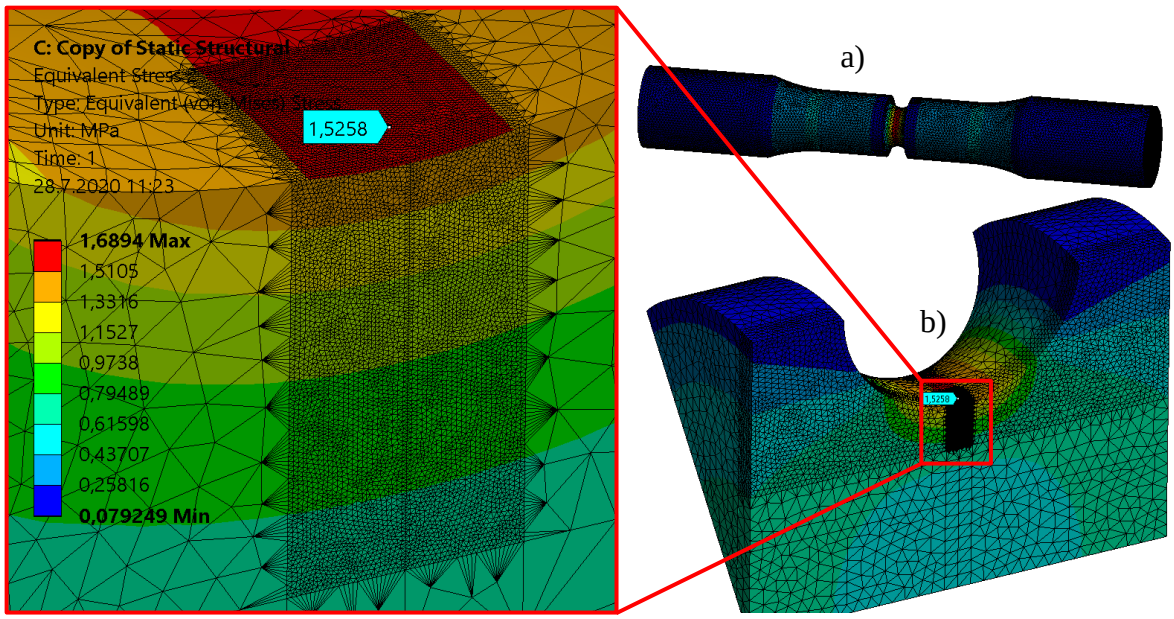

Figure 62. Von Mises stress [MPa]. a) global model and b) local model. The global model is loaded axially with 1 MPa load to obtain the stress distribution at the notch root. Node spacing at the notch root along the surface normal is 0.003 mm.

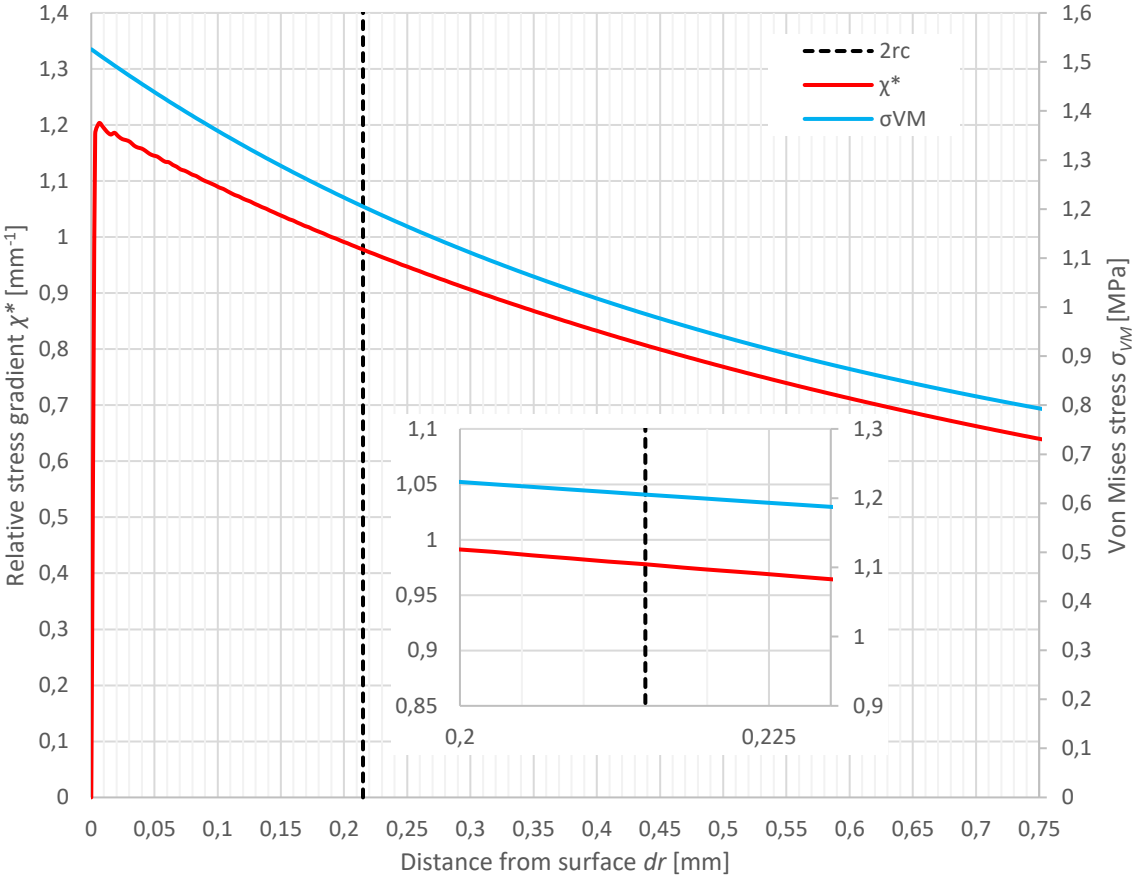

Figure 63. Calculated relative stress gradient χ^* for the GJS-500 test specimen. $\chi^* = 0.9778$ mm^{-1} at the distance of $L = 2r_c = 0.215$ mm.

2.9.3 Determination of stress components for multiaxial fatigue analysis

Stress matrix of the critical point for multiaxial fatigue analysis at every load step/increment can be obtained from FE-analysis results. Nodal stress matrices can be exported from FE-solution and used in Findley or Dang Van multiaxial analysis methods. Stress matrix is expressed as follows:

$$[\sigma] = \begin{bmatrix} \sigma_x & \tau_{xy} & \tau_{xz} \\ \tau_{xy} & \sigma_y & \tau_{yz} \\ \tau_{xz} & \tau_{yz} & \sigma_z \end{bmatrix} \tag{2.245}$$

Examples of proportional and non-proportional load cases are shown in Figures 64 and 65. When non-proportional loading is considered, the time points at which the matrix is obtained should be chosen with appropriate increment so that the response is recorded accurately.

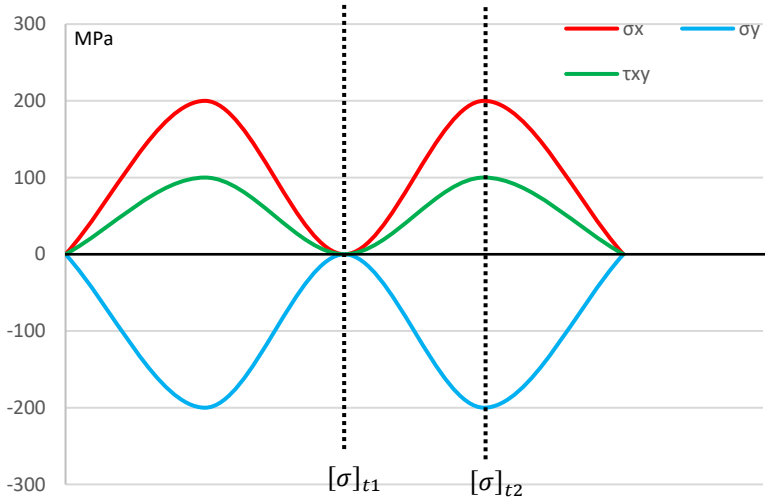

Figure 64. Proportional load case with two time increments and the corresponding stress matrices of the critical point.

The load cycle in Figure 64 yields the following according to Findley criterion when $\sigma_{aR=-1}$ = 537 MPa and $\sigma_{aR=0}$ = 411 MPa:

$\Delta\tau$ = 192.8 MPa

σ_n = 132.3 MPa

θ = 163.50°

φ = 90°

D = 129.5 MPa

$S_{F,ver}$ = 3.3730

$S_{F,rad}$ = 2.7661

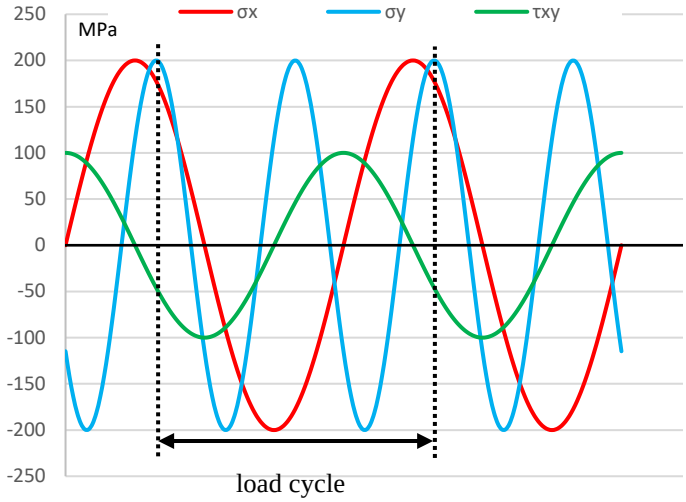

	σ_x	σ_y	τ_{xy}
1.	173.2	199.2	-50.0
2.	68.4	17.4	-94.0
3.	0.0	-114.7	-100.0
4.	-100.0	-199.2	-86.6
5.	-187.9	-17.4	-34.2
6.	-200.0	114.7	0.0
7.	-173.2	199.2	50.0
8.	-68.4	17.4	94.0
9.	0.0	-114.7	100.0
10.	100.0	-199.2	86.6
11.	187.9	-17.4	34.2
12.	200.0	114.7	0.0
13.	173.2	199.2	-50.0

Figure 65. Non-proportional load case. The load cycle has been divided in 13 time increments in an effort to capture the maximum shear stress range and normal stress. For comparison, the same load cycle is divided in 37 time increments to show the possible difference in the maximum Findley damage.

The load cycle in Figure 65 yields the following according to Findley criterion when 13 load increments or ~7 increments along the period of the highest frequency are used, and $\sigma_{aR=-1}$ = 537 MPa and $\sigma_{aR=0}$ = 411 MPa:

$\Delta\tau$ = 337.7 MPa

σ_n = 235.1 MPa

θ = 137.75°

φ = 90°

D = 237.6 MPa

$S_{F,ver}$ = 1.7148

$S_{F,rad}$ = 1.5080

However, when the load cycle is divided in 37 load increments or ~19 increments along the period of the highest frequency, the following is obtained:

$\Delta\tau$ = 347.9 MPa

σ_n = 234.7 MPa

θ = 137.75°

φ = 90°

D = 242.6 MPa

$S_{F,ver}$ = 1.6647

$S_{F,rad}$ = 1.4766

The angle of the critical plane is the same, and there is only ~2 % difference in maximum Findley damage between 13 and 37 load increments. Therefore, using about 10 load increments along the period of the highest frequency should give adequately accurate results (in other words the load cycle in figure 65 divided into 20 increments). Figure 66 shows the critical plane and stress element.

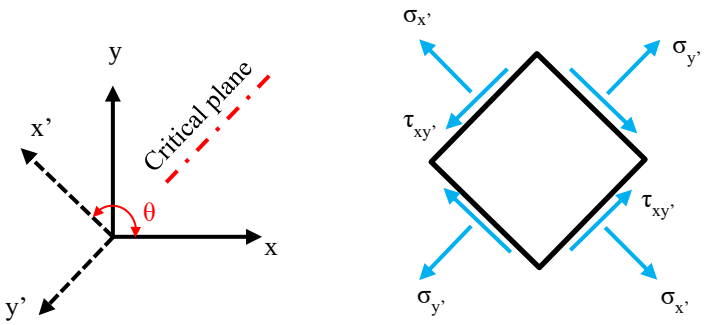

Figure 66. According to Findley criterion the critical plane is perpendicular to XY-plane with the loading presented in Figure 64.

3 RESULTS

The results of this work are composed of flowcharts of the introduced fatigue analysis method and an example analysis of a relatively simple component and load case. An effort is made with the flowcharts and the example calculation to clarify how the new analysis method should be conducted, and what kind of inputs and outputs are required from the programmed analysis tool.

3.1 New method

The new analysis method is presented in the following flowcharts. The flowcharts define the main steps of the analysis process while the background is explained in previous chapters.

The new method requires at least the following values from the user:

Yield strength: $R_{p0.2}$ (normative or tested)

Ultimate strength: R_m (normative or tested)

Ultimate compressive strength: R_{mc} (normative or tested)

Allowed failure probability: λ (some values are shown in table 6)

Table 6. Some λ values for different failure probabilities.

P [%]	λ*
2.3	-2
0.1	-3.09
0.01	-3.719
0.001	-4.265

* $P = 1 - R = \frac{1}{\sqrt{2\pi}} \int_{-\infty}^{\lambda} e^{-\frac{x^2}{2}} dx \rightarrow \lambda = \ldots$

Default values should be available for some variables if no other information is given by the user. However, there should be possibility for the users to input these themselves. Default values are shown in table 7.

Table 7. Default values for some variables if no other information is available.

	Steel	**GJS**
$\boldsymbol{\sigma_{0.2}}$ **[MPa]***	$R_{p0.2}$ (tested) or 1.06·$R_{p0.2}$ (normative)	
$\boldsymbol{\sigma_b}$ **[MPa]***	R_m (tested) or 1.06·R_m (normative)	
$\boldsymbol{\sigma_{b,comp}}$ **[MPa]***	-	R_{mc} (tested) or 1.06·R_{mc} (normative)
$\boldsymbol{\sigma_{aR=-1}}$ **[MPa]**	$1.04(0.144\sigma_b + 0.309\sigma_{0.2}) + 56$	$0.1798\sigma_b + 0.11845\sigma_{0.2} + 60.6699$
$\boldsymbol{A_{eff}}$ **[mm^2]**	225	1039
$\boldsymbol{k}$ **[-]**	$0.1 - 0.00035\sigma_b$	$0.000261 \cdot \sigma_b - 0.65493$
$\boldsymbol{\sigma_{aR=0}}$ **[MPa]**	$\frac{\sigma_{aR=-1}}{1-k}$	
$\boldsymbol{\Delta K_{th,R=-1}}$ **[N/mm$^{3/2}$]**	$31.62 \cdot (-0.0038\sigma_b + 15.5)$**	

* Requires user input

** reference: Chapetti 2010, p. 261.

3.1.1 Haigh diagram

Analysis begins with the construction of Haigh diagram.

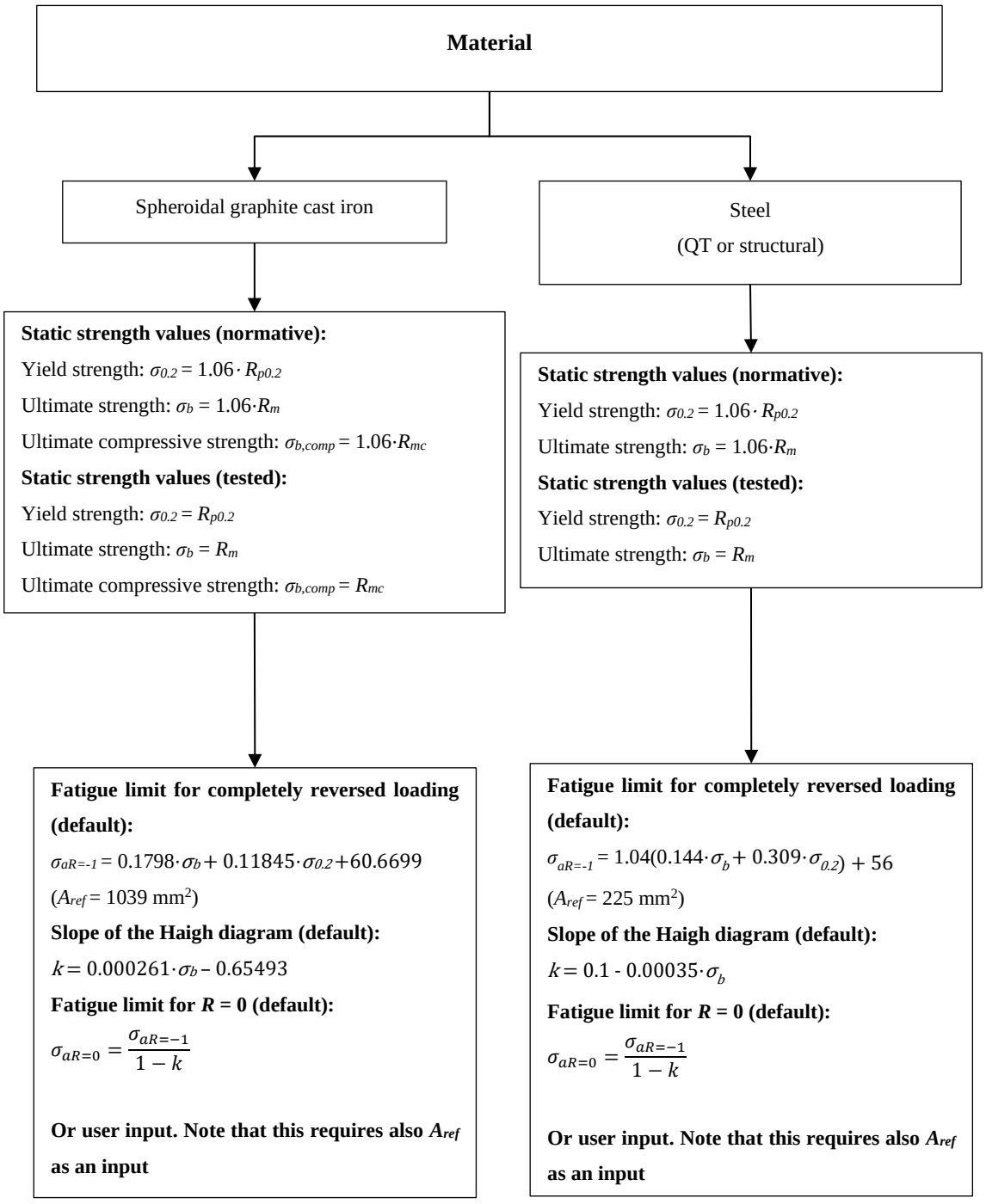

Haigh diagrams

GJS | Structural steel | QT-steel

Linear part:

($\sigma_{m2} < \sigma_m < \sigma_{m1}$)

$$\sigma_{m2} = \frac{\sigma_{aR=-1} - \sigma_{0.2}}{1-k}$$

$$\sigma_{m1} = \frac{\sigma_{0.2} - \sigma_{aR=-1}}{1+k}$$

$$\sigma_{af} = \sigma_{aR=-1} + k\sigma_m$$

Compression side:

$$\sigma_{m,P0} = \sigma_{b,comp}$$

$$\sigma_{a,P0} = 0$$

$$\sigma_{m,P1} = \frac{\sigma_{aR=-1} + \sigma_{b.comp}}{1-k}$$

$$\sigma_{a,P1} = \sigma_{aR=-1} + k\sigma_{m,P1}$$

$$\sigma_{m,P2} = \frac{\sigma_{aR=-1} + \sigma_{0.2}}{1-k}$$

$$\sigma_{a,P2} = \sigma_{aR=-1} + k\sigma_{m,P2}$$

B-spline:

$$\sigma_{af} = 2t \cdot (1-t) \cdot \sigma_{a,P1} + t^2 \cdot \sigma_{a,P2}$$

$$\sigma_m = (1-t)^2 \cdot \sigma_{m,P0} + 2t \cdot (1-t) \cdot \sigma_{m,P1} + t^2 \cdot \sigma_{m,P2}$$

, where *t* is calculated with eq. (2.13)

Tensile side

$$\sigma_{m,P0} = \frac{\sigma_{0.2} - \sigma_{aR=-1}}{1+k}$$

$$\sigma_{a,P0} = \sigma_{aR=-1} + k\sigma_{m,P0}$$

$$\sigma_{m,P1} = \frac{-\sigma_{aR=-1}}{k}$$

$$\sigma_{a,P1} = 0$$

$$\sigma_{m,P2} = \sigma_b$$

$$\sigma_{a,P2} = 0$$

B-spline:

$$\sigma_{af} = (1-t)^2 \cdot \sigma_{a,P0}$$

$$\sigma_m = (1-t)^2 \cdot \sigma_{m,P0} + 2t \cdot (1-t) \cdot \sigma_{m,P1} + t^2 \cdot \sigma_{m,P2}$$

, where *t* is calculated with eq. (2.13)

Linear part: ($\sigma_{m,P2} < \sigma_m < \sigma_{mR=0}$)

$$\sigma_{m,P2} = \frac{\sigma_{aR=-1} - \sigma_{0.2}}{2(1-k)}$$

$$\sigma_{mR=0} = \frac{\sigma_{aR=-1}}{1-k}$$

$$\sigma_{af} = \sigma_{aR=-1} + k\sigma_m$$

Structural steel:

$$R_m^* \approx 1.3\sigma_b$$

QT-steel:

$$R_m^* = \frac{(1+2M) \cdot \sigma_{aR=-1}}{M \cdot (2+M)}$$

, where $M = -k$

Compression side:

$$\sigma_{m,P0} = -R_m^*$$

$$\sigma_{a,P0} = 0$$

$$\sigma_{m,P1} = \frac{R_m^* - \sigma_{aR=-1}}{k-1}$$

$$\sigma_{a,P1} = \sigma_{aR=-1} + k\sigma_{m,P1}$$

$$\sigma_{m,P2} = \frac{\sigma_{aR=-1} - \sigma_{0.2}}{2(1-k)}$$

$$\sigma_{a,P2} = \sigma_{aR=-1} + k\sigma_{m,P2}$$

B-spline:

$$\sigma_{af} = (1-t)^2\sigma_{a,P0} + 2t(1-t)\sigma_{a,P1} + t^2\sigma_{a,P2}$$

$$\sigma_m = (1-t)^2\sigma_{m,P0} + 2t(1-t)\sigma_{m,P1} + t^2\sigma_{m,P2}$$

, where *t* is calculated with eq. (2.13).

Structural steel tensile side:

$$\sigma_{af} = A\sigma_m^2 + B\sigma_m + C$$

$$\sigma_{m1} = \frac{\sigma_{0.2} - \sigma_{aR=-1}}{1+k}$$

$$\sigma_{a1} = \sigma_{aR=-1} + k\sigma_{m1}$$

$$A = \frac{k\sigma_{m1} - \sigma_{a1} - kR_m^*}{(R_m^* - \sigma_{m1})^2}$$

$$B = k - 2A\sigma_{m1}$$

$$C = A\sigma_{m1}^2 + \sigma_{a1} - k\sigma_{m1}$$

QT-steel tensile side:

$$\sigma_{af} = \sigma_{aR=-1}\left(\frac{1-b}{2-b} + \sqrt{\frac{1}{(2-b)^2} - \frac{b\sigma_m}{(2-b)R_m^*}}\right)$$

$$b = \frac{2(1+2M)}{2+2M-M^2}$$

, where $M = -k$

Effective area A_{eff}

Nodal coordinates ***x*, *y*** and ***z*** from FE-model

Element shape functions N_i

Global coordinates within the element:

$$X(\xi,\eta) = \sum_{i=1}^{n} N_i \boldsymbol{x}_i$$

$$Y(\xi,\eta) = \sum_{i=1}^{n} N_i \boldsymbol{y}_i$$

$$Z(\xi,\eta) = \sum_{i=1}^{n} N_i \boldsymbol{z}_i$$

Partial derivatives and area element *dA*:

$$dA(\xi,\eta) = \sqrt{dA_x^2 + dA_y^2 + dA_z^2}\, d\xi d\eta$$

$$dA_x = \frac{\partial Y}{\partial \xi}\cdot\frac{\partial Z}{\partial \eta} - \frac{\partial Z}{\partial \xi}\cdot\frac{\partial Y}{\partial \eta}$$

$$dA_y = -\left(\frac{\partial X}{\partial \xi}\cdot\frac{\partial Z}{\partial \eta} - \frac{\partial Z}{\partial \xi}\cdot\frac{\partial X}{\partial \eta}\right)$$

$$dA_z = \frac{\partial X}{\partial \xi}\cdot\frac{\partial Y}{\partial \eta} - \frac{\partial Y}{\partial \xi}\cdot\frac{\partial X}{\partial \eta}$$

Area of the element face (for triangular element):

$$A_j = \int_0^1 \int_0^{1-\eta} dA_j(\xi,\eta)\, d\xi d\eta = \frac{1}{2}\cdot\sum_{i=1}^{n} W_i \cdot dA_j(\xi_i,\eta_i)$$

, where W_i, ξ_i and η_i can be found in Appendix IV and n is number of Gauss integration points

Reliability and effective area:

$$\lambda_j = \frac{1}{s_{ln}} \ln\left(\frac{\sigma_{aj}}{\sigma_{a,max}}\right)$$

, where σ_a is the average stress amplitude of the elemental face

$$R_j = 1 - P_j = \frac{1}{\sqrt{2\pi}}\int_{\lambda_j}^{\infty} e^{-\frac{x^2}{2}}\, dx$$

$$A_{eff} = \sum_{j=1}^{n} \frac{\ln R_j}{\ln 0.5}\cdot A_j$$

, where n is number of elements

K-T diagram (optional)

↓

Defect distribution of material:

Logarithmic median of defect size:

μ_{ln} = user input

Logarithmic SD of defect size:

s_{ln} = user input

Median defect size:

$a_{med} = e^{\mu_{ln}}$

Defect distribution function (log-normal):

$f(a) = \frac{1}{s_{ln} a \sqrt{2\pi}} e^{-\frac{(\ln a - \mu_{ln})^2}{2 s_{ln}^2}}$ (PDF)

$F(a) = \frac{1}{s_{ln}\sqrt{2\pi}} \int_0^a \frac{1}{a} e^{-\frac{(\ln a - \mu_{ln})^2}{2 s_{ln}^2}} da$ (CDF)

↓

KT-diagram:

Intrinsic crack length:

$\sigma_{af}(a_{med}) = \frac{\Delta K_{th}}{2F\sqrt{\pi(a_{med}+a_0)}} = \sigma_{aR=-1} \rightarrow a_0 = \ldots$

El Haddad curve (fatigue limit as a function of defect size):

$\sigma_{aR=-1}(a) = \frac{\Delta K_{th}}{2F\sqrt{\pi(a+a_0)}}$

F = 0.713 (surf. crack)

F = 0.637 (int. crack)

Defect distribution (log-normal) of GJS-500-7 reference test specimen. Logarithmic SD of fatigue limit is $s_{ln} = s_r = 0.1$. (Mod. Rabb 2017, p. 168.)

ΔK_{th}=310.82 N/mm$^{3/2}$, $\sigma_{af}(a_{med})$ = 195.5 MPa

a_0 = 0.202 mm

Logarithmic median μ_{ln}	5.27
Logarithmic SD $s_{ln}(a)$	0.38
Median defect a_{med} [µm]	194.4
Mean defect a_{mean} [µm]	209.0
Standard deviation s [µm]	82.4
Relative SD s_r	0.394

Defect distribution (log-normal) of 34CrNiMo6+QT reference test specimen. Logarithmic SD of fatigue limit is $s_{ln} = s_r = 0.065$. (Mod. Rabb 2017, p. 163.)

ΔK_{th}=350.13 N/mm$^{3/2}$, $\sigma_{af}(a_{med})$ = 607.5 MPa

a_0 = 0.0404 mm

Logarithmic median μ_{ln}	2.45
Logarithmic SD $s_{ln}(a)$	0.484
Median defect a_{med} [µm]	11.60
Mean defect a_{mean} [µm]	13.04
Standard deviation s [µm]	6.70
Relative SD s_r	0.514

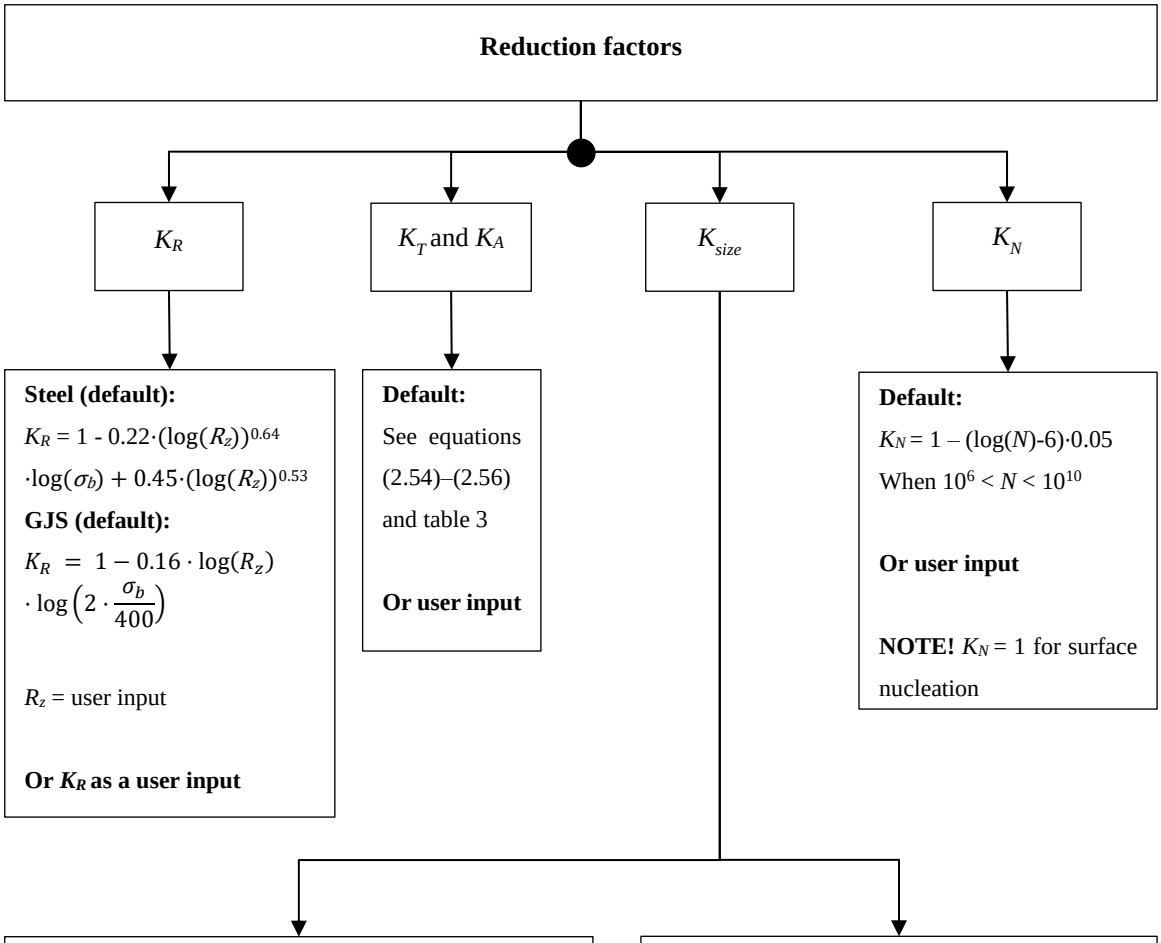
Reduction factors
K_R
K_T and K_A
K_{size}
K_N
Steel (default):
K_R = 1 - 0.22·(log(R_z))$^{0.64}$ ·log(σ_b) + 0.45·(log(R_z))$^{0.53}$
GJS (default):
$K_R = 1 - 0.16 \cdot \log(R_z) \cdot \log\left(2 \cdot \frac{\sigma_b}{400}\right)$
R_z = user input
Or K_R as a user input
Default:
See equations (2.54)–(2.56) and table 3
Or user input
Default:
K_N = 1 – (log(N)-6)·0.05
When $10^6 < N < 10^{10}$
Or user input
NOTE! K_N = 1 for surface nucleation
The weakest link theory:
Number of links:
$n = \frac{A_{eff}}{A_{ref}}$ when $A_{eff} > A_{ref}$
$n = \frac{A_{ref}}{A_{eff}}$ when $A_{eff} < A_{ref}$
Reliability and failure probability:
$R = \sqrt[n]{0.5}$
$P = 1 - R = \frac{1}{\sqrt{2\pi}} \int_{-\infty}^{\lambda} e^{-\frac{x^2}{2}} dx \rightarrow \lambda = \ldots$
Size factor:
$K_{size} = e^{-\lambda s_{ln,C90}}$ when $A_{eff} > A_{ref}$
$K_{size} = e^{-\lambda s_{ln,C10}}$ when $A_{eff} < A_{ref}$
, where s_{ln} is according to table 1 or 2
K-T diagram if defect distribution is known:
Return period:
$n = \frac{A_{eff}}{A_{ref}}$
$P = \frac{n}{n+1}$
Extrapolated defect size:
$F(a_{ext}) = P \rightarrow a_{ext} = \ldots$
, where $F(a)$ is CDF of material defect distribution.
Fatigue limit of the machine element:
$\sigma_{aR=-1,me} = \frac{\Delta K_{th}}{2F\sqrt{\pi(a_{ext} + a_0)}}$
Size factor:
$K_{size} = \frac{\sigma_{aR=-1,me}}{\sigma_{aR=-1,ref}}$ when $A_{eff} < A_{ref}$
$K_{size} = \frac{\sigma_{aR=-1,ref}}{\sigma_{aR=-1,me}}$ when $A_{eff} > A_{ref}$
, where $\sigma_{aR=-1,ref}$ is as follows (Rabb 2017, p 161, 168):
$\sigma_{aR=-1,ref,steel} = 607.5\ MPa$
$\sigma_{aR=-1,ref,GJS} = 195.5\ MPa$
and $\Delta K_{th,GJS}$=310.82 N/mm$^{3/2}$
$\Delta K_{th,steel}$ = 350.13 N/mm$^{3/2}$

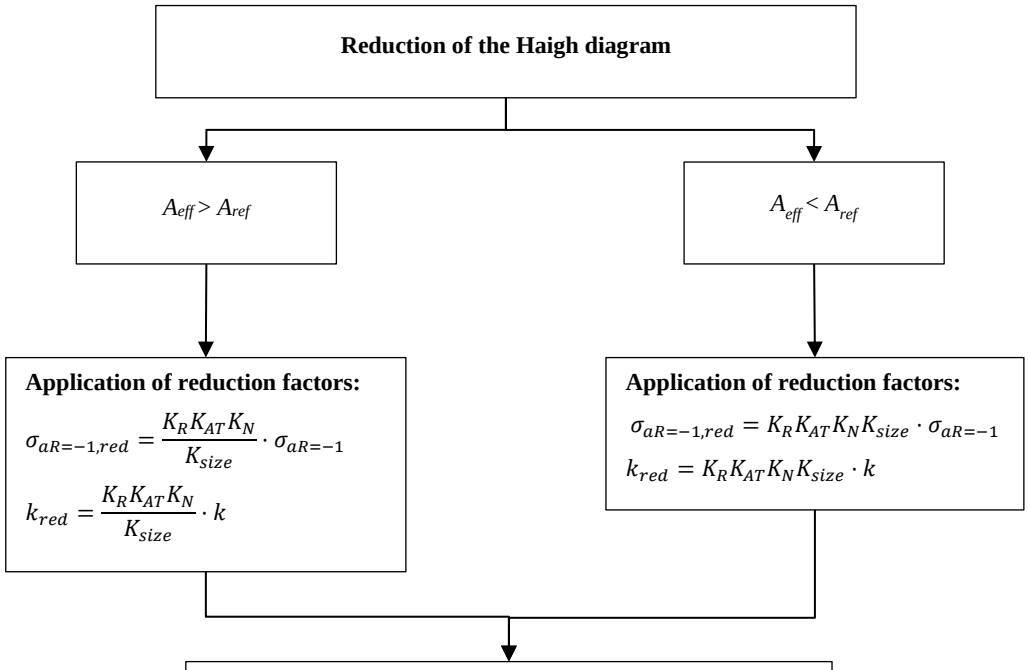
Reduction of the Haigh diagram
$A_{eff} > A_{ref}$
$A_{eff} < A_{ref}$
Application of reduction factors:
$\sigma_{aR=-1,red} = \frac{K_R K_{AT} K_N}{K_{size}} \cdot \sigma_{aR=-1}$
$k_{red} = \frac{K_R K_{AT} K_N}{K_{size}} \cdot k$
Application of reduction factors:
$\sigma_{aR=-1,red} = K_R K_{AT} K_N K_{size} \cdot \sigma_{aR=-1}$
$k_{red} = K_R K_{AT} K_N K_{size} \cdot k$
Allowed failure probability and safety factor:
$S_F = e^{-\lambda s_{ln,C90}}$
, where λ is defined according to the failure probability.
$\sigma_{aR=-1,red,P} = \frac{\sigma_{aR=-1,red}}{S_F}$
$k_{red,P} = \frac{k_{red}}{S_F}$
$\sigma_{aR=0,red,P} = \frac{\sigma_{aR=-1,red,P}}{1 - k_{red}}$
Reduced diagram is then compiled with the same equations as the mean diagram but using the reduced values.
Note! If cumulative damage analysis is needed, the reduction with S_F is performed after Findley multiaxial analysis, see flowchart on page 137.

3.1.2 Loading

If load history causes multiaxial stresses, Findley damage criterion is utilized in calculation of equivalent mean stress and amplitude. The equivalent values can then be used in cumulative damage analysis.

The angle θ_{eq} of critical plane for equivalent loading may be different for different levels of stress spectrum. In that case it is conservative to choose the plane with maximum Findley damage as the critical plane and make the cumulative damage summation as if all the stress levels were affecting the same plane (at least if the difference in angles is not significant). Analysis according to Findley criterion is shown in the next flowchart and cumulative damage analysis is shown in the next chapter.

Findley

Starting values:

Range and increment for rotation angles:

θ_{min} = user input φ_{min} = user input

θ_{max} = user input φ_{max} = user input

$d\theta$ = user input $d\varphi$ = user input

Reduced fatigue strength values (P = 50 %):

$\sigma_{aR=-1,red}$ = Haigh diagram $\sigma_{aR=0,red}$ = Haigh diagram

Stress matrices of load steps from FEA:

$[\sigma_i(t)]$

Findley parameters:

$\frac{k+\sqrt{1+k^2}}{2k+\sqrt{1+4k^2}} = \frac{\sigma_{aR=0,red}}{\sigma_{aR=-1,red}} \quad \rightarrow \quad k.=\ldots$

$$f = \frac{k+\sqrt{1+k^2}}{2} \cdot \sigma_{aR=-1,red}$$

Rotation of the stress element:

$[\sigma_i'(t)] = \boldsymbol{Q}^T[\sigma_i(t)]\boldsymbol{Q}$

Calculation of $\Delta\tau$ and σ_n on all studied planes:

$\Delta\tau$ = longest chord between two shear stress states. After the chord has been calculated, check the radius of the smallest enclosing circle, and choose the most conservative of the two.

$\sigma_n = \sigma_{x'}$

Maximum Findley damage and safety factors:

$$D = \left(\frac{\Delta\tau}{2} + k\sigma_n\right)_{max}$$

$$S_{F,ver} = \frac{f - k\sigma_n}{\tau_a}$$

$$S_{F,rad} = \frac{f}{D} = \frac{f}{\frac{\Delta\tau}{2} + k\sigma_n}$$

Determination of equivalent mean stress and amplitude:

see eqs. (2.193)–(2.203)

3.1.3 S-N curve and cumulative damage analysis

S-N curves are constructed using relative stress gradient χ^*. Damage sum is composed of low cycle (base S-N curve) and high cycle (Haibach extension) parts.

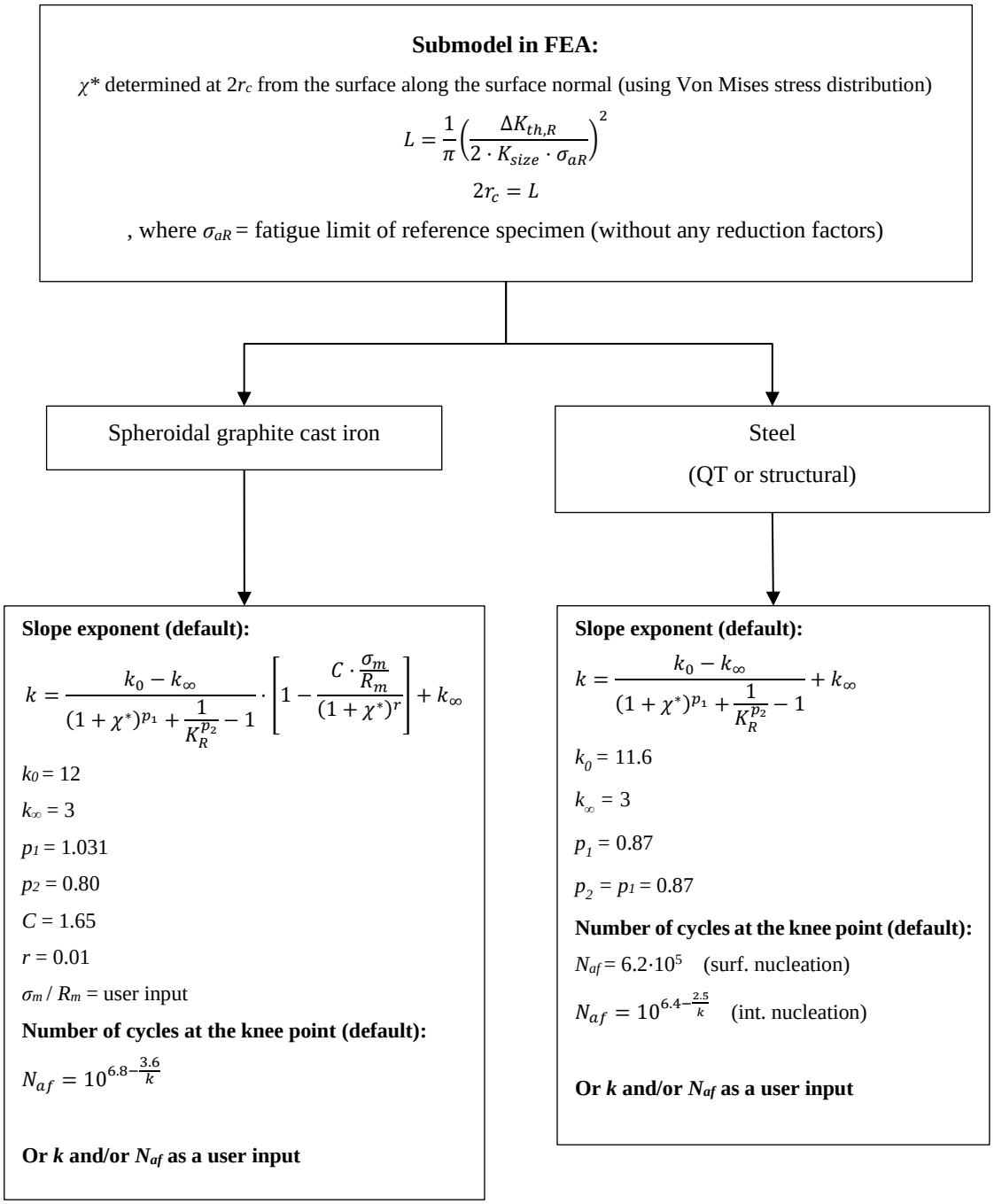

Base S-N curve (median):

$$N = N_{af}\left(\frac{\sigma_{af}}{\sigma_a}\right)^k$$

Base S-N curve (reduced):

Safety factor:

$S_F = e^{-\lambda s_{ln}}$, where λ according to allowed failure probability.

Reduced curve:

$$\sigma_{af,P} = \frac{\sigma_{af}}{S_F}$$

$$N_P = N_{af}\left(\frac{\sigma_{af,P}}{\sigma_a}\right)^k$$

Haibach extension into high cycle area (median):

$$N_H = N_{af}\left(\frac{\sigma_{af}}{\sigma_a}\right)^{2k-l}$$

, where:

l = 1 for rolled and forged steel components

l = 2 for cast and welded components

Haibach extension into high cycle area (reduced):

Logarithmic standard deviation of life:

$s_N = k s_{ln}$

Standard deviation of fatigue strength for extension:

$$s_{ln,H} = \frac{s_N}{2k-l}$$

Safety factor for extension:

$S_{F,H} = e^{-\lambda s_{ln,H}}$

Reduced curve:

$$\sigma_{af,PH} = \frac{\sigma_{af}}{S_{F,H}}$$

$$N_{PH} = N_{af}\left(\frac{\sigma_{af,PH}}{\sigma_a}\right)^{2k-l}$$

Damage sum:

Low cycle (base S-N curve):

$$D_{LC} = \frac{1}{N_{af}}\sum n_i\left(\frac{\sigma_{ai}}{\sigma_{af,P}}\right)^k$$

High cycle (Haibach):

$$D_{HC} = \frac{1}{N_{af}}\sum n_j\left(\frac{\sigma_{ai}}{\sigma_{af,PH}}\right)^{2k-l}$$

Total:

$D = D_{LC} + D_{HC}$

	Allowed damage sum *D*	
	Constant σ_m	Variable σ_m
Non welded components (rolled, forged)	0.3	0.1
Welded and cast components	0.5	0.2
Machined components	1.0	1.0

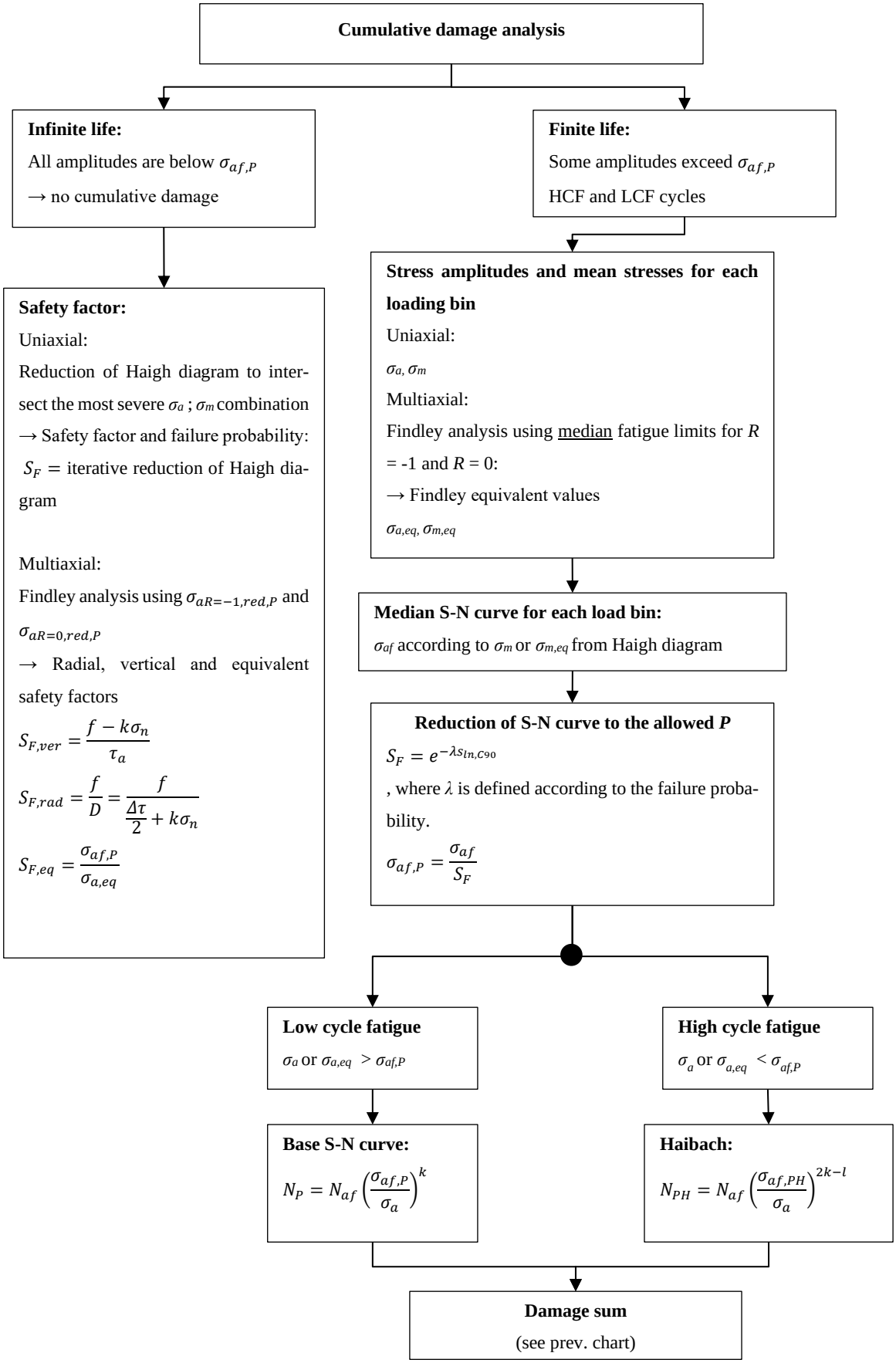
Cumulative damage analysis
Infinite life:
All amplitudes are below $\sigma_{af,P}$
→ no cumulative damage
Finite life:
Some amplitudes exceed $\sigma_{af,P}$
HCF and LCF cycles
Safety factor:
Uniaxial:
Reduction of Haigh diagram to intersect the most severe σ_a ; σ_m combination
→ Safety factor and failure probability:
S_F = iterative reduction of Haigh diagram
Multiaxial:
Findley analysis using $\sigma_{aR=-1,red,P}$ and $\sigma_{aR=0,red,P}$
→ Radial, vertical and equivalent safety factors
$S_{F,ver} = \frac{f - k\sigma_n}{\tau_a}$
$S_{F,rad} = \frac{f}{D} = \frac{f}{\frac{\Delta\tau}{2} + k\sigma_n}$
$S_{F,eq} = \frac{\sigma_{af,P}}{\sigma_{a,eq}}$
Stress amplitudes and mean stresses for each loading bin
Uniaxial:
σ_a, σ_m
Multiaxial:
Findley analysis using median fatigue limits for R = -1 and R = 0:
→ Findley equivalent values
$\sigma_{a,eq}, \sigma_{m,eq}$
Median S-N curve for each load bin:
σ_{af} according to σ_m or $\sigma_{m,eq}$ from Haigh diagram
Reduction of S-N curve to the allowed P
$S_F = e^{-\lambda s_{ln,c90}}$
, where λ is defined according to the failure probability.
$\sigma_{af,P} = \frac{\sigma_{af}}{S_F}$
Low cycle fatigue
σ_a or $\sigma_{a,eq} > \sigma_{af,P}$
High cycle fatigue
σ_a or $\sigma_{a,eq} < \sigma_{af,P}$
Base S-N curve:
$N_P = N_{af}\left(\frac{\sigma_{af,P}}{\sigma_a}\right)^k$
Haibach:
$N_{PH} = N_{af}\left(\frac{\sigma_{af,PH}}{\sigma_a}\right)^{2k-l}$
Damage sum
(see prev. chart)

Required output:

Haigh diagrams:

- Fatigue limit for P = 50 % and for reduced P for R = -1
- Fatigue limit for P = 50 % and for reduced P for R = 0
- Slope for P = 50 % and for reduced P
- Fatigue limit for a user specified mean stress

Findley:

- Findley parameters f and k
- Shear stress range and normal stress of the critical plane
- Angles of the critical plane
- Findley damage of each level of load spectrum D
- Radial and vertical safety factors
- Equivalent stress values
- Equivalent angle of the critical plane
- Equivalent safety factor

S-N curves and cumulative damage analysis:

- k and N_{af}
    - Steel: one k for all levels of stress spectrum
    - GJS: k depends on the mean stress → different k for each level of stress spectrum and thus also different N_{af} for each level
- $\sigma_{af,P=50\%}$ and $\sigma_{af,P=red.}$
- Fatigue life N_{LC} or N_{HC} for each level of stress spectrum
- Damage D_{LC} or D_{HC} for each level of stress spectrum
- Total damage sums for $D_{LC,tot}$ and $D_{HC,tot}$, and total damage sum $D_{tot} = D_{LC,tot} + D_{HC,tot}$

3.2 Analysis of a notched component

As an example, a simple component made of GJS-500 shown in figure 67 is analysed using the method described in the previous chapter. The component is loaded with constant tension and variable torsion. The loading is presented in table 8.

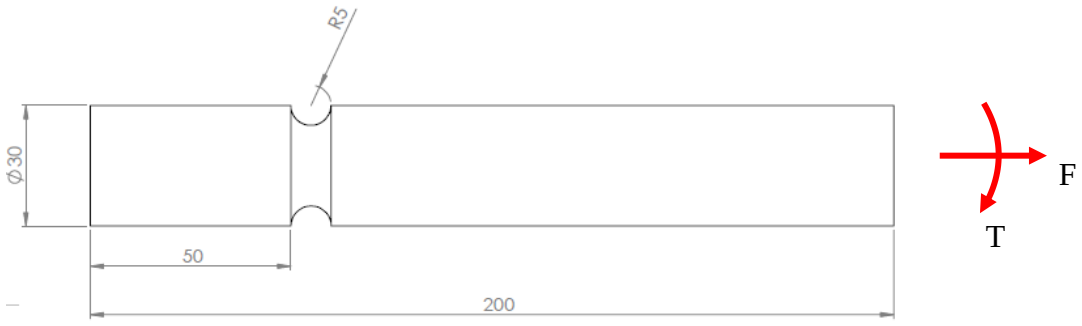

Figure 67. The component used in the example analysis.

Table 8. Loading.

Bin	**F [N]**	**T [Nmm]**		***n***
	Constant	Min	Max	
1.	19 000	0	200 000	4 500
2.	19 000	0	50 000	250 000
3.	19 000	0	62 840	150 000
4.	19 000	0	180 000	6 000
5.	19 000	0	78 550	200 000

Only the main steps of the analysis are listed below. More detailed calculation is presented in Appendix VIII.

1. Haigh diagrams

The following static strength values from EN-1563:2018 (2018, p. 8, 28) are used as starting values:

$\sigma_{0.2} = 1.06 \cdot 320 = 339.2$ MPa

$\sigma_b = 1.06 \cdot 500 = 530$ MPa

$\sigma_{b,comp} = 1.06 \cdot 800 = 848$ MPa

Fatigue limit for R = -1, fatigue limit for R = 0 and slope k of the reference Haigh diagram:

$\sigma_{aR=-1} = 196.1$ MPa

$\sigma_{aR=0} = 129.1$ MPa

$k = -0.5166$

Effective area calculation is done using all the element faces on the notch surface. Due to loading conditions, the whole circumference of the notch needs to be considered in the effective area calculation. Figure 68 shows von Mises stress distribution at the notch root with the maximum loading (bin 1). According to calculation, effective area for the component is $A_{eff} = 113.9$ mm^2.

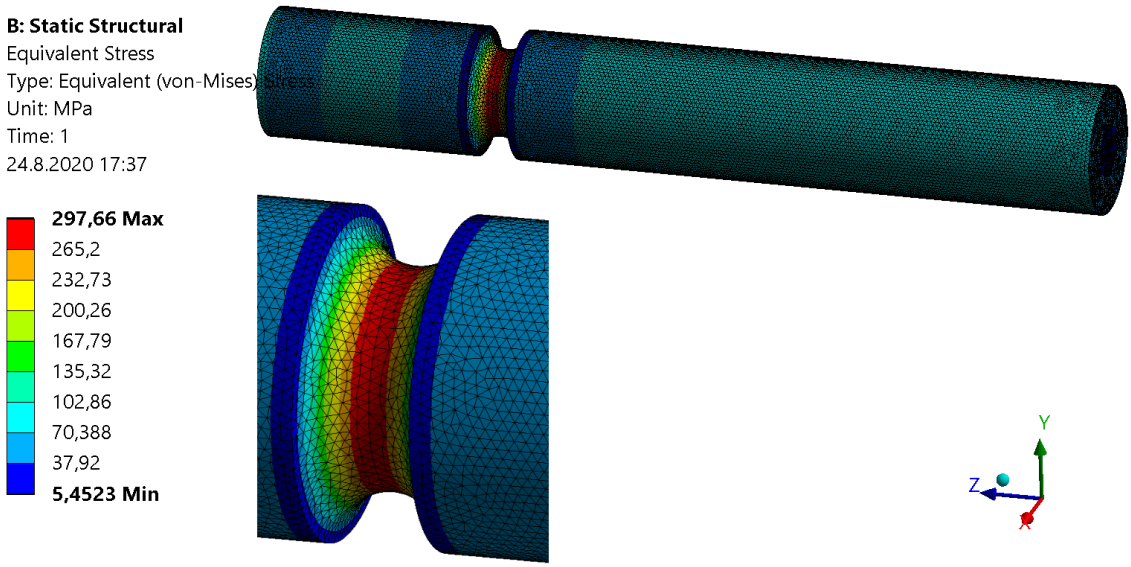

Figure 68. Von Mises stress distribution with the maximum loading (bin 1).

The following reduction factors are applied to reference specimen values:

K_{size} = 1.131 (A_{ref} = 1039 mm^2, A_{eff} = 113.9 mm^2)

K_R = 0.79 (R_z = 200 µm, casting surface)

K_{AT} = 1

K_N = 1

The reduced values (component values) for fatigue limits and slope:

$\sigma_{aR=-1,red} = 175.3$ MPa

$\sigma_{aR=0,red} = 119.9$ MPa

$k_{red} = -0.4616$

Haigh diagrams (P = 50 %) for reference specimen and component are shown in figure 69.

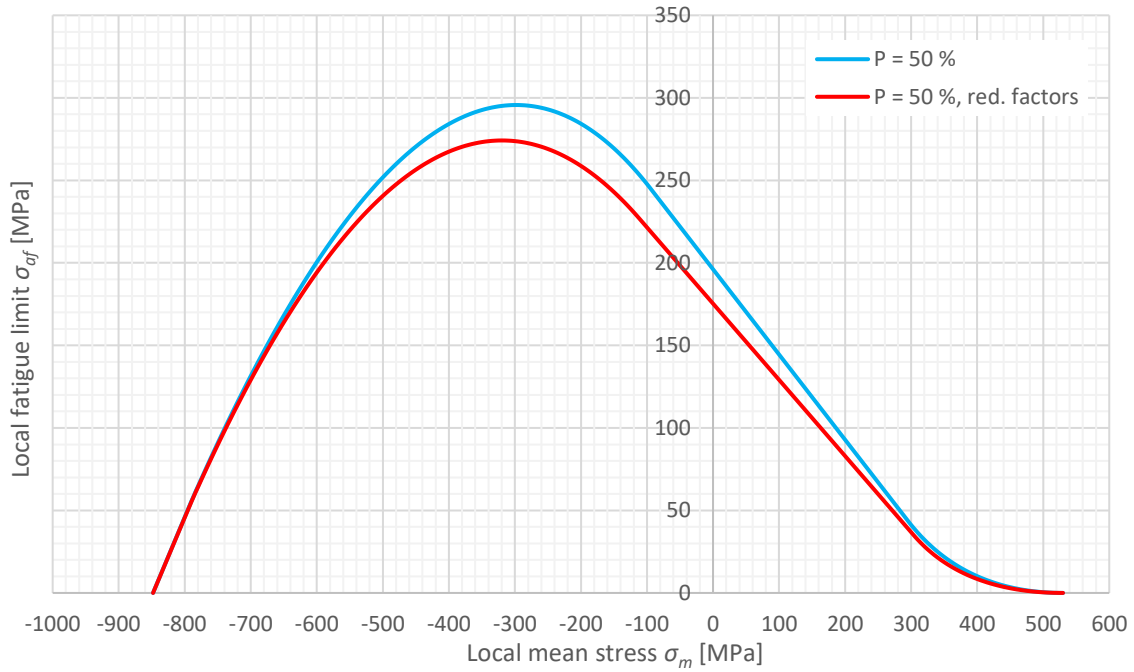

Figure 69. Haigh diagrams for P = 50 % for reference specimen and component.

2. Relative stress gradient χ^*

First, the critical distance for S-N curve slope exponent determination is calculated:

$$2r_c = L = \frac{1}{\pi}\left(\frac{\Delta K_{th,R=-1}}{2 \cdot K_{size} \cdot \sigma_{aR=-1}}\right)^2 = \frac{1}{\pi}\left(\frac{429.0\ \mathrm{N/mm^{3/2}}}{2 \cdot 1.131 \cdot 196.1\ MPa}\right)^2 = \underline{0.298\ mm}$$

Then, relative stress gradient χ^* is obtained at the distance of $2r_c$ from the surface along the surface normal using von Mises stress distribution. The submodel used in determination of χ^* is shown in figure 70 and von Mises stress distribution and χ^* are shown in figure 71.

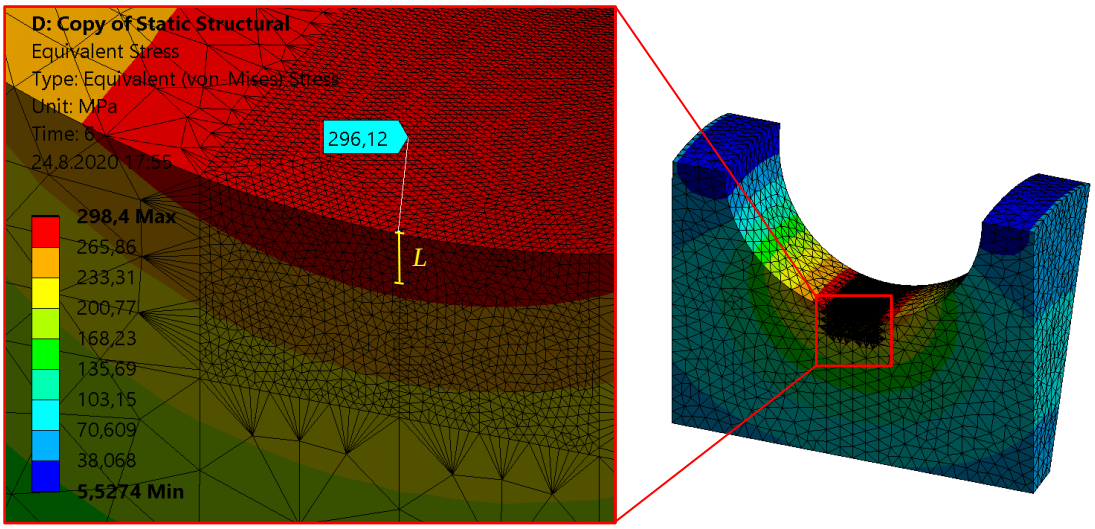

Figure 70. The submodel used in determination of relative stress gradient χ^*.

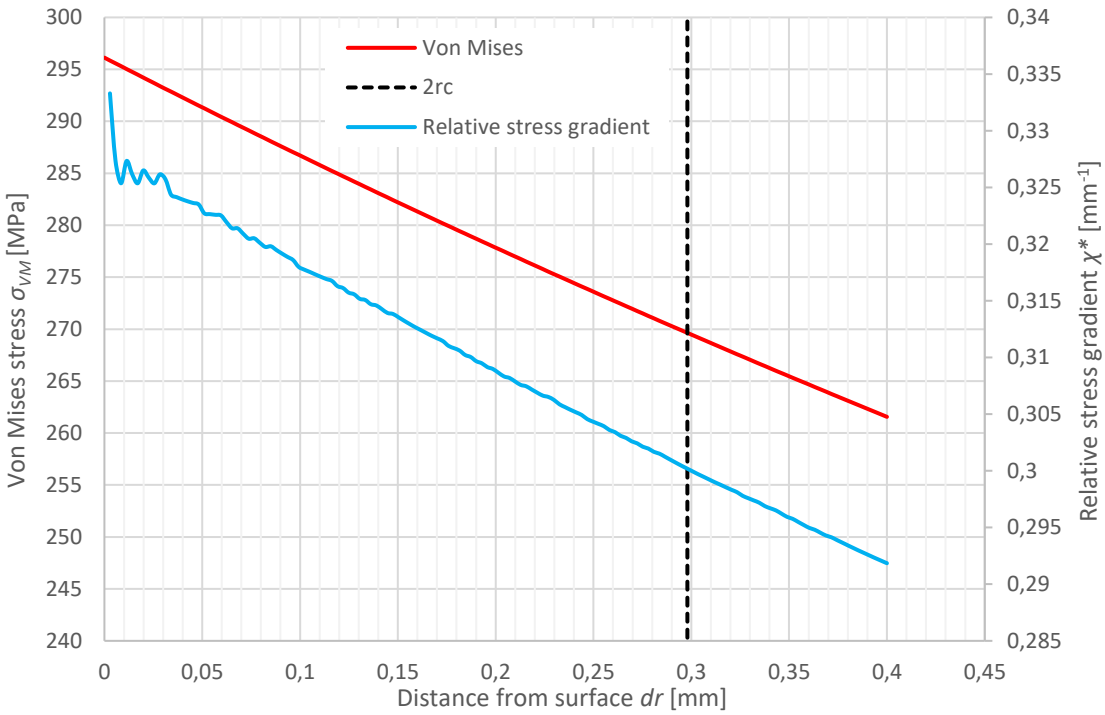

Figure 71. Von Mises stress distribution and relative stress gradient at the notch root. χ^* = 0.30 mm^{-1} at the distance of $2r_c$ = 0.298 mm.

3. Loading

The loading presented in table 8 causes the stress history shown in table 9 and figure 72 at the critical point.

Table 9. Maximum and minimum stresses of each loading bin [MPa].

Bin		σ_x	σ_y	σ_z	τ_{xy}	τ_{yz}	τ_{xz}
1.	Max	24.2	0	107.7	0	0	161.5
	Min	24.2	0	107.7	0	0	0
2.	Max	24.2	0	107.7	0	0	40.4
	Min	24.2	0	107.7	0	0	0
3.	Max	24.2	0	107.7	0	0	50.7
	Min	24.2	0	107.7	0	0	0
4.	Max	24.2	0	107.7	0	0	145.3
	Min	24.2	0	107.7	0	0	0
5.	Max	24.2	0	107.7	0	0	63.4
	Min	24.2	0	107.7	0	0	0

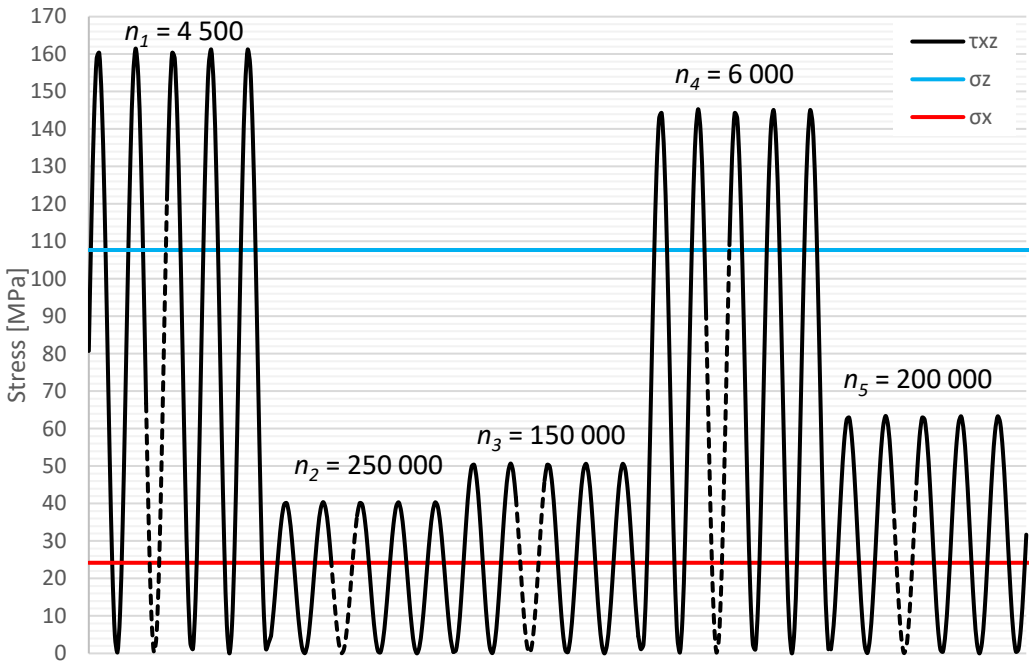

Figure 72. Stress history.

4. Findley

Findley analysis results and equivalent values are presented in table 10. It can be seen that the angle of the critical plane for equivalent loading differs between bins. Conservatively, it is assumed here that the angle θ_{eq} is the same for all bins and damages of individual bins are summed. Figure 73 shows different load bins in a Findley diagram.

Table 10. Findley analysis results. f = 137.1 MPa and k = 0.4624

Bin	$\Delta\tau$	σ_n	D	θ	φ	$S_{F,rad}$	$S_{F,ver}$	$\sigma_{m,eq}$	$\sigma_{a,eq}$	θ_{eq}	$S_{F,eq}$*
1.	129.8	195.6	155.3	0	18.3	0.883	0.719	87.6	159.7	27.2	0.845
2.	36.5	121.0	74.2	0	12.8	1.848	4.450	82.4	55.5	20.5	2.471
3.	45.0	126.4	80.9	180	166.3	1.694	3.498	81.8	65.0	21.9	2.115
4.	117.6	185.1	144.4	0	18.0	0.950	0.876	86.5	146.0	26.8	0.927
5.	54.9	133.8	89.3	0	15.0	1.535	2.740	82.0	76.1	23.1	1.805

* $S_{F,eq}$ = fatigue limit at $\sigma_{m,eq}$ divided by $\sigma_{a,eq}$

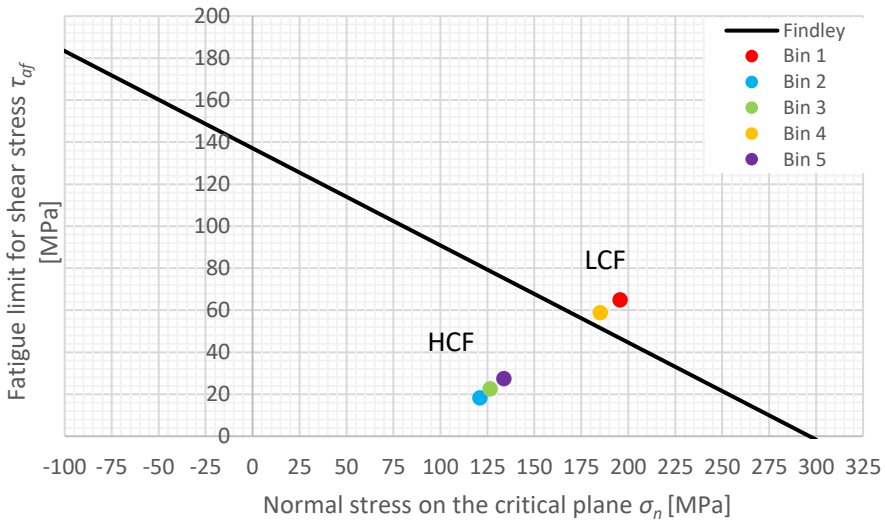

Figure 73. Findley diagram. f = 137.1 MPa and k = 0.4624.

5. S-N curves

Let us use failure probability of P = 0.1 %. Slope exponents calculated using χ^* and fatigue lives at the knee point according to equation (2.145) are shown in table 11.

Table 11. Equivalent stresses, slope exponents and fatigue lives at knee-point.

Bin	$\sigma_{a,eq}$	$\sigma_{m,eq}$	k	N_{af}
1	159.7	87.6	7.316	2031948
2	55.5	82.4	7.411	2061901
3	65	81.8	7.423	2065335
4	146	86.5	7.336	2038312
5	76.1	82	7.419	2064191

Fatigue limits for median S-N curves, safety factors (P = 0.1 %), reduced fatigue limits, fatigue lives and damage sums are shown in table 12. The total damage (LCF + HCF) is D_{tot} = 0.1991 which is below the allowed damage D_{allow} = 0.2 (see table 4) for casting surface.

Table 12. Fatigue limits, fatigue lives and damage sums (P = 0.1 %).

Bin	σ_{af} (med)	S_F	s_N	$s_{ln,H}$	$S_{F,H}$	
1 (LCF)	134.9	1.449	0.878	0.070	1.240	
2 (HCF)	137.3	1.449	0.889	0.069	1.239	
3 (HCF)	137.5	1.449	0.891	0.069	1.239	
4 (LCF)	135.4	1.449	0.880	0.069	1.239	
5 (HCF)	137.5	1.449	0.890	0.069	1.239	
Bin	$\sigma_{af,P=0.1\%}$	$\sigma_{af,PH}$	N	n	D_{LC}	D_{HC}
1 (LCF)	93.1	108.801	39156	4500	0.1149	
2 (HCF)	94.7	110.787	14576797703	250000		0.0001276
3 (HCF)	94.9	111.016	2000357218	150000		0.00056
4 (LCF)	93.4	109.221	77115	6000	0.0778	
5 (HCF)	94.9	110.940	260797621	200000		0.0057195
				Σ	0.19273099	0.0064071
				D_{tot}	0.1991	

Calculation of K_{size} using K-T diagram (optional)

In the example above, statistical size factor K_{size} is calculated using the weakest link theory (see calculation in Appendix VIII). Another possibility would be to use the defect distribution of the material and K-T diagram.

Defect distribution for GJS-500-7 provided by Rabb (2017, p. 168) is shown in table 13 and the corresponding K-T diagram is shown in figure 74. Using the method explained in chapter 2.2.3 median defect size and tested fatigue limit are fitted together. Fitting is done using $\sigma_{aR=-1}$ = 195.3 MPa (tested) and ΔK_{th} = 310.82 N/mm$^{3/2}$.

Table 13. Defect distribution (log-normal) of GJS-500-7 reference test specimen. Logarithmic SD of fatigue limit is $s_{ln} = s_r = 0.1$. (Mod. Rabb 2017, p. 168.)

Logarithmic median μ_{ln}	5.27
Logarithmic SD $s_{ln}(a)$	0.38
Median defect a_{med} [µm]	194.4
Mean defect a_{mean} [µm]	209.0
Standard deviation s [µm]	82.4
Relative SD s_r	0.394

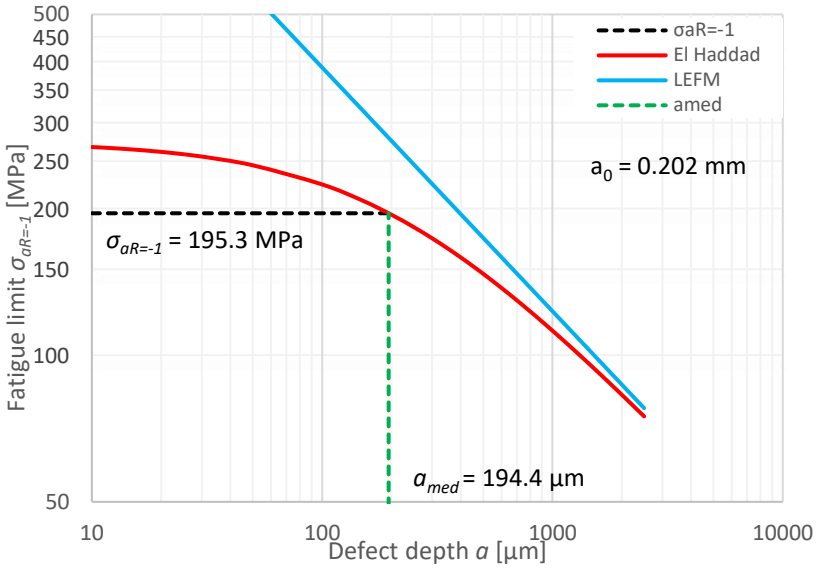

Figure 74. K-T diagram for GJS-500-7 (Mod. Rabb 2017, p. 169).

Using return period, the following is obtained:

$$n = \frac{A_{eff}}{A_{ref}} = \frac{113.92\ mm^2}{1039\ mm^2} = 0.10964$$

$$P = \frac{n}{n+1} = 0.09881$$

This is used to extrapolate the expected defect size in the component:

$$F(a_{ext}) = P \ \rightarrow \ solve\ a_{ext} \ \rightarrow \ \underline{a_{ext} = 119.15\ \mu m}$$

, where $F(a_{ext}) = \frac{1}{s_{ln}\sqrt{2\pi}} \int_0^{a_{ext}} \frac{1}{a} e^{-\frac{(\ln a - \mu_{ln})^2}{2s_{ln}^2}} da$

or

$$P = 0.09881 \quad \rightarrow \quad \lambda = -1.28836$$

$$K_{size,defect} = e^{-\lambda s_{ln}} = e^{1.28836 \cdot 0.38} = 1.6316$$

$$a_{ext} = \frac{a_{med}}{K_{size,defect}} = \frac{194.4\ \mu m}{1.6316} = \underline{119.14\ \mu m}$$

According to K-T diagram, fatigue limit of the component is then:

$$\sigma_{aR=-1,component} = \frac{\Delta K_{th}}{2 \cdot F\sqrt{\pi(a_{ext} + a_0)}} = \frac{310.82\ N/mm^{3/2}}{2 \cdot 0.713 \cdot \sqrt{\pi(0.11915\ mm + 0.202\ mm}} = 217.0\ MPa$$

Fatigue limit for reference specimen according to K-T diagram and defect distribution is as follows:

$$\sigma_{aR=-1,KTref} = \frac{\Delta K_{th}}{2 \cdot F\sqrt{\pi(a_{med} + a_0)}} = \frac{310.82\ N/mm^{3/2}}{2 \cdot 0.713 \cdot \sqrt{\pi(0.1944\ mm + 0.202\ mm}} = 195.3\ MPa$$

And K_{size} is thus:

$$K_{size} = \frac{\sigma_{aR=-1,component}}{\sigma_{aR=-1,KTref}} = \frac{217.0\ MPa}{195.3\ MPa} = \underline{1.111}$$

cf. K_{size} = 1.131 calculated using the weakest link theory.

Note that K-T diagram uses ΔK_{th} = 310.82 N/mm$^{3/2}$ which differs considerably from the default value calculated with equation provided in table 7. This value is used here because it was also used in fitting the El Haddad curve and defect size (Rabb 2017, p. 167). Since K_{size} is relative value, possible error in ΔK_{th} does not cause major problems. As the K-T diagram itself is based on tested fatigue limit and defect distribution by Rabb (2017, p. 168–169), it should give accurate results for K_{size} calculation.

Also, as is mentioned by Rabb (2017, p. 164, 171) it is advisable to use K-T diagram to calculate K_{size} when $n < 0.1$ (using return period) for a notch to avoid under-dimensioning with steel. However, in case of GJS when $n < 0.1$ (using return period) for a notch TCD should be taken into account because otherwise K-T diagram underestimates K_{size} (which is conservative but, in some cases too much so). Therefore, conclusion is that the weakest link theory may be used for GJS and steel when $0.1 < n < 1$.

Local fatigue limit of the notch according to TCD

According to TCD, the critical amplitude is at the distance of $r_c = L / 2$ from the surface of the notch. This means that using K_{size} (from K-T diagram) and fatigue limit of reference specimen, "nominal" fatigue limit at the distance of r_c for the notch is obtained. In order to obtain fatigue limit on the surface of the notch, stress gradient has to be considered. (Rabb 2020d.)

$$L = \frac{1}{\pi}\left(\frac{\Delta K_{th,R=-1}}{2 \cdot K_{size} \cdot \sigma_{aR=-1}}\right)^2 = \frac{1}{\pi}\left(\frac{429.0\ \mathrm{N/mm^{3/2}}}{2 \cdot 1.111 \cdot 196.1\ MPa}\right)^2 = 0.309\ mm$$

$$r_c = \frac{L}{2} = \underline{0.154\ mm}$$

, where $K_{size} \cdot \sigma_{aR=-1} = \sigma_{aR=-1,notch,nom}$ (nominal fatigue limit of the notch).

Taking stress gradient into account, fatigue limit on the surface of the notch can be obtained (Rabb 2020d):

$$\sigma_{aR=-1,notch} = \frac{\sigma_{VM,max,notch}}{\sigma(r_c)_{VM,notch}} \cdot \sigma_{aR=-1,notch,nom} = \frac{296.13\ MPa}{281.90\ MPa} \cdot 217.9\ MPa = \underline{228.9\ MPa}$$

$$K_{size,TCD} = \frac{\sigma_{aR=-1,notch}}{\sigma_{aR=-1}} = \frac{228.9\ MPa}{196.1\ MPa} = 1.167$$

cf. $K_{zise} = 1.111$ according to K-T diagram (5 % difference). This shows what was mentioned earlier; K-T diagram underestimates K_{size} with GJS when $n < 0.1$ (now $n \approx 0.11$ but effect can already be seen).

4 ANALYSIS AND DISCUSSION

It seems that most of the problems encountered with the analysis method from DNVGL-ST-0361 can be solved with the proposed probabilistic method. Firstly, the use of nominal stresses is no longer necessary, and local stresses from finite element analysis can be fully utilized. Secondly, multiaxial stresses can now be handled more accurately and thirdly, determination of failure probability is now easier.

Proposed Haigh diagrams seem to agree reasonably well with test data found in literature. New diagrams and diagrams from DNVGL-ST-0361 are shown together in figures 22–24 but since there is no information about the size of test specimens used in defining the equations in DNVGL-ST-0361, comparison is somewhat difficult. For GJS however, it seems that the new diagrams should be more conservative because slope of the linear part is steeper.

Using relative stress gradient to calculate S-N curve slope exponent allows to abandon the use of notch factor and nominal stresses. When relative stress gradient is obtained at the depth of L from the surface of the component, the effect is similar to what is observed when notch sensitivity is considered in nominal stress method (Rabb 2020d). This supports the applicability of the new method.

Effective area calculation with the method shown here is quite laborious. Exportation of nodal coordinates from Ansys have to be automated in some way in order to effectively use the computation procedure shown in chapter 2.9.1. It was also found that computation time for elemental surface areas was rather long when there was a large number of elements and therefore, symmetry should be exploited whenever possible. In the example analysis, about 1300 elemental face areas were calculated and this took over six minutes. Especially the computation of partial derivatives and the cross product $d\xi \times d\eta$ is very time consuming, so if better algorithms and tools for this can be found, they should be utilized.

Multiaxial stresses are handled with Findley criterion. This seems to be the best suited option because it can be used for both steel and cast iron in proportional and non-proportional loading cases. The requirements for computation capacity at least in complex cases are relatively

high but there are possibilities to optimize the calculation procedure. For example, Down-Hill simplex algorithm greatly decreases the computation time compared to program that does not incorporate any optimization (Rabb 2020e, Lönnqvist 2008, p. 171–172).

According to Rabb (2017, p. 164, 171) K-T diagram should be used to calculate statistical size factor for notched steel components when $A_{eff} / A_{ref} < 0.1$ to avoid under-dimensioning. Because of this, the use of K-T diagram in calculation of K_{size} was presented in the flowcharts and in the example analysis in chapter 3.2. It is advisable that K-T diagram is included as an option in the new analysis method so that if a very sharp notch is encountered, K_{size} calculated with the weakest link theory can be compared to K_{size} calculated with K-T diagram. Even though there may be some error in ΔK_{th} value, it does not cause problems when K-T diagram is used to calculate K_{size} because K_{size} is a relative value.

As was shown in the example analysis, K-T diagram may underestimate K_{size} in a case of a sharp notch when material is GJS. This is true also for steel with very sharp notches and it happens because stress intensity drops considerably over a large material defect on the surface and the critical point is thus located below the surface. Because of this TCD may have to be considered to avoid over-dimensioning. Therefore, it is advisable to include the possibility to calculate K_{size} according to TCD so that when very sharp notches are encountered, the effect explained above can be taken into account.

The flowcharts in chapter 3.1 give the most important steps and equations of the analysis process. If analyses are desired to be made before a fully functional tool is ready, a few of the steps should still be automated because of the amount of computation required. These include the calculation of Findley equivalent values for all levels of load spectrum in case of finite life, and perhaps the effective area calculation. Rest of the steps can be calculated manually with reasonable effort for example in Excel.

Some of the problems that still remain concern the use of fracture mechanics, multiaxial fatigue analysis and cumulative damage analysis. Currently, defining fatigue strength directly from K-T diagram is not possible, or at least not accurate enough, due to lack of accurate ΔK_{th} values. This in turn makes it difficult to define allowable defect sizes for critical areas, which is something that was initially required to be part of the analysis method. Also,

even though some defect distributions can be found, it would be beneficial to have more research on them with different materials.

The problems in multiaxial fatigue analysis are associated with the differences in the direction of the critical plane between different levels of load spectrum. In the example analysis it was conservatively assumed that all the levels affect the same plane since the differences in angles were not very large. Supposing though, that there was a large difference in angles, there could be some problems with this at least in terms of physical interpretation. Another thing to note is that plasticity in case of Findley criterion was not covered here.

There may be some problems with the use of Palmgren-Miner cumulative damage analysis. One, that is also pointed out by Rabb (2017, p. 319), is the sequence effect of loading. This means that the Palmgren-Miner theory does not consider the order in which the different load levels affect the component, which would be of importance if there was for example an occasional overload causing yielding at the notch root. Notch root plasticity would affect the local residual stresses which may even be favorable in terms of fatigue because compressive residual stress would diminish the effect of consequent high cycle loading. Thus, there would be difference in anticipated fatigue lives depending on at which point during the load history these overloads occur. (Schijve 2009, p. 300–302.)

4.1 Further research

The first thing to do in terms of further development would be the programming work. Even though the steps of the analysis process are presented here, surely there is a lot of work to program everything into a fully functional tool. After the basics presented in this work have been assembled into a working tool there are possibilities to develop different parts of the analysis method further.

The method proposed here could be developed further by having reliable test data for $\Delta K_{th.}$ This would also include the question about the crack closure which apparently does not occur with small cracks such as material defects (Rabb 2017, p. 529–530). Research on ΔK_{th} would perhaps allow the use of K-T diagram more extensively and then for example the definition of quality requirements for critical areas in terms of allowable defect size would be possible.

Also, surface roughness could be taken into account with the methods such as the one by Murakami presented in chapter 2.2.1 which are based on fracture mechanics. With these kinds of methods, it could be possible to combine effect of surface roughness and defect size, but this would probably require some verification by testing.

Another development area would be the use of the Palmgren-Miner cumulative damage analysis. Since this has been found to have some shortcomings, a more accurate method could be based on fracture mechanics. There is also a need to research how to define number of cycles in non-proportional load cases when cumulative damage analysis is performed.

One more aspect to clarify would be residual stresses and their effect. Residual stresses as such were not addressed here very extensively but they may have a significant effect on fatigue life. Lastly, it would be beneficial to perform a test with a real component and real loading conditions and see how accurately the proposed method is capable of predicting the outcome.

5 CONCLUSION

The most important goal of this thesis was to define the steps of a probabilistic fatigue analysis process for spheroidal graphite cast iron, quenched and tempered steel and structural steel in such a way that an automated analysis tool could be programmed. The motivation for this were the problems encountered in the use of the method presented in DNVGL-ST-0361, especially with the use of nominal stresses.

The results of this work give a starting point for programming a modern fatigue analysis tool. Already based on the results, it is possible to analyze at least simple components without any programming work, but more complex loading cases or larger geometries may require that at least parts of the analysis method are automated. The method presented in this thesis is a good starting point for developing more sophisticated and automated method to be used in complex loading cases and with complex geometries.

With the proposed method, it is possible to abandon the use of nominal stresses and utilize local stresses which are more easily available when finite element analysis is used. This is especially important with complex geometries for which the definition of nominal stress may be impossible.

A way to handle proportional and non-proportional multiaxial loading cases was presented. Findley criterion seems to be suitable because it can be used for both cast iron and steel.

A definitive answer for definition of allowable defect size for critical areas was not found. However, the method for this was presented, and with more reliable and extensive test data this could be utilized in the future.

LIST OF REFERENCES

Altair Engineering. 2020. Multiaxial Stress-Life Technical Background. [Altair Engineering eFatigue webpage]. [Referred 12.5.2020]. Available: https://www.efatigue.com/multiaxial/background/stresslife.html

Anderson, T. L. 2005. Fracture mechanics: Fundamentals and Applications. Third edition. Taylor & Francis Group, LLC. 610 p.

Ansys Help. 2020. Submodeling. [Ansys Help webpage]. [Referred 28.7.2020]. Available: https://ansyshelp.ansys.com/account/secured?returnurl=/Views/Secured/corp/v195/wb_sim/ds_submodeling.html?q=submodeling. Service requires a user license.

Božic, Ž. Schmauder, S. Mlikota, M. Hummel, M. 2014. Multiscale fatigue crack growth modelling for welded stiffened panels. Fatigue & Fracture of Engineering Materials & Structures 2014, Vol.37(9), p. 1043-1054.

BS 7910. 2013. Guide to methods for assessing the acceptability of flaws in metallic structures. Third edition. BSI Standards Limited. 478 p.

Bronshtein, I. Semendyayev, K. Musiol, G. Mühlig, H. 2015. Handbook of Mathematics. Sixth edition. Springer-Verlag Berlin Heidelberg. 1255 p.

Chapetti, M. 2010. Prediction of threshold for very high cycle fatigue ($N > 10^7$ cycles). Procedia Engineering 2010, Vol.2 (1), p. 257–264.

Cook, R. Malkus, D. Plesha, M. 1989. Concepts and applications of finite element analysis. 3rd edition. John Wiley & Sons, Inc. 630 p.

DNVGL-ST-0361. 2016. Machinery for wind turbines. DNV GL AS. 106 p.

Dowling, N. 2013. Mechanical Behavior of Materials. Fourth edition. Pearson Education Limited. 975 p.

Downing, S. & Socie, D. 1982. Simple rainflow counting algorithms. International Journal of Fatigue, Vol. 4(1), p. 31–40.

Eidel, B. Hartmaier, A. Gumbsch, P. 2010. Atomistic Simulation Methods and their Application on Fracture. In: Reinhard, P. Gumbsch, P. (Editors). Multiscale Modelling of Plasticity and Fracture by Means of Dislocation Mechanics. CISM Courses and Lectures, vol. 522. SpringerWienNewYork. p. 1–58.

El Haddad, M. Smith, K. Topper, T. 1979. Fatigue crack propagation of short cracks. Journal of Engineering Materials and Technology, Vol. 101, Issue 1. p. 42–46.

Gärtner, B. 2013. Smallest Enclosing Balls of Points – Fast and Robust in C++. ETH Zürich, Department of Computer Science, Institute of Theoretical Computer Science. [ETH Zürich webpage]. [Referred 29.7.2020.] Available: https://people.inf.ethz.ch/gaertner/subdir/software/miniball.html

Haibach, E. 2006. Betriebsfestigkeit: Verfahren und Daten zur Bauteilberechnung. Third edition. Springer-Verlag Berlin Heidelberg. 759 p.

Henttonen, J. Oinonen, J. Uusitalo, S. 2007. Tekniikan Matematiikka 1. 2.–3. painos. Helsinki: Edita Prima Oy. 385 p.

Henttonen, J. Peltomäki, J. Uusitalo, S. 2006. Tekniikan Matematiikka 2. 2. painos. Helsinki: Edita Prima Oy. 368 p.

Khan Academy. 2020. Surface area integrals. [Khan Academy webpage]. [Referred 9.7.2020]. Available: https://www.khanacademy.org/math/multivariable-calculus/integrating-multivariable-functions/surface-integrals-articles/a/surface-area-integrals

Kontkanen, P. Lehtonen, J. Luosto, K. 2012. Pyramidi 6: Todennäköisyys ja tilastot. 1. painos. Sanoma Pro Oy. 171 p.

Laukkanen, A., Holmberg, K., & Wallin, K. 2013. Multiscale modelling of engineering materials. In: T. Laitinen, & K. Wallin (Editors). Multiscale modelling and design for engineering application. VTT Technology, No. 77. VTT Technical Research Centre of Finland. p. 9–17.

Leimkuhler, B. Matthews, C. 2015. Molecular Dynamics With Deterministic and Stochastic Numerical Methods. Springer International Publishing Switzerland. 443 p.

Lönnqvist, C. 2008. Consistent Multiaxial Fatigue Analysis. Vaasa: 2008. Master's thesis. Helsinki University of Technology, Faculty of Engineering and Architecture, Department of Applied Mechanics. 266 p.

Meyer, N. 2014. Effects of Mean Stress and Stress Concentration on Fatigue Behavior of Ductile Iron. Master's thesis. The University of Toledo. 184 p.

Milella, P. 2013. Fatigue and Corrosion in Metals. Springer-Verlag Italia. 844 p.

Mlikota, M. Schmauder, S. Božic, Ž. 2018. Calculation of the Wöhler (S-N) curve using a two-scale model. International Journal of Fatigue 2018, Vol. 114. p. 289–297.

Mlikota, M. Staib, S. Schmauder, S. Božic, Ž. 2017. Numerical determination of Paris law constants for carbon steel using a two-scale model. Journal of Physics: Conference Series, Vol. 843(1). 10 p.

Mourier, C. 2002. Nennspannungsunabhängige Lebensdauervorhersage auf der Grundlage linear elastischer Finite-Elemente-Methode Berechnungen. Berlin: 2002. Doctoral dissertation. Technischen Universität Berlin, Fakultät für Verkehrs- und Maschinensysteme. 189 p.

Murakami, Y. 2002. Metal Fatigue: Effects of Small Defects and Nonmetallic Inclusions. Elsevier Science Ltd. 369 p.

Nygårds, M. 2003. Microstructural Finite Element Modeling of Metals. Stockholm: 2003. Doctoral Thesis. Royal Institute of Technology, Department of Solid Mechanics. 34 p.

Pallarés-Santasmartas, L. Albizuri, J. Avilés, A. Avilés, R. 2018. Mean Stress Effect on the Axial Fatigue Strength of DIN 34CrNiMo6 Quenched and Tempered Steel. Metals; Basel Vol. 8, Issue 4. 2018. p. 213–231.

Pilkey, W. 1997. Peterson's stress concentration factors. 2nd edition. John Wiley & Sons, Inc. 524 p.

Rabb, R. 2013. Todennäköisyysteoriaan pohjautuva väsymisanalyysi. Helsinki: BoD – Books on Demand. 459 p.

Rabb, R. 2017. Väsyminen ja todennäköisyysteoria. Oulu: Oulun yliopisto. 619 p.

Rabb, R. 2020a. S-N-Käyrän kaltevuuseksponentti. [private e-mail]. Receivers: Joona Kauppila, Toni Kilpeläinen, Timo Björk. Sent 14.7.2020, 15.16 o'clock (GMT +0200). Attachment: "Kaltevuuseksponentti.docx".

Rabb, R. 2020b. Jännitysgradientti ja kaltevuuseksponentti. [private e-mail]. Receivers: Joona Kauppila, Toni Kilpeläinen, Timo Björk. Sent 17.7.2020, 16.08 o'clock (GMT +0200). Attachment: "k-GJS, korjaus.docx", "k-teräs, korjaus.docx".

Rabb, R. 2020c. Rajasykliluku. [private e-mail]. Receivers: Joona Kauppila, Toni Kilpeläinen, Timo Björk. Sent 16.8.2020, 16.50 o'clock (GMT +0200). Attachment: "Rajasykliluku.docx".

Rabb, R. 2020d. Teräksen ja pallografiittivaluraudan S-N-käyrien kaltevuuseksponentit. [private e-mail]. Receivers: Joona Kauppila, Toni Kilpeläinen, Timo Björk. Sent 23.8.2020, 17.41 o'clock (GMT +0200). Attachment: "k-GJS, Update.docx", "k-teräs, Update.docx".

Rabb, R. 2020e. Ohjelma simplex.f. [private e-mail]. Receivers: Toni Kilpeläinen. Sent 1.4.2020, 12.16 o'clock (GMT +0200). Attachment: "Simplex.big.docx".

Råde, L. Westergren, B. 2014. Mathematics Handbook for Science and Engineering. Lund: Studentlitteratur AB. 562 p.

Schijve, J. 2009. Fatigue of Structures and Materials. Springer Science+Business Media B.V. 622 p.

SFS-EN 1563. 2018. Valut. Pallografiittivaluraudat. 5. painos. Helsinki: Suomen Standardisoimisliitto SFS ry. 85 p.

SFS-EN ISO 683-2. 2018. Lämpökäsiteltävät teräkset, seosteräkset ja automaattiteräkset. Osa 2: Seostetut nuorrutusteräkset. Helsinki: Suomen Standardisoimisliitto SFS ry. 81 p.

SFS-EN 10025-2. 2019. Kuumavalssatut rakenneteräkset. Osa 2: Seostamattomat rakenneteräkset. Tekniset toimitusehdot. 2. painos. Helsinki: Suomen Standardisoimisliitto SFS ry. 76 p.

Sperle, J. 2013. Influence of Parent Metal Strength on the Fatigue Strength of Parent Material with Machined and Thermally Cut Edges. Welding in the World 52, p. 79–92

Statics How To. 2020a. Bessel's Correction: Why Use N-1 For Variance/Standard Deviation? [Statics How To webpage]. [Referred 18.3.2020]. Available: https://www.statisticshowto.datasciencecentral.com/bessels-correction/

Statics How To. 2020b. Sample Variance: Simple Definition, How to Find it in Easy Steps. [Statics How To webpage]. [Referred 18.3.2020]. Available: https://www.statisticshowto.datasciencecentral.com/probability-and-statistics/descriptive-statistics/sample-variance/

Susmel, L. 2006. The theory of critical distances: a review of its applications in fatigue. Engineering Fracture Mechanics 2008, Vol.75(7), p. 1706-1724.

The Switch. 2020. Welcome to the world of The Switch. [The switch webpage]. [Referred 7.9.2020]. Available: https://theswitch.com/

Tampere University of Technology. 2015. Chapter 6: Fatigue. [web document]. [Referred 13.5.2020]. Available: http://www.tut.fi/rakmek/rak_33060/harj/fatigue_models.pdf

Tanaka, S. Nisitani, H. Teranishi, T. Fujisaki, W. 1995. Effect of Mean Stress on Fatigue Strength of Ferritic Spheroidal Graphite Cast Iron. Transactions of the Japan Society of Mechanical Engineers Series A, Volume 61, Issue 586, 1995. p. 1160–1164.

Taylor, D. 2007. The theory of critical distances. Engineering Fracture Mechanics 2008, Vol.75(7), p. 1696-1705.

TGL 19341/01. 1988. Festigkeitsnachweis für Bauteile aus Eisengußwerkstoffen; Berechnung. Leipzig: Verlag für Standardisierung. 14 p.

Ukrainetz, P. 1960. The effect of the mean stress on the endurance limit. Vancouver: 1960. Master's thesis. The University of British Columbia, Department of Mechanical Engineering. 42 p.

Weber, B. Kenmeugne, B. Clement, J.C. Robert, J.L. 1999. Improvements of multiaxial fatigue criteria computation for a strong reduction of calculation duration. Computational Materials Science 1999, Vol.15(4), p. 381–399.

Weyer, S. Fröhlich, A. Riesch-Opperman, H. Cizelj, L. Kovac, M. 2002. Automatic finite element meshing of planar Voronoi tessellations. Engineering Fracture Mechanics 2002, Vol.69(8), p. 945–958.

Test data from Meyer (2014) and Tanaka et al. (1995).

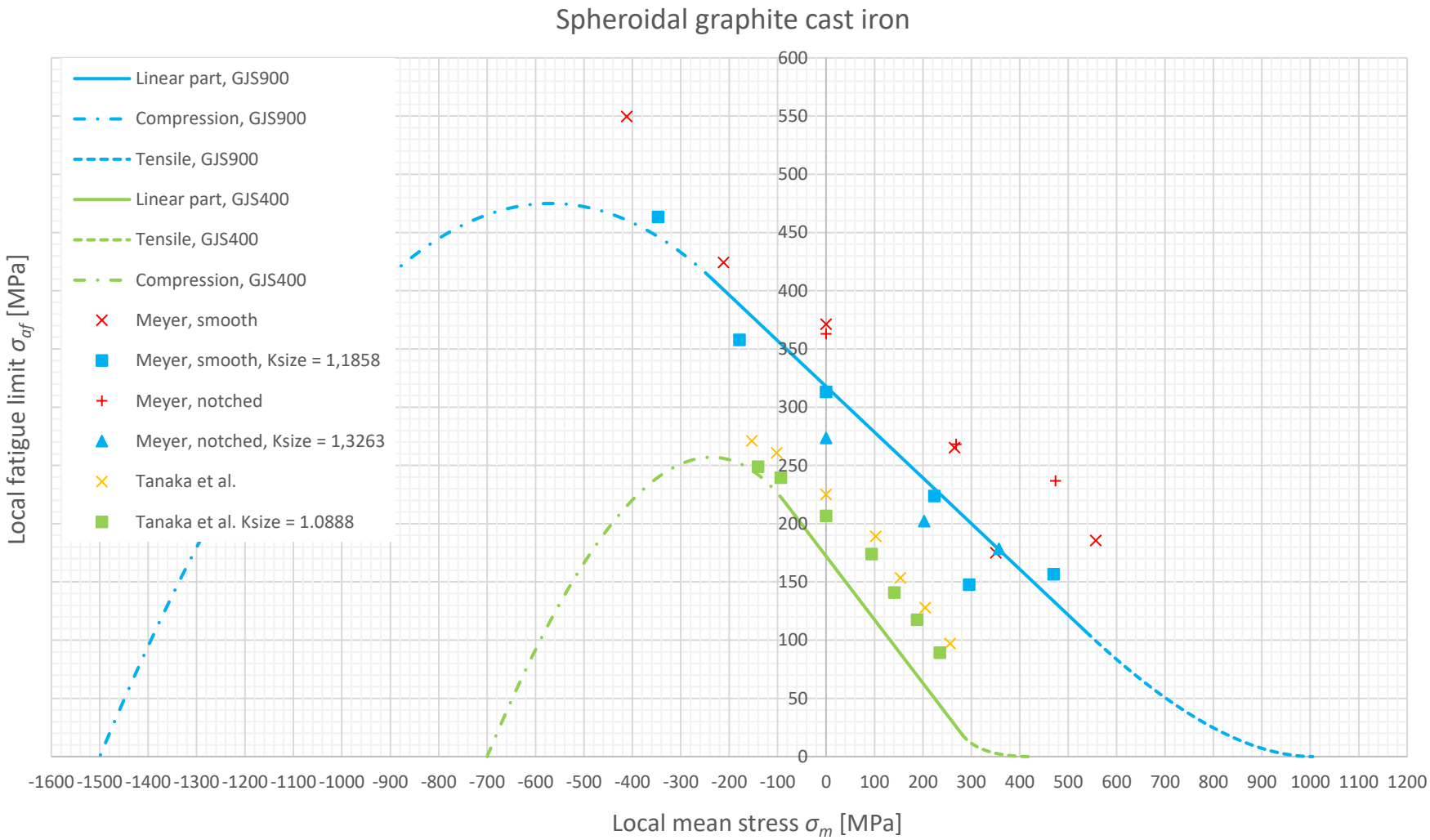

Test data from Pallarés-Santasmartas et al. (2018).

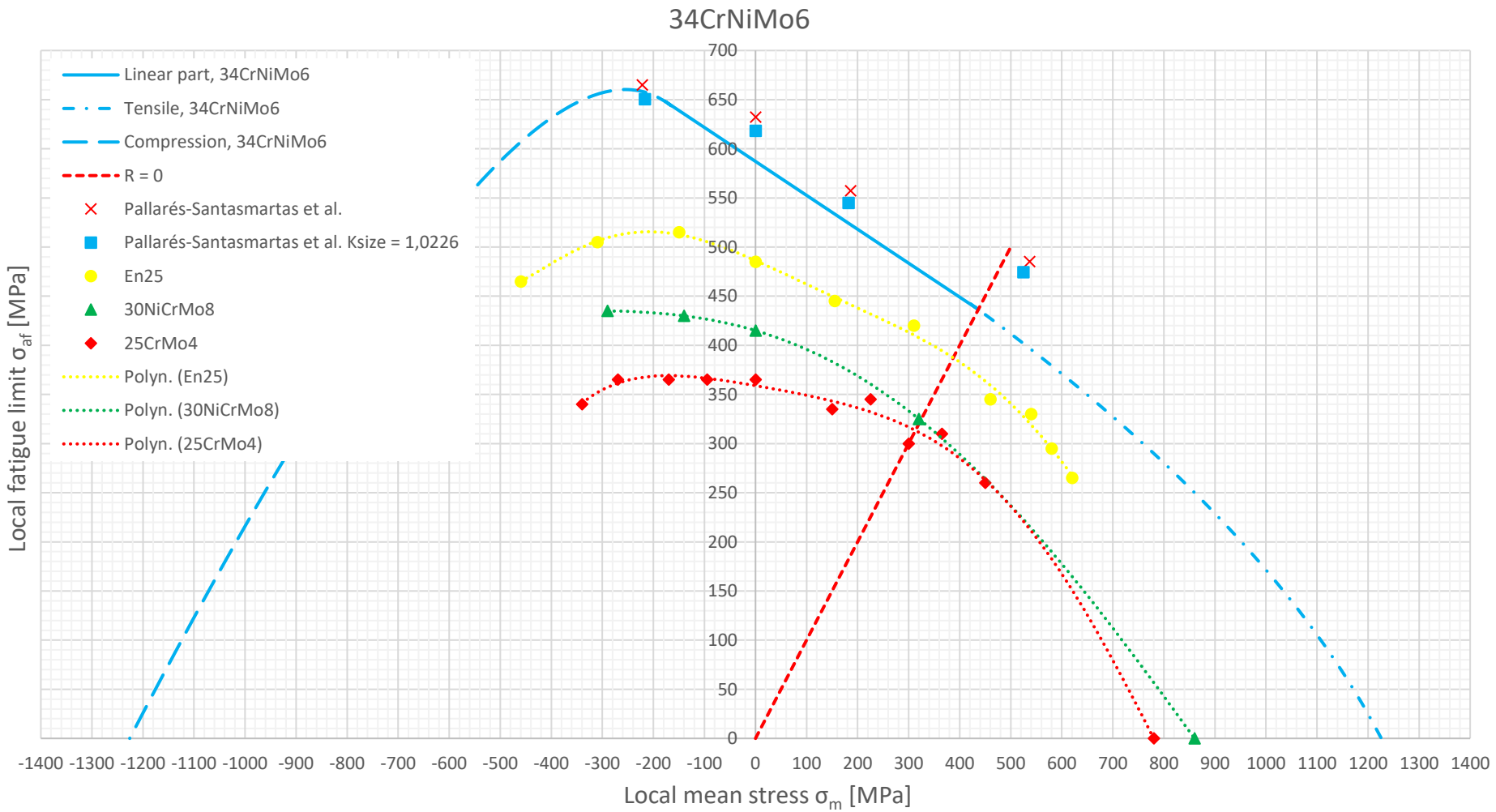

Test data from Ukrainetz (1960).

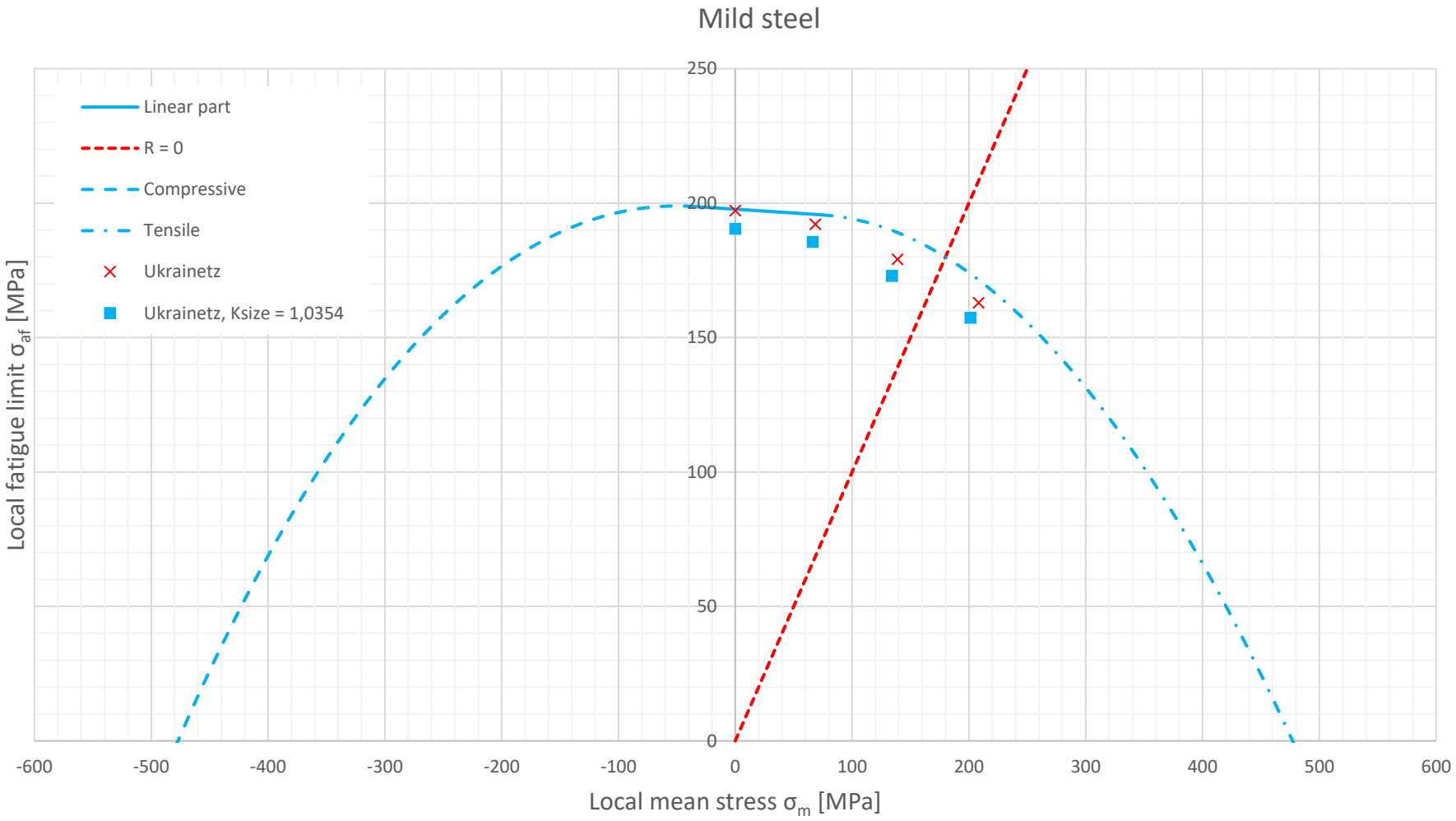

Rain-flow cycle counting (Mod. Rabb 2017, p. 410)

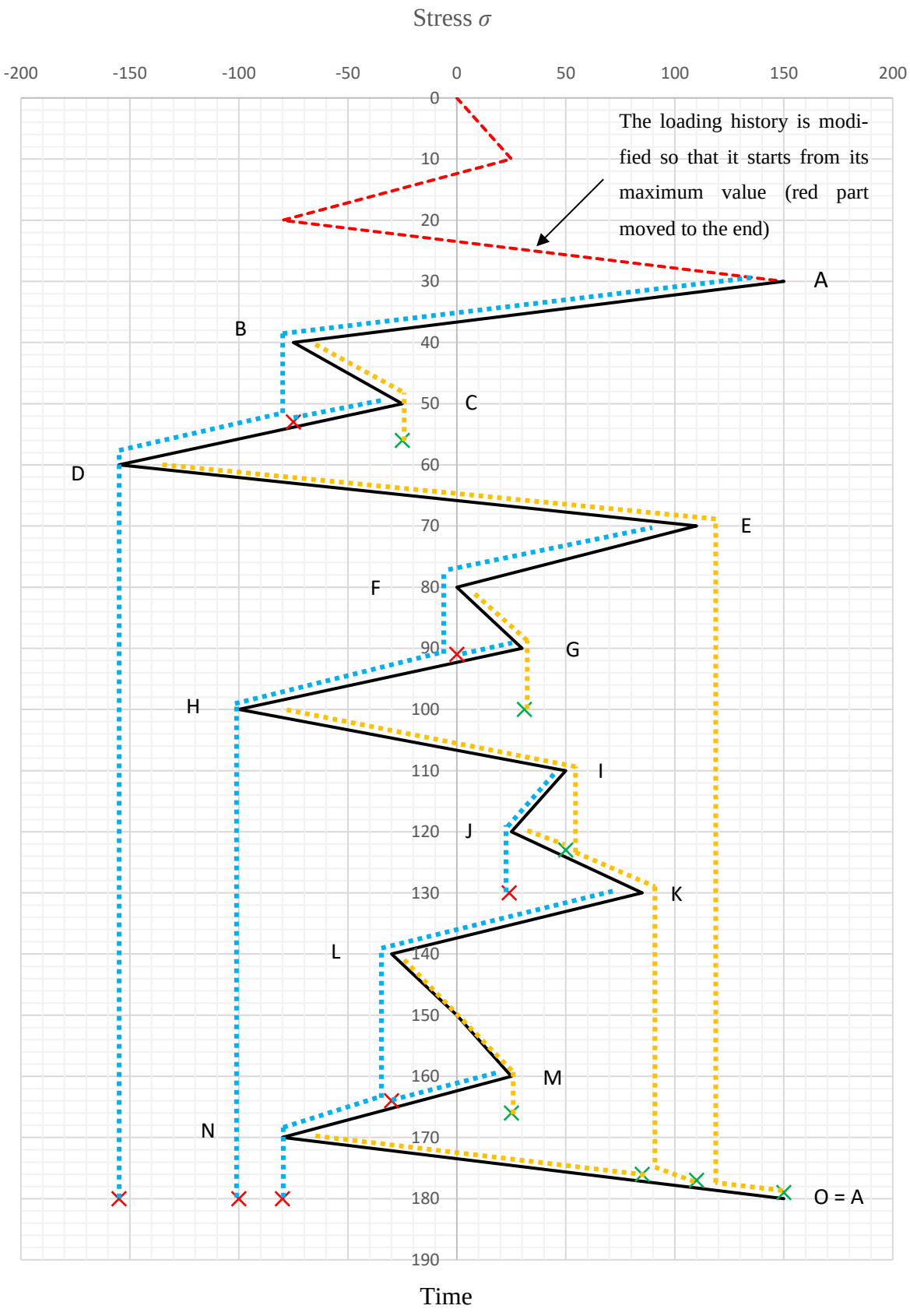

Half cycles from “Rain-flows”, amplitudes and mean stresses.

	End points		**Half cycles**	
	Stress	Time	σ_a	σ_m
A	-155	180	152,5	-2,5
C	-75	53	25	-50
E	-100	180	105	5
G	0	91	15	15
I	24	130	12,5	37,5
K	-80	180	82,5	2,5
M	-30	164	27,5	-2,5

	End points		**Half cycles**	
	Stress	Time	σ_a	σ_m
B	-25	56	25	-50
D	150	179	152,5	-2,5
F	31	100	15	15
H	110	177	105	5
J	50	123	12,5	37,5
L	25	166	27,5	-2,5
N	85	176	82,5	2,5
O				

	Full cycles	
	σ_a	σ_m
A-D	152,5	-2,5
C-B	25	-50
E-H	105	5
G-F	15	15
I-J	12,5	37,5
K-N	82,5	2,5
M-L	27,5	-2,5

Determination of the principal stresses from a stress matrix (Rabb 2017, p. 463).

$$\begin{bmatrix} \sigma_x - \sigma & \tau_{xy} & \tau_{xz} \\ \tau_{xy} & \sigma_y - \sigma & \tau_{yz} \\ \tau_{xz} & \tau_{yz} & \sigma_z - \sigma \end{bmatrix} \cdot \begin{bmatrix} l \\ m \\ n \end{bmatrix} = \begin{bmatrix} 0 \\ 0 \\ 0 \end{bmatrix} \quad \text{(IV.1)}$$

Eigenvalues are obtained from the determinant of the matrix:

$$\begin{vmatrix} \sigma_x & \tau_{xy} & \tau_{xz} \\ \tau_{xy} & \sigma_y & \tau_{yz} \\ \tau_{xz} & \tau_{yz} & \sigma_z \end{vmatrix} = 0 \quad \text{(IV.2)}$$

Invariants of the stress matrix $[\sigma]$:

$$I_1 = \mathrm{tr}[\sigma] = \sigma_x + \sigma_y + \sigma_z \quad \text{(IV.3a)}$$

$$I_2 = \begin{vmatrix} \sigma_x & \tau_{xy} \\ \tau_{xy} & \sigma_y \end{vmatrix} + \begin{vmatrix} \sigma_x & \tau_{xz} \\ \tau_{xz} & \sigma_z \end{vmatrix} + \begin{vmatrix} \sigma_y & \tau_{yz} \\ \tau_{yz} & \sigma_z \end{vmatrix} = \sigma_x\sigma_y + \sigma_x\sigma_z + \sigma_z\sigma_z - \tau_{xy}^2 - \tau_{yz}^2 - \tau_{xz}^2 \quad \text{(IV.3b)}$$

$$I_3 = |[\sigma]| = \begin{vmatrix} \sigma_x & \tau_{xy} & \tau_{xz} \\ \tau_{xy} & \sigma_y & \tau_{yz} \\ \tau_{xz} & \tau_{yz} & \sigma_z \end{vmatrix} = \sigma_x\sigma_y\sigma_z + 2\tau_{xy}\tau_{yz}\tau_{xz} - \sigma_x\tau_{yz}^2 - \sigma_y\tau_{xz}^2 - \sigma_z\tau_{xy}^2 \quad \text{(IV.3c)}$$

The principal stresses are then solved from the following cubic equation:

$$\sigma^3 - I_1\sigma^2 + I_2\sigma - I_3 = 0 \quad \text{(IV.4)}$$

Let us use the following substitution:

$$\sigma = z + \frac{I_1}{3} \quad \rightarrow \quad z^3 + pz + q = 0$$

, where:

$$p = I_2 - \frac{I_1^2}{3}, \qquad q = \frac{I_1 I_2}{3} - I_3 - \frac{2I_1^3}{27}$$

Let us use the following notation:

$$r = \sqrt{-\frac{p}{3}}$$

$$\varphi = \frac{1}{3}\cos^{-1}\left(-\frac{q}{2r^3}\right)$$

This yields the following solutions which are the three principal stresses:

$$\sigma_1 = 2r \cdot \cos(\varphi) + \frac{I_1}{3} \quad \text{(IV.5a)}$$

$$\sigma_2 = 2r \cdot \cos(\varphi + 120°) + \frac{I_1}{3} \quad \text{(IV.5b)}$$

$$\sigma_3 = 2r \cdot \cos(\varphi + 240°) + \frac{I_1}{3} \quad \text{(IV.5c)}$$

The principal stresses are organized in descending order:

$\sigma_I \geq \sigma_{II} \geq \sigma_{III}$

The direction cosines *l*, *m* and *n* in respect to the coordinate axes are solved from the following:

$$\begin{cases} \tau_{xy}l + (\sigma_y - \sigma)m + \tau_{yz}n = 0 \\ \tau_{xz}l + \tau_{yz}m + (\sigma_z - \sigma)n = 0 \\ l^2 + m^2 + n^2 = 1 \end{cases} \quad \text{(IV.6)}$$

$$A = \begin{vmatrix} \sigma_y - \sigma & \tau_{yz} \\ \tau_{yz} & \sigma_z - \sigma \end{vmatrix} = (\sigma_y - \sigma)(\sigma_z - \sigma) - \tau_{yz}^2 \quad \text{(IV.7a)}$$

$$B = -\begin{vmatrix} \tau_{xy} & \tau_{yz} \\ \tau_{xz} & \sigma_z - \sigma \end{vmatrix} = -\tau_{xy}(\sigma_z - \sigma) + \tau_{yz}\tau_{xz} \quad \text{(IV.7b)}$$

$$C = \begin{vmatrix} \tau_{xy} & \sigma_y - \sigma \\ \tau_{xz} & \tau_{yz} \end{vmatrix} = \tau_{xy}\tau_{yz} - \tau_{xz}(\sigma_y - \sigma) \quad \text{(IV.7c)}$$

$$\frac{l}{m} = \frac{A}{B} \quad \text{(IV.8a)}$$

$$\frac{m}{n} = \frac{B}{C} \quad \text{(IV.8b)}$$

$$\frac{l}{n} = \frac{A}{C} \quad \text{(IV.8c)}$$

$$R = \sqrt{A^2 + B^2 + C^2} \quad \text{(IV.9)}$$

$$l = \pm\frac{A}{R} \quad \text{(IV.10a)}$$

$$m = \pm\frac{B}{R} \quad \text{(IV.10b)}$$

$$n = \pm\frac{C}{R} \quad \text{(IV.10c)}$$

APPENDIX IV

Gauss integration points and weight coefficients for triangular element (Mod. Cook, Malkus & Plesha 1989, p. 182, 184).

Points	Multiplicity	Area Coordinates ξ_1, ξ_2, ξ_3			Weights W_i
		1-point formula	degree of precision 1		
A	1	0.33333 33333 33333	0.33333 33333 33333	0.33333 33333 33333	1.00000 00000 00000
		3-point formula	degree of precision 2		
B	3	0.66666 66666 66667	0.16666 66666 66667	0.16666 66666 66667	0.33333 33333 33333
		3-point formula	degree of precision 2		
M	3	0.50000 00000 00000	0.50000 00000 00000	0.00000 00000 00000	0.33333 33333 33333
		4-point formula	degree of precision 3		
A	1	0.33333 33333 33333	0.33333 33333 33333	0.33333 33333 33333	−0.56250 00000 00000
B	3	0.60000 00000 00000	0.20000 00000 00000	0.20000 00000 00000	0.52083 33333 33333
		6-point formula	degree of precision 4		
B	3	0.81684 75729 80459	0.09157 62135 09771	0.09157 62135 09771	0.10995 17436 55322
C	3	0.10810 30181 68070	0.44594 84909 15965	0.44594 84909 15965	0.22338 15896 78011
		7-point formula	degree of precision 5		
A	1	0.33333 33333 33333	0.33333 33333 33333	0.33333 33333 33333	0.22500 00000 00000
B	3	0.79742 69853 53087	0.10128 65073 23456	0.10128 65073 23456	0.12593 91805 44827
C	3	0.47014 20641 05115	0.47014 20641 05115	0.05971 58717 89770	0.13239 41527 88506
		12-point formula	degree of precision 6		
B	3	0.87382 19710 16996	0.06308 90144 91502	0.06308 90144 91502	0.05084 49063 70207
D	3	0.50142 65096 58179	0.24928 67451 70910	0.24928 67451 70910	0.11678 62757 26379
ns	6	0.63650 24991 21399	0.31035 24510 33784	0.05314 50498 44817	0.08285 10756 18374
		13-point formula	degree of precision 7		
A	1	0.33333 33333 33333	0.33333 33333 33333	0.33333 33333 33333	−0.14957 00444 67682
D	3	0.47930 80678 41920	0.26034 59660 79040	0.26034 59660 79040	0.17561 52574 33208
B	3	0.86973 97941 95568	0.06513 01029 02216	0.06513 01029 02216	0.05334 72356 08838
ns	6	0.63844 41885 69810	0.31286 54960 04874	0.04869 03154 25316	0.07711 37608 90257

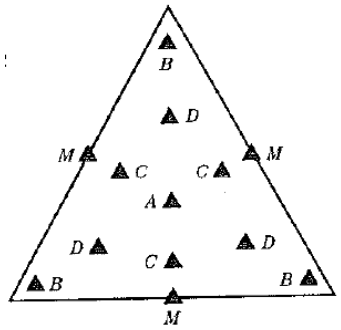

NOTE! Area coordinates correspond natural coordinates: $\xi_1 = \xi$, $\xi_2 = \eta$ and $\xi_3 = 1 - \xi - \eta$

Sorting the nodal coordinates data for effective area calculation in Excel.

The tet10 elements located on the surface on the area of interest can have four different orientations, which determines the nodes that are located on the surface of the component (see fig 75). Thus, the calculation procedure presented in Appendix VI has four different possibilities for calculation of the global coordinates within the element face.

This is of importance because the area is calculated with shape functions of T6 element which has only six nodes; nodes N1, N2 and N3 are the corner nodes and nodes N4, N5 and N6 are the midside nodes. This entails that some of the nodes of Tet10 element, which has 10 nodes, have to be renumbered to match the correct shape functions.

Presented below is one way to do this. Assuredly, the same could be achieved more easily for example by programming a macro for Ansys but there was no possibility to do this within this thesis due to lack of programming skills and time. Therefore, mainly MS-Excel was utilized.

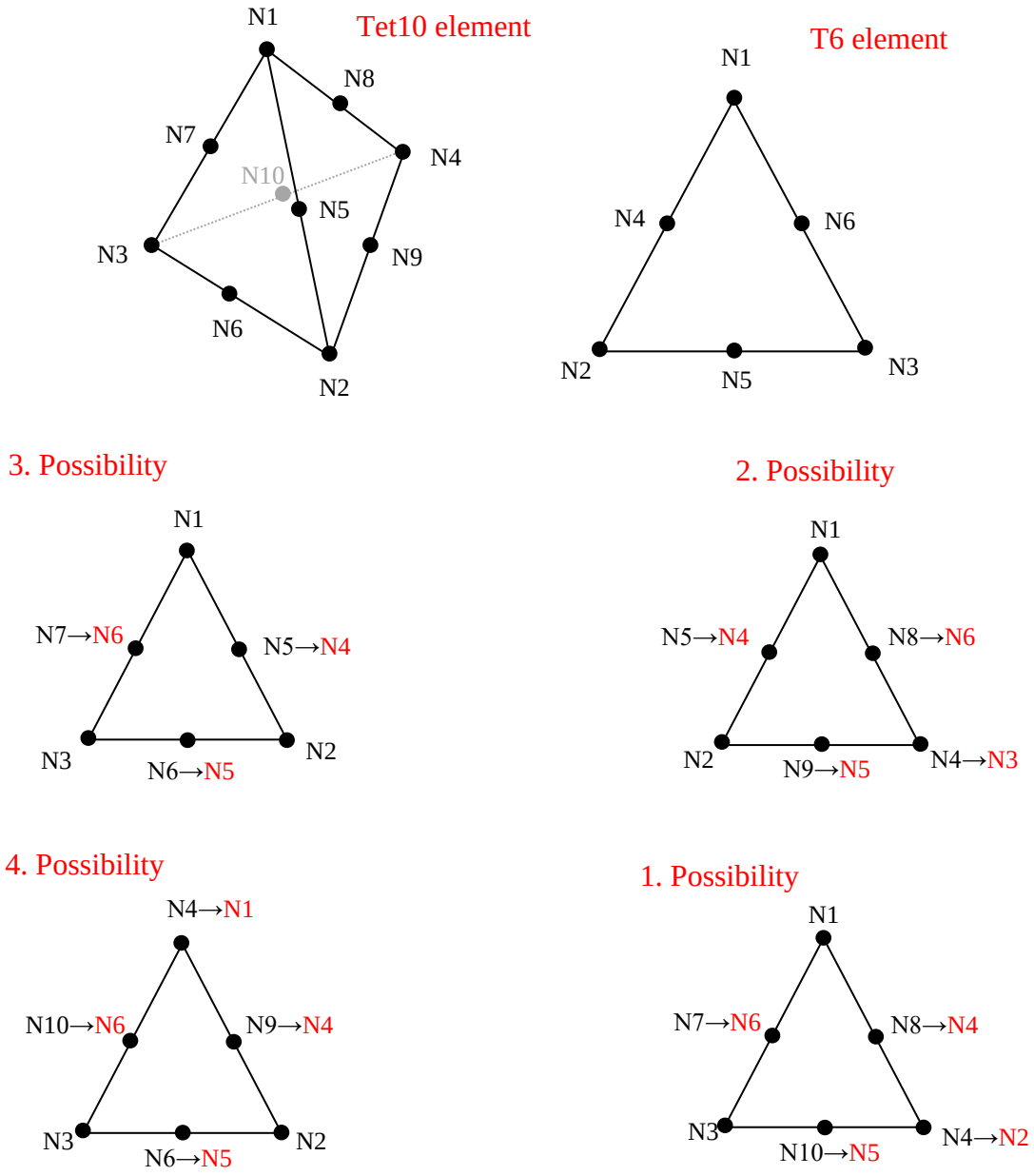

Figure 75. Different orientations of tet10 element in respect to the component surface. Red nodes are the new node numbers for the original tet10 node numbers.

First, the surface nodes of each element located on the area of interest have to be found. No direct way to export these was found, so they are searched using Excel (see figures 76 and 77).

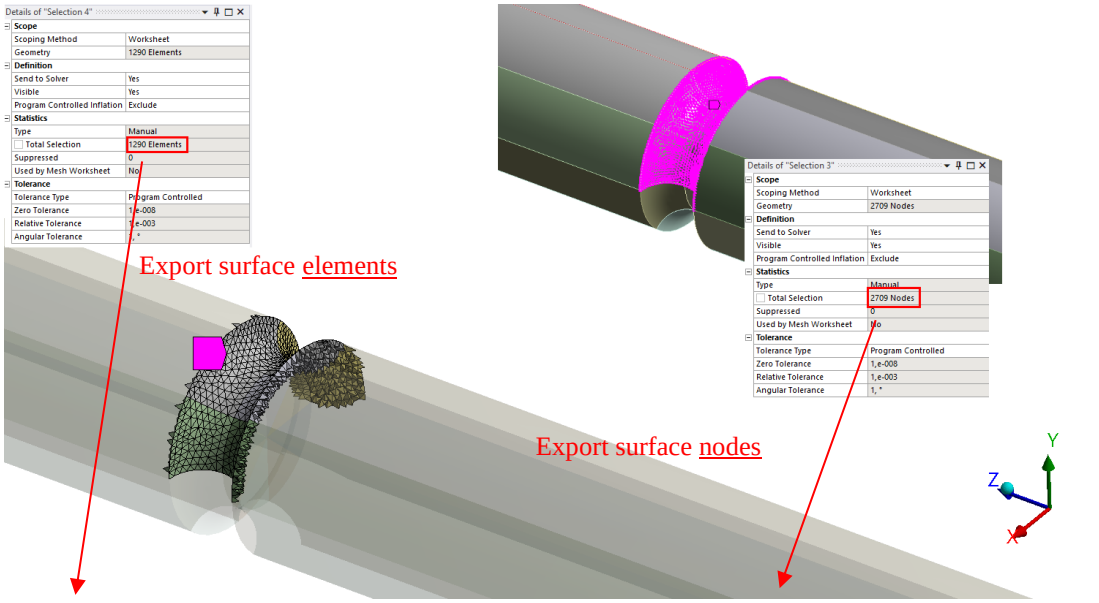

Element Number	Element Type	Nodes									
139	Tet10	3547	3567	3561	50659	242233	242330	242232	242239	242374	242335
141	Tet10	3547	3548	3567	50659	242231	242241	242233	242239	242247	242374
838	Tet10	5	3532	50589	3533	209389	242137	209394	209390	242129	242144
840	Tet10	5	3533	50589	6	209390	242144	209394	209386	209400	209405
912	Tet10	4	3532	3531	50581	209379	242122	209378	209383	242136	242128
920	Tet10	4	5	3532	50581	209375	209389	209379	209383	209393	242136
1122	Tet10	7	50570	8	3535	209416	209427	209408	209412	242159	209422
1127	Tet10	7	50570	3535	3534	209416	242159	209412	209411	242151	242145
4411	Tet10	3535	50354	3552	3560	242158	242276	242153	242154	242328	242269
4986	Tet10	187	188	3524	43528	211236	211247	211240	211242	211249	242074
4987	Tet10	1	43458	3	188	209349	209369	209343	209345	211248	209364
5100	Tet10	190	191	3526	42543	211262	211274	211266	211267	211277	242089
5102	Tet10	85	21075	3541	86	210281	242192	210279	210277	210287	210285
5177	Tet10	189	42774	190	3525	211258	211268	211251	211255	242082	211265
5183	Tet10	186	187	3523	43247	211226	211239	211230	211232	211241	242068
5185	Tet10	87	88	21077	3546	210290	210299	210294	210292	210298	242226
5187	Tet10	86	21076	3542	87	210288	242200	210286	210284	210293	210291
5188	Tet10	90	91	21080	3545	210309	210319	210313	210311	210318	242221
5189	Tet10	191	42524	192	3527	211276	211286	211271	211275	242096	211283
5303	Tet10	192	42474	193	3528	211285	211294	211280	211284	242103	211292
5321	Tet10	3527	3554	45163	3528	242095	242287	242097	242093	242101	242105
5322	Tet10	192	3528	3527	45163	211284	242093	211283	211287	242105	242097
5329	Tet10	182	45166	3519	3537	211190	242041	211186	211187	242166	242038
5330	Tet10	182	3519	45166	183	211186	242041	211190	211183	211197	211202
5359	Tet10	3540	3561	3562	45179	242184	242329	242185	242186	242331	242339
5360	Tet10	3539	3561	3540	45179	242178	242184	242176	242179	242331	242186
5361	Tet10	3540	3562	3541	45179	242185	242190	242183	242186	242339	242193
5510	Tet10	81	45238	182	3537	210255	211191	210251	210252	242167	211187
5513	Tet10	80	182	81	45238	210244	210251	210242	210247	211191	210255
5588	Tet10	3525	3526	3552	45265	242079	242087	242081	242083	242090	242271
5593	Tet10	190	3526	3525	45265	211266	242079	211265	211269	242090	242083

Node Number	X Location (mm)	Y Location (mm)	Z Location (mm)
1	0	10	-55
2	7.0711	7.0711	-55
3	0.98017	9.9518	-55
4	1.9509	9.8079	-55
5	2.9028	9.5694	-55
6	3.8268	9.2388	-55
7	4.714	8.8192	-55
8	5.5557	8.3147	-55
9	6.3439	7.7301	-55
29	10.607	10.607	-50
80	0	15	-50
81	0.98105	14.968	-50
82	1.9579	14.872	-50
83	2.9264	14.712	-50
84	3.8823	14.489	-50
85	4.8216	14.204	-50
86	5.7403	13.858	-50
87	6.6343	13.453	-50
88	7.5	12.99	-50
89	8.3336	12.472	-50
90	9.1314	11.9	-50
91	9.8902	11.278	-50
182	0	14.025	-50.096
183	0	13.087	-50.381
184	0	12.222	-50.843

Figure 76. Surface elements and surface nodes have to be exported separately from Ansys because importing just the nodes will not give the corresponding element and importing just the elements gives all the nodes (also the four nodes below the surface).

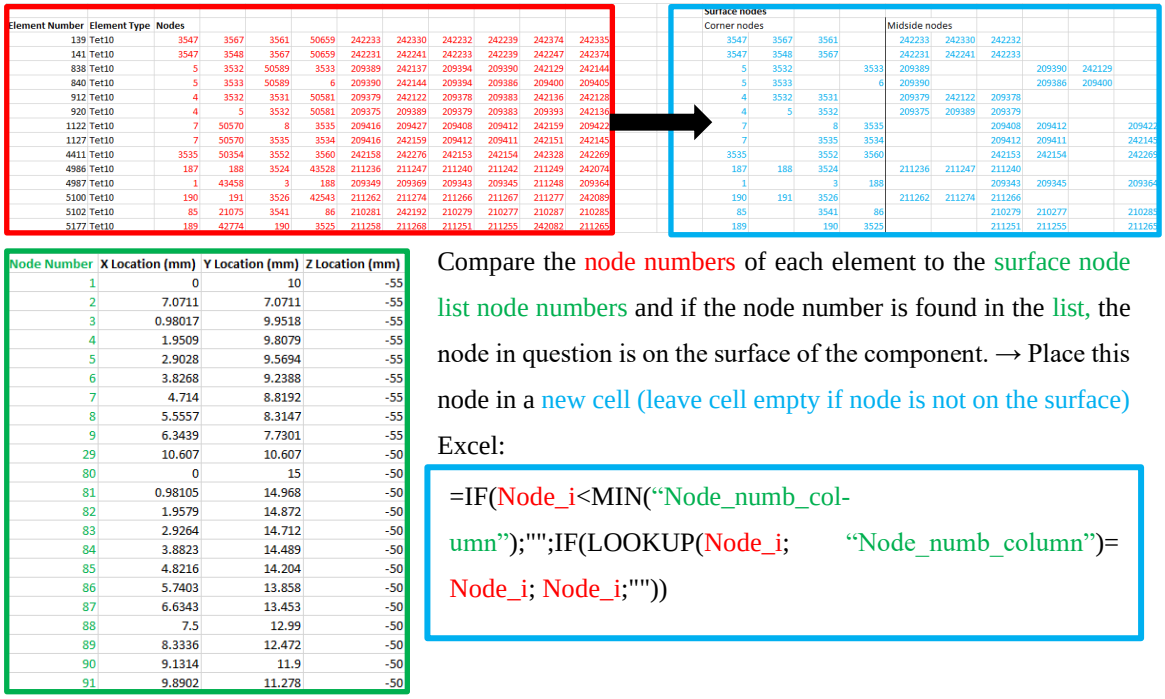

Figure 77. Searching the nodes that are on the surface of the component.

Next, the elements and the corresponding surface nodes (in light blue in figures 77 and 78) are separated into four groups based on their orientation.

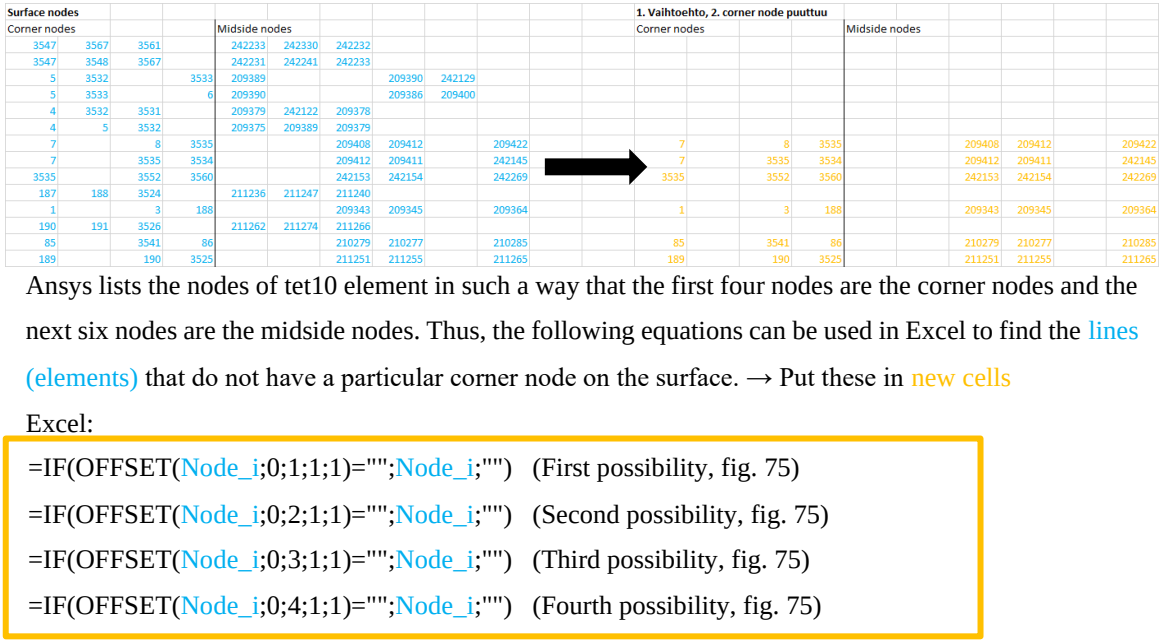

Figure 78. Sorting the elements with different orientations into respective groups. There are four different groups (four different orientations). Only the first possibility is shown in figure.

Next, X, Y and Z coordinates for each node need be searched from the surface node list (inside green boundary in figures 77 and 79).

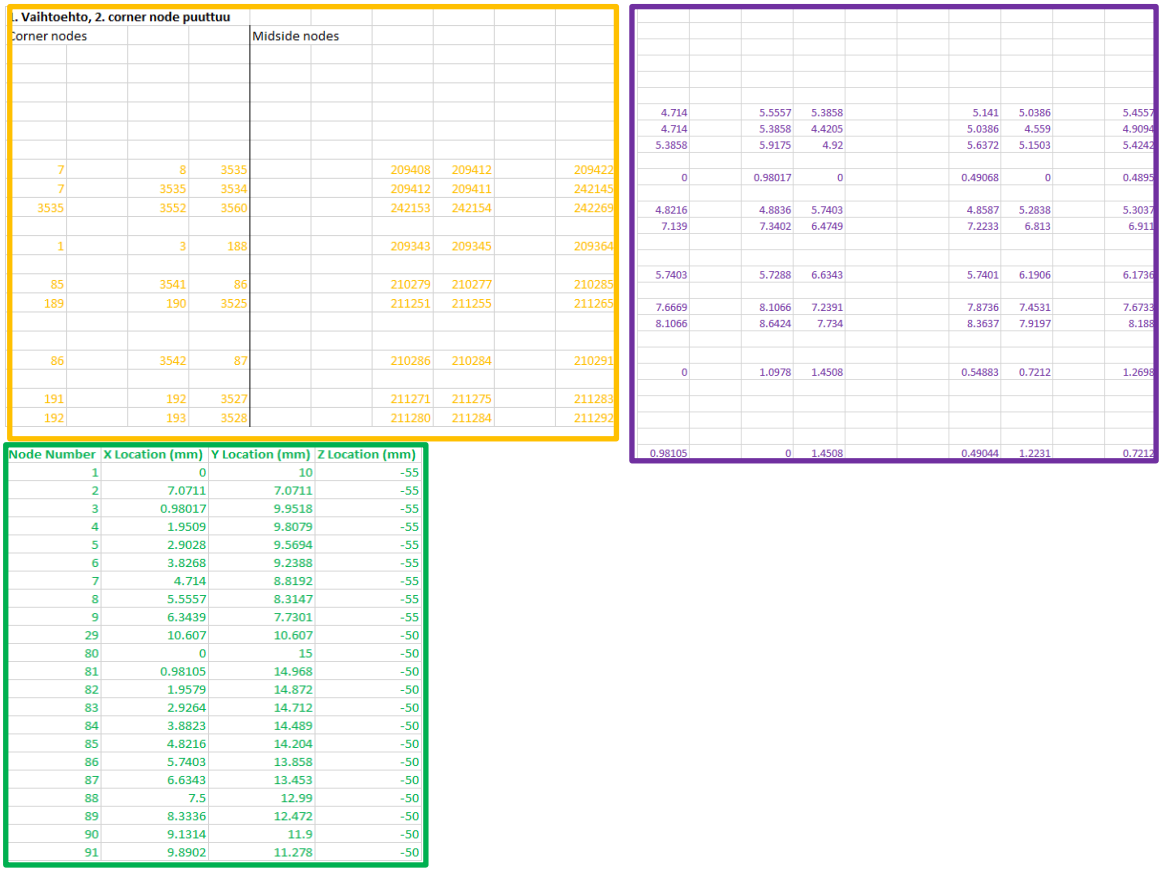

1. Vaihtoehto, 2. corner node puuttuu

Corner nodes			Midside nodes		
7	8	3535	209408	209412	209422
7	3535	3534	209412	209411	242145
3535	3552	3560	242153	242154	242269
1	3	188	209343	209345	209364
85	3541	86	210279	210277	210285
189	190	3525	211251	211255	211265
86	3542	87	210286	210284	210291
191	192	3527	211271	211275	211283
192	193	3528	211280	211284	211292

4.714	5.5557	5.3858	5.141	5.0386	5.4557
4.714	5.3858	4.4205	5.0386	4.559	4.9094
5.3858	5.9175	4.92	5.6372	5.1503	5.4242
0	0.98017	0	0.49068	0	0.4895
4.8216	4.8836	5.7403	4.8587	5.2838	5.3037
7.139	7.3402	6.4749	7.2233	6.813	6.911
5.7403	5.7288	6.6343	5.7401	6.1906	6.1736
7.6669	8.1066	7.2391	7.8736	7.4531	7.6733
8.1066	8.6424	7.734	8.3637	7.9197	8.188
0	1.0978	1.4508	0.54883	0.7212	1.2698
0.98105	0	1.4508	0.49044	1.2231	0.7212

Node Number	X Location (mm)	Y Location (mm)	Z Location (mm)
1	0	10	-55
2	7.0711	7.0711	-55
3	0.98017	9.9518	-55
4	1.9509	9.8079	-55
5	2.9028	9.5694	-55
6	3.8268	9.2388	-55
7	4.714	8.8192	-55
8	5.5557	8.3147	-55
9	6.3439	7.7301	-55
29	10.607	10.607	-50
80	0	15	-50
81	0.98105	14.968	-50
82	1.9579	14.872	-50
83	2.9264	14.712	-50
84	3.8823	14.489	-50
85	4.8216	14.204	-50
86	5.7403	13.858	-50
87	6.6343	13.453	-50
88	7.5	12.99	-50
89	8.3336	12.472	-50
90	9.1314	11.9	-50
91	9.8902	11.278	-50

X coordinates for the nodes of the first possible orientation. The coordinates can be found from the surface node list with the following equations.

X coordinate:

```
=IF(ISNUMBER(INDEX("Surf_nodes_x_loc_column";MATCH(Node_i;"Node_numb_column";0)))=TRUE;INDEX("Surf_nodes_x_loc_column";MATCH(Node_i;"Node_numb_column";0));"")
```

Y coordinate:

```
=IF(ISNUMBER(INDEX("Surf_nodes_y_loc_column";MATCH(Node_i;"Node_numb_column";0)))=TRUE;INDEX("Surf_nodes_y_loc_column";MATCH(Node_i;"Node_numb_column";0));"")
```

Z coordinate:

```
=IF(ISNUMBER(INDEX("Surf_nodes_z_loc_column";MATCH(Node_i;"Node_numb_column";0)))=TRUE;INDEX("Surf_nodes_z_loc_column";MATCH(Node_i;"Node_numb_column";0));"")
```

Figure 79. Searching X, Y and Z coordinates for surface nodes.

After the coordinates for X, Y and Z are found for all orientations, they are saved in separate text files (empty cells need be removed). These text files are then used as input for calculation procedure shown in Appendix VI. Searching the coordinates like shown above will result in 12 text files i.e. four files for each coordinate axis (one for each orientation).

In addition, von Mises stress is needed for effective area calculation. Here, von Mises stress was exported from Ansys for each surface node and the average of nodal values was used for the element. The von Mises stress values for the nodes of a certain element can be searched with the same equation as is used to search the coordinate values but, in this case, "Surf_nodes_x_loc" column has to be replaced by column containing surface node stresses. Note that the nodal values, be it the coordinates or stresses, have to be sorted in ascending order according to node number for the equations to work properly.

Part of a calculation sheet for effective area is shown in figure 80.

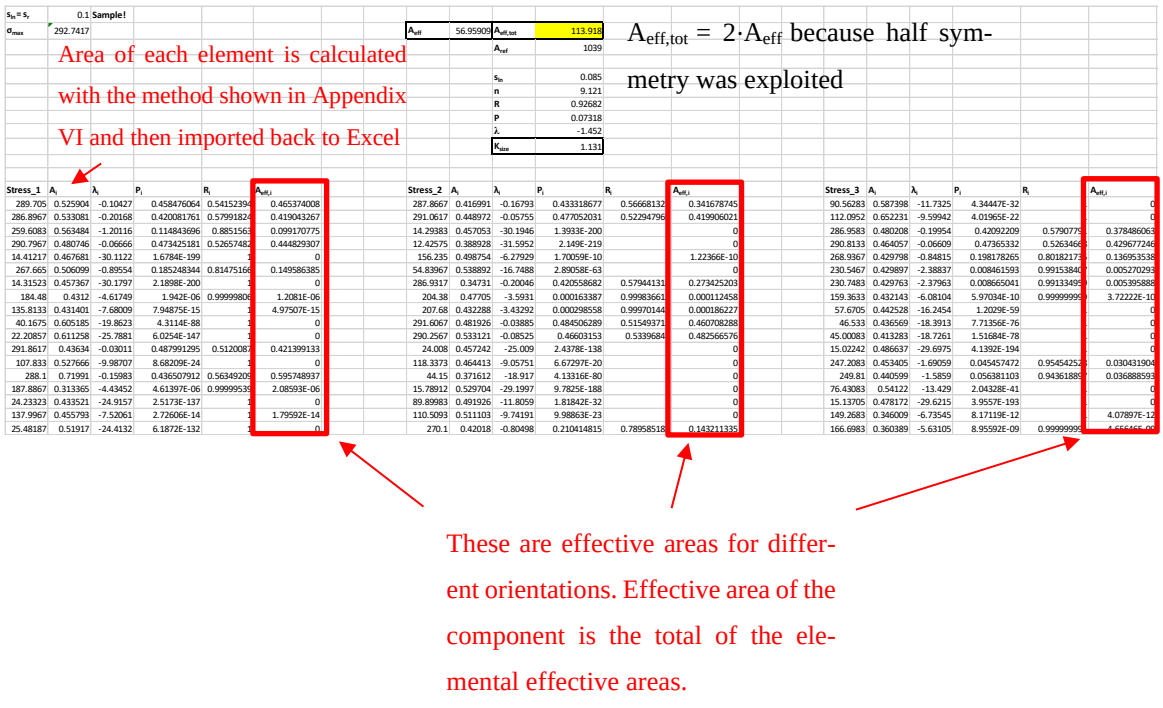

Figure 80. Calculation sheet of effective area and K_{size} according to the weakest link theory.

Calculation of the element face area in SMath Studio Desktop.

Area of a surface composed of quadtratic triangular (T6) elements

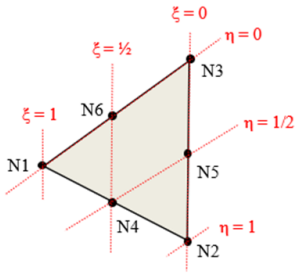

Global nodal coordinates from FEA (Ansys)

Shape functions (in reference coordinates ξ and η)

Global x, y and z coordinates within the element

Surface element

Areas of the element faces

Total surface area:

$$A_{tot} := \left(\sum A_1\right) + \left(\sum A_2\right) + \left(\sum A_3\right) + \left(\sum A_4\right) = 583,8361$$

$$exportData_{CSV}\left(A_1; "pinta\text{-}alat\_1"\right) = 1$$

$$exportData_{CSV}\left(A_2; "pinta\text{-}alat\_2"\right) = 1$$

$$exportData_{CSV}\left(A_3; "pinta\text{-}alat\_3"\right) = 1$$

$$exportData_{CSV}\left(A_4; "pinta\text{-}alat\_4"\right) = 1$$

Total area of the element faces. According to 3D model, the corresponding area should be 581.22 mm^2. Calculation procedure works well.

Global nodal coordinates from FEA (Ansys)

```
x1 := importData("C:\Users\Joona\Desktop\Diplomityö\Di-työ\Esimerkki\x1.txt")
x2 := importData("C:\Users\Joona\Desktop\Diplomityö\Di-työ\Esimerkki\x2.txt")
x3 := importData("C:\Users\Joona\Desktop\Diplomityö\Di-työ\Esimerkki\x3.txt")
x4 := importData("C:\Users\Joona\Desktop\Diplomityö\Di-työ\Esimerkki\x4.txt")

y1 := importData("C:\Users\Joona\Desktop\Diplomityö\Di-työ\Esimerkki\y1.txt")
y2 := importData("C:\Users\Joona\Desktop\Diplomityö\Di-työ\Esimerkki\y2.txt")
y3 := importData("C:\Users\Joona\Desktop\Diplomityö\Di-työ\Esimerkki\y3.txt")
y4 := importData("C:\Users\Joona\Desktop\Diplomityö\Di-työ\Esimerkki\y4.txt")

z1 := importData("C:\Users\Joona\Desktop\Diplomityö\Di-työ\Esimerkki\z1.txt")
z2 := importData("C:\Users\Joona\Desktop\Diplomityö\Di-työ\Esimerkki\z2.txt")
z3 := importData("C:\Users\Joona\Desktop\Diplomityö\Di-työ\Esimerkki\z3.txt")
z4 := importData("C:\Users\Joona\Desktop\Diplomityö\Di-työ\Esimerkki\z4.txt")
```

Shape functions (in reference coordinates ξ and η)

$$\zeta := 1 - \xi - \eta$$

$$N_1 := \xi \cdot (2 \cdot \xi - 1) \qquad N_4 := 4 \cdot \xi \cdot \eta$$

$$N_2 := \eta \cdot (2 \cdot \eta - 1) \qquad N_5 := 4 \cdot \eta \cdot \zeta$$

$$N_3 := \zeta \cdot (2 \cdot \zeta - 1) \qquad N_6 := 4 \cdot \zeta \cdot \xi$$

A Snippet of the text file containing nodal X-coordinates (x1.txt)

NODE→ ELEMENT ↓	N1	N2	N3	N4	N5	N6
E1	4.714	5.5557	5.3858	5.141	5.0386	5.4557
E2	4.714	5.3858	4.4205	5.0386	4.559	4.9094
E3	5.3858	5.9175	4.92	5.6372	5.1503	5.4242
E4	0	0.98017	0	0.49068	0	0.4895
E5	4.8216	4.8836	5.7403	4.8587	5.2838	5.3037
E6	7.139	7.3402	6.4749	7.2233	6.813	6.911
…	…	…	…	…	…	…
…	…	…	…	…	…	…

Global x, y and z coordinates within the element

1. Possibility

$n := \text{rows}(x_1) = 462$

Red refers to original Ansys node numbering

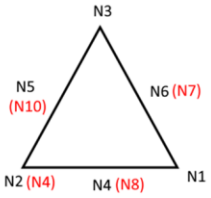

for $i := 1; i \le n; i := i + 1$

$X_i := N_1 \cdot x_{1,i1} + N_2 \cdot x_{1,i3} + N_3 \cdot x_{1,i2} + N_4 \cdot x_{1,i5} + N_5 \cdot x_{1,i6} + N_6 \cdot x_{1,i4}$

for $i := 1; i \le n; i := i + 1$

$Y_i := N_1 \cdot y_{1,i1} + N_2 \cdot y_{1,i3} + N_3 \cdot y_{1,i2} + N_4 \cdot y_{1,i5} + N_5 \cdot y_{1,i6} + N_6 \cdot y_{1,i4}$

for $i := 1; i \le n; i := i + 1$

$Z_i := N_1 \cdot z_{1,i1} + N_2 \cdot z_{1,i3} + N_3 \cdot z_{1,i2} + N_4 \cdot z_{1,i5} + N_5 \cdot z_{1,i6} + N_6 \cdot z_{1,i4}$

2. Possibility

$n := \text{rows}(x_2) = 430$

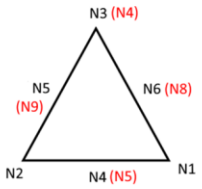

for $i := 1; i \le n; i := i + 1$

$X_i := N_1 \cdot x_{2,i1} + N_2 \cdot x_{2,i2} + N_3 \cdot x_{2,i3} + N_4 \cdot x_{2,i4} + N_5 \cdot x_{2,i6} + N_6 \cdot x_{2,i5}$

for $i := 1; i \le n; i := i + 1$

$Y_i := N_1 \cdot y_{2,i1} + N_2 \cdot y_{2,i2} + N_3 \cdot y_{2,i3} + N_4 \cdot y_{2,i4} + N_5 \cdot y_{2,i6} + N_6 \cdot y_{2,i5}$

for $i := 1; i \le n; i := i + 1$

$Z_i := N_1 \cdot z_{2,i1} + N_2 \cdot z_{2,i2} + N_3 \cdot z_{2,i3} + N_4 \cdot z_{2,i4} + N_5 \cdot z_{2,i6} + N_6 \cdot z_{2,i5}$

3. Possibility

$n := \text{rows}(x_3) = 398$

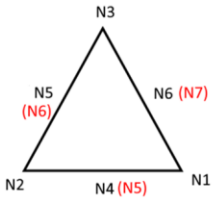

for $i := 1; i \le n; i := i + 1$

$X_i := N_1 \cdot x_{3,i1} + N_2 \cdot x_{3,i2} + N_3 \cdot x_{3,i3} + N_4 \cdot x_{3,i4} + N_5 \cdot x_{3,i5} + N_6 \cdot x_{3,i6}$

for $i := 1; i \le n; i := i + 1$

$Y_i := N_1 \cdot y_{3,i1} + N_2 \cdot y_{3,i2} + N_3 \cdot y_{3,i3} + N_4 \cdot y_{3,i4} + N_5 \cdot y_{3,i5} + N_6 \cdot y_{3,i6}$

for $i := 1; i \le n; i := i + 1$

$Z_i := N_1 \cdot z_{3,i1} + N_2 \cdot z_{3,i2} + N_3 \cdot z_{3,i3} + N_4 \cdot z_{3,i4} + N_5 \cdot z_{3,i5} + N_6 \cdot z_{3,i6}$

4. Possibility

$n := \text{rows}(x_4) = 1$

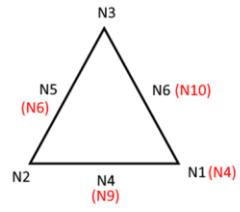

for $i := 1; i \le n; i := i + 1$

$X_i := N_1 \cdot x_{4,i3} + N_2 \cdot x_{4,i1} + N_3 \cdot x_{4,i2} + N_4 \cdot x_{4,i5} + N_5 \cdot x_{4,i4} + N_6 \cdot x_{4,i6}$

for $i := 1; i \le n; i := i + 1$

$Y_i := N_1 \cdot y_{4,i3} + N_2 \cdot y_{4,i1} + N_3 \cdot y_{4,i2} + N_4 \cdot y_{4,i5} + N_5 \cdot y_{4,i4} + N_6 \cdot y_{4,i6}$

for $i := 1; i \le n; i := i + 1$

$Z_i := N_1 \cdot z_{4,i3} + N_2 \cdot z_{4,i1} + N_3 \cdot z_{4,i2} + N_4 \cdot z_{4,i5} + N_5 \cdot z_{4,i4} + N_6 \cdot z_{4,i6}$

Surface element

$n := \text{rows}(x_1)$

for $i := 1; i \le n; i := i + 1$

$$dA_{x1}{}_i := \frac{d}{d\xi} Y_1{}_i \cdot \frac{d}{d\eta} Z_1{}_i - \frac{d}{d\xi} Z_1{}_i \cdot \frac{d}{d\eta} Y_1{}_i$$

for $i := 1; i \le n; i := i + 1$

$$dA_{y1}{}_i := -\left(\frac{d}{d\xi} X_1{}_i \cdot \frac{d}{d\eta} Z_1{}_i - \frac{d}{d\xi} Z_1{}_i \cdot \frac{d}{d\eta} X_1{}_i\right)$$

for $i := 1; i \le n; i := i + 1$

$$dA_{z1}{}_i := \frac{d}{d\xi} X_1{}_i \cdot \frac{d}{d\eta} Y_1{}_i - \frac{d}{d\xi} Y_1{}_i \cdot \frac{d}{d\eta} X_1{}_i$$

for $i := 1; i \le n; i := i + 1$

$$dA_1{}_i := \sqrt{dA_{z1}{}_i^{\,2} + dA_{y1}{}_i^{\,2} + dA_{x1}{}_i^{\,2}}$$

$$dA_1(\xi ; \eta) := dA_1$$

$n := \text{rows}(x_2)$

for $i := 1; i \le n; i := i + 1$

$$dA_{x2}{}_i := \frac{d}{d\xi} Y_2{}_i \cdot \frac{d}{d\eta} Z_2{}_i - \frac{d}{d\xi} Z_2{}_i \cdot \frac{d}{d\eta} Y_2{}_i$$

for $i := 1; i \le n; i := i + 1$

$$dA_{y2}{}_i := -\left(\frac{d}{d\xi} X_2{}_i \cdot \frac{d}{d\eta} Z_2{}_i - \frac{d}{d\xi} Z_2{}_i \cdot \frac{d}{d\eta} X_2{}_i\right)$$

for $i := 1; i \le n; i := i + 1$

$$dA_{z2}{}_i := \frac{d}{d\xi} X_2{}_i \cdot \frac{d}{d\eta} Y_2{}_i - \frac{d}{d\xi} Y_2{}_i \cdot \frac{d}{d\eta} X_2{}_i$$

for $i := 1; i \le n; i := i + 1$

$$dA_2{}_i := \sqrt{dA_{z2}{}_i^{\,2} + dA_{y2}{}_i^{\,2} + dA_{x2}{}_i^{\,2}}$$

$$dA_2(\xi ; \eta) := dA_2$$

$n := \text{rows}(x_3)$

for $i := 1; i \le n; i := i + 1$

$$dA_{x3}{}_i := \frac{d}{d\xi} Y_3{}_i \cdot \frac{d}{d\eta} Z_3{}_i - \frac{d}{d\xi} Z_3{}_i \cdot \frac{d}{d\eta} Y_3{}_i$$

for $i := 1; i \le n; i := i + 1$

$$dA_{y3}{}_i := -\left(\frac{d}{d\xi} X_3{}_i \cdot \frac{d}{d\eta} Z_3{}_i - \frac{d}{d\xi} Z_3{}_i \cdot \frac{d}{d\eta} X_3{}_i\right)$$

for $i := 1; i \le n; i := i + 1$

$$dA_{z3}{}_i := \frac{d}{d\xi} X_3{}_i \cdot \frac{d}{d\eta} Y_3{}_i - \frac{d}{d\xi} Y_3{}_i \cdot \frac{d}{d\eta} X_3{}_i$$

for $i := 1; i \le n; i := i + 1$

$$dA_3{}_i := \sqrt{dA_{z3}{}_i^{\,2} + dA_{y3}{}_i^{\,2} + dA_{x3}{}_i^{\,2}}$$

$$dA_3(\xi ; \eta) := dA_3$$

$n := \text{rows}(x_4)$

for $i := 1; i \le n; i := i + 1$

$$dA_{x4}{}_i := \frac{d}{d\xi} Y_4{}_i \cdot \frac{d}{d\eta} Z_4{}_i - \frac{d}{d\xi} Z_4{}_i \cdot \frac{d}{d\eta} Y_4{}_i$$

for $i := 1; i \le n; i := i + 1$

$$dA_{y4}{}_i := -\left(\frac{d}{d\xi} X_4{}_i \cdot \frac{d}{d\eta} Z_4{}_i - \frac{d}{d\xi} Z_4{}_i \cdot \frac{d}{d\eta} X_4{}_i\right)$$

for $i := 1; i \le n; i := i + 1$

$$dA_{z4}{}_i := \frac{d}{d\xi} X_4{}_i \cdot \frac{d}{d\eta} Y_4{}_i - \frac{d}{d\xi} Y_4{}_i \cdot \frac{d}{d\eta} X_4{}_i$$

for $i := 1; i \le n; i := i + 1$

$$dA_4{}_i := \sqrt{dA_{z4}{}_i^{\,2} + dA_{y4}{}_i^{\,2} + dA_{x4}{}_i^{\,2}}$$

$$dA_4(\xi ; \eta) := dA_4$$

Areas of the element faces

$$\eta_{Gauss} := \begin{bmatrix} 0,333333333333333 \\ 0,600000000000000 \\ 0,200000000000000 \\ 0,200000000000000 \end{bmatrix} \quad \xi_{Gauss} := \begin{bmatrix} 0,333333333333333 \\ 0,200000000000000 \\ 0,600000000000000 \\ 0,200000000000000 \end{bmatrix} \quad w := \begin{bmatrix} -0,562500000000000 \\ 0,520833333333333 \end{bmatrix}$$

$$A_1 := \frac{1}{2} \cdot \sum_{i=1}^{1} w_1 \cdot dA_1\left(\xi_{Gauss_i}; \eta_{Gauss_i}\right) + \frac{1}{2} \cdot \sum_{i=2}^{4} w_2 \cdot dA_1\left(\xi_{Gauss_i}; \eta_{Gauss_i}\right)$$

$$A_2 := \frac{1}{2} \cdot \sum_{i=1}^{1} w_1 \cdot dA_2\left(\xi_{Gauss_i}; \eta_{Gauss_i}\right) + \frac{1}{2} \cdot \sum_{i=2}^{4} w_2 \cdot dA_2\left(\xi_{Gauss_i}; \eta_{Gauss_i}\right)$$

$$A_3 := \frac{1}{2} \cdot \sum_{i=1}^{1} w_1 \cdot dA_3\left(\xi_{Gauss_i}; \eta_{Gauss_i}\right) + \frac{1}{2} \cdot \sum_{i=2}^{4} w_2 \cdot dA_3\left(\xi_{Gauss_i}; \eta_{Gauss_i}\right)$$

$$A_4 := \frac{1}{2} \cdot \sum_{i=1}^{1} w_1 \cdot dA_4\left(\xi_{Gauss_i}; \eta_{Gauss_i}\right) + \frac{1}{2} \cdot \sum_{i=2}^{4} w_2 \cdot dA_4\left(\xi_{Gauss_i}; \eta_{Gauss_i}\right)$$

APPENDIX VII

Determination of the smallest enclosing circle (Mod. Weber et al. 1999, p. 393).

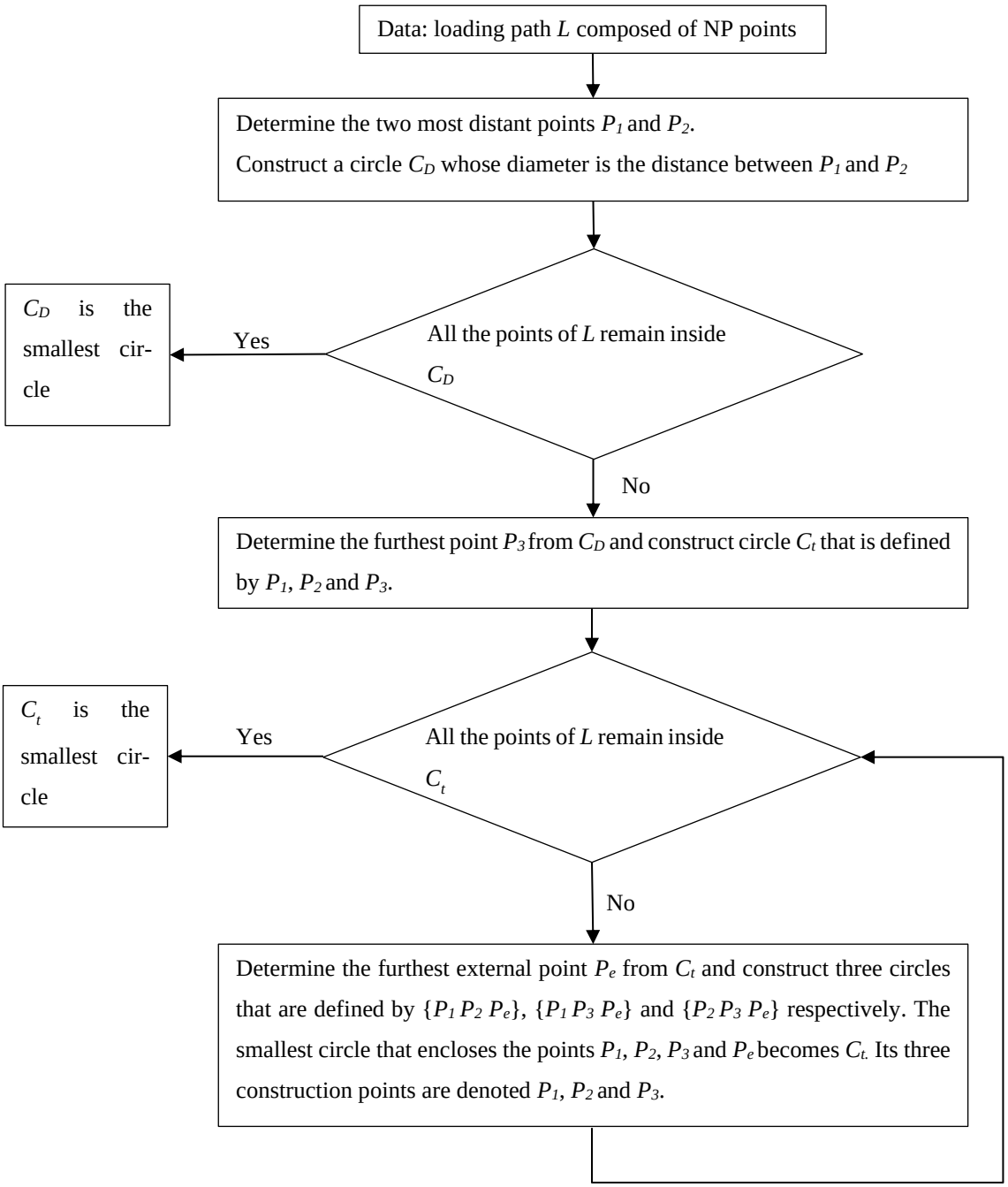

Analysis of a notched component from chapter 3.2.

Haigh diagrams:

$R_{p0.2}$	320	339.2		**K_{size}**	1.131
R_m	500	530		**K_R**	0.79
R_{mc}	-800	-848		**K_{AT}**	1
				K_N	1
k	-0.5166			**k_{red}**	-0.4617
$\sigma_{aR=-1}$	196.1			**$\sigma_{aR=-1,red}$**	175.3
$\sigma_{aR=0}$	129.3			**$\sigma_{aR=0}$**	119.9
Linear part				**Linear part, red.**	
σ_{m1}	295.9			**σ_{m1}**	304.5
σ_{af1}	43.3			**σ_{af1}**	34.7
σ_{m2}	-94.3			**σ_{m2}**	-112.1
σ_{af2}	244.9			**σ_{af2}**	227.1
Plastic tensile side				**Plastic tensile side, red.**	
Start P0:				**Start P0:**	
$\sigma_{m,P0}$	295.9			$\sigma_{m,P0}$	304.5
$\sigma_{a,P0}$	43.3			$\sigma_{a,P0}$	34.7
Intermediate P1:				**Intermediate P1:**	
$\sigma_{m,P1}$	379.7			$\sigma_{m,P1}$	379.7
$\sigma_{a,P1}$	0.0			$\sigma_{a,P1}$	0.0
End P2:				**End P2:**	
$\sigma_{m,P2}$	530.0			$\sigma_{m,P2}$	530.0
$\sigma_{a,P2}$	0.0			$\sigma_{a,P2}$	0.0

Plastic compression side				**Plastic compression side, red.**	
Start P0:				**Start P0:**	
$\sigma_{m,P0}$	-848			$\sigma_{m,P0}$	-848
$\sigma_{a,P0}$	0			$\sigma_{a,P0}$	0
Intermediate P1:				**Intermediate P1:**	
$\sigma_{m,P1}$	-429.815			$\sigma_{m,P1}$	-460.19434
$\sigma_{a,P1}$	418.1847			$\sigma_{a,P1}$	387.80566
End P2:				**End P2:**	
$\sigma_{m,P2}$	-94.328			$\sigma_{m,P2}$	-112.11675
$\sigma_{a,P2}$	244.872			$\sigma_{a,P2}$	227.08325

Statistical size factor using the weakest link theory:

$A_{eff,tot}$	113.918
A_{ref}	1039
s_{ln}	0.085
n	9.121
R	0.92682
P	0.07318
λ	-1.452
K_{size}	1.131

Excel:

λ = NORM.S.INV(***P***)

The weakest link theory:

Number of links:

$n = \frac{A_{eff}}{A_{ref}}$ when $A_{eff} > A_{ref}$

$n = \frac{A_{ref}}{A_{eff}}$ when $A_{eff} < A_{ref}$

Reliability and failure probability:

$R = \sqrt[n]{0.5}$

$P = 1 - R = \frac{1}{\sqrt{2\pi}} \int_{-\infty}^{\lambda} e^{-\frac{x^2}{2}} dx \rightarrow \lambda = \ldots$

Size factor:

$K_{size} = e^{-\lambda s_{ln,C90}}$ when $A_{eff} > A_{ref}$

$K_{size} = e^{-\lambda s_{ln,C10}}$ when $A_{eff} < A_{ref}$

, where s_{ln} is according to table 1 or 2

Calculation of A_{eff} is shown in Appendices V and VI.

S-N curves and cumulative damage analysis:

k_0	12		R_m	530		
k_∞	3		$\chi^*(r_c)$	0.3		
p_1	1.031		K_R	0.79		
p_2	0.8					
C	1.65					
r	0.01					
k and N_{af}:						
$\sigma_{a,eq}$	$\sigma_{m,eq}$	k	N_{af}			
159.7	87.6	7.316	2031948			
55.5	82.4	7.411	2061901			
65	81.8	7.423	2065335			
146	86.5	7.336	2038312			
76.1	82	7.419	2064191			
Failure probability:						
λ	-3.09					
P	0.001					
$s_{ln,C90}$	0.12					
S_F	1.449					
k_{red}	-0.4617431					
$\sigma_{aR=-1,red}$	175.314115					
Bin	σ_{af} **(med)**	S_F	s_N	$s_{ln,H}$	$S_{F,H}$	
1 (LCF)	134.9	1.449	0.878	0.070	1.240	
2 (HCF)	137.3	1.449	0.889	0.069	1.239	
3 (HCF)	137.5	1.449	0.891	0.069	1.239	
4 (LCF)	135.4	1.449	0.880	0.069	1.239	
5 (HCF)	137.5	1.449	0.890	0.069	1.239	
Bin	$\sigma_{af,P}$	$\sigma_{af,PH}$	N	n	D_{LC}	D_{HC}
1 (LCF)	93.1	108.801	39156	4500	0.1149	
2 (HCF)	94.7	110.787	14576797703	250000		0.0001276
3 (HCF)	94.9	111.016	2000357218	150000		0.00056
4 (LCF)	93.4	109.221	77115	6000	0.0778	
5 (HCF)	94.9	110.940	260797621	200000		0.0057195
				Σ	0.19273099	0.0064071
				D_{tot}	0.1991	

Slope exponent (default):

$$k = \frac{k_0 - k_\infty}{(1+\chi^*)^{p_1} + \frac{1}{K_R^{p_2}} - 1} \cdot \left[1 - \frac{C \cdot \frac{\sigma_m}{R_m}}{(1+\chi^*)^r}\right] + k_\infty$$

Number of cycles at the knee point (default):

$$N_{af} = 10^{6.8 - \frac{3.6}{k}}$$

Safety factor:

$S_F = e^{-\lambda s_{ln}}$, where λ according to allowed failure probability.

$s_N = k s_{ln}$ $s_{ln,H} = \frac{s_N}{2k-l}$ $S_{F,H} = e^{-\lambda s_{ln,H}}$

$$\sigma_{af,P} = \frac{\sigma_{af}}{S_F} \qquad \sigma_{af,PH} = \frac{\sigma_{af}}{S_{F,H}}$$

$$N_P = N_{af}\left(\frac{\sigma_{af,P}}{\sigma_a}\right)^k \qquad N_{PH} = N_{af}\left(\frac{\sigma_{af,PH}}{\sigma_a}\right)^{2k-l}$$